

**Characterization of silicon microstrip sensors,
front-end electronics, and prototype tracking
detectors for the CBM experiment at FAIR**

Dissertation
zur Erlangung des Doktorgrades
der Naturwissenschaften

vorgelegt beim Fachbereich Physik
der Johann Wolfgang Goethe-Universität
in Frankfurt am Main

von
Iurii Sorokin
aus Vinnitsa

Frankfurt am Main 2013
(D 30)

vom Fachbereich Physik der Johann Wolfgang Goethe-Universität
als Dissertation angenommen.

Dekan: Prof. Dr. Joachim Stroth

Gutachter: Prof. Dr. P. Senger

Prof. Dr. Joachim Stroth

Datum der Disputation:

Contents

Abstract	5
Kurzfassung	7
1 Introduction	9
1.1 The Compressed Baryonic Matter experiment	10
1.1.1 The physics case	10
1.1.2 The experimental setup	13
1.2 The Silicon Tracking System	17
1.2.1 Requirements	17
1.2.2 Design and layout	18
1.2.3 Sensors	19
1.2.4 Front-end electronics	20
1.2.5 Performance simulations	21
2 Prototype components	23
2.1 Sensors	23
2.2 Front-end electronics	30
2.3 Prototype tracking stations	31
2.3.1 Electronics connection schemes	31
2.3.2 Prototype tracking stations	34
3 Evaluation of signal and noise in a silicon strip detector	36
3.1 Evaluation of the signal amplitude	36
3.2 Evaluation of the equivalent noise charge	41
3.3 Evaluation of the noise rate	43
3.3.1 The Rice formula	43
3.3.2 Test of the Rice formula applicability to real systems	45
4 Measurement of the passive electrical characteristics of silicon strip sensors	50
4.1 Probe station	51
4.2 Capacitance measurement with LCR meter	51

4.3	Bulk I-V characteristic	53
4.4	Bulk C-V characteristic	54
4.5	Interstrip resistance	56
4.6	Bias resistance	58
4.7	Strip leakage current	59
4.8	Coupling capacitance	60
4.9	Capacitance of implant to neighboring strips	64
4.10	Capacitance of a strip to the neighbors	70
4.11	Capacitance of the fan-out boards	72
5	Characterization of the n-XYTER readout ASIC	73
5.1	Chip architecture	73
5.2	n-XYTER operation	75
5.3	Optimization of the register settings	75
5.4	Dependence of the amplitude and the noise on the input load . . .	77
5.5	Dependence of the n-XYTER response on the pulse width	79
5.6	Gain calibration	80
5.6.1	Generation of the reference charge pulses	80
5.6.2	Calibration results	82
5.6.3	Uncertainty estimate	84
5.6.4	Cross-check with a silicon detector	86
6	Electronic noise reduction	88
6.1	Noise of the bias voltage power supply	88
6.2	Common-mode noise of the FEE power supplies	91
6.3	Noise coupling through the 230 V power line	93
6.4	Noise radiation from the n-XYTER digital back end	95
6.5	Noise shunting	96
6.6	Noise from the switched-mode DC-DC converters on the ROC . .	97
7	Operation of prototype detector systems	99
7.1	Universal Read-Out Controller (ROC)	99
7.2	Data acquisition system	102
7.3	ROC and FEB configuration	102
7.4	GO4-based analysis	104
7.5	EPICS for slow control	106
8	Measurements of noise and amplitude response to β^- and γ radiation	107
8.1	Measurement of the noise and the baselines	107
8.2	Cluster and spacepoint reconstruction	108
8.3	Measurement of the amplitude response to β^- and γ radiation . .	109
8.4	Amplitude vs. bias voltage in a CBM02 sensor	113

8.5	Reproducibility of the amplitude measurement	119
9	Study of the amplitude response of the CBM02 sensors on a proton beam	122
9.1	Experimental setup	122
9.2	Time correlation with the reference scintillator signal	124
9.3	Beam intensity and temporal structure	125
9.4	Beam profile	125
9.5	Baseline measurement and stability	127
9.6	Total cluster amplitude	128
9.6.1	Qualitative analysis of the spectra	128
9.6.2	Total cluster amplitude and its dependence on the bias voltage	135
9.6.3	Correlation of the total cluster amplitude on the p- and the n-sides	138
9.7	Major strip amplitude	139
9.8	Time resolution	141
9.9	Experience with the floating FEE	142
10	Test of the radiation hardness of CBM04 sensors on a proton beam	145
10.1	Experimental setup	145
10.2	Individual events and cluster reconstruction	147
10.3	1-strip cluster amplitude in irradiated sensors	147
10.4	Track fitting and residual distributions	149
	Summary	153
	Conclusions and outlook	160
	Zusammenfassung	161
	References	169
	Acknowledgements	175
	Curriculum Vitae	177

Abstract

The Compressed Baryonic Matter (CBM) experiment will explore the phase diagram of strongly interacting matter in the region of high net baryonic densities. The matter at the extreme conditions will be studied in collisions of a heavy ion beam with a fixed heavy element target.

The present work is devoted to the development of the main component of the CBM experiment — the Silicon Tracking System (STS). The STS has to enable reconstruction of up to 1000 charged particle tracks per nucleus-nucleus interaction at the rate of up to 10 MHz, provide a momentum resolution $\Delta p/p$ of 1 %, and withstand the radiation load of up to 10^{14} $n_{\text{eq}}/\text{cm}^2$ (n_{eq} — neutron equivalent). The STS will be based on double-sided silicon microstrip sensors, that will be arranged in 8 planes in the aperture of the dipole magnet. Self-triggering readout electronics will be located on the periphery of the detecting planes, and connected to the sensors with low mass microcables.

In the stage of R&D, as well as in the stages of pre-series and series production, characterization of the sensors, of the front-end electronics, and of the complete detector modules has to be performed. In the present work the required techniques were developed, and the performance of the latest detector prototypes was evaluated. A particular attention is paid to evaluation of the signal amplitude, as it is one of the most important detector characteristics.

Techniques for measuring the passive electrical characteristics of the sensors were developed. These include: the coupling and the interstrip capacitances, the interstrip resistance, the bias resistance, the strip leakage current, the bulk capacitance, and the bulk leakage current. The techniques will be applied for the quality assurance of the sensors during the pre-series and the series production.

Extensive characterization of the prototype readout chip, n-XYTER, was performed. The register settings were optimized, and the dependence of the amplitude response on the input load, as well as on the pulse width was determined. The preamplifier input capacitance was extracted. A thorough gain calibration is done and verified with an independent signal source (silicon pad diode). Taking the advantage of the available tools, the Rice formula for estimation of the noise rate in the self-triggering systems was validated on the n-XYTER chip, which enabled to apply it for defining the shaping times of the dedicated STS readout chip STS-XYTER.

Three prototype tracking detectors were assembled. Their design was refined to suppress the electronic noise from the external sources (power supplies etc.). The successful solutions for the noise suppression will be applied in designing the STS detector module.

Amplitude response of the assembled prototype detectors to β^- and γ radiation, as well as to 3 GeV/c protons was measured. To check if the observed values are as should be expected, an accurate analytical model of the detector was developed. The model takes into account the processes of charge sharing between the strips, as well as the finiteness of the input capacitance of the front-end electronics. With the sensor prototypes CBM02, CBM03', and CBM04 (assuming the same interstrip and coupling capacitance as in CBM02) the observed most probable signal amplitude is systematically lower by around 20 % than the expected from the model. Presumably, it is connected with the design of the sensors. If a similar amplitude deficit will be observed with the newest CBM05 sensors, a detailed investigation of the effect has to be carried out.

Radiation hardness of the CBM04 sensors was studied. No degradation of the signal amplitude after neutron irradiation to 10^{12} n_{eq}/cm² is observed. After irradiation to 10^{13} n_{eq}/cm², the signal amplitude drops down by 8 % and 18 % on the n- and the p-side respectively, which is considered as acceptable. Further studies with irradiation up to 10^{14} n_{eq}/cm² are still to be performed.

Kurzfassung

Das Compressed Baryonic Matter (CBM) Experiment wird das Phasendiagramm stark wechselwirkender Materie in Bereichen hoher baryonischer Dichten untersuchen. Materie unter diesen extremen Bedingungen wird in Kollisionen von einem Schwerionenstrahl mit einem Target bestehend aus schweren Elementen untersucht werden.

Die vorliegende Arbeit behandelt die Entwicklung des zentralen CBM Detektorsystems — des Siliziumspurdetektors STS. Dessen Aufgabe ist die Rekonstruktion der Spuren aus den Wechselwirkungen des SIS-100 oder SIS-300-Ionenstrahls mit dem Target. Bis zu 1000 geladene Teilchen werden pro Kernreaktion erzeugt; die Kollisionsraten werden bis zu 10 MHz betragen. Die Impulsmessung der Spuren im Feld des supraleitenden Dipolmagneten soll mit einer Auflösung von bis zu $\Delta p/p = 1\%$ erfolgen. Der STS wird aus doppelseitigen Silizium-Mikrostreifensensoren aufgebaut, die mit selbsttriggernder Elektronik ausgelesen werden. Die Sensoren werden auf acht planaren Stationen angeordnet, die unter einem polaren Öffnungswinkel von 2.5° – 25° im Dipolmagneten installiert werden. Die selbsttriggernde Ausleseelektronik, die mit den Sensoren über ultraleichte Mikrokabel verbunden werden, wird an der Peripherie der Ausleseebenen befestigt werden.

In der Entwicklungs- als auch in der Vorserien- und Serienproduktionsphase ist es notwendig, die Eigenschaften der Sensoren, der Ausleseelektronik als auch kompletter Detektormodule zu bestimmen. In der vorliegenden Arbeit wurde hierzu die erforderlichen Methoden entwickelt und die Performance der jüngsten Detektor-Prototypen ermittelt. Als wichtigste Detektoreigenschaft wurde hierbei besonderes Augenmerk auf die Signalamplitude gelegt.

Methoden zur Messung der passiven elektrischen Eigenschaften wurden entwickelt. Diese beinhalten die Kopplungs- und Zwischenstreifenkapazität, den Zwischenstreifenwiderstand, den Vorwiderstand, den Streifen-Leckstrom, die Gesamtkapazität und den Gesamt-Leckstrom. In der Vorserien- und Serienproduktion werden diese Methoden Anwendung finden.

Eine umfangreiche Charakterisierung des Prototypen-Auslesechips wurde durchgeführt. Hierzu wurden die Registereinstellungen optimiert und die Abhängigkeit der erhaltenen Signalamplitude von der Amplitude und Pulsbreite des Eingangssignals bestimmt. Des Weiteren wurde die Eingangskapazität des

Vorverstärkers ermittelt und eine sorgfältige Eichung der Verstärkung durchgeführt, welche mit einer unabhängigen Signalquelle (Pad-Diode) verifiziert werden konnte. Es zeigte sich, dass die Rice-Formel, die zur Abschätzung der Rauschzählrate in selbsttriggernden Systemen dient, auf den n-XYTER-Chip angewendet werden kann, weshalb sie zur Festlegung der Shaping-Time des speziell als STS-Auslesechip entwickelten STS-XYTER herangezogen werden kann.

Drei Trackingdetektor-Prototypen wurden zusammengebaut. Das entsprechende Design wurde hinsichtlich der Unterdrückung von elektronischem Rauschen optimiert (z.B. Spannungsversorgung). Die hinsichtlich der Unterdrückung von elektronischem Rauschen erfolgreiche Lösung wird auf das Design der STS-Detektormodule angewendet.

Die Amplitudenausbeute der zusammengebauten Prototyp-Detektoren bei Beschuss mit β^- - und γ -Strahlung sowie 3 GeV/c Protonen wurde vermessen. Um zu überprüfen, ob die beobachteten Werte den erwarteten entsprechen, wurde ein analytisches Detektormodell entwickelt. Das Modell berücksichtigt Prozesse der Ladungsaufteilung zwischen Streifen als auch die endliche Eingangskapazität der Front-end-Elektronik. Die Sensor-Prototypen CBM02, CBM03', und CBM04 (unter der Annahme der zu CBM02 identischen Zwischenstreifen- und Kopplungskapazität) zeigen eine gegenüber dem Modell um etwa 20% reduzierte, wahrscheinlichste Amplitude. Vermutlich ist dies mit dem Sensordesign in Verbindung zu bringen. Wird ein vergleichbarer Amplitudenverlust ebenfalls bei der neuesten Sensorgeneration CBM05 beobachtet, muss eine detaillierte Untersuchung des Effekts erfolgen.

Die Strahlenhärte des CBM04-Sensors wurde untersucht. Es wurde keine Abschwächung der Signalamplitude nach Neutronenbeschuss mit von 10^{12} n_{eq}/cm² festgestellt. Nach Neutronenbeschuss von 10^{13} n_{eq}/cm² fällt die die Signalamplitude um 8 % auf der n-Seite und um 18 % auf der p-Seite, was als akzeptabel angesehen wird. Weitere Studien mit Bestrahlung von bis zu 10^{14} n_{eq}/cm² stehen aus.

Chapter 1

Introduction

In the past decades substantial experimental and theoretical efforts have been devoted to the study of the properties of strongly interacting matter at extreme temperatures and densities. The interest to this field of physics is driven by the predictions of existence of another state of matter, the Quark-Gluon Plasma (QGP), consisting of unbound quarks and gluons [1, 2]. QGP is remarkable because so far no free quarks or gluons have been observed. Confinement of quarks is the fundamental property of QCD, that has not been fully understood yet. Investigation of the strongly interacting matter at high densities and temperatures, where QGP is expected to exist, should therefore help to improve our knowledge on the confinement and QCD.

Another very important phenomenon, that is expected to take place in QGP, is the restoration of the chiral symmetry. At low temperatures and densities the chiral symmetry is broken in QCD, which results in the fact that the hadrons are massive. The Higgs mechanism breaks the chiral symmetry explicitly, and gives to the quarks their current masses. For the hadrons, consisting of the light quarks (u and d), the sum of the current masses of the valence quarks is only around 1 % of the mass of the hadron. The major fraction of the hadron mass is generated by the interaction of the quarks with the chiral condensate [9] (spontaneous chiral symmetry breaking). The latter effect is expected to vanish in QGP. Studying the matter at extreme conditions should therefore help to understand better the mechanisms of the mass generation.

The transition between the hadronic and the QGP phase is also a matter of discussion. A sketch of the phase diagram of the strongly interacting matter is illustrated in Fig. 1.1. Lattice QCD calculations, performed at low net baryonic densities, show a crossover (i.e. a smooth transition) between baryonic matter and QGP [4, 5]. At high net baryonic densities a first order phase transition is predicted [6, 7, 8].

There are models, that predict also other phases of strongly interacting matter, such as the quarkyonic phase [12], and the color superconductor [10, 11], but so far no evidences for their existence have been found.

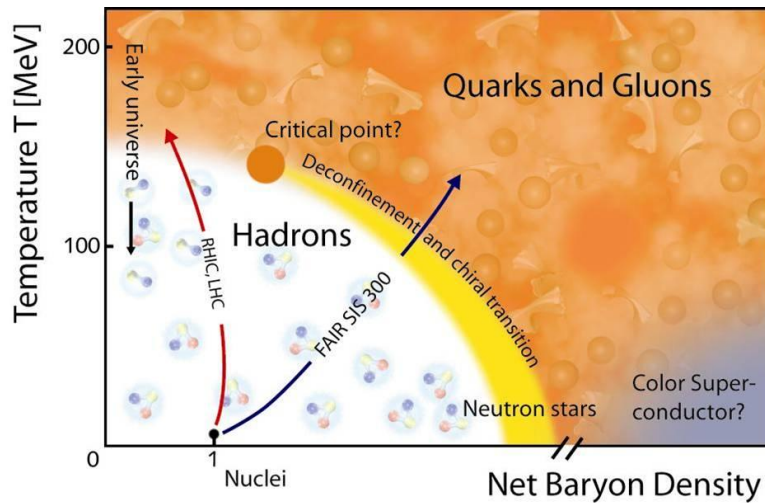


Figure 1.1: A sketch of the phase diagram of strongly interacting matter.

It is argued that QGP filled the universe in the first microseconds after the Big Bang, and now can exist in the cores of compact stellar objects, such as neutron stars. The equation of state of strongly interacting matter is therefore of great interest for astrophysics.

Matter in extreme states is studied in collisions of nuclei in experiments at AGS (BNL, Brookhaven), SIS-18 (GSI, Darmstadt), SPS (CERN, Geneva), RHIC (BNL, Brookhaven), LHC (CERN, Geneva). A next generation experiment, the Compressed Baryonic Matter (CBM) experiment at FAIR (Darmstadt), will explore the phase diagram of strongly interacting matter in the region of highest net baryonic densities, achievable in heavy ion collisions. So far this region of the phase diagram has been only poorly investigated. The present work is devoted to the development of the main element of the CBM experimental setup — the Silicon Tracking System.

1.1 The Compressed Baryonic Matter experiment

1.1.1 The physics case

The Compressed Baryonic Matter (CBM) experiment is aiming at exploration the QCD phase diagram in the region of high net baryonic densities. It will operate at the Facility for Antiproton and Ion Research (FAIR) [13] in Darmstadt.

The main physics questions CBM is going to address, are:

- Is there a transition from hadronic matter to QGP at high net baryonic

densities? If yes, is it a first order phase transition? Where is the phase boundary? What is the location of the critical endpoint?

- Is the chiral symmetry restored at high net baryonic densities? Does the restoration of the chiral symmetry coincide with the onset of deconfinement?
- What are the properties of hadrons in dense baryonic matter?
- What is the equation of state (EOS) of the dense strongly interacting matter in the region of high net baryonic densities?
- Are there other phases of strongly interacting matter?

To address these questions CBM will investigate collisions of heavy ion and proton beams with fixed, heavy element targets, at beam energies from 2 to 35 AGeV (up to 45 AGeV for light nuclei and 90 AGeV for protons). With large beam intensity very high reaction rates can be achieved, which results in unprecedented statistical significance. Hence, particles with extremely low production cross sections can be identified.

Resting upon the fixed target approach and the large beam intensities CBM is aiming to achieve unprecedented sensitivity in particle reconstruction. In Figure 1.2 a calculation of the particle multiplicities times branching ratio in central Au–Au collisions at 25 AGeV, calculated with the HSD transport code [14] and the statistical model [15]. For the vector mesons ρ , ω , ϕ , J/ψ , ψ' , the decay into lepton pairs is assumed, and for the D-mesons the hadronic decay into kaons and pions. CBM will measure particle yields which vary by 15 orders of magnitude.

The rich physics program of the CBM experiment includes the studies of both the bulk and the rare probe observables, and the main of them are summarized below.

Strangeness production. Enhanced strangeness production was proposed as a possible signal for the QGP long ago ([16]). In the parton-parton interaction scenarios strange quarks are expected to be produced more abundantly than in hadronic reaction scenarios. As a result, the yields of strange particles, scaled by the number of participating nucleons, expected to be higher in heavy ion collisions with creation of a QGP than in p+p interactions. This effect is expected to be especially pronounced for multistrange hyperons. Indeed, at SPS enhancement of the yields of all strange particles was observed in Pb+Pb collisions [17, 18, 19].

These results show that strangeness production is an essential observable with possible connection to a phase transition. Systematic high-precision measurements of these observables as function of collision energy appear a very promising strategy for the detailed investigation of the deconfinement phase transition.

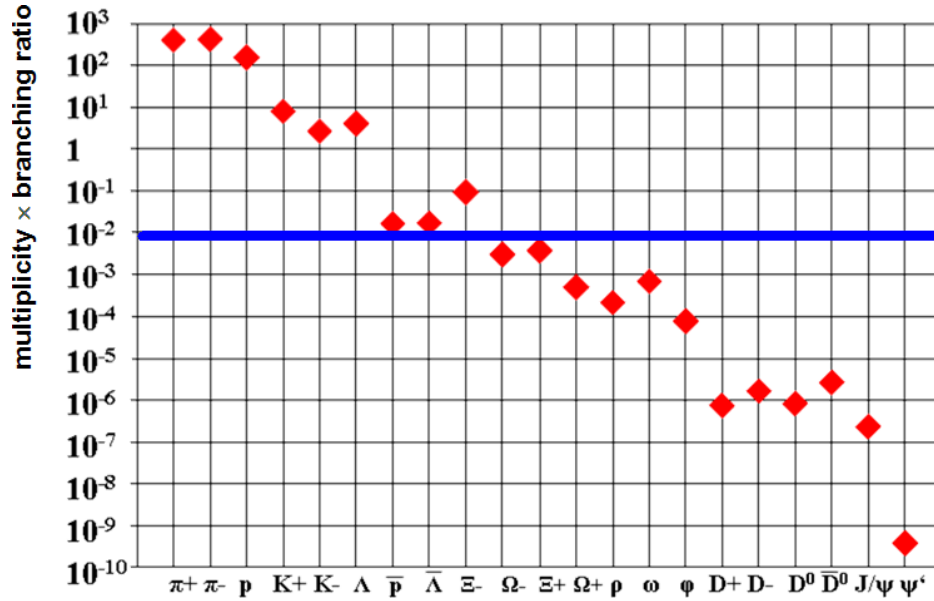


Figure 1.2: Particle multiplicities times branching ratio in central Au–Au collisions at 25 AGeV (see text). The blue line indicates the sensitivity in particle reconstruction, achieved by other experiments in this energy range in heavy ion collisions. At CBM all the specified particles are going to be measured.

Collective flow. Anisotropy of the particle yields in the momentum space, or collective flow, gives valuable information on the space-time evolution of the fireball. Thus, the strength of the elliptic flow and its dependence on the particle transverse momentum can shed light on the degrees of freedom which prevail in the early stage of the collision. For example, the observed scaling of the elliptic flow with the number of constituent quarks at RHIC [20] (which is however, not confirmed at LHC) is interpreted as a direct signature for partonic collectivity.

The comparison of data to hydrodynamical calculations with and without quark matter EoS, and to hadron transport models with and without early partonic phase, can help to answer the question whether QGP has been formed in heavy-ion collisions.

Dileptons. Restoration of the chiral symmetry leads to a degeneration of the spectral functions of chiral partners such as the ρ -meson and the a_1 -meson. While the a_1 -meson is very difficult to measure in the nuclear medium, the in-medium spectral function of the ρ -meson is accessible via the measurement of its decay into lepton pairs.

Experimental results on dimuon invariant mass spectra are compatible with the assumption of a broadening of the ρ -meson in-medium mass distribution [21]. However also hadronic many-body effects contribute to the broadening.

Open and hidden charm. Because of its large mass, charm quarks can be produced only in the hard processes in the early stage of the collision. The production is sensitive to the nature (partonic or hadronic) of the medium. In a partonic medium the energy threshold for production of a $c\bar{c}$ pair is smaller than the threshold for production of charmed hadrons in a hadronic medium. Therefore, the yields of charmed hadrons is a sensitive probe to the state in the fireball on the initial state of the collision.

As $c\bar{c}$ pairs are produced back-to-back, it is more probable that they hadronize in open charm mesons, rather than in charmonium. During the evolution of the fireball, the charm quarks (or open charm hadrons) undergo exchange of the momentum with the medium, which depends strongly on the state of the medium (hadronic or partonic). Therefore, momentum distributions, correlations, and elliptic flow of open charm hadrons is another important diagnostic probe of the prevailing degrees of freedom on the early collision stage.

Charmonium states is another observable, sensitive to the conditions in the fireball. In a deconfined medium charmonium states are expected to dissociate into c and \bar{c} quarks due to the color screening effects [22].

This effect was investigated in the NA50 and NA60 experiments in the Pb+Pb and In+In collisions at 158 AGeV [23]. The J/ψ yield was measured as a function of the number of the participating nucleons (N_{part}) and compared to the expected yield. The expected yield was calculated from the J/ψ production cross section measured in p+A collisions at the same beam energy. The measured yield agreed with the expectation in both Pb+Pb and In+In collisions at N_{part} up to 200, whereas in central Pb+Pb collisions a suppression of the J/ψ yield by up to 20–30 % was observed.

Event-by-event fluctuations. In the vicinity of the deconfinement phase transition critical density fluctuations have been predicted to cause non-statistical event-by-event fluctuations of experimental observables. Thus, for example, the ratios of hadron yields, are expected to provide evidence of a phase transition, as shown by lattice QCD calculations [24]. In [25] it has been argued that event-by-event fluctuations directly reflect thermodynamic properties of the system near its critical point. Especially higher moments (skewness, kurtosis) of the fluctuations are expected to be particularly sensitive in the vicinity of the critical endpoint [26].

1.1.2 The experimental setup

The challenging physics program of the CBM experiment requires high performance detector system. The charged products of the nuclear interactions have to be identified with high efficiency, and their momentum has to be reconstructed with high resolution. Secondary vertices need to be identified with the precision

on the order of tens of microns. Leptons need to be separated from the pion background. Finally, the reaction plane need to be reconstructed.

The experimental setup is shown in Fig. 1.3. CBM will operate in two configurations: one optimized for reconstruction of electrons, the other — for muons. Below each of the detector subsystems will be briefly described. The Silicon Tracking System will be described separately in the next section.

Micro-Vertex Detector. The main task of the Micro-Vertex Detector is to enable the reconstruction of open-charm and open-bottom particles by displaced vertices. MVD will also provide additional information for the tracking algorithms, improving the reconstruction efficiency and momentum resolution, especially at the low momenta. Finally, it can help to resolve events that overlap in time, if their primary vertices are sufficiently separated in space.

The Micro-Vertex Detector is going to be based on silicon pixel sensors. The choice is motivated by the expected extremely high particle densities in the MVD detector stations (up to about 3 hits/mm²/collision [27, pp. 52-54]). The sensors are going to be organized in 3 stations at the distance of 5, 10 and 15 cm from the target. Each station will consist of two layers of sensors, organized in a staggered way. The stations will be placed in a vacuum chamber, together with the target.

It is decided to use sensors of monolithic active pixel (MAPS) type. The choice is driven by the requirement of low material budget [28]. The current working sensor prototype is MIMOSA-26 [29]. Finally, sensors of this family are going to be used. As a supporting structure for the sensors CVD-diamond sheets will be used. This will provide good mechanical stability in combination with low material budget. The CVD-diamond support will also serve as a heat sink for the sensors (diamond has around five times higher thermal conductivity than copper).

Ring Imaging Cherenkov Detector (RICH). The task of the RICH detector is to identify electrons and positrons, and especially discriminate them from pions, in the momentum range below 10 GeV/c. Therefore, as the radiator CO₂ will be used, providing the threshold of Cherenkov light radiation for pions of 4.65 GeV/c.

RICH will be located behind the dipole magnet, about 1.6 m downstream of the target. As photon detectors MAPMTs (such as, for example H8500 from Hamamatsu Photonics) are going to be used. Mirrors (Al+MgF₂ coating) will be used to direct the light to the MAPMTs.

Simulations predict up to about 100 Cherenkov rings per central Au+Au collision at 25 AGeV. To reliably reconstruct such events, high detector granularity and large number of channels is required (currently planned around 55000 channels). Thanks to the expected large number of photons emitted per electron, a pion suppression factor of around 500 is expected to be achieved.

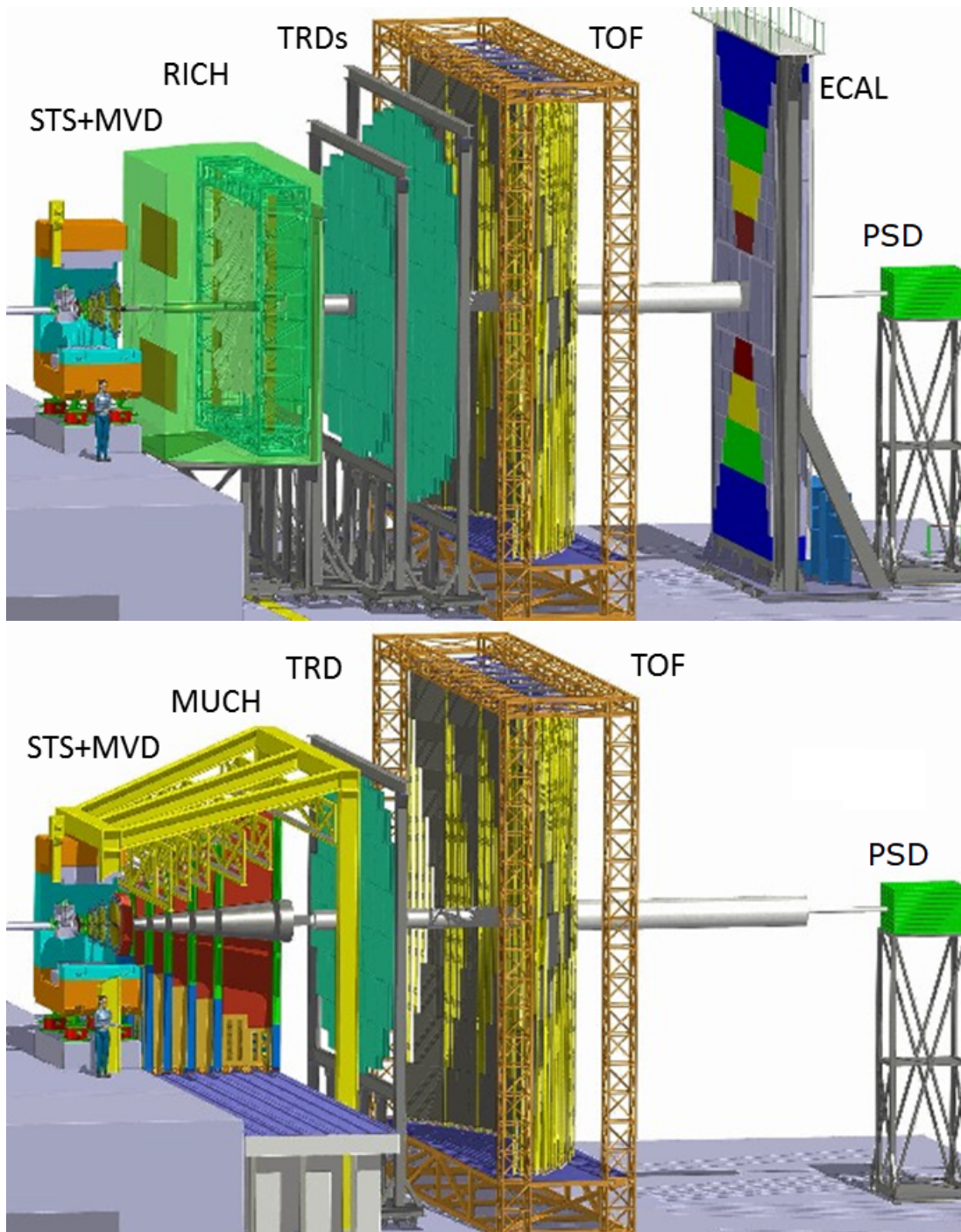


Figure 1.3: The CBM experimental setup in the electron configuration (top), and in the muon configuration (bottom)

Muon detector (MUCH). The experimental challenge for muon measurements at CBM is to identify low-momentum muons in an environment of high particle densities. In order to reduce the muon background from the meson decays the muon detector has to be as compact as possible. It will be located right after the Silicon Tracking System.

The muon detector will employ the standard filtering technique. The final design of the muon detector will consist of 6 absorbers (60 cm carbon, then 20 cm, 20 cm, 30 cm, 35 cm and 100 cm of iron) and 18 gaseous tracking chambers located in triplets behind each absorber slab. Between the absorbers, triplets of tracking detectors (stations) will be installed. For J/ψ measurements at SIS-100 a MUCH start version with 3 chamber triplets has been found to be sufficient.

The expected hit densities in the first MUCH station are of about 0.3 hits/cm² per central Au-Au collision. At the reaction rate of 10 MHz this translates into hit rate of 3 MHz/cm². To cope with such high hit rates, GEMs are going to be used as the tracking detectors. In the last stations, where the hit rates are much smaller, and larger areas have to be covered, straw tubes will be used.

Transition Radiation Detector (TRD). The task of the TRD is to separate the electron and positron candidates from the pion background. The particle identification is based on the effect that ultrarelativistic charged particles produce transition radiation when traverse a boundary between media with different dielectric constants. To detect the produced transition radiation multiwire proportional chambers (MWPC) will be used.

TRD will consist of three stations, located at 5 m, 7.2 m, and 9.5 m from the target, behind the Muon or the Cherenkov detector. Each station will have four detecting layers.

The expected pion suppression factor with 9 layer detector is above 100 at an electron detection efficiency of 90%. TRD will be effective at momenta above 1.5 GeV/c ($\gamma \geq 1000$). For measurements at SIS-100 only one station with three detector layers will be used as an intermediate tracker between the STS and the TOF wall.

Time of Flight wall. For identification of low momentum hadrons the time of flight method is going to be used. The stop detector is the Time of Flight wall. It is located around 6 m downstream the target in the configuration at SIS-100 and 10 m in the configuration at SIS-300. The detector will have to provide time resolution of around 80 ps, and cope with hit rates of up to 20 kHz/cm². To achieve it, multigap resistive plate chambers (MRPC) are going to be used. Simulations predict efficient separation of kaons from pions in the momentum range up to 3.5 GeV/c, and protons from kaons — up to 6 GeV/c [30].

Electromagnetic calorimeter. In CBM, the electromagnetic calorimeter is required to measure direct photons and neutral mesons, decaying into photons. The calorimeter will be composed of a stack of 140 layers of 1 mm lead converter, interleaved with 1 mm layers of scintillator. Similar calorimeters work(ed) successfully in the HERA-B, PHENIX and LHCb experiments. In the design particular emphasis is put on a good energy resolution and a high pion suppression factor.

Projectile spectator detector. The projectile spectator detector is a forward hadron calorimeter, which will be used to determine the centrality and the orientation of the reaction plane. These collision parameters are of crucial importance for studying the event-by-event fluctuations. In addition, the flow analysis requires to measure the reaction plane in a way that does not involve the collision participants. PSD will measure the number of spectator nucleons.

PSD is a full compensating lead-scintillator calorimeter. It will consist of 44 modules of area 20×20 cm² each. The modules will be made out of 60 lead/scintillator layers. The scintillation light will be read out with Multi-Avalanche Photo-Diodes (MAPD) via wavelength shifting fibers.

1.2 The Silicon Tracking System

The task of the Silicon Tracking System (STS) is to reconstruct the tracks of the charged particles, created in the heavy ion collisions, and to measure their momenta with high resolution. STS will be located in the aperture of the dipole magnet, directly downstream the Micro-Vertex detector.

1.2.1 Requirements

To fulfill the challenging physics program of the CBM experiment the following requirements have to be satisfied [31]:

- reconstruction of up to 1000 tracks per collision (charged multiplicity in central A+A collisions)
- reconstruction of up to 10^6 events per second (maximum rate of minimum bias collisions)
- track reconstruction efficiency $\geq 95\%$ at momenta ≥ 1 GeV/c
- single hit reconstruction efficiency better than 99%
- momentum resolution $\Delta p/p$ around 1% at $p \geq 1$ GeV/c
- time resolution 10 ns

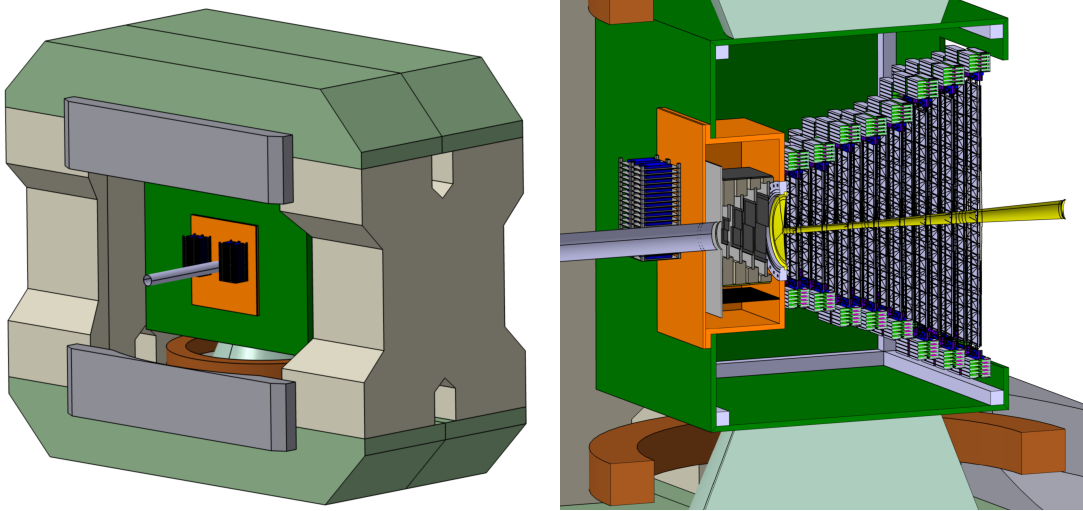


Figure 1.4: Left: CAD model of the dipole magnet with the STS inside (green box). Right: CAD models of the STS and the MVD (orange box) are shown. Eight STS half-stations with the front-end electronics on the periphery can be seen. The beampipe is shown in yellow and light blue, and the magnet coil is in brown.

- radiation hardness 10^{13} n_{eq} during the operation at SIS-100, and 10^{14} n_{eq} at SIS-300 (required in the innermost region of the first stations)
- acceptance in polar angle $2.5^\circ < \Theta < 25^\circ$

1.2.2 Design and layout

The Tracking System will be based on double-sided silicon microstrip sensors, arranged in eight planar stations, perpendicular to the beam axis (Fig. 1.4). The stations will be located at the distances from 30 cm to 100 cm from the target, with about 10 cm spacing from each other. The readout electronics will be placed outside of the detector acceptance, in order to minimize the material budget, and connected to the sensors with microcables. The sensors will be mounted on low mass carbon-fiber support structures.

The positioning of the sensors within the stations has been optimized with respect to physics performance (evaluated with the full detector simulation) and construction effort. In Fig. 1.5 the layout of one of the stations is shown as an example. Generally, sensors of three different sizes are going to be used: 6.2×6.2 cm², 6.2×4.2 cm², and 6.2×2.2 cm². The sensors have same number of strips, but different strip length. The smaller sensors will be placed in the inner region of the stations, close to the beam pipe, to adopt to the large hit densities (Fig. 1.6). The outer region will be covered with large sensors. In the most outer region the sensors are going to be daisy-chained in order to reduce the number of

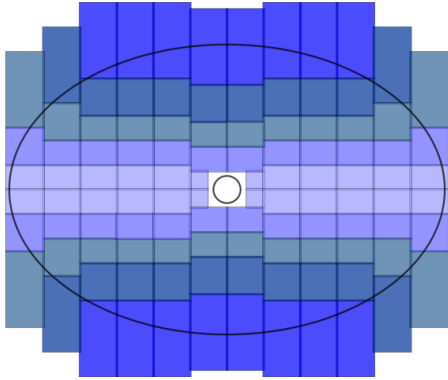


Figure 1.5: Layout of sensors in the third STS station.

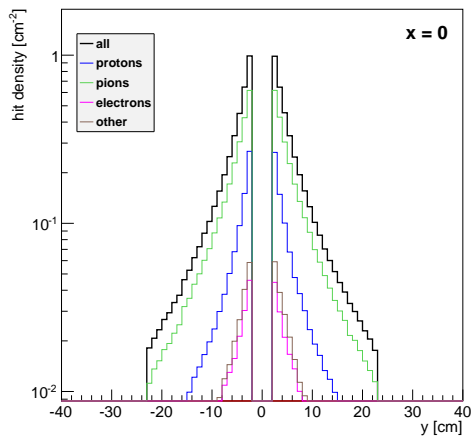


Figure 1.6: Hit density in the third STS station. Average value for minimum-bias Au+Au collision at 25 AGeV is shown.

readout channels. The holes in the vicinity of the beampipe will be closed with sensors of smaller, non-standard size. Sensors will be positioned with overlaps, to leave no dead area between them.

1.2.3 Sensors

In order to keep the material budget at the minimum, double-sided sensors are going to be applied in the STS. The strips on the n-side of the sensor will be at the right angle with respect to the sensor edges (like in Fig. 2.4), while on the p-side the strips will be inclined by 7.5° (like in Fig. 2.3). This allows to keep the number of ghost hits at minimum, while still enables sufficient resolution in the along-the-strip direction [33].

The stereoangle of 7.5° results in having shorter strips at the edges to the sensor (Fig. 1.7). The short-length strips are interconnected with each other as shown in Fig. 1.7. This enables to read out all strips from one side of the detector, which is highly desirable from the engineering point of view.

Two approaches to interconnect the short-length strips are considered. The preferred way is to do it with the second metalization layer on the sensor. However, the recent findings in LHCb shown that the second metalization layer may lead to degradation of the signal amplitude [34, 35]. In addition, fabrication of the second metalization layer complicates the production process, and may result in lower sensor yield or worse sensor quality. An alternative approach is to interconnect the short-length strips with a microcable, placed directly on the sensor surface (Fig. 1.8). Additional contact pads have to be foreseen for this.

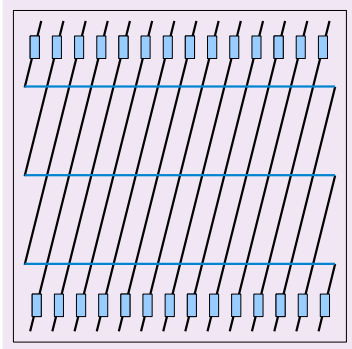


Figure 1.7: Schematic illustration of interconnection of the short-length strips. Three short-length strips are depicted on the left edge of the sensor, and three on the right. The blue lines represents their interconnection. The full sensor area can be read out from only one (top or bottom) edge of the sensor.

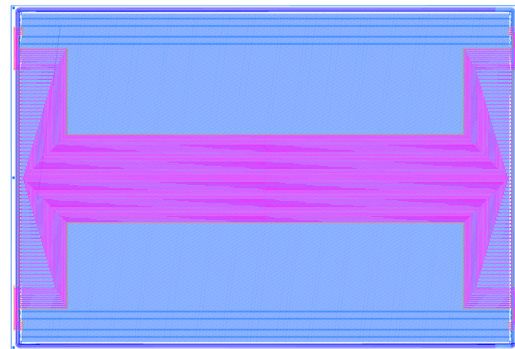


Figure 1.8: Layout of the microcable to interconnect the short-length strips (in magenta) on top of the sensor (in blue). The readout cable (not shown) can be attached either at the top or the bottom edge.

The sensors are going to be produced on $300\ \mu\text{m}$ thick, n-type wafers. There will be 1024 strips per each sensor side (two interconnected short-length strips are counted as one), positioned with the pitch of $58\ \mu\text{m}$.

The sensors will feature integrated AC-coupling, in order to avoid the need of the leakage current compensation circuitry in the front-end electronics. The strips will be biased over polysilicon resistors and optionally, in addition, over punch-through structures. The strips on the n-side will be isolated with the p-spray technique. The sensors will be operated at around -5°C , to avoid the reverse annealing effects under irradiation. More details on the sensors are given in section 2.1.

1.2.4 Front-end electronics

To read out the signals from the sensors a dedicated STS-XYTER readout chip (STS X and Y coordinate, Time and Energy Readout chip) is being developed. It is a 128 channel, low power, self-triggering, charge-integrating chip with amplitude and time readout.

In order to achieve good amplitude resolution and low noise rate in combination with good time resolution, each readout channel of the chip has two shapers with distinct rise times (1.9). The fast shaper (rise time $30\ \text{ns}$) is used for triggering and time measurement. Its output is fed to the discriminator with adjustable threshold. When the discriminator is fired, the timestamp is latched and a trigger

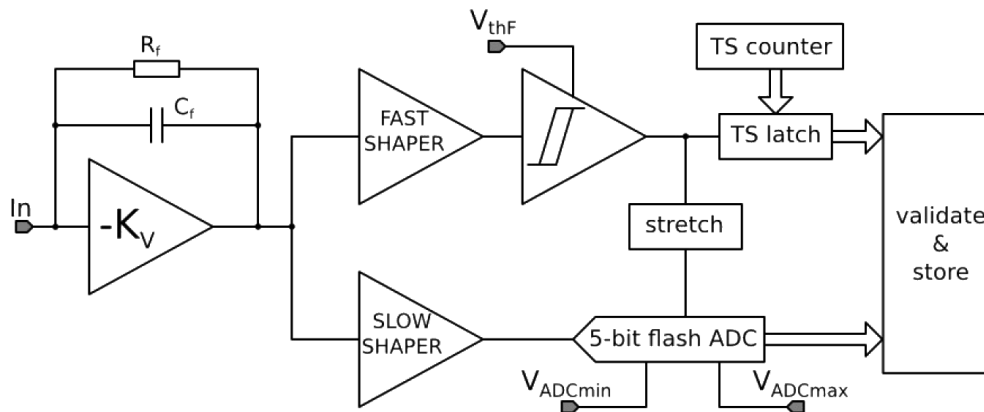


Figure 1.9: Architecture of one channel of the STS-XYTER chip.

signal is sent to the slow lane.

The slow shaper (rise time 80 ns) is used for amplitude measurement and vetoing of fake triggers (that are caused by the electronic noise, and not by a physical signal). Its output is continuously digitized with the 5-bit flash ADC. If, at the moment of trigger arrival, the ADC output exceeded the predefined digital threshold, then a hit is produced.

The analog front-end of the STS-XYTER resembles, to some degree, the front-end of the n-XYTER chip [36, 37]. Currently, n-XYTER chip is used as a prototype. It is described in details in Chapter 5.

1.2.5 Performance simulations

Evaluation of the expected tracking performance was done on a sample of central Au+Au events at 25 AGeV (projectile energy), generated with UrQMD [38]. The track propagation through the detector was performed with GEANT3 [39]. The detector model included the sensors and the microcables, which make the dominant contribution to the material budget. The track reconstruction was done with a cellular automaton based algorithm [40].

The reconstructed tracks were matched with the simulated particles in the following way. If a track includes at least 70% of the hits created by a particle then the track is associated with the particle. A particle is considered as reconstructed, if at least one track is associated with it. If more than one track is associated with a particle, the best track is selected, and the others are called clones. If a reconstructed track is not associated with any particle, it is called a ghost.

The reconstruction efficiency is defined as the ratio of the reconstructed particles to the reconstructible. A particle is considered as reconstructible if it traversed the sensitive areas of at least four stations. Among the all reconstructible particles various subsets are defined. The reference subset includes reconstructible particles with momentum larger than 1 GeV/c. The primary and

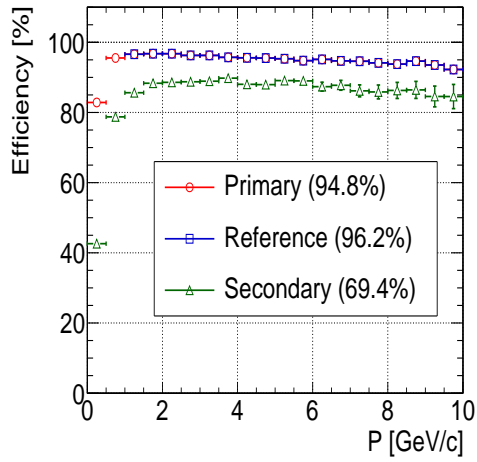


Figure 1.10: Track reconstruction efficiency for various particle subsets (see text) as a function of the momentum.

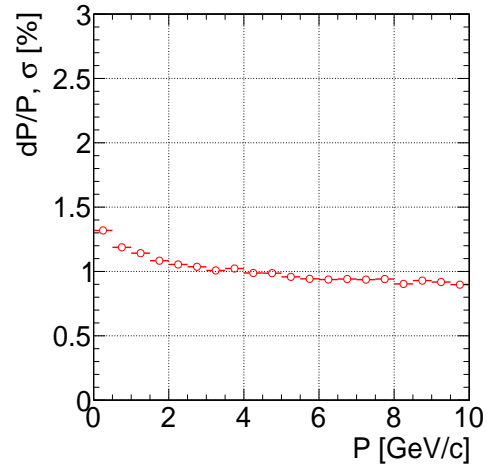


Figure 1.11: Momentum resolution, obtained for all reconstructible tracks.

the secondary subsets include particles from the reference subset that originate from the primary or, respectively, a secondary vertex.

Reconstruction efficiencies around 95 % for particles with more than 1 GeV/c momentum were obtained (Fig. 1.10, left). The drop of the efficiency low momenta is caused by the multiple scattering. The achieved momentum resolution is around 1 % (Fig. 1.11).

Chapter 2

Prototype components

Important milestones in development of the Silicon Tracking System are construction, operation, and characterization of prototype detector systems. In this chapter the prototype components, the sensors and the front-end electronics, as well as the prototype detector systems will be described.

2.1 Sensors

By the moment of completing this work (November 2013) six batches of prototype sensors for the Silicon Tracking System were available. They all were designed and fabricated at CiS [32] (Erfurt, Germany).

The all the prototype sensors were produced on 285 μm thick n-type silicon (on 4-inch wafers). All sensors were double-sided (except CBM03'), and featured integrated AC-coupling.

The distinct characteristics of the sensors are the geometrical layout, the techniques for the strip biasing, the n-side strip isolation, the resistivity of the substrate silicon, and some other characteristics. The detailed features on each sensor batch will be described below.

CBM01 Batch. CBM01 is the first batch of prototype sensors. It included the full-size prototype sensor, referred to as CBM01, with 1024 strips per side, as well as baby sensors of two types: CBM01B1 and CBM01B2. Both the baby sensors have 256 strip per side. The main layout characteristics of the sensors are summarized in Table 2.1.

An important feature of the full-size CBM01 sensor is that the strips on the p-side of it are inclined at the 15° stereoangle with respect to the strips on the n-side (Fig. 2.1). The short strips at the edges of the p-side are interconnected with each other with metal traces, fabricated in the second metallization layer. On the n-side of the sensor, as well on the both sides of the baby sensors (CBM01B1 and CBM01B2) the strips are orthogonal to the detector edges (Fig. 2.2).

	CBM01	CBM01B1	CBM01B2
<i>Strips per side</i>	1024	256	256
<i>Strip pitch</i>	50.7 μm	80 μm	50.7 μm
<i>Strip width</i>	18 μm	40 μm	18 μm
<i>Stereo angle</i>	15°	90 °	90°
<i>Chip size</i>	54.9×53.9 mm ²	22.4×22.4 mm ²	14.9×14.9 mm ²
<i>AC pads per strip</i>	2	4	4
<i>DC pads per strip</i>	0	2	1
<i>2nd metal layer</i>	on the p-side	none	none

Table 2.1: Main layout characteristics of the CBM01 sensors.

In all the CBM01 sensors the strip are biased with the punch-through technique. The n-side strips are isolated using p-spray technique. The sensors were fabricated on float-zone, 3-4 k Ω cm resistivity silicon wafers.

CBM02-SPID Batch. The aim of producing this batch was to try out various technological solutions for improvement of the radiation hardness. The following design parameters were varied: the strip pitch, the strip biasing technique, the insulation of the strips on the n-side, and the structure of the guard rings. Detailed specification of the sensor prototypes is given in the Table 2.2.

CBM03 Batch. The CBM03 batch was another iteration in production of full-size prototype sensors. The geometrical layout of the full-size sensor was modified, as compared to the CBM01 sensors, in order to simplify the bonding of the micro-cables to it. In the CBM01 sensors the AC pads on the p-side are inclined at 15° with respect to the edges, which makes it complicated to TAB-bond the cable to them, and makes it necessary to produce different cables for the p- and the n-side. In the CBM03 full-size sensors, the strips on the both sides are inclined at 7.5° with respect to the edges, such that the stereoangle between the strips on the opposite sides remains the same as in CBM01 (15°). This enabled to position the AC pads at the right angle with respect to the sensor edges on the both sides (Fig. 2.3). This came at the price of having the short-length strips on the both sides of the sensor. To interconnect the short strips (this is needed in order to read out all the strips from one side of the sensor), the second metallization layer had to be fabricated on the both sides of the sensor. This made the manufacturing process more complicated, and finally lead to failures in production (the insulating layer between the metal strips and the implants turned out to contain numerous defects, appearing as ohmic shorts between the

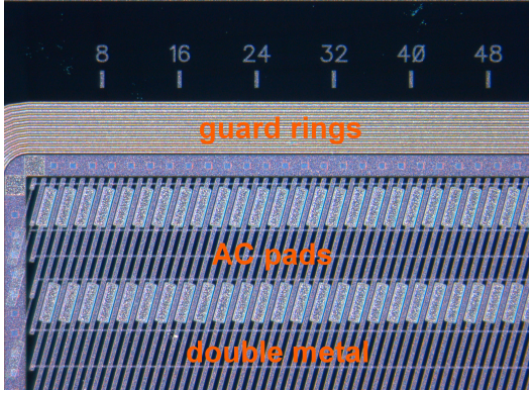


Figure 2.1: Close-up of the p-side of a full-size CBM01 sensor. The metal traces, interconnecting the short strips, are the thin horizontal lines.



Figure 2.2: Close-up of the n-side of a CBM01 baby sensor. The n-side of the full-size CBM01 sensor, looks similar.

Sensor	Strip pitch	Biasing technique	n-side isolation	Guard rings
<i>Twpsp12</i>	80 μm	punch	p-spray	p-side
<i>Twpsp13</i>	80 μm	punch + poly-Si	p-stop	p-side
<i>Twpsp14</i>	80 μm	punch	p-spray	p-side
<i>Twpsp15</i>	80 μm	poly-Si	p-spray	p-side
<i>Twpsp2</i>	50 μm	poly-Si	p-spray	p-side
<i>Twpsp22</i>	50 μm	punch	p-spray	p-side
<i>Twpsp23</i>	50 μm	punch + poly-Si	p-stop	p-side
<i>Twpsp24</i>	50 μm	punch + poly-Si	field plate	p-side
<i>Twpsp25</i>	50 μm	punch	p-spray	both sides

Table 2.2: Technology variations within the CBM02 sensor family.

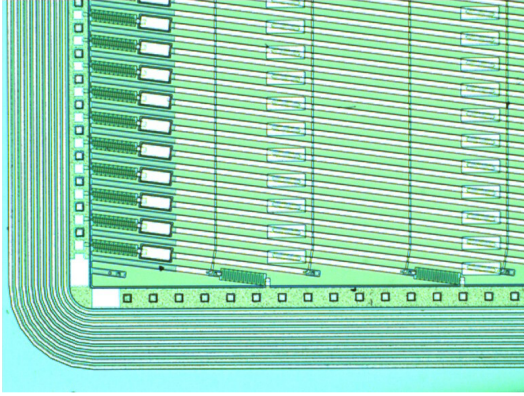


Figure 2.3: Close-up of the p-side of a full-size CBM03 sensor. The strips and the DC pads are inclined by 7.5° with respect to the sensor edges, but the AC pads (the middle and the right pad rows) are at the right angle.

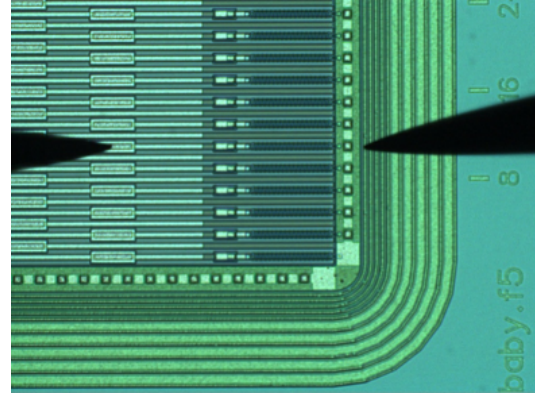


Figure 2.4: Close-up of the n-side of a CBM03 baby sensor.

metal strips and the implants).

In addition to the full-size sensor, the CBM03 wafer included also small baby-sensors, and test structures.

In all CBM03 sensors the insulation of the strips on the n-side was done with the p-spray technique. For the strip biasing both the poly-silicon resistors and punch-through structures were implemented.

CBM03' Batch. After discovering the defects in the insulating layer between the implants and the strips in the sensors from the CBM03 batch, a decision was taken to try out various technological solutions to improve the quality of the insulator. In particular, it was decided to fabricate sensors with increased thickness of the insulating layer, as well as to add additional layers of different substances to the insulator: Si_3N_4 as an additional insulating layer, and a layer of poly-silicon to reduce the mechanical stress on the insulating layer, caused by subsequent processes). A summary of the technological changes is presented in Table 2.3.

The CBM03' sensors were produced single-sided. It was considered that the experience with the processing of only one side (a successful improvement of the insulator quality or a failure) can be extrapolated to the production of double-sided sensors, because the same technological processes are applied. Production of CBM03' as single-sided sensors allowed to save the expenses. Moreover, most of the photomasks were reused from the the CBM03 batch.

Layer	Parameter variation	Values
A) dielectric layer	1) ON (SiO₂+Si₃N₄) 2) ONO	ON: O: increase from 150 to 200 nm, N: increase from 90 to 120 nm ONO: 200 nm O + 120 nm N +100 nm O
B) buffer layer (poly silicon)	1) with, normal doping, like in poly silicon resistors 2) with, high doping 3) without	1) + 2) 450 nm 3) to be realized in one baby detector
C) via layer (between 1 st and 2 nd metal)	1) normal thickness 2) thick	1) 800 nm SiO ₂ 2) 1000 nm (max. 1500 nm)
D) 2 nd metal layer	1) normal thickness 2) thick	1) 800 nm 2) 1000 nm or thicker (max. 1500 nm)

Table 2.3: Changes in the technology of production of the CBM03' sensors with respect to the CBM03 sensors. "ON" stands for Oxide-Nitride —a combination of the SiO₂ and Si₃N₄ layers, and "ONO" — for Oxide-Nitride-Oxide.

CBM04 Batch. In this batch of sensors a novel technique of strip isolation on the n-side, based on Schottky junction (metal-semiconductor junction) was investigated.

Additional metal strips were deposited between the readout strips, directly on the semiconductor surface. The junction causes a depletion of a thin layer the semiconductor in the vicinity of the metal, and hence, isolates the implants from each other. Photographs of sensors without and with the intermediate metal strips are shown in Fig. 2.5 and Fig. 2.6 respectively.

It was expected by the designers of the sensors that the metal-semiconductor junction will result in smaller field intensity in the vicinity of the junction, as compared to the conventional techniques, as p-stop or p-spray, thus enabling operation of the sensors at higher bias voltages without the breakdown. Another advantage of this technique is that the intermediate metal strips can be fabricated at the same process stage as the readout strips, so no additional photomask will be required for the isolation structures (as compared to the p-stop technique).

The CBM04 wafer included several various sensor types, with distinct design parameters. The summary of the sensor types is given in Table 2.4.

Tests of CBM04 sensors revealed certain disadvantages of the Schottky isolation (rapid increase of the leakage current with the bias voltage, and other), and the development of this technology was discontinued.

CBM05 Batch. In this batch the finalized layout and fabrication technologies are verified before the serial production. The sensors are produced in three various sizes: 6.2×6.2 cm², 6.2×4.2 cm², and 6.2×2.2 cm², according to the last layout of the STS. The 6.2×6.2 cm² sensors were produced at CiS (Erfurt, Germany), and named CBM05. The 4.2×2.2 cm², and 6.2×2.2 cm² are to be produced by Hamamatsu Photonics (Japan), and named CBM05H4, and CBM05H2s respectively.

The main change in the layout of these sensors, with respect to the previous

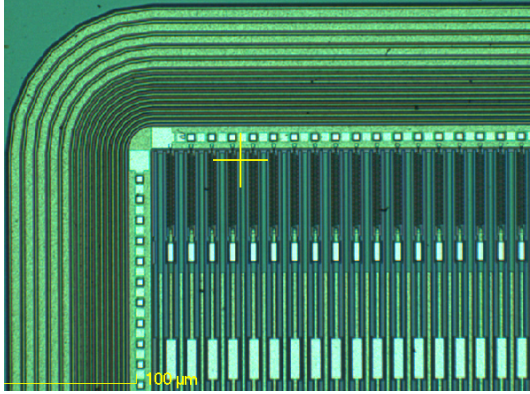


Figure 2.5: Close up of the n-side of a bo4pr sensor from the CBM04 batch, with polysilicon + punch-through biasing and uneven guard ring spacing.

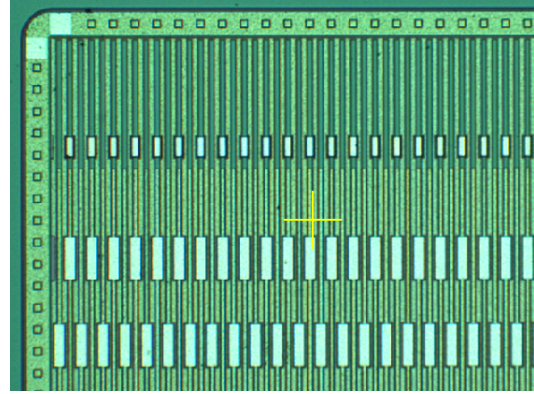


Figure 2.6: Close up of the n-side of a bo5tb sensor from the CBM04 batch. One can see intermediate metal strips between the readout strips.

Sensor type	Biasing technique	Guard rings on sides	Width of Schottky contact	Schottky contact passivation
<i>bo4pr</i>	poly-Si	p and n	no	—
<i>bo4pa</i>	poly-Si	p and n	18	closed
<i>bo4pw</i>	poly-Si	p	18	closed
<i>bo4nx</i>	poly-Si + punch	p	18	open
<i>bo5tb</i>	punch	p	21	open

Table 2.4: Technology variations for different sensor types within the CBM04-FSD wafer.

batches, is that the strips on the n-side were made orthogonal to the detector edges. This was done in order to eliminate the need in the second metalization layer on at least one side and simplify the production process. The stereoangle in these sensors was decreased to 7.5° . The last simulations of the CBM detector showed that a decent performance can be still achieved with such stereoangle [33].

The design of CBM05 sensors (only $6.2 \times 6.2 \text{ cm}^2$) is based on the design of CBM03 and CBM03' with certain improvements. First of all, the insulating layer between the metal strips and the implants is made thicker, according to the experience with the CBM03' sensors. In addition, in comparison to the previous sensors, in CBM05, the metal strips, as well as the interconnections in the second metalization layer, were made thicker in order to reduce their resistance, and hence reduce the thermal noise.

The CBM05H4 sensors will be produced in two variations: with and without the interconnection of the short strips on the p-side with the second metalization layer. An alternative to the second metalization layer is to interconnect the short strips with a microcable, placed on top of the sensor. The reason to abandon the approach of interconnecting the short strips with the second metalization layer is the recent observation of an unexpected charge loss in the LHCb sensors [34, 35], that is now considered to be caused by the interconnections in the second metalization layer.

The CBM05H2s sensors will be produced single-sided. Two sensors of type CBM05H2s, one with orthogonal, and one with inclined by 7.5° strips, will be mounted back-to-back to reconstruct the positions of the particles in two coordinates. The reason for making the $6.2 \times 2.2 \text{ cm}^2$ sensors single-sided, is that they will be placed in the first STS stations, close to the beam, where the radiation load is the highest. Single-sided sensors, generally, have much better radiation hardness. The material budget in the inner part of STS will still remain low, because in the inner part there will be no readout cables, stretching above the sensors.

Demonstrator boards. To operate the prototype sensors they were mounted on fan-out PCBs, as shown in Fig. 2.7, 2.8, and 10.1. A detachable connection to the front-end electronics is made in order to be able to reuse the same front-end electronics for many demonstrators. The physical interface is made compatible with the n-XYTER based FEBs (described in section 2.2).

The demonstrators with baby sensors were produced in order to study the basic properties of the sensors. The demonstrators with the full-size sensors (Fig. 2.8) and realistic microcables were used to simulate the operation in realistic conditions, with large channel capacitance and crosstalk.

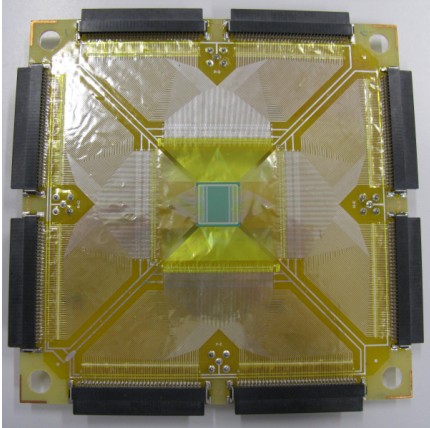


Figure 2.7: Demonstrator board, based on a CBM02 baby sensor.

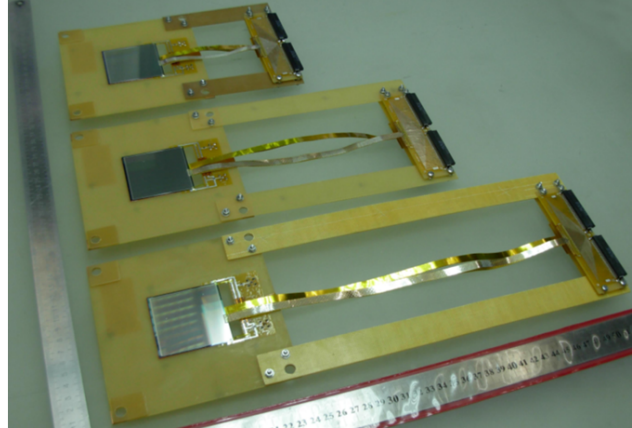


Figure 2.8: Demonstrator boards, based on full-size CBM01 sensors, with realistic three-layer microcables of various length.

2.2 Front-end electronics

During the sensor R&D phase, before the STS-XYTER was designed, produced, and put into operation, its technological predecessor, n-XYTER [36, 37], was used as a prototype readout chip.

n-XYTER (neutron-X-Y-Time-Energy Readout) is a 128-channel self-triggering readout ASIC, capable of measuring both signal amplitude and time of occurrence. It was originally developed within the EU-FP6 NMI3 DETNI project for solid-state and gaseous neutron detectors. At present, due to its self-triggering design, high rate capability, high gain and bipolar front-end, the chip is widely used to read-out silicon and gaseous detectors, as well as photomultipliers, in various projects at GSI/FAIR (Darmstadt, Germany) and in other laboratories. n-XYTER suits very well for prototyping of the STS detectors. Still, it can not be applied in the final setup because of the large power consumption, insufficient rate capability, too large noise rate (caused by the short shaping time, that is necessary for good time resolution), and inconvenient back-end interface. More detailed description of the n-XYTER ASIC is given in chapter 5.

Based on the n-XYTER chip, general purpose front-end boards (FEBs) were produced at GSI (Fig. 2.9). The board hosted an ADC for digitization of the n-XYTER analog output, as well as auxiliary electronics for n-XYTER and ADC operation. The board is mounted on an aluminum block for temperature stabilization of the n-XYTER. Such boards were used in all the detector prototypes built so far.



Figure 2.9: General purpose front-end board (FEB), based on n-XYTER chip (board revision D).

2.3 Prototype tracking stations

2.3.1 Electronics connection schemes

Before assembling the prototype tracking detectors, the connection of the front-end electronics (FEE) to the sensor has to be defined. But it turns out that there is more than one connection scheme possible. They will be discussed in this subsection, and the optimal will be selected. The decision will be made with the aim to apply the same scheme in the final STS setup, and not only in the prototype systems.

In the STS AC-coupled sensors are going to be used. This allows to apply front-end electronics without leakage current compensation circuitry, and to avoid additional power consumption and heat production. But it also allows to operate the front-end electronics at a potential, different from the potential of the corresponding side of the sensor. This leads to the fact that the front-end electronics can be connected to the sensor in several different ways. The difference is only where the ground of the FEE is connected.

The first way is to connect the grounds of the front-end electronics at the both sensor sides to the ground of the bias voltage power supply. This ground can be made the ground of the system. This scheme is shown in Fig. 2.10. The advantages of this scheme are: first, the FEE on both sensor sides remains grounded, and no special care about its isolation has to be taken (in contrast to the floating connection scheme, that will be presented below); and second, the FEE on both sensor sides can be powered from the same power domain, which makes the system simpler.

But this connection scheme has also a severe shortcoming. On the high voltage side of sensor the voltage drop on the coupling capacitors is almost equal to the

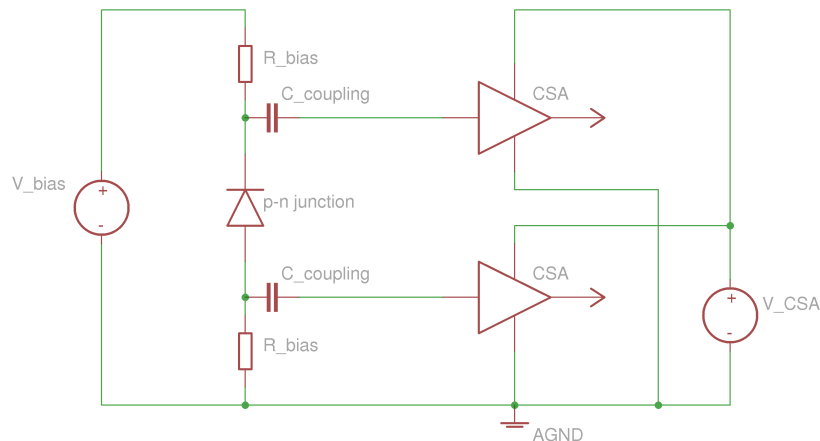


Figure 2.10: Sensor readout with FEE at the common ground.

bias voltage (there is a small voltage drop on the biasing structure as well as between the FEE input and the ground). This introduces a high risk in operation of the system. If one of the coupling capacitors does not sustain the bias voltage and breaks down the bias voltage will drop on the FEE input. This will damage the FEE channel, or possibly the whole readout chip. But what is more severe, it will not be possible to bias the sensor anymore, because the biasing current will flow through the broken coupling capacitance. In a small (prototype) system this can be fixed by disconnecting the damaged strip from the FEE. But in the STS there will be no such possibility, so a single failed coupling capacitor will make inoperative.

The breakdown voltage of the coupling capacitors can be increased, but this requires to increase the thickness of the insulating layer. The latter is undesirable, as it would decrease the coupling capacitance, and hence the signal amplitude (the dependence of the signal amplitude on the coupling capacitance is discussed in chapter 3). Moreover, simple increase of the thickness of the insulating layer does not guarantee high breakdown voltage for all strips: the insulating layer may be fabricated nonuniform in thickness or with defects. Often sensors have a few strips with defective coupling capacitors already after fabrication.

The bias voltage can be split between the coupling capacitors on the two sensor sides. This is achieved in the second connection scheme (Fig. 2.11) at the price of double number of the high voltage power supplies.

Splitting the bias voltage drop between two detector sides relaxes the requirements to the breakdown voltage of the coupling capacitors. Yet, it does not eliminate the risk.

The third way is to connect the grounds of the FEE to the respective side sensor (Fig. 2.12). This mode of FEE operation will be referred to as floating. In this case the voltage drop on the coupling capacitor would not exceed a few volts. Indeed, it is equal to the voltage drop on the biasing structure plus (or minus

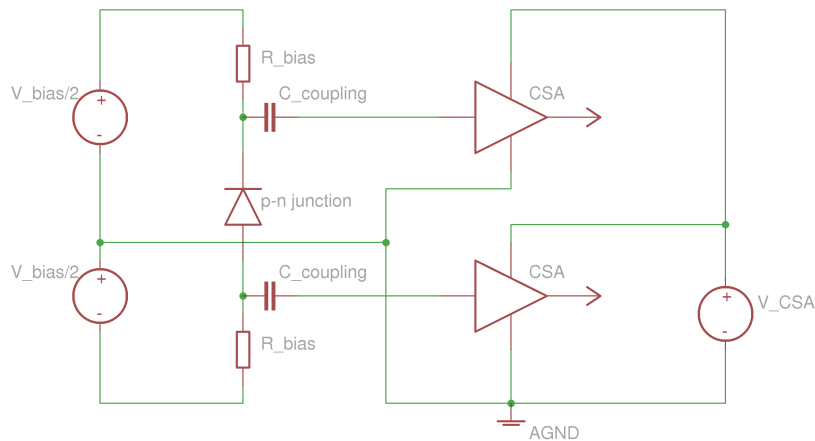


Figure 2.11: Sensor readout with FEE at the common ground, with the bias voltage drop split equally between the coupling capacitors on the both sides.

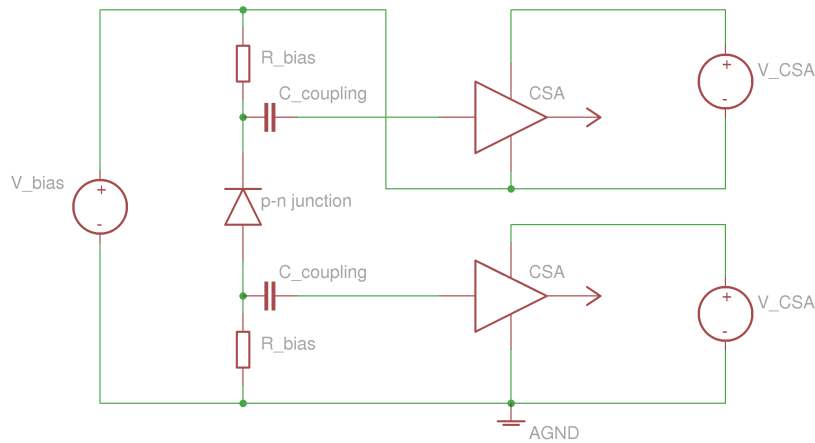


Figure 2.12: Sensor readout with floating FEE

depending on the side) the voltage on the FEE input w.r.t. the FEE ground.

The floating mode of operation has two very important advantages. First, it eliminates the risk of breakdown of the coupling capacitors. And second, if one of the coupling capacitors appears defective already after fabrication, the sensor can still be used. Only a small current will flow in through the broken coupling capacitor in the FEE input. And only this FEE channel will be affected, while the rest of the readout chip will work normally. So the sensor can still be biased and operated, even if some of the coupling capacitors are defective.

The risk of coupling capacitors breakdown forces CBM-STs to use the floating readout scheme. Operating floating FEE will require significant engineering effort. First of all, the FEE on the high voltage side of each module would require a separate power domain (because it has to be possible to control the bias volt-

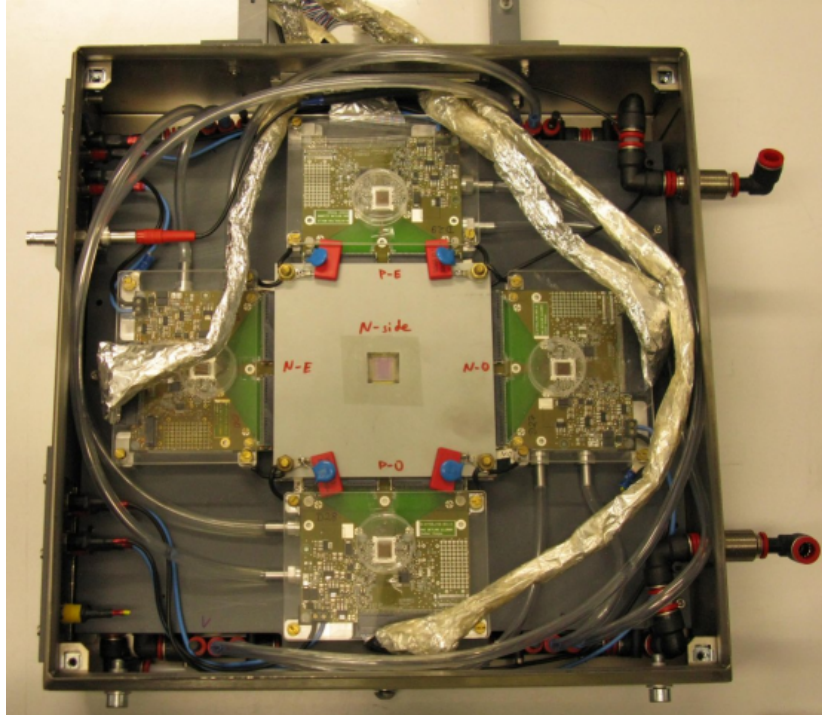


Figure 2.13: One of the assembled prototype tracking stations. The sensor can be seen in the very middle. The fan-out board is covered with a metal shield to suppress the electromagnetic pick-up. The front-end boards with n-XYTERs are connected from each of the sides.

age on each module independently). Also, a DC-decoupling interface between the floating FEE and the data transport hardware (that is grounded) will be needed. Finally, safety concerns have to be taken into account. Floating FEE is successfully operated in ALICE ITS [41].

2.3.2 Prototype tracking stations

After the front-end electronics connection scheme were defined, three prototype tracking detector stations were assembled. (Fig. 2.13). The first two constructed stations were based on CBM02-baby sensors, while the third one included CBM04-FSD sensors. The sensors were exchanged with other when necessary. In all other respects the stations were similar.

The sensors had 256 strips on each side, so two n-XYTER chips per sensor side were used for readout. The temperature of the n-XYTERs was stabilized with water cooling, in order to minimize the baseline drift. Since the floating connection scheme was applied, it was important to ensure a reliable electrical isolation of the front-end boards from the cooling blocks, on which they were mounted.

The stations were assembled in metal boxes, which provided a mechanical protection of the fragile components as well as shielded the sensitive front-end electronics from external electromagnetic interference. It also protected the sensor from the ambient light.

Two windows, one in front, and behind the sensor, were made in the box to let a particle beam pass through with minimum scattering. The windows were closed with a thin opaque film.

These three stations were used to characterize the prototype sensors.

Chapter 3

Evaluation of signal and noise in a silicon strip detector

Characterization of a detector system includes a comparison of the observed signal amplitude and noise with the expected ones. It is therefore necessary to have a model that allows to evaluate the expected signal and noise, for the given parameters of the system.

Signal amplitude and the equivalent noise charge in silicon strip detectors are often evaluated by detailed CAD simulations of all components of the system: the sensor, the front-end electronics, and the signal transmission line, interconnecting the first two (if it affects the signal significantly). However, a decent estimate can be already obtained with analytical calculations under certain approximations. Such calculations will be done in this chapter. A similar calculation was presented in [42], and next two sections follow it to a certain extent.

3.1 Evaluation of the signal amplitude

The amount of charge, that is integrated in the readout electronics is in general not equal to the free charge, that is created in the sensor by the ionizing radiation. This is because of such effects as: inefficiency of charge collection in the sensor (because of various reasons), charge sharing between the strips in the sensor, charge division between the sensor and the charge-sensitive amplifier (CSA), and ballistic deficit.

The simple model developed here will not consider the losses of charge during the collection. It will rather consider only the ratio of the total charge, integrated in the readout electronics, to the charge, collected on the respective doping implants. The charge collection inefficiency, if known, can be taken into account as an additional factor. Parameters for the model will be taken from chapter 4.

The model will be built with assumption of no ballistic deficit. The time structure of the signal will be completely ignored. Ballistic deficit is an effect

of degradation of the output amplitude of a shaper in case of stretching of the input signal. It can occur when the discharge time of the shaper is comparable to the time duration of the signal. In this case by the end of signal integration a fraction of the integrated charge will be lost in discharging.

The time duration of the signal, arriving at the inputs of the readout electronics, is determined by two processes. The first is the charge collection in the sensor. The typical collection time of electrons in 300 μm silicon sensors (operated beyond the full depletion, and not heavily irradiated) is around 10 ns, and for holes this time is around 30 ns [43, p. 18].

The signal can also be stretched in the transmission line between the sensor and the readout electronics. In case of CBM-STs, the cables, connecting the sensors and the readout electronics, will have at most $R_{cable} = 30 \Omega$ resistance, and the total capacitance of a sensor, together with the cable will be at most $C_{total} = 50 \text{ pF}$ capacitance (inductances are negligible). Therefore, the signal stretching will not exceed $R_{cable}C_{total} = 1.5 \text{ ns}$, and is negligible.

The assumption of no ballistic deficit is therefore valid for the slow shapers of n-XYTER ($\tau_{rise} = 130 \text{ ns}$) and the STS-XYTER ($\tau_{rise} = 80$) but is not valid for the fast shapers of the chips (τ_{rise} is 19 ns and 30 ns respectively).

The charge sensitive amplifier, connected to the strip of interest, will be considered as a simple capacitance of value $C_{CSA} = C_f \cdot A$, where C_f is the feedback capacitance and A is the open loop gain. The CSAs, connected to the neighboring strips will be considered just as virtual grounds. The output signal amplitude in the readout electronics is assumed to be proportional to the integrated charge.

The processes of charge sharing between the strips in the sensor, as well as of charge division between the sensor and the charge-sensitive amplifier, can not be neglected, and will be considered here in details.

In Figure 3.1 a simplified equivalent circuit of one side of a sensor, with the readout electronics connected, is shown. Only the essential for the charge sharing components are shown here: C_{iDC} and C_{iAC} the components of the interstrip capacitance, C_c is the coupling capacitances, and C_b is the capacitance to the opposite side of the sensor (from “backplane”, following the established for single-sided sensors terminology).

In this circuit each implant, as well as each metal strip, is shown as a single node, neglecting its resistivity. The resistivity of the implants (typically few times 100 $\text{k}\Omega/\text{cm}$) is in general can not be neglected, but below it will be shown that taking it into account leads to the same result. The bias resistors are also not shown in this figure. It is assumed that they are sufficiently large, so that no signal escapes through them.

First, the case when the charge is collected only on one implant. A small fraction of the charge will couple to the neighboring strips, but it is assumed that this amount of charge is below the threshold of the readout electronics, so that it remains undetected.

Suppose the charge, collected on one implant is Q_{coll} . Then the change of the

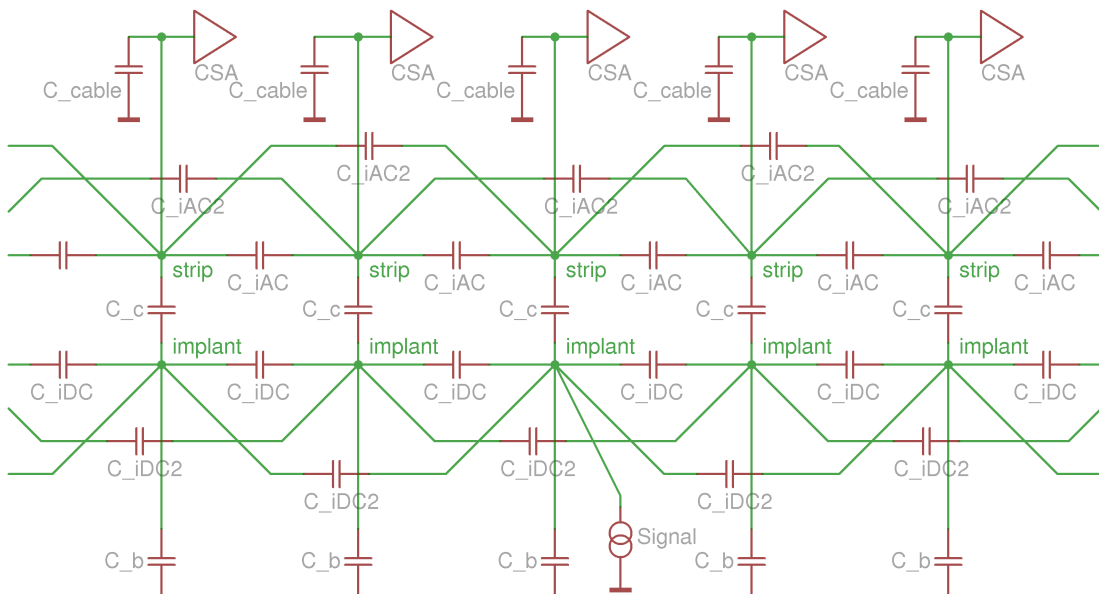


Figure 3.1: Equivalent circuit of the sensor for signal evaluation. Each metal strip and each implant are considered as single nodes (resistivity of the implants is neglected). Capacitance of metal strips and implants to their first (nearest) and second neighbors are shown. Capacitance to further neighbors is omitted for simplicity. For designations of the components see the text.

potential of the implant will be:

$$\Delta U_{implant} = \frac{Q_0}{C_{implant_total}} \quad (3.1)$$

where $C_{implant_total}$ is the total capacitance from the implant to the ground and all virtual grounds:

$$C_{implant_total} = C_{iDC_tot} + \frac{C_c \cdot (C_{cable} + C_{CSA} + C_{iAC_tot})}{C_c + C_{cable} + C_{CSA} + C_{iAC_tot}} + C_b \quad (3.2)$$

Here C_{iDC_tot} is the capacitance of the implant to the ground through all neighboring strips and implants, and C_{iAC_tot} is the capacitance of the strip to the ground (or virtual grounds) through all neighboring strips. C_{CSA} is the input capacitance of the charge sensitive amplifier, and C_{cable} is the capacitance of the cable. Because the input capacitance of the preamplifier C_{CSA} is much larger than the coupling capacitance C_c , the last equation can be simplified to:

$$C_{implant_total} = C_{iDC_tot} + C_c + C_b \quad (3.3)$$

Knowing $\Delta U_{implant}$, the charge, coupled to the metal strip will be:

$$Q_{coupled_to_strip} = \Delta U_{implant} \cdot C_c = Q_{coll} \cdot \frac{C_c}{C_c + C_{iDC_tot} + C_b} \quad (3.4)$$

The potential of the strip will change by:

$$\Delta U_{strip} = \frac{Q_{coupled_to_strip}}{C_{CSA} + C_{cable} + C_{iAC_total} + \frac{C_c(C_{iDC_tot} + C_b)}{C_c + C_{iDC_tot} + C_b}} \quad (3.5)$$

Neglecting $C_{iDC_total} + C_b$ compared to C_c in the last equation, the charge, integrated in the CSA, will be:

$$Q_{int} = Q_{coupled_to_strip} \cdot \frac{C_{CSA}}{C_{CSA} + C_{cable} + C_{iAC_tot} + C_{iDC_tot} + C_b} \quad (3.6)$$

The sum $C_{iAC_tot} + C_{iDC_tot}$ is approximately equal to the total capacitance from a metal strip to other metal strips (including the direct coupling through C_{iAC1} , C_{iAC2} , ..., as well as the coupling via the implants). It is a valid approximation when $C_c \gg C_{iDC1}, C_{iDC2}, \dots$, which is usually the case.

Finally, the ratio of the integrated to the collected charge is:

$$\left(\frac{Q_{int}}{Q_{coll}} \right)_{1_strip_clusters} = \frac{C_c}{C_c + C_{iDC_tot} + C_b} \cdot \frac{C_{CSA}}{C_{CSA} + C_{cable} + C_{i_tot} + C_b} \quad (3.7)$$

In this equation the first factor corresponds to the charge sharing between the strips in the sensor, while the second corresponds to charge division between the sensor, the cable and the CSA.

The values C_{iDC_tot} and C_{i_tot} can be expressed through the C_{iAC1} , C_{iDC1} , C_{iAC2} , C_{iDC2} , ..., and C_c . It is, however, not necessary, because experimentally it is easier to measure C_{iDC_tot} and C_{i_tot} (see chapter 4).

Now let us consider the case when the charge is collected on two implants, and detected in the both corresponding readout channels. In this case the equation for Q_{int} (sum of the integrated charges in the two readout channels, in this case) can be easily obtained if the capacitive coupling of implants and strips to the second and further neighbors is neglected.

Suppose the two implants have collected charge Q_{coll}^A and Q_{coll}^B . A certain amount of charge ΔQ , will flow from one implant to another. But since there is no intention to calculate the amount of charge, integrated in each of the two readout channels separately, but only a sum of them (Q_{int}), it is also not necessary to calculate ΔQ . Then it can be considered that there is no charge transfer between the collecting implants ($\Delta Q = 0$), but the charge, collected on the implants, was $Q_{coll}^A - \Delta Q$ and $Q_{coll}^B + \Delta Q$. The calculations then can be done as if there was no C_{iDC1} capacitor between the collecting implants, and the problem boils down to the problem, when signal on only one strip was collected. Summing up the integrated in two channels charge gives:

$$\left(\frac{Q_{int}}{Q_{coll}}\right)_{2_strip_clusters} = \frac{C_c}{C_c + C_{iDC1} + C_b} \cdot \frac{C_{CSA}}{C_{CSA} + C_{cable} + C_{i1} + C_b} \quad (3.8)$$

where C_{i1} is the between two neighboring strips, including the coupling via the corresponding implants, but excluding the coupling via the other neighbors. In the approximation of zero coupling to far neighbors $C_{iDC_tot} \approx 2C_{iDC1}$, and $C_{i_tot} \approx 2C_{i1}$. Then, the equation for Q_{int} can be rewritten in more intuitive form, like if the two strips, collecting the charge, were interconnected:

$$\left(\frac{Q_{int}}{Q_{coll}}\right)_{2_strip_clusters} = \frac{2C_c}{2C_c + C_{iDC_tot} + 2C_b} \cdot \frac{2C_{CSA}}{2C_{CSA} + 2C_{cable} + C_{i_tot} + 2C_b} \quad (3.9)$$

Similarly, for 3-strip clusters:

$$\left(\frac{Q_{int}}{Q_{coll}}\right)_{3_strip_clusters} = \frac{3C_c}{3C_c + C_{iDC_tot} + 3C_b} \cdot \frac{3C_{CSA}}{3C_{CSA} + 3C_{cable} + C_{i_tot} + 3C_b} \quad (3.10)$$

Now, let us consider how the resistivity of the implant affects the charge sharing process. The charge is collected on a short piece of implant. Depending on the incidence angle of the detected particle, the length of this piece can be up to few hundred micrometers, still much less than the length of the strip. The collected charge would not distribute evenly along the whole implant because of the high resistivity of the implant, but rather only spread a little in both directions along it. For a specific resistance of the implant $\rho_{imp} = 200 \text{ k}\Omega/\text{cm}$, specific coupling capacitance $\varsigma_c = 15 \text{ pF}/\text{cm}$, and charge collection time $\tau_{coll} =$

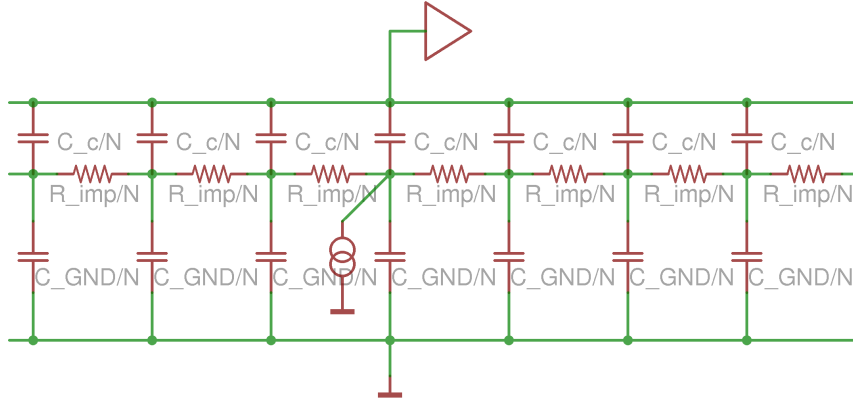


Figure 3.2: Equivalent circuit showing one strip and its capacitive coupling to the surrounding virtual grounds. The distributed coupling capacitance (C_c) and implant resistance of the strip (R_{imp}) is shown as a series of lumped components (C_c/N and R_{imp}/N). The surrounding virtual grounds (neighboring implants and the backplane) are shown as a single node (in the bottom). The distributed capacitance to them ($C_{GND} = C_{iDC} + C_b$) is also shown as a number of lumped elements (C_{GND}/N).

30 ns, this spread is on the order of $\sqrt{\tau_{coll}/(\rho_{imp} \epsilon_c)} = 1$ mm. Therefore, the capacitance, through which the charge would couple to the metal strip, is not the total coupling capacitance of the whole strip, but the coupling capacitance of a short piece of it. This, however, would not affect the resulting signal amplitude, because the effective total capacitance to ground also scales proportionally to the length of the piece, over which the charge is spread. Hence, the ratio of coupling capacitance C_c to the total capacitance to the ground $C_{iDC,tot} + C_b$ stays the same (Fig. 3.2). The second factor in the equation for Q_{int}/Q_{coll} (i.e. $C_c/(C_c + C_{iDC,tot} + C_b)$) is not affected by the resistance of the implant.

The expected ratios of the integrated to the collected charge were evaluated for the CBM02 and CBM03' sensors (Table 3.1). The parameters of the model were taken from chapter 4. The backplane capacitance, which is on the order of 0.1 pF/cm, was neglected in these calculations, as compared to the interstrip capacitance. The dominant contribution to the uncertainty comes from the uncertainty of the capacitance of an implant to the neighboring strips. The other contributions to the uncertainty were neglected. Possible systematic uncertainties, caused by the model approximations are not included here.

3.2 Evaluation of the equivalent noise charge

There are three major sources of noise in silicon strip detector systems: the noise of the charge-sensitive preamplifier, the thermal noise of resistive structures

Sensor	Side	Q_{int}/Q_{coll} 1-strip clust.	Q_{int}/Q_{coll} 2-strip clust.	Q_{int}/Q_{coll} 3-strip clust.
CBM02	p	0.953 ± 0.012	0.967 ± 0.006	0.973 ± 0.004
CBM02	n	0.938 ± 0.013	0.960 ± 0.007	0.967 ± 0.005
CBM03'	p	0.924 ± 0.025	0.953 ± 0.013	0.962 ± 0.009

Table 3.1: Expected ratio of the charge, integrated in the the front-end electronics to the charge, collected on one and two strips. The values are not evaluated for the CBM04 and CBM05 sensors, because the necessary parameters of the model (the coupling and the interstrip capacitances) were not yet measured.

(metal strips, cable traces, biasing structure) and the shot noise of the leakage current.

If the noise voltage spectral density of the CSA is known, then the equivalent noise charge (ENC) can estimated with the formula [43]:

$$ENC_{preamp}^2 = 3.6 \cdot 10^4 \left[\frac{e^2 n s}{(pF)^2 (nV)^2 / Hz} \right] e_n^2 \frac{C^2}{\tau} \quad (3.11)$$

It is valid under assumption of a FET-based CSA (negligible input current) with an CR-RC shaper.

The thermal and the shot noise can be estimated with the formulae [43]:

$$ENC_{shot}^2 = 12 \left[\frac{e^2}{nA \cdot ns} \right] I_{leak} \tau \quad (3.12)$$

$$ENC_{therm}^2 = 6 \cdot 10^5 \left[\frac{e^2 k \Omega}{ns} \right] \frac{\tau}{R_p} \quad (3.13)$$

Again, this is valid only for a CR-RC shaper, but for other shapers the result is of the same order.

Since the different noise sources is not correlated with each other, they add up in quadrature:

$$ENC_{total}^2 = ENC_{preamp}^2 + ENC_{thermal}^2 + ENC_{shot}^2 \quad (3.14)$$

For the CSA of n-XYTER the noise voltage spectral density of the not known. In [36] the results of the numerical simulations are specified:

$$ENC_{n-XYTER_fast} = 26.9e/pF + 200e \quad (3.15)$$

$$ENC_{n-XYTER_slow} = 12.7e/pF + 233e \quad (3.16)$$

However, they do not agree with the measurement, as described in section 5.4:

$$ENC_{n-XYTER_slow} = 37e/pF + 450e \quad (3.17)$$

Because of this mismatch the ENC was not calculated for the assembled prototype detector systems.

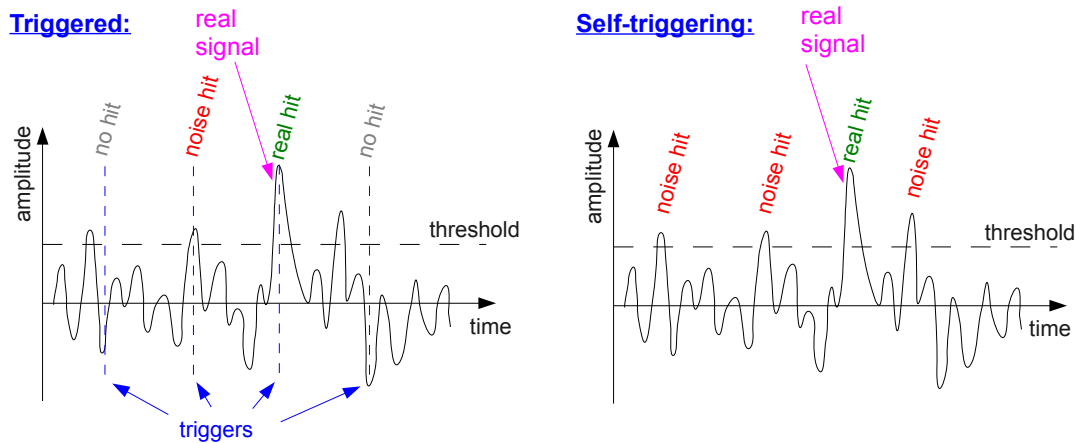


Figure 3.3: A sketch, illustrating the difference between a triggered and a self-triggering system. In a triggered system a noise hit is produced when the instantaneous noise amplitude exceeds the threshold *and* at the same moment a trigger comes, whereas in a self-triggering system a noise hit is already produced as soon as the instantaneous noise amplitude exceeds the threshold.

3.3 Evaluation of the noise rate

The rate of noise hits is an another important characteristic of a detector system. If not payed enough attention to, an excessive noise rate can not only worsen the quality of the data by introducing a large background, but also completely obstruct the data taking by overwhelming the data acquisition system. This is especially threatening to self-triggering systems, as CBM-STS is going to be, which are intrinsically much more vulnerable to the noise, as compared to conventional, triggered systems.

In point of the noise rate, the fundamental difference between a triggered and a self-triggering system is that in a triggered system a noise hit is produced when the instantaneous noise amplitude exceeds the threshold *and* at the same moment a trigger comes, whereas in a self-triggering system a noise hit is already produced as soon as the instantaneous noise amplitude exceeds the threshold (Fig. 3.3). This requirement of a coincidence with the trigger makes a triggered system intrinsically more tolerable to the noise, as compared to a self-triggering one.

3.3.1 The Rice formula

In a self-triggering system a noise hit is generated when the noise waveform undergoes a positive¹ transition with respect to the threshold level, and if in the

¹positive transition for positive signals, and negative — for negative signals

same time the system is not busy with generating (or recovering after generation of) another hit. Assuming that the dead time in the system is small, the noise rate equals to the rate of such transitions, and can be estimated with the following formula [44] (original work [45]):

$$f_t = \frac{f_0}{2} \exp\left(-\frac{\nu_t^2}{2\sigma^2}\right) \quad (3.18)$$

where f_t — is the rate, at which the noise waveform crosses the threshold ν_t , and f_0 is the rate at which it crosses the zero level. This formula is often referred to as the Rice formula (after the author).

The zero crossing rate f_0 is determined by the noise power spectral density $w(f)$ at the discriminator input [44]:

$$f_0 = 2 \sqrt{\frac{\int_0^{\infty} f^2 w(f) df}{\int_0^{\infty} w(f) df}} \quad (3.19)$$

Assuming that the noise is dominated by the white voltage noise of the input transistor v_n , the noise power spectrum at the discriminator input is:

$$w(f) = v_n \frac{C_t^2}{C_f^2} |H(\omega)|^2 \quad (3.20)$$

where C_t is the total capacitance at the preamplifier input, C_f is feedback capacitance of the charge sensitive preamplifier and $H(j\omega)$ is the transfer function of the shaper.

For n-XYTER, the transfer function of the fast shaper can be approximated with a transfer function of a CR-(RC)³ filter:

$$H(j\omega) = \frac{j\omega\tau}{(1 + j\omega\tau)^4} \quad (3.21)$$

where τ is the shaping time (19 ns). Substituting this in eq. 3.19, and performing the integration, one obtains a simple expression for f_0 :

$$f_0^{\{n-XYTER\}} = \frac{1}{\pi\tau} = 16.8 \text{ MHz} \quad (3.22)$$

The Rice formula is going to be applied for estimating the noise rates in STS. It is therefore reasonable to check how well it actually describes the noise rate in real systems. This will be done in the next section.

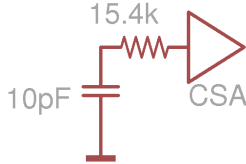


Figure 3.4: Noise source for the test of the Rice formula

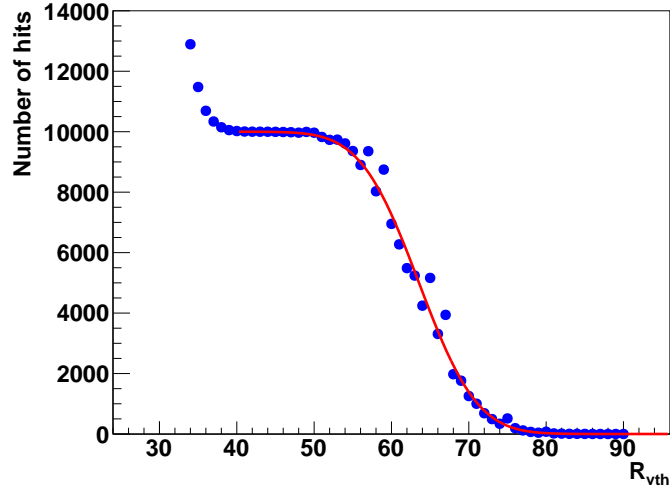


Figure 3.5: Number of detected hits (both the test pulses and the noise) as a function of the v_{th} register value ($R_{v_{th}}$). 10000 Test pulses were applied to the input of the channel during each measurement. The noise source (Fig. 3.4) was also always connected to the input.

3.3.2 Test of the Rice formula applicability to real systems

Applicability of the Rice formula to real systems was tested on one channel of the n-XYTER chip. For this test, first of all, a source of large and stable in time noise was required. Large noise is preferable in order to achieve better relative accuracy in the measurement of the equivalent noise charge. As a source of such noise a series combination of a resistor (15.4 kOhm) and a capacitor (10 pF) was taken (Fig. 3.4).

The noise source was connected to one randomly chosen channel of an n-XYTER chip, and the noise rate was measured as a function of the threshold register value $R_{v_{th}}$ (Fig. 3.9). To make a comparison with eq. 3.18, the threshold in the data (i.e. in Fig. 3.9), and in the calculation has to be expressed in the same units. It is natural to express it in the physical units of charge, but this requires to know the correspondence between the n-XYTER threshold register value $R_{v_{th}}$ and the threshold value in the units charge ν_t (i.e. threshold calibration). It was not available at the point of performing this work. Instead of performing this calibration, it was simpler to express both the threshold and the equivalent noise charge in the units of n-XYTER threshold register. In this case, in addition, the equivalent noise charge σ need to be expressed in the units of the threshold register.

To determine the equivalent noise charge in units of the threshold register, a technique, which is often called S-curve scan, was applied. The test pulse

generator was activated, and the pulses were fed into the same channel, where the noise source was connected. Then number of hits per a constant time interval (10 s) was measured as a function of the threshold (Fig. 3.5). During each measurement 10000 pulses were fed in into the selected channel.

At the thresholds around 50 and below, all the fed pules were detected. At thresholds below about 40, a certain number of noise hits was also detected (that is why the number of hits increases with decrease of the threshold below 40). At thresholds starting from around 50 and higher the pulses become gradually cut of by the threshold. The decrease is smooth because of the presence of the noise. Indeed, a pulse with amplitude below the threshold can still be detected if the instantaneous amplitude of the noise at the moment of the injection of the pulse is large enough, so that the sum of the amplitudes of the pulse and the noise exceeds the threshold. And vice versa: a pulse, which amplitude exceeds the threshold, may be undetected if the instantaneous value of the noise is large and opposite to the polarity of the pulse at the moment of the pulse injection.

The equivalent noise charge can be extracted from the width of the transition of the S-curve (Fig. 3.5). For this analytical shape of the curve has to be derived, where the ENC will enter as a parameter. Then this analytical function will be fit to the data and the ENC can can be extracted.

As it was discussed above, a pulse of amplitude A_p will be detected with threshold ν_t and instantaneous amplitude of the noise A_n if:

$$A_n > \nu_t - A_p \quad (3.23)$$

The noise can be considered uncorrelated with the pulses, and to be distributed according to a Gaussian:

$$p_n(A_n) = \frac{1}{\sigma\sqrt{2\pi}} \exp\left(-\frac{A_n^2}{2\sigma^2}\right) \quad (3.24)$$

where σ is the equivalent noise charge. Then the probability $p_d(\nu_t)$ of detecting a pulse of amplitude A_p at threshold ν_t , is:

$$p_d(\nu_t) = \text{probability}(A_n > (\nu_t - A_p)) = \int_{\nu_t - A_p}^{\infty} p_n(A_n) dA_n \quad (3.25)$$

If N_{fed} pulses, were fed into the channel, the expected number of detected pulses $N_{det}(\nu_t)$ is:

$$N_{det}(\nu_t) = N_{fed} \int_{\nu_t - A_p}^{\infty} \frac{1}{\sigma\sqrt{2\pi}} \exp\left(-\frac{A_n^2}{2\sigma^2}\right) dA_n \quad (3.26)$$

Now to fit this function to the data, the threshold in units of charge ν_t has to be expressed through setting of the `vth` register R_{vth} . Assuming that the

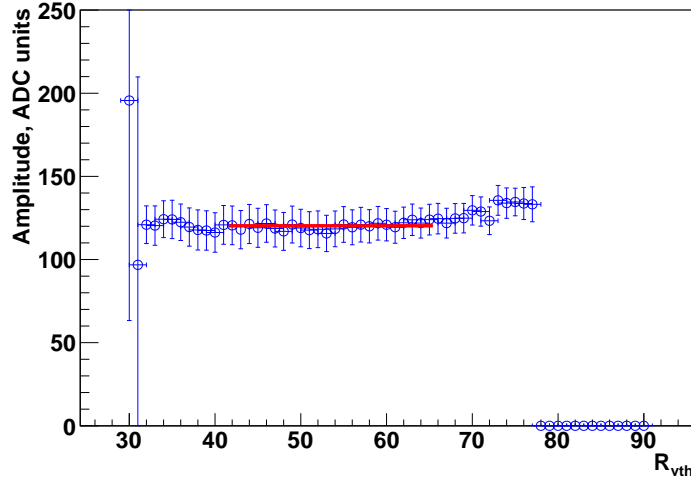


Figure 3.6: Pulse amplitude in the slow branch of the selected n-XYTER channel, measured with various values R_{vth} of the threshold register.

threshold ν_t is linear with R_{vth} , with some offset:

$$\nu_t = \alpha + \beta R_{vth} \quad (3.27)$$

the previous equation transforms as follows:

$$\begin{aligned} N_{det}(\nu_t) &= N_{det}(\alpha + \beta R_{vth}) = N_{fed} \int_{\alpha + \beta R_{vth} - A_p}^{\infty} \frac{1}{\sigma \sqrt{2\pi}} \exp\left(-\frac{A_n^2}{2\sigma^2}\right) dA_n = \\ &= N_{fed} \int_{R_{vth} - (A_p - \alpha)/\beta}^{\infty} \frac{1}{\sigma \sqrt{2\pi}} \exp\left(-\frac{(\beta A_n)^2}{2\sigma^2}\right) d(\beta A_n) = \quad (3.28) \\ &= N_{fed} \int_{R_{vth} - (A_p - \alpha)/\beta}^{\infty} \frac{1}{(\sigma/\beta) \sqrt{2\pi}} \exp\left(-\frac{A_n^2}{2(\sigma/\beta)^2}\right) dA_n \end{aligned}$$

By fitting this function to the S-curve (Fig. 3.5) the noise in the units of the threshold register σ/β and the value $(A_p - \alpha)/\beta$ is extracted. The latter is the value of R_{vth} , at which the threshold ν_t would be equal to the pulse amplitude, if R_{vth} could take non-integer values. The fit yielded the noise $\sigma/\beta = 5.92 \pm 0.03$ units of the threshold register.

As a cross-check, the stability of the pulse amplitude, as measured in the slow branch of the selected n-XYTER channel, was measured as a function of the vth register value (Fig. 3.6). The amplitude remains stable in the range where a sufficient (for a stable fit) number of pulses is detected ($R_{vth} \leq 77$), and when the noise is not distorting the measurement ($R_{vth} \geq 32$).

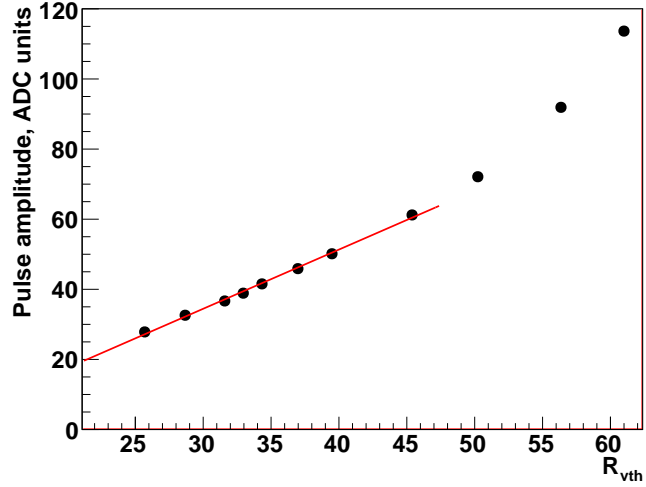
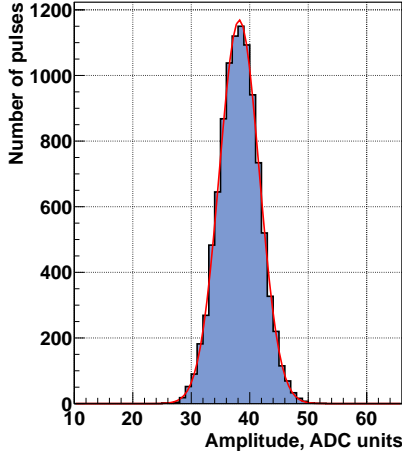


Figure 3.7: Example distribution of the amplitudes of the test pulses from the n-XYTER built-in generator, measured in the slow branch of the channel, and digitized with an external ADC.

Figure 3.8: Pulse amplitude in the slow branch of the selected n-XYTER channel (vertical axis), and the corresponding threshold register value R_{vth} , at which the threshold equals to the amplitude of the pulse in the fast branch.

Now, the threshold in the units of the threshold register has to be determined. It is not just equal to the setting of the threshold register R_{vth} because of the offset α (eq. 3.27). It is equal to

$$\frac{\nu_t}{\beta} = \frac{\alpha}{\beta} + R_{vth} \quad (3.29)$$

To determine the threshold offset α/β , the S-curve scan, as described above, was repeated for various pulse amplitudes. In each case the value $(A_p - \alpha)/\beta$ was extracted. In addition, the pulse amplitude A_p , as measured by the n-XYTER, was determined. Detailed description of measuring the amplitude with n-XYTER can be found in Here only an example distribution of the measured amplitudes of each individual pulse will be shown (Fig. 3.7).

The value $R_{vth} = (A_p - \alpha)/\beta$ was plotted versus the pulse amplitude (Fig. 3.8). By extrapolating the dependence to $A_p = 0$, the threshold offset was determined ($-\alpha/\beta = 9.6 \pm 0.9$ threshold register units).

Now the expected noise rate for each value of R_{vth} can be calculated (Fig. 3.9). The uncertainty of the calculation comes from the uncertainty in the measured threshold offset. The statistical uncertainty on the noise rate measurement is negligible. Despite of the difference between the measurement and the calculation reaching factor of about 2, it is still considered as a very good agreement, because the comparison covers 6 orders of magnitude in the noise rate. Also one has

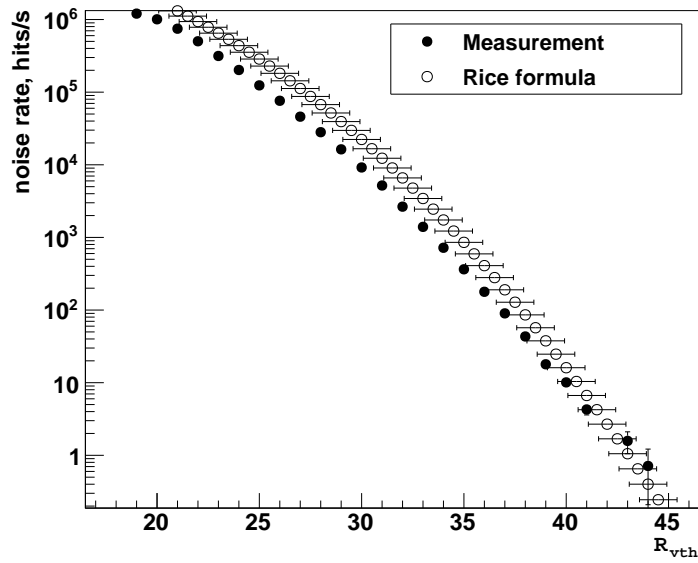


Figure 3.9: Comparison between the measured, and the predicted by the Rice formula, noise rates at different thresholds.

to keep in mind that none of the model parameters was fit to the noise rate measurement, and the model gives a good prediction for both the shape as well as scale of the dependence. It is therefore concluded that the Rice formula gives a good estimate of the noise rate and it will be applied to estimate the noise rate in the STS setup.

Chapter 4

Measurement of the passive electrical characteristics of silicon strip sensors

Passive electrical characteristics of silicon strip sensors are the resistances and the capacitances (or the I-V and the C-V characteristics) of their various constituent parts. There are several reasons, that make it important to study the passive electrical characteristics:

- passive electrical characteristics enter as parameters in models for estimating the performance of the sensors
- a deviation of certain characteristics from the nominal values can indicate a defect in the sensor; therefore measurement of passive electrical characteristics is a good approach for quality assurance
- these characteristics are macroscopic observables, with which one can study microscopic properties of the sensors as well as processes in them

Among the most important characteristics are:

- I-V and C-V characteristics of the sensor bulk
- coupling capacitance
- interstrip capacitances
- interstrip resistance
- resistance or I-V characteristic of the biasing structure
- resistance of the metal strip

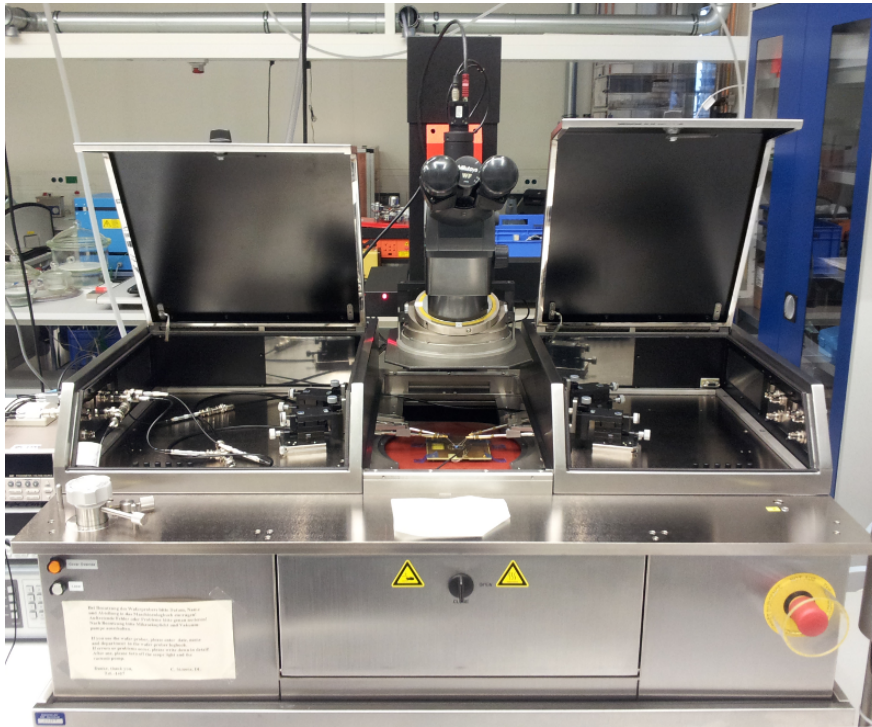


Figure 4.1: Probe station Süss PA300 with a sensors in the special fixture mounted on the chuck (the red round in the middle). Four probe needles are contacting the sensor from the sides.

4.1 Probe station

All measurements, described in this chapter, were performed on the probe station Süss PA300 (Fig. 4.1). The sensors were mounted in special fixtures for applying the bias voltage and placed on the chuck of the probe station. Four probes, ending with tungsten needles with $5\ \mu\text{m}$ tip radius, were used to establish the contact with the AC and the DC pads on the sensor. To position the needles precisely on the contact pads the probe station is equipped with a microscope. For automation of the measurements on numerous contact pads the probe station allows to move the chuck three directions with submicron precision, and rotate it by up to 7.5° in the horizontal plane.

The probe station also provided an electromagnetically shielded and light-tight environment for the measurements.

4.2 Capacitance measurement with LCR meter

Nowadays the most common approach to measure capacitance is to apply on the device under test (DUT) a sinusoidal voltage, and by measuring the induced

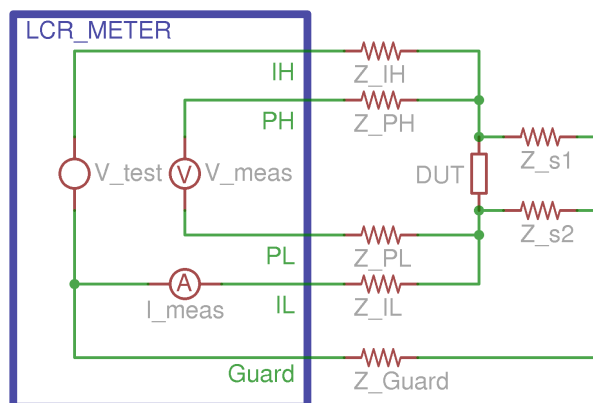


Figure 4.2: Equivalent circuit of the LCR meter and its connection to the device under test (DUT). The Z_{s1} and Z_{s1} represent the stray impedances (to the housing, for example), or any other impedances parallel to the DUT.

current and its phase shift (w.r.t. the applied voltage) determine the capacitance. Most, if not all, modern capacitance and LCR meters work on this principle. An alternative approach to measure capacitance can be to apply on the device under test a rectangular voltage pulse and to measure the conducted charge. The latter approach was applied, for example, in the BELLE-SVD project for measurement of interstrip capacitance [46, 47]. In this work an LCR meter with a sine wave test signal, Quadtech 7600 [48], was used.

Correct usage of the LCR meter requires basic knowledge about its operation. Without going into details of actual implementation of the device, only its equivalent circuit will be shown (Fig. 4.2). One can think of LCR meter as consisting of a source of the test voltage V_t , a voltmeter, measuring the voltage on the DUT V_m , and an ammeter, measuring the current through the DUT I_m . In this circuit all devices can be considered as ideal¹. The LCR meter also measures the phase shift θ between the voltage V_m and current I_m . From the measured V_m , I_m , and θ LCR meter evaluates the real and imaginary parts of the impedance of the DUT (assuming an equivalent circuit, as selected by the operator).

The device under test is connected to LCR meter with four wires: two wires to supply the test current, and two to measure the actual voltage on the device under test (Kelvin connection). Because the current through the voltmeter is very small, the voltage drop on impedances Z_{PH} and Z_{PL} is also very small and can be neglected. The voltage drop on Z_{IH} and Z_{IL} doesn't affect the measured current, of course.

The guard terminal is needed to exclude the effect of the stray and other par-

¹The voltmeter is usually implemented as a differential amplifier with FETs in the first stage, so its resistive input impedance is very large, and the capacitive input impedance is dominated by the capacitance of the leads. The ammeter is implemented as a feedback ammeter [49, p. 13], which ensures a very small burden voltage.

allel to the DUT impedances. Indeed, in the configuration, as shown in Fig. 4.2, the current that flows through Z_{s1} will not add up to the measured current, providing $Z_{s2} \gg Z_{Guard}$.

The connection of a device under test to LCR meter is usually done with coaxial cables. There is, of course, a large capacitance between the inner lead and the shield of a coaxial cable (for RG174 cable, that was used in the present work it is 1 pF/cm [50]). This capacitance adds up to the Z_{s1} and Z_{s2} , and if kept within reasonable limits, does not affect the measurement.

In order to achieve the best accuracy, LCR meter should always be zeroed before the measurement: quick open and short, if the measurement is done at a fixed frequency and test voltage, or full open and short, if a frequency or a voltage sweep is performed. If a voltage sweep is performed, it should not cross the 1 V margin, because different circuitry is used in the LCR meter for the dynamical range below 1 V test voltage, and 1 V above. If the device was zeroed at test voltage ≤ 1 V, this zeroing is not valid at voltages >1 V.

If very small capacitances are measured (the interstrip capacitance for example), the LCR meter should operated at the slow accuracy, with median measurement enabled. Also measuring the open loop capacitance of the device before or after each measurement is a good practice to ensure there is no systematic error because of the stray capacitances.

It is often recommended to avoid any DC current to flow into the terminals of the LCR meter. DC current can be blocked by large capacitors. Attention has to be payed to the operation frequencies of the capacitor. Special RF/Microwave ceramic capacitors is the best choice.

If the measurement is done in an unshielded environment, it is a good practice to interconnect the shields of the LCR meter leads at their end (close to the DUT). This will shunt the pick-up in the loop, formed by the LCR meter leads.

4.3 Bulk I-V characteristic

The current-voltage characteristic provides information about the resistivity of the bulk, from which one can deduce the effective doping concentration, and its profile along thickness of the sensor. It can also indicate defects in the bulk and the breakdown voltage of the detector. For irradiated sensors the bulk current can become large, and the shoot noise can make a significant contribution to the total noise.

In some cases, for example when the effective doping concentration has to be determined, the voltage drop on the biasing structures has to be taken into account. If the strips are biased through the punch-through structures, the I-V characteristic of the latter has to be measured separately, and the voltage drop on it (at the observed leakage current) has to be subtracted. If polysilicon resistors are used for biasing then the voltage drop need be taken into account only if the

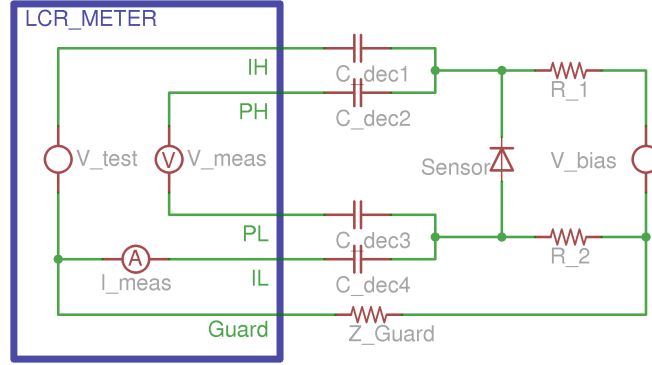


Figure 4.3: Measurement of C-V characteristic of sensor bulk.

sensor is heavily irradiated, and the leakage current is large. Normally, however, the per-strip leakage current does not exceed the nA level, and given the biasing resistors are on the order of 1 M Ω , the voltage drop (nA·M Ω =mV) is negligible.

The leakage current depends strongly on the temperature of the sensor. Therefore, in order to be able to make meaningful comparison between different measurements, it is necessary to perform them at the same temperature, usually either at 20° C or at 0° C [51]. If a measurement was performed at a different temperature, the leakage current should be normalized to one of the above mentioned temperatures according to the formula:

$$I \propto T^2 \cdot \exp\left(\frac{-E_0}{2k_B T}\right)$$

where $E_0 = 1.12$ eV is the band gap width, and $k_B = 8.62$ eV/K is the Boltzmann constant. ($I_{20^\circ}/I_{0^\circ} = 5.839$).

The RD50 collaboration [52] recommends to measure the I-V characteristic both with increasing and decreasing voltage ramps, and if a difference is observed, the decreasing bias voltage ramp mode should be preferred, as giving usually more repeatable results [51]. The author recommends in such case to increase the ramp time.

4.4 Bulk C-V characteristic

To measure the bulk C-V characteristic, the LCR meter and the bias voltage source must be simultaneously connected to the sensor (Fig 4.3). This introduces two problems. The first problem is that the bias voltage must not reach the terminals of the LCR meter, otherwise the LCR meter might be damaged by the high voltage. Also, depending on the implementation of the LCR meter, a constant current running through it might distort the measurement. This problem is easy to overcome: the LCR meter is DC-decoupled from the sensor with the for capacitors $C_{dec1}..C_{dec4}$.

The decoupling capacitors must not distort the measurement. For this C_{dec2} and C_{dec3} must be much larger than the input capacitance of the PH and PL terminals. The exact values of the input capacitance of the PH, PL terminals is not known, but it is assumed to be on the picofarad level. In the present setup C_{dec2} and C_{dec3} were chosen to be 1 nF, which should be sufficiently large.

The capacitor C_{dec1} should be either comparable to C_{Sensor} or much larger than it. Then sufficient fraction of the test voltage will drop on the sensor, and its capacitance can be measured accurately. Since the capacitance of the sensor can be as high as 10 nF (sensors with area of tens of cm^2 at zero or low bias voltages, for example: [53, p. 17]), C_{dec1} is also chosen to be 10 nF.

C_{dec4} has to be so large that its impedance is negligible compared to R_2 (the role of R_2 is explained below). This will ensure that all the current, that passed through the sensor runs in the ammeter, and not to the guard terminal. Since R_2 was selected to be 100 k Ω , the C_{dec4} is selected to be 1.5 μF . As C_{dec4} a combination of a small high-frequency capacitor and a large (1.5 μF) low-frequency capacitor can be used. This will enable to perform the measurement in a broad range of frequencies.

Another problem with the measurement of the bulk C-V characteristic is that the bias voltage source appears in parallel to the sensor. If no special measures are taken, its output capacitance (usually very large) adds up to the capacitance measured by the LCR meter. This problem can be overcome by introducing the resistor R_2 and grounding one terminal of the voltage source (by connecting it to the guard terminal of the LCR meter). Providing $R_2 \gg Z_{Guard}$, the current that passed through the bias voltage source, will run in the guard terminal, rather than in the ammeter. Therefore, the capacitance of the biasing voltage source will not add up to the capacitance measured by the LCR meter.

Additional requirements to R_2 are that, on one hand, it should be much larger than the impedance of C_{dec4} (otherwise a fraction of the test current from the sensor will leak to the guard). On the other hand it should not be too large, so that the drop of the bias voltage on it is not too large. Assuming that the leakage current of the sensor can reach up to 100 μA (for irradiated sensors) and requiring the voltage drop on R_2 not to exceed 10 V, the value of R_2 is chosen to be 100 k Ω .

The resistance R_1 serves to direct the test current of the LCR meter to the sensor, and not to let it leak to the bias voltage source. If there was no R_1 resistor, the test voltage would drop on capacitor C_{dec1} . The resistance R_1 should be just comparable, or larger than the impedance of C_{dec1} . In this point R_1 of 10 k Ω is sufficient. Again, too large value of R_1 would lead to a large drop of the bias voltage when measuring irradiated detectors. For maintaining the test voltage at low frequencies, when the impedance of C_{dec1} becomes larger, it is better to increase C_{dec1} , rather than increasing R_1 .

4.5 Interstrip resistance

Decent performance of a silicon strip detector requires sufficient isolation of the strips. The signal charge, collected on an implant must not flow to the neighboring strips, but predominantly into the readout electronics (if CSA-based readout electronics is used). This is ensured, if the interstrip resistance is much larger than the input impedance of the readout electronics [43, p. 101, 292]. The latter lies usually in the range 100–1000 Ω . Therefore, in point of charge collection, the interstrip resistance of ~ 100 k Ω should be sufficient.

Since interstrip resistance appears in parallel to the signal source, its thermal noise gives a contribution to the total noise in the system. It is usually required that this contribution is negligible compared to other sources of noise. The corresponding limitation on the interstrip resistance (R_i) can be obtained using the formula [43]:

$$R_i[M\Omega] > \frac{24^2 \cdot \tau[ns]}{(ENC_{R_i}[e^-])^2}$$

For a shaping time of 50 ns and required $ENC < 100 e^-$, one obtains the limitation $R_i > 2.9M\Omega$

Even though the interstrip resistance of a few megohms should be sufficient for normal detector operation, it is often required that the interstrip resistance is above 100 M Ω or more (for example: [54]). According to [55], this is just because a large safety factor is put in in order to compensate for possible fabrication process variations and failures.

In practical devices the interstrip resistance can range from 10^6 to 10^{12} Ω (for example: [56, 57, 58, 59]).

Measurement of the interstrip resistance is well described in [56]. Another work in this topic is [60].

Following [56], interstrip resistance can be measured in the next way (Fig. 4.4). A test voltage V_t is applied to one implant and the potential V_m of the neighboring implant is measured. If I_i is the current through the interstrip resistance, then

$$R_i = \frac{V_t - V_m}{I_i} \quad (4.1)$$

The current I_i can be determined from the voltage drop on R_d . R_d is the resistance from the implant B to the bias ring through it's bias resistor and it's right neighboring implants. While R_d will be determined below, let's now evaluate I_i :

$$I_i = \frac{V_m}{R_d} - I_{leak} \quad (4.2)$$

The current I_i is often measured by connecting a picoammeter in parallel to the bias resistor. This is, however, not a good way because the on modern (feedback) picoammeters there is always a burden voltage present, which is typically on

the order of $100 \mu\text{V}$ ($200 \mu\text{V}$ for Keithley 6487, that is used in the CBM-STs laboratory). This voltage will cause a current to flow through the bias resistor: $V_{burden}/R_b = 200\mu\text{V}/1.5\text{M}\Omega = 0.13 \text{ nA}$. This is a significant current, as compared to the current through the interstrip resistance, that has to be detected: $V_t/R_i = 1\text{V}/1\text{G}\Omega = 1 \text{ nA}$. In principle, it must be possible to measure the burden voltage of the picoammeter as a function of the measured current and to correct for it. However, a more reliable method is to determine the interstrip current I_i from the voltage between implant B and the bias ring. Modern voltmeters, can have internal resistance on the level of $\sim\text{G}\Omega$ and more, and will not distort the measurement.

In order to get rid of the leakage current in the equations, one usually varies V_t in the range of \pm few volts, and measures the slope $S = dV_m/dV_t$. The variation of the leakage current in this case can be neglected, because V_1 varies on the microvolt level. Equations 4.1, 4.2 can be then rewritten:

$$dI_i R_i = dV_t - dV_m$$

$$dI_i R_d = dV_m$$

Combining them one obtains

$$\frac{R_i}{R_d} = \frac{dV_t}{dV_m} - 1 = \frac{1}{S} - 1 \quad (4.3)$$

To determine R_d one can express it through the R_i and the total resistance from the implant to the bias ring R_0 :

$$R_0 = \frac{R_d(R_i + R_d)}{R_d + R_i + R_d}$$

Applying 4.3, and solving with respect to R_i :

$$R_i = R_0 \left(\frac{1}{S} - S \right) \quad (4.4)$$

R_0 can be measured by applying voltage and measuring current between the implant and the bias ring. Again, the leakage current will introduce an offset in the voltage, so R_0 should be determined from the slope dV/dI .

One effect, that should be taken into account is the resistance of the connection from the voltage source and the ammeter to the bias ring R_c (Fig. 4.5). This resistance is mainly the resistance of the wire bond to to the sensor. It can reach a few ohms. It turns out that the drop of the V_t voltage on it, can not be neglected. It will add up to the V_m and affect the measured slope S . The voltage on R_c :

$$V_c = V_t \frac{R_c}{R_0 + R_c}$$

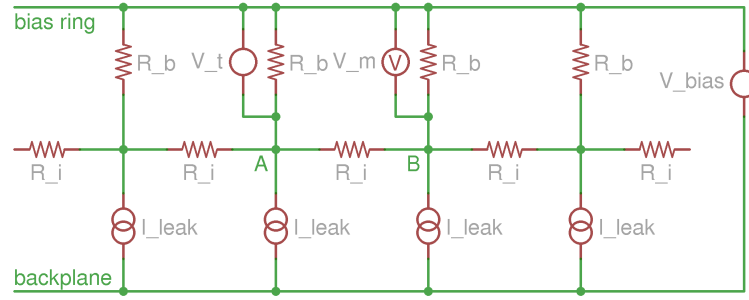


Figure 4.4: Equivalent circuit for measuring the interstrip resistance.

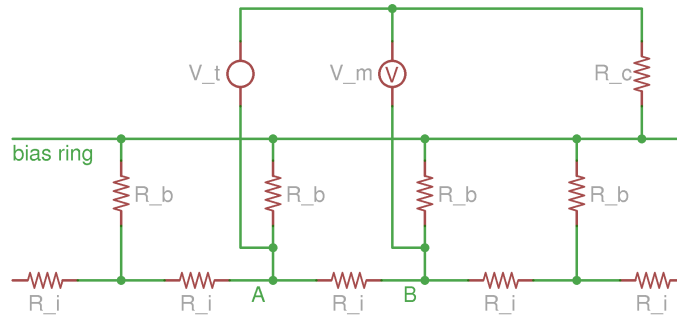


Figure 4.5: Equivalent circuit for measuring the interstrip resistance, showing the resistance of the connection from the voltage source and the ammeter to the bias ring R_c .

then it's effect on the slope

$$S_c = \frac{dV_c}{dV_t} = \frac{R_c}{R_0 + R_c}$$

This effect can be taken into account by measuring the slope for far implant, and subtracting it from the slope of implant B.

4.6 Bias resistance

If the interstrip resistance is much larger than the bias resistance, the latter can be measured simply by connecting a source-measure unit across it (Fig. 4.6). The leakage current I_{leak} will give a constant offset to the measured current I_m . To get rid of it, one can variate the test voltage V_t and determine the bias resistance from the slope:

$$R_b = \frac{V_t}{I_b} = \frac{dV_t}{dI_b} = \frac{dV_t}{d(I_m - I_{leak})} = \frac{dV_t}{dI_m}$$

In case the interstrip resistance is comparable to the bias resistance, the latter can be determined from R_0 and interstrip resistance R_i as measured in 4.5. From

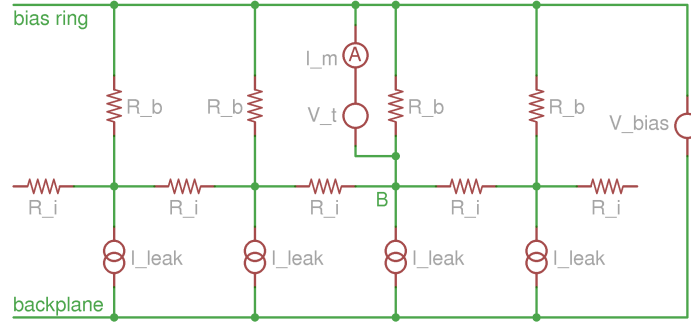


Figure 4.6: Equivalent circuit for measuring the bias resistance.

equations for R_d and R_0 :

$$\frac{1}{R_d} = \frac{1}{R_b} + \frac{1}{R_i + R_d}$$

$$\frac{1}{R_0} = \frac{1}{R_d} + \frac{1}{R_i + R_d}$$

one obtains:

$$R_b = \frac{2R_0^2}{R_i} + \sqrt{\frac{4R_0^4}{R_i^2} + R_0^2}$$

4.7 Strip leakage current

Measuring the leakage currents of individual strips can be useful in sensor R&D. For example, if a localized defect in the bulk leads to an excessive leakage current, the position of defect can be found by measuring the leakage currents of individual strips. Variation of the strip leakage current can indicate the uniformity of the bulk properties and fabrication processes.

A popular, but erroneous method to measure strip leakage current is to connect a picoammeter between the implant and the bias ring. Like in case of interstrip resistance, this method doesn't take into account the presence of a burden voltage on the picoammeter (see 4.5). This leads to the fact that the bias resistance shunts the picoammeter and the measured value turns out to be different from the actual leakage current. The current through the bias resistance is V_{burden}/R_{bias} can be on the order of $100\mu\text{V}/1\text{M}\Omega = 0.1\text{ nA}$, which is not negligible.

The correct way to determine the leakage current is to evaluate it from the bias resistance (section 4.6) and the voltage drop on it: $I_{leak} = V_b/R_b$.

4.8 Coupling capacitance

Coupling capacitance is the capacitance between the implant and the metal strip. It blocks the DC voltage between the implant and the input of the readout electronics, thus enabling to use readout electronics without DC-current compensation circuitry. It also couples the signal from the implant to the metal strip and to the readout electronics.

Three characteristics of the coupling capacitors are important for good performance of the detector system: the actual value of the coupling capacitance, the voltage it can stand without a breakdown, and the yield of non-defective coupling capacitors during the manufacturing.

The coupling capacitance C_c should be large compared to the capacitance $C_{i,tot}$ of the implant to its neighbors. Then most of the charge ($C_c/(C_c + C_{i,tot})$) will be coupled to the readout electronics (see 3.1 for details).

The coupling capacitors have to stand sufficient voltage without a breakdown. If the front-end electronics is operated in the floating mode, then the voltage drop on the coupling capacitance does not exceed a few volts (see Section 2.3.1). If a common ground readout scheme is used, then the coupling capacitance have to stand the full bias voltage (with a safety factor). In accelerator experiments a beam loss may result in a large instantaneous particles flux through the detector, which would cause a huge signal current and an additional voltage drop on the coupling capacitors (For example: [61, 62]). If such process is possible, the insulating layer between the implant and the strip has to be designed accordingly (in addition to such protection measures as the punch-through biasing).

When a double-sided sensor is read out with electronics at the common ground, a single broken capacitor (on the high voltage side of the sensor) results in inoperability of the whole detector module, because the sensor can not be biased. In such case it is very important to have as small as possible fraction of defective capacitors, and to test all coupling capacitances before operating the detector.

In the present section only the measurement of the coupling capacitance value will be discussed.

To measure the coupling capacitance the sensing terminals of LCR meter are connected to the AC and the DC pad of the selected strip. If no other actions are done, then in addition to the current through the tested coupling capacitance, extra currents will flow through C_{iDC} to the nearest neighboring implants, then through C_c to the metal layers of the neighboring strips, and through C_{iAC} to the metal layer of the tested strip. Similar currents will also flow through the further neighbors. These currents will add up with the current through the selected coupling capacitance. As a result, the measured capacitance will be (considering only the two nearest neighboring strips):

$$C_{meas} \approx C_c + \frac{1}{\frac{1}{C_{iDC}} + \frac{1}{C_{iAC}} + \frac{1}{C_c}} \approx C_c + \frac{C_{iDC}C_{iAC}}{C_{iDC} + C_{iAC}}$$

To exclude the contribution of the coupling through the neighboring strips, they can be connected to the ground of the LCR meter. (Fig. 4.7). In the present work, in the measurements with the CBM02 and CBM03' sensors, four strips on each side from the strip under test were grounded, and in the measurement with the CBM05 sensor — one strip on each side from the strip under test was grounded. Later it turned out that the contribution of the coupling through the neighboring strips was negligible, and the grounding was not necessary. Indeed, the results with and without the grounding were compared on one strip of one sensor (Fig. 4.10) and the difference is 0.1% of the absolute value (explanation of the figures and the procedure of evaluation of the capacitance will be described below).

The coupling capacitance should be measured at frequencies, that are much smaller than $1/(2\pi R_{imp}C_c)$, where R_{imp} — is the resistance of the implant, and C_c — is the coupling capacitance. The reason for this is that the implant has high resistivity (order of 100 k Ω /cm), and it will impede the applied test voltage (Fig. 4.8). At frequencies, comparable with $1/(2\pi R_{imp}C_c)$, or higher, the far, from the contacted DC-pad, end of the implant (the left end in Fig. 4.8) will not follow the applied test voltage from the LCR meter, and the current through the corresponding portion of the coupling capacitance will be suppressed. As a result, only a portion of the coupling capacitance, that is close to the DC-pad, will be measured by the LCR meter. This effect is also reported in [63, 64, 65]. The LCR meter can not properly take into account the resistance of the implant (by measuring the phase shift and determining only the imaginary part of the impedance), because the implant and the coupling capacitance can not be considered as a series connection of lumped components.

Because the frequency $1/(2\pi R_{imp}C_c)$, below which the coupling capacitance should be measured, was not known in advance, the coupling capacitance was always measured as a function of the frequency in a broad frequency range, and the values at the plateau were taken as the true coupling capacitance. In the measurements with the CBM02 and CBM03' sensors the results at the lowest frequencies were also discarded because at the low frequencies the relative accuracy of the measurement becomes slightly worse.

Coupling capacitance was measured in one CBM02, one CBM03', and one CBM05 sensors. The sensors were always kept biased above the full depletion during the measurements.

In case of CBM02 and CBM03' sensors, the measurements were done on 3 strips on each side (there is only one structured side — the p-side — in the CBM03' sensor), while on the CBM05 sensor the coupling capacitance was measured only for one strip on one side. The strips for the test were selected far from the edges of the sensor, as well as from each other (in case of CBM02 and CBM03' sensors).

The measurements were done on the probe station (4.1). As mentioned above, the strips, neighboring to the tested ones, were grounded. In case of the CBM02 and CBM03' sensors, the four nearest neighboring strips on each side were inter-

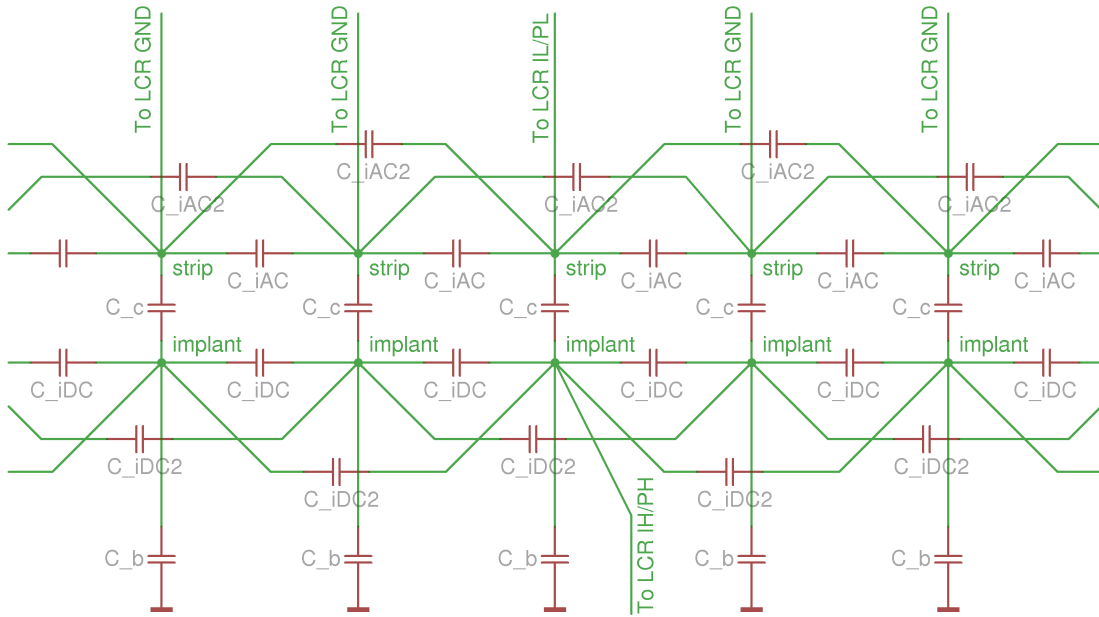


Figure 4.7: Simplified equivalent circuit of one side of the sensor and connection scheme for measurement of the coupling capacitance. Each implant is shown here as a single node (it's resistivity of the implants is neglected) for simplicity. An equivalent circuit of a single strip, without neglecting the resistance of the implant is shown in Fig. 4.8. Capacitance of metal strips and implants to their first (nearest) and second neighbors are shown. Capacitances to further neighbors are omitted here for simplicity. Grounding of the neighboring strips, as shown on the diagram, is optional.

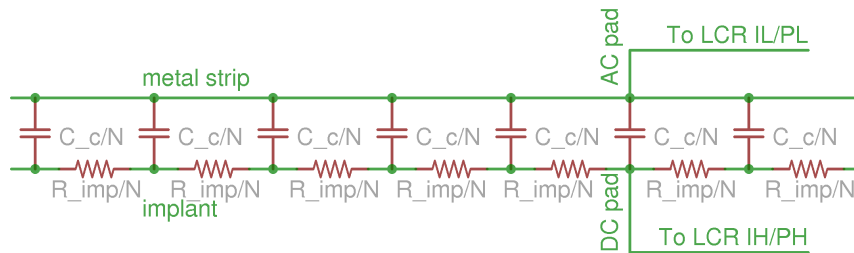


Figure 4.8: Simplified equivalent circuit of one strip and the connection for the coupling capacitance measurement. The distributed coupling capacitance (C_c) and implant resistance of the strip (R_{imp}) is shown as a series of lumped components (C_c/N and R_{imp}/N). Capacitance to the neighboring strips, as well as to the backplane is omitted here for simplicity.

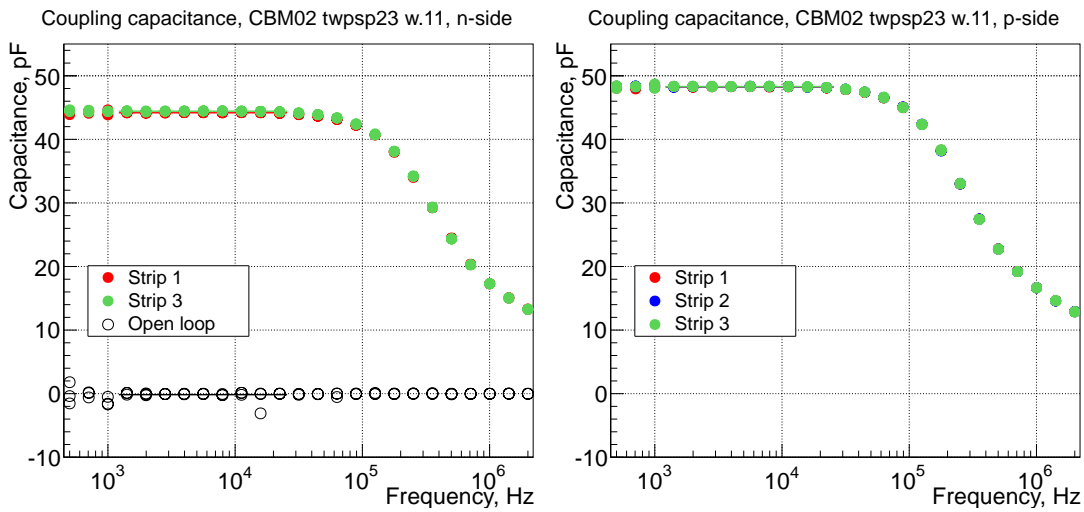


Figure 4.9: Coupling capacitance on the n- (left), and the p-side (right) of a CBM02 baby sensor.

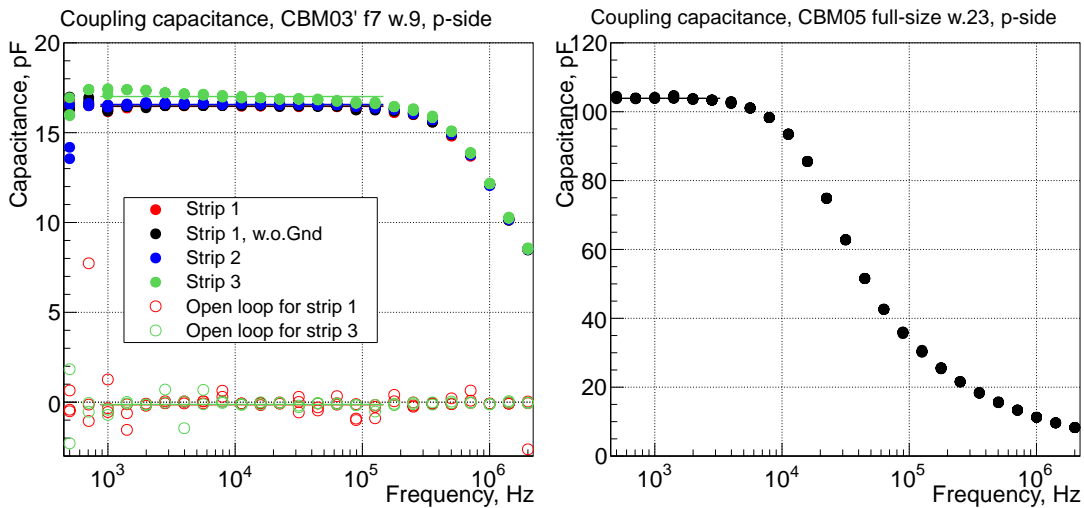


Figure 4.10: Coupling capacitance on the p-side of CBM03' baby sensor (strip length 9.6 mm). The measurement without grounding the neighboring strips is marked "w.o.Gnd".

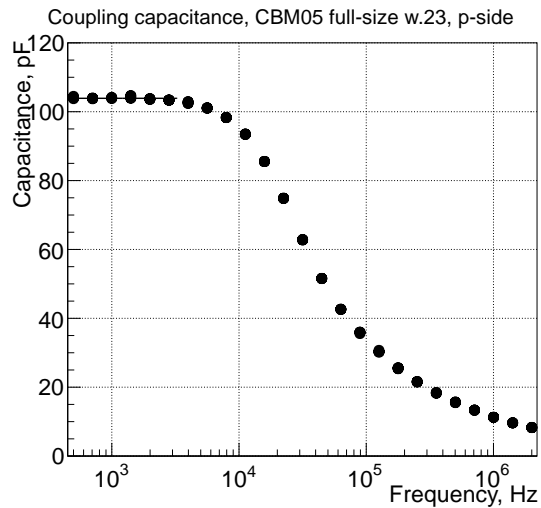


Figure 4.11: Coupling capacitance on the p-side of CBM05 full-size sensor (strip length 59.4 mm).

Sensor, side	Coupling capacitance, pF/cm	Frequency range, kHz
CBM02, p-side	37.8	1.410–22.38
CBM02, n-side	34.7	1.410–22.38
CBM03', p-side	17.2	0.998–125.9
CBM05, p-side	17.5	0.500–2.814
CBM05, n-side	not measured	—

Table 4.1: Coupling capacitance in the prototype CBM sensors

connected with each other with wire bonds (Fig. 4.12), and one of the interconnected neighboring strips on each side was contacted with a grounded probe needle. On the n-side of the CBM02 sensor one of the strips under test was, because of the failure in the wire bonding, shorted to a neighboring strip, and therefore the results of the corresponding measurement on it are not shown (Fig. 4.9, left). In case of the CBM05 sensor, only the pair of the nearest neighboring strips were grounded, by contacting them with grounded probe needles. Each measurement was repeated three times, and all the results are shown (points are overlapping, and indiscriminating on the plots). Also the open loop capacitance was measured, to ensure a proper zeroing of the device. The obtained results are shown in Figs. 4.9, 4.10, and 4.11.

The frequency range, to determine the coupling capacitance from, was defined individually for each sensor and each side. This range was selected just by eye (the associated with this systematic error is considered to be tolerable), as the range, where the capacitance is constant with the frequency. The capacitance value was determined by a χ^2 fit of a constant (a horizontal line) to the data points, and the average value over the tested strips was taken. The open loop capacitance was subtracted (except for the CBM05 sensor). The open loop capacitance was also determined by a χ^2 fit of a constant, in the same frequency range as the coupling capacitance. The obtained results are summarized in Table 4.1. Proceeding from the usual requirement, that the coupling capacitance is at least factor 10 larger than the interstrip capacitance (reported in 4.9), the observed coupling capacitance values are on the satisfactory level.

4.9 Capacitance of implant to neighboring strips

One of the quantities, that is needed to calculate the expected signal amplitude, is the capacitance of an implant to the all surrounding virtual grounds, except the capacitance to its own metal strip (Section 3.1). This quantity is the sum of the capacitance to the backplane, and the capacitance of the implant to all

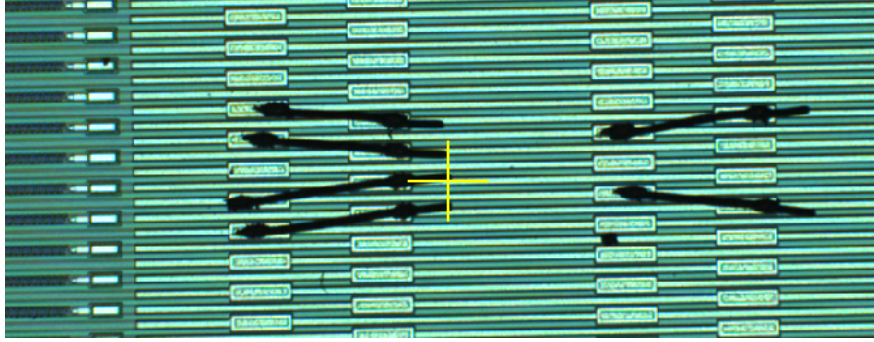


Figure 4.12: Strips, interconnected with wire bonds for the measurements of the coupling capacitance, the capacitance of an implant to the neighboring strips, and the total strip capacitance. Photograph made on the CBM03' sensor.

the strips on the same side in total (only the near neighbors contribute). While the backplane capacitance can be determined from the full bulk capacitance, the capacitance of an implant to the neighboring strips has to be measured separately. This will be described in the present section.

The circuit diagram for measuring the capacitance of an implant to neighbors is shown in Fig. 4.13. As mentioned above, only the near neighbors are expected to contribute to the total capacitance of the implant. Since it was not known, how many neighboring strip on each side should be included in the measurement, it was decided to measure the capacitance of an implant to four neighboring strips on each side from the strip under test, which should be more than sufficient. For this, the neighboring strips were interconnected with each other with wire bonds, as shown in Fig. 4.12. This was necessary, because only four probe needles were available in the probe station: one was used to apply the test voltage on the implant, one — to ground the strip over the implant, and the other two — to pick the induced current from the two groups of neighboring strips.

Alternatively to measuring the total capacitance of an implant to all its neighbors at once, it is theoretically possible to measure the its capacitance to the first, second, and further neighbors individually. Such approach is, however, practically more complicated: first, because more measurements need to be done, and secondly, because each of the contributions is small, so the relative error of each of the individual measurements would be larger. Therefore, it was preferred to measure the capacitance of an implant to all neighbors at once, even though it requires the wire bonding.

In the measurement of an implant capacitance to the neighbors, it is important to connect the bias ring of the tested side of the sensor to the ground of the LCR meter. Otherwise, the test current will flow in the IL/PL terminals of the LCR meter over the bias rail, through the bias resistors. This current will dominate over the current through the $C_{iDC,tot}$, if $1/(2\pi f C_{iDC,tot}) \gg R_b$, or at frequencies

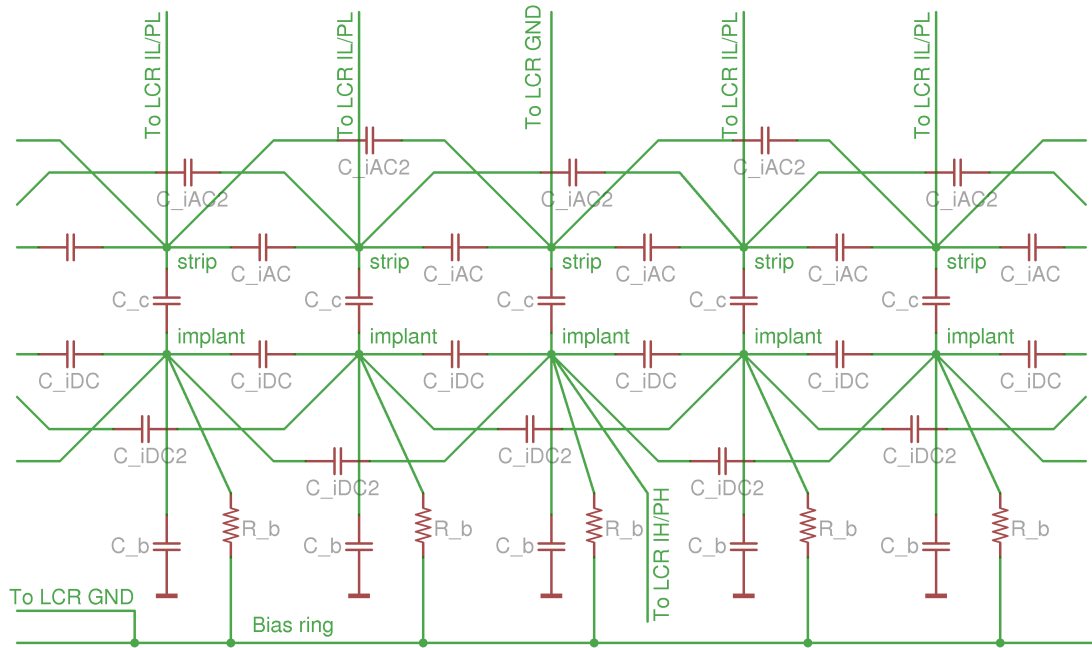


Figure 4.13: Simplified equivalent circuit of one side of the sensor and connection scheme for measuring the capacitance of an implant to the neighbors. Each implant is shown here as a single node, neglecting its resistivity (an equivalent circuit of a single strip-implant couple, without neglecting the resistance of the implant is shown in Fig. 4.8). Capacitance of metal strips and implants to their first (nearest) and second neighbors are shown, while the capacitances to further neighbors are omitted here for simplicity.

$f \ll 1/(2\pi R_b C_{iDC_tot}) \approx 0.16$ MHz, assuming $R_b = 1$ M Ω , and $C_{iDC_tot} = 1$ pF, which is an approximate value for baby sensors.

Similarly to the case of measuring the coupling capacitance, the resistance of the implant hinders the measurement of the implant capacitance to the neighbors at high frequencies: the far end of the implant does not follow the applied test voltage, and the measurement yields a smaller result. The measurement should be done at frequencies, significantly below $1/(2\pi R_{imp} C_c)$, where R_{imp} — is the total resistance of the implant, and C_c — is the coupling capacitance (here it is the coupling capacitance, that is relevant, because it makes the major contribution to the total capacitance of the implant). Again, because this frequency is not known in advance, all measurements are done as a function of the frequency, in a broad range.

Unlike with the coupling capacitance, the capacitance of an implant to the neighbors drops down at the very low frequencies. This happens because the implant is not directly coupled to the neighboring strips, but over the neighboring implants. The neighboring implants (as well as the selected implant) are connected over the bias resistors to the bias rail and the bias rail is connected to the guard of LCR meter. At very low frequencies the impedance of C_c becomes large compared to R_b and the neighboring implants become effectively grounded. So, the capacitance of an implant to neighbors is measured correctly, if $1/(2\pi f C_c) \ll R_b$, or $f \gg 1/(2\pi R_b C_c)$. Typical values for baby detectors, $R_b = 1$ M Ω , $C_c = 30$ pF, result in minimal measurement frequency: $f \approx 5$ kHz.

The capacitance of an implant to neighbors was measured on one CBM02 and one CBM03' sensors. The sensors were kept biased beyond the full depletion voltage during all measurements. The measurements were done in less than a minute after applying the bias voltage. This may affect the result of the measurement — a different experimental group, that performed their measurements on different sensors, reports a change of the interstrip capacitance with time, after applying the bias voltage [66]. In addition, the open-loop capacitance was measured for each individual strip. In the measurement of the open loop capacitance, the IH/PH and the grounding needles of the LCR meter were left in contact with the sensor, and the IL/PL needles were disconnected from the sensor (lifted up by around a millimeter).

The obtained results are shown in Figs. 4.14, 4.15. Each measurement was repeated three times, and all the data points are shown on the plots. Because of a failure in wire-bonding of the neighbors of Strip 2 on the n-side of the CBM02 sensor, the neighboring strips were shorted to the strip over the implant under test, and the results of the measurements were, therefore, discarded.

Despite of a poor accuracy, the main features are discernible on the plots: a plateau is visible in the frequency range 10^4 – 10^5 Hz, and after 10^5 Hz a decrease of the capacitance is observed (because of the resistance of the implant). However, at low frequencies, below 10^4 Hz, instead of the expected drop of the capacitance (because the neighboring implants are grounded over the bias resistors), other

Sensor, side	Implant capacitance, pF/cm	Frequency range, kHz
CBM02, p-side	1.0±0.5	3.976–63.12
CBM02, n-side	1.4±0.5	11.21–89.18
CBM03', p-side	1.0±0.5	11.21–63.12

Table 4.2: Capacitance of an implant to the neighboring strips in the prototype CBM sensors

features are observed. On the n-side of the CBM02 sensor (Fig. 4.14, left), for Strip 1 a slight drop of the capacitance is observed, while from the above considerations a drop to (almost) zero is expected. For the Strip 3, contrariwise, a rise of the capacitance is observed. This observation could not be explained, and the result was not used for determining the capacitance of an implant. The scattering of the data points on the p-side of CBM02 and CBM03' sensors is also not explained.

Nevertheless, the capacitance of an implant to the neighbors was evaluated by χ^2 fitting a horizontal line to the data points in the plateau region (exact fitting range is specified in the Table 4.2). The plateau range was determined by-eye. The associated systematic error is considered to be negligible compared to the error, caused by the poor accuracy and poor reproducibility of the measurements. The open loop capacitance was also determined by a χ^2 fitting with a horizontal line, in the same range as for the implant capacitance. The open loop capacitances was subtracted from the implant capacitances, and the average value was taken. The results are summarized in Table 4.2.

The value for the n-side of the CBM02 sensor was determined in a special way. In 4.10 it will be shown that in the selected frequency range a special effect, presumably an effective increase of the dielectric constant, caused by the presence of the accumulation layer, gives a contribution to the capacitance. This contribution was determined in 4.10 (0.8 pF), and was subtracted from the observed value (2.2 pF). The contribution of this low-frequency effect has to be subtracted, because, the signal lies, in the frequency domain, in the range of hundreds of megahertz (the charge collection and integration takes place within the time of tens of nanoseconds), so this effect is not expected to exhibit.

To each of the evaluated values a conservative uncertainty estimate of 0.5 pF was assigned. It will be seen in Sections 8.3, and 9.6.2 that even with such, probably overestimated, uncertainty, it is possible to draw definite conclusions on the relation between the expected and the observed signal amplitude.

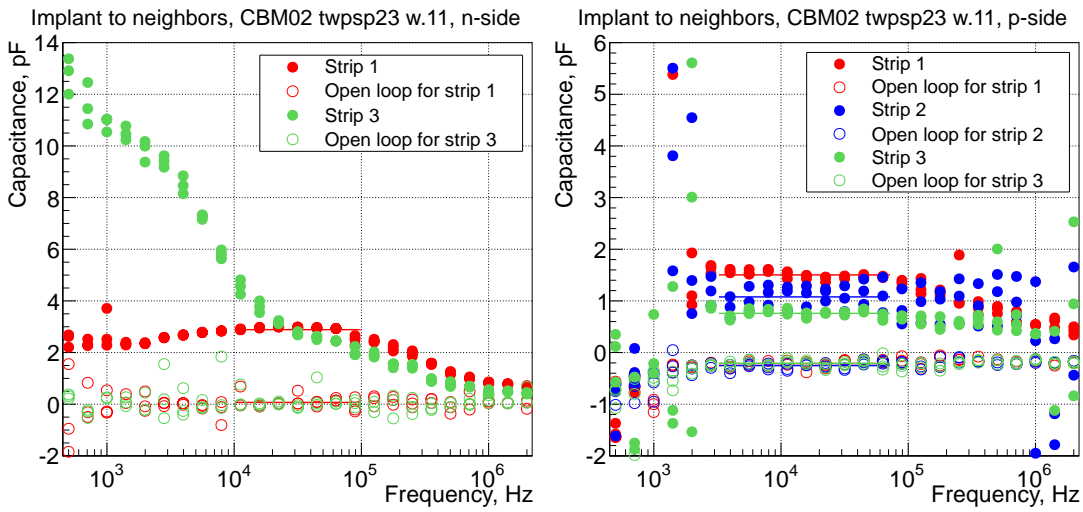


Figure 4.14: Total capacitance of an implant to the neighboring strips on the n- and the p-side of the CBM02 sensor.

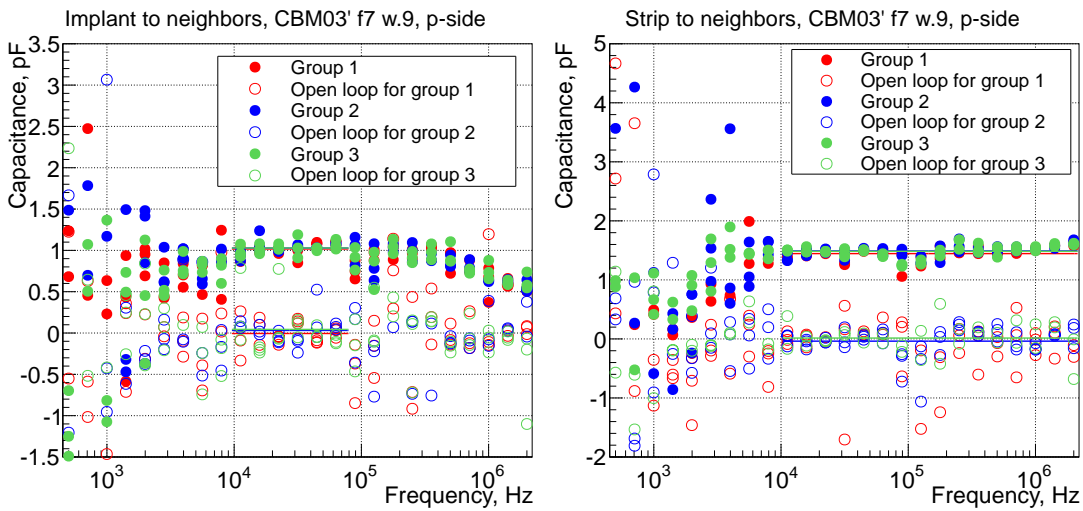


Figure 4.15: Total capacitance of an implant to the neighboring strips on the p-side of the CBM03' sensor (single-sided). Figure 4.16: Total capacitance of a strip to the neighboring strips on the p-side of the CBM03' sensor (single-sided).

4.10 Capacitance of a strip to the neighbors

Both the signal amplitude and the noise depend on the total capacitance of the readout channel. The latter consists mainly of the total capacitance of a strip and the capacitance of the analog cable (or the fan-out PCB, like in case of the current prototype detectors), connecting the sensor to the front-end electronics. The dominant contribution to the total capacitance of a strip comes from its capacitance to the neighboring strips.

The equivalent circuit of the sensor, as well as the connection of the LCR meter for the measurement of the total strip capacitance, are shown in Fig. 4.17. The measurement principle is similar to the measurement of the capacitance of an implant to the neighbors (Section 4.9): the test voltage is applied to one strip, and the induced current is picked from the neighboring strips (four on each side of the tested strip, in this case).

The measurements of the total strip capacitance were done on the same sensors, and the same strips, as in Section 4.9. Similarly to the measurement of the implant capacitance to the neighbors, the bias ring of the tested side was connected to the ground of the LCR meter, in order to avoid the coupling between the strips through the bias resistors at low frequencies (order of $1/(2\pi R_b C_c) \approx 5$ kHz), and extend the measurement frequency range. The results of the measurements are shown in Figs. 4.18 and 4.16.

Unexpectedly, at the p-side of the CBM02 sensor, an increase of the capacitance at low frequencies (below around 8 kHz) is observed, even though the bias ring was grounded. This effect is not understood. On the p-side of the CBM03' sensor the measured capacitance value exhibit large fluctuations. These fluctuations can not be explained by a poor accuracy of the meter at low frequencies, because no such fluctuations are observed at the n-side of the CBM02 sensor (the absolute value of the capacitance is on the same order of magnitude). This effect also could not be explained, and requires additional studies. On the n-side of the CBM02 sensor, yet another effect is observed: the capacitance rise with the decrease of the frequency. A possible explanation of this effect is that there is an electron accumulation layer between the strips on the n-side, which effectively increases the dielectric constant of the material at intermediate frequencies. The measurement on the strip 2 is not shown because the strip under test was, by accident, shorted to the neighboring strips during the wire-bonding.

Despite of the unexpected features on the plots, the total capacitance of the strip was determined in each case. The plateau region on each of the plots was fitted with a horizontal line, and the average (over the strips) value was taken. The results are summarized in Table 4.3. The observed values are reasonable.

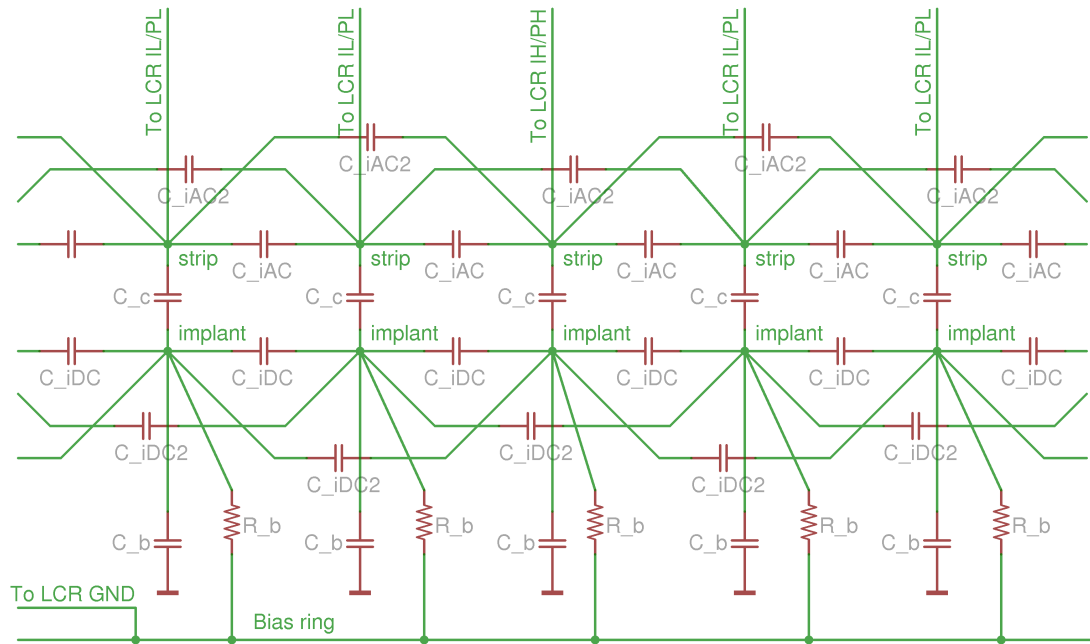


Figure 4.17: Simplified equivalent circuit of one side of the sensor and connection scheme for measuring the capacitance of an implant to the neighbors. Each implant is shown here as a single node, neglecting its resistivity (an equivalent circuit of a single strip-implant couple, without neglecting the resistance of the implant is shown in Fig. 4.8). Capacitance of metal strips and implants to their first (nearest) and second neighbors are shown, while the capacitances to further neighbors are omitted here for simplicity.

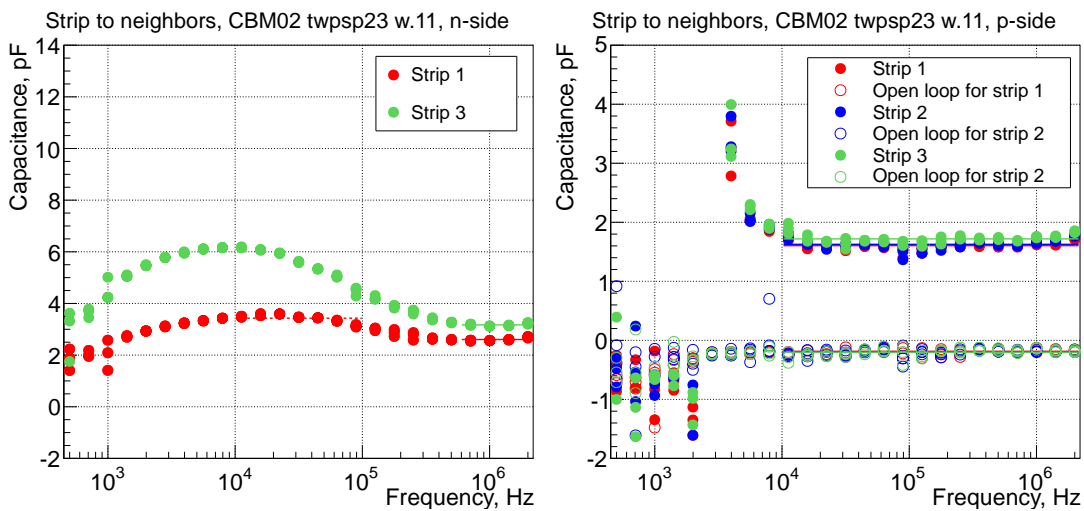


Figure 4.18: Total capacitance of a strip to the neighboring strips on the n- and the p-side of the CBM02 sensor.

Sensor, side	Strip capacitance, pF/cm	Frequency range, kHz
CBM02, p-side	1.4	11.21–2000
CBM02, n-side	2.2	709.2–2000
CBM03', p-side	1.5	11.21–2000

Table 4.3: Capacitance of a strip to the neighboring strips in the prototype CBM sensors

4.11 Capacitance of the fan-out boards

In the present work, during the measurements of the amplitude response, the sensors were mounted on fan-out boards, as shown in Figs. 2.7, and 10.1. The capacitance of the traces of the board adds up with the total capacitance of the strip, and affects (to a small degree) the signal amplitude. The capacitance of the traces of the boards were measured, in order to take it into account in the calculation of the signal amplitude (Section 3.1). For the shortest traces the obtained value is 4.7 pF, and for the longest — 6.2 pF. To simplify the calculations, and average value of 5.5 pF was taken for the estimate of the signal amplitude, and the error on this value was calculated as $(6.2-4.7)/\sqrt{12} \approx 0.4$ pF. The applied approximations do not affect the result of the calculation of the signal amplitude (Section 3.1), and better accuracy is unnecessary.

Chapter 5

Characterization of the n-XYTER readout ASIC

On the stage of early detector prototyping, before the dedicated STS readout chip was designed, its technological predecessor, n-XYTER [36, 37], was used as a prototype readout chip.

n-XYTER (neutron-X-Y-Time-Energy Readout) is a 128-channel self-triggering readout ASIC, capable of measuring both signal amplitude and time of occurrence. It was originally developed within the EU-FP6 NMI3 DETNI project for solid-state and gaseous neutron detectors. At present, due to its self-triggering design, high rate capability, high gain and bipolar front-end, the chip is widely used to read out silicon detectors, gaseous detectors, and photomultipliers in various projects at GSI as well as in other laboratories. n-XYTER suits very well for prototyping of the STS detector systems.

Before coming to the actual measurements with silicon detectors, it is important to properly configure the readout chip. Also, amplitude calibration of the readout chip is necessary to interpret the data. The configuration and characterization of the chip is described in this chapter.

5.1 Chip architecture

Readout chain of every n-XYTER channel starts with a charge-sensitive preamplifier, after which the signal is split and sent into two shapers: the fast and the slow, with peaking times 19 and 130 ns respectively. (Fig. 5.1).

The fast shaper output is used for triggering and time measurement. When the signal in the fast shaper exceeds a defined threshold and the comparator (see Fig. 5.1) is fired, hit generation starts: the timestamp of the hit is stored in an in-channel FIFO and the peak detection and hold (PDH) circuit is activated.

The small rise time of the fast shaper, together with the time walk compensation (TWC) circuit, allow to achieve a good time resolution of the chip.

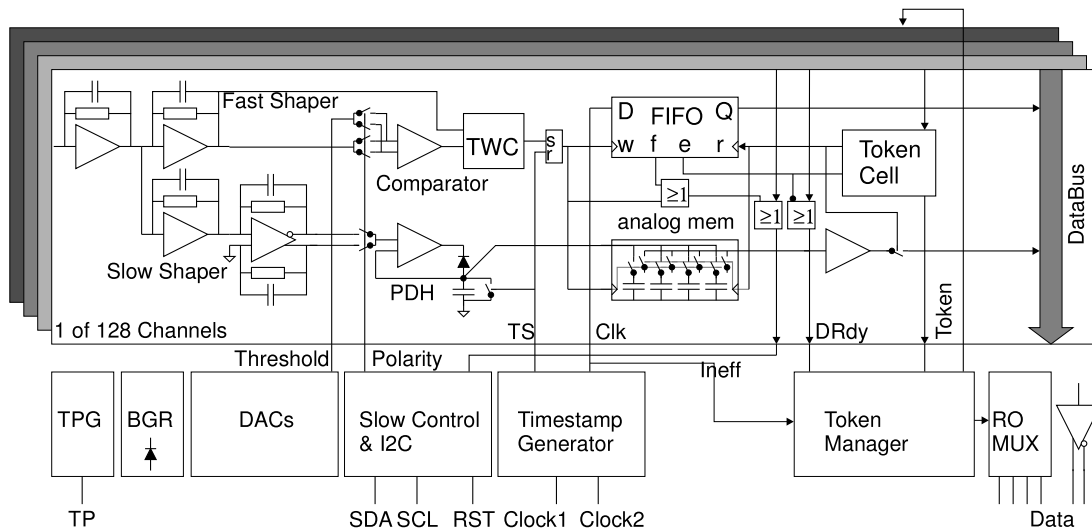


Figure 5.1: Simplified diagram of n-XYTER architecture [36]. A single readout channel together with the common logical part is shown. The analog input together with the preamplifier is in the top left corner.

The slow shaper provides the signal for low noise peak height analysis. The peak detection and hold circuit is basically a fast voltage follower connected over a diode to a capacitor, so that the capacitor is being charged on the leading edge of the pulse, but doesn't discharge on the trailing one. The PDH circuit stays active for a certain time, and then the voltage on the capacitor is latched to the analog memory. Since the n-XYTER chip has no built-in ADC the amplitude information is provided as an analog voltage level.

The DC offset of the slow shaper is not rejected inside n-XYTER. It is present at the analog output and has to be determined and subtracted by the user. Moreover, this offset has, unfortunately, a large temperature coefficient, so for accurate amplitude measurements a temperature stabilization of the chip as well as continuous monitoring of the DC offset are necessary.

Transmission of hits out of the chip starts as soon as there is at least one hit in the FIFO buffer of one of the channels. Data transmission is done synchronously with the clock. All n-XYTER channels share a single analog output port for amplitude information and 8-bit digital bus to transport 4 bytes of data with the channel number, the time stamp and some auxiliary information. The arbitration for the usage of the outputs is realized with a token ring.

n-XYTER operation is controlled with 46 8-bit registers, accessible over i²c bus.

5.2 n-XYTER operation

Based on the n-XYTER chip, general purpose front-end boards (FEBs) were produced at GSI (Fig. 2.9). These kinds of boards were used for the calibration work presented here. Each FEB hosts an AD9228 ADC for amplitude digitization as well as auxiliary electronics, required for chip operation. Because of the large temperature drift of n-XYTER 1.0, the boards are mounted on cooling blocks and the temperature is stabilized with circulating water. The interface between the front-end board and PC is provided by a SysCore v2 board [67]. Data acquisition is done with DABC [68].

To determine the DC offset in the n-XYTER analog output, the chip is switched to the externally-triggered mode and triggered from SysCore. Provided that no real signal is coming into the n-XYTER in coincidence with the trigger, the measured output value is the offset.

In most today's applications n-XYTER is used in conjunction with AD9228 ADC operated in 12-bit mode, with reference voltage of 1 V (dynamical range: -1 V..1 V). Therefore, for convenience, the signal amplitudes will be expressed in units of the ADC LSB (least significant bit). The amplitudes (without the DC offset) can be converted back to mV as: $U[mV] = A[LSB] \cdot 2000 \text{ mV}/4095 \text{ LSB}$.

5.3 Optimization of the register settings

The Vbfb register. The Vbfb register controls the resistance in the preamplifier feedback, which by-turn determines the discharge time of the preamplifier. A larger value of Vbfb results in a smaller resistance, and a shorter discharge time.

The discharge time has to be, on one hand, much longer than the peaking time of the shaper, then maximal possible peak height on the shaper output is achieved. The contrary situation, when the preamplifier discharges by a significant fraction before the shaper output reaches the peak, and the peak height is reduced, is called *ballistic deficit*.

On the other hand, the discharge time must be small compared to the average input pulse rate, otherwise the preamplifier can run into saturation.

n-XYTER response was measured as a function of the Vbfb register value on one readout channel at the negative polarity (Fig. 5.2). No discernible drop in amplitude is seen up to Vbfb value of 60. The value of 50 is chosen for further n-XYTER operation. The observed drop of n-XYTER output amplitude at small register values is not explained.

The VbiasF register. The VbiasF register controls the DC offset of the fast shaper. Optimally, it has to be set such, that the DC offset is close to the edge of the linear dynamic range of the shaper, because it allows to achieve the maximal possible linear swing for the signal. For positive input pulses the signal in the

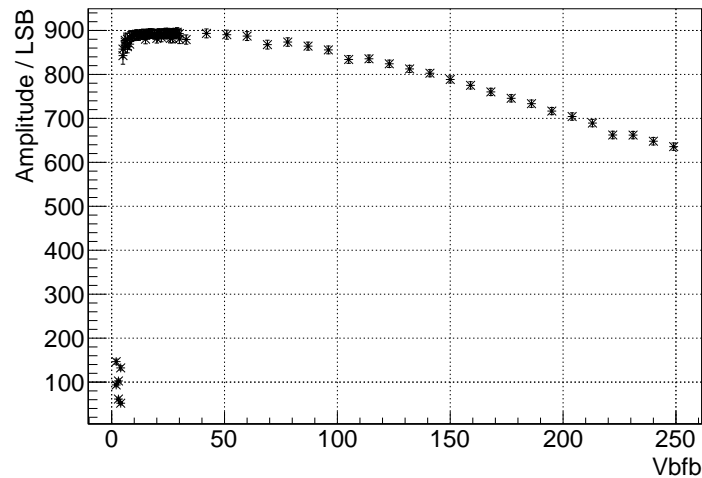


Figure 5.2: n-XYTER output amplitude as a function of the Vbfb register value

fast shaper is negative, so the DC offset should be close to the upper edge of the linear region and vice versa. An improper setting of VbiasF will limit the linear swing of the signal, and hence, narrow the range of pulse amplitudes that can be discriminated.

VbiasF has also a little effect on the rise time, the reminder and the undershoot. An increase of the register value (decrease of the offset) leads to a slight decrease of these three values.

The recommended in [36] VbiasF settings are: 103 for negative polarity, and 95 for positive. However, in one of the experiments, by looking at the analog output of the fast shaper it was found that at large pulse amplitudes (that are still within the linear range of the slow shaper of the n-XYTER) the amplitude in the fast shaper is saturated. Therefore it was decided to optimize the settings.

The DC offset of the fast shaper has been measured as a function of the VbiasF register value on the test channel of one n-XYTER (FEB D53). The signal was read over a voltage repeater (that is installed on the FEB by design) with an oscilloscope and a high-gain differential probe. The results are shown in Fig. 5.3. The experimental points only within the linear range were recorded. At VbiasF below 80, or above 130 DC offset starts changing nonlinearly. The linear range of the fast shaper is therefore approximately 0.5–1.8 V. In order to use the maximum So the register settings 90 and 120 for the positive and the negative polarities respectively will be more proper. The parametrization for the obtained dataset is:

$$V_{DC}^{fast} [V] = 2.46 - 5.90 \cdot 10^{-3} \cdot VbiasF - 6.99 \cdot 10^{-5} \cdot VbiasF^2$$

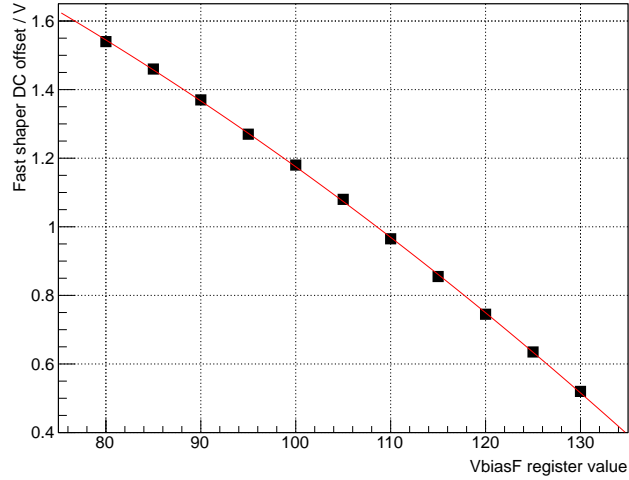


Figure 5.3: DC offset of the fast shaper as a function of the VbiasF register value.

5.4 Dependence of the amplitude and the noise on the input load

Given a constant input charge, n-XYTER output amplitude will depend on the capacitance, presented to its input (not to be confused with the input capacitance of n-XYTER). This is because n-XYTER, as any feedback charge preamplifier, has a finite (though large) input capacitance (see Section 3.1). The input capacitance of n-XYTER is needed to be known to make precise measurements of the signal charge in the silicon strip sensors. It can be evaluated by measuring the output amplitude versus the capacitance on the input, with a constant input charge.

In addition, the output amplitude can be affected by any resistance between the signal source (silicon strip sensor) and n-XYTER. In the present detector prototypes, or the future STS detector modules, it is the resistance of the metal strips and the analog cables. A series resistance on the n-XYTER input is not expected to change the total integrated charge, but only to stretch the signal in time. If the stretching is small compared to the rise time of the shapers, it is not expected to affect the output amplitude. Nevertheless, it was decided to test these considerations experimentally.

A dedicated setup was assembled to measure the n-XYTER output amplitude as well as the noise as a function of the capacitance and the resistance at the n-XYTER input (Fig. 5.4). Two capacitors were connected to the n-XYTER input over the switches. This allowed to select one of the four capacitance on the n-XYTER input: 4.57, 26.56, 51.77 or 73.44 pF. The capacitance was measured when the setup was already assembled, in order to make sure that the parasitics are taken into account. A variable resistor was inserted to simulate the resis-

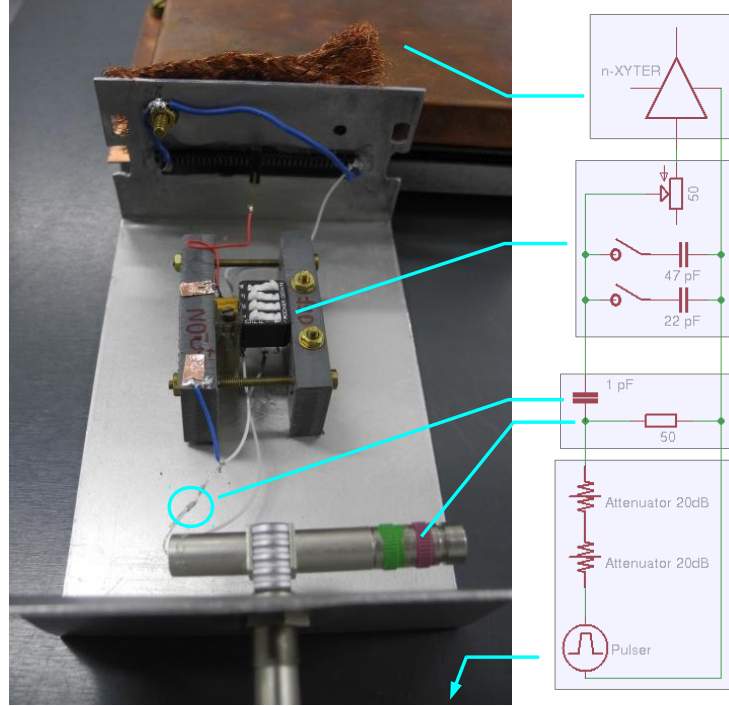


Figure 5.4: The setup for measuring the n-XYTER output amplitude versus the input load, and its circuit diagram.

tance of the readout cables. The 50 Ohm resistor served to match to the output impedance of the pulse generator.

To generate the input pulses, voltage steps from a laboratory pulse generator were attenuated down to the amplitude of 3.8 mV, and passed over a capacitor (1.05 pF) to the n-XYTER input. The values were selected such that the output charge pulse amplitude is close to the signal from 1 MIP in 285 μm silicon detector ($Q_{MIP} = 3.65$, $Q_{injected} = C \cdot \Delta U = 4.0$ fC). The transition time of the voltage steps, and therefore the width of the charge pulses was 10 ns.

The n-XYTER output signal was measured as a function of the capacitance at the input with various resistances in series, and the results are shown in fig. 5.5. The amplitude was normalized to the amplitude with the minimum capacitance at the input and series resistance.

As it was initially expected, it can be seen that as long as the series resistance is kept small ($\leq 50\Omega$) it does not affect the output amplitude.

To determine the n-XYTER input capacitance the data was fitted with a straight line, and the slope was determined: $d\eta/dC_p = 3.41 \cdot 10^{-3} \text{ pF}^{-1}$. The input capacitance is

$$C_{inp} = -\frac{1}{\frac{d\eta}{dC_p}} \approx 313\text{pF}$$

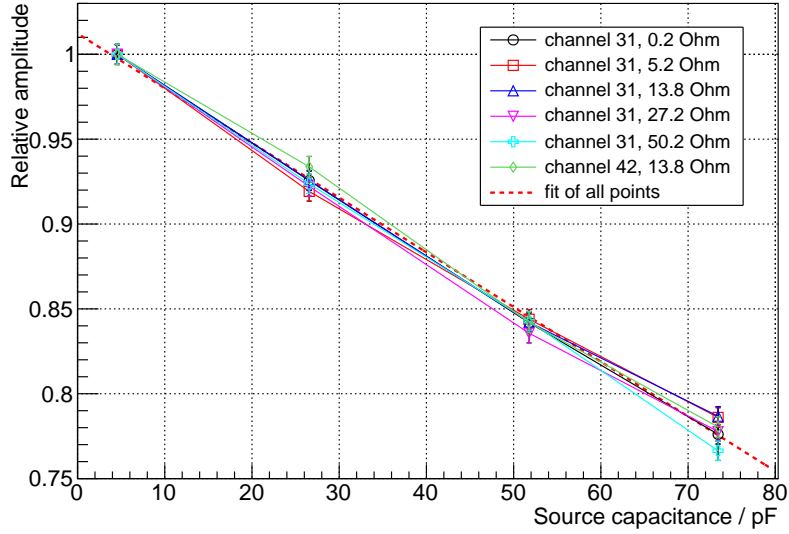


Figure 5.5: The n-XYTER output amplitude versus the capacitance at the input, given a constant input pulse charge.

In the same experiment the noise (in the slow shaper) as a function of the input load was measured. The procedure of the noise measurement is described in details in 8.1. The results are shown in Fig. 5.6. The thermal noise of the resistance gives a negligible contribution to the noise. The observed noise of the preamplifier exceeds the estimate from the simulation [36] by a factor of about 2.5. This discrepancy could not be explained.

5.5 Dependence of the n-XYTER response on the pulse width

Dependence of n-XYTER response on the width of the injected charge pulse was checked with one readout channel at both positive and negative polarities. The width of the pulse was adjusted by changing the transition time of the voltage step from the pulse generator. The amplitude of the voltage step, and consequently the injected charge were kept fixed.

As expected, the output amplitude remains constant up to the point, when the pulse width becomes comparable with the peaking time of the slow shaper (130 ns). Then the amplitude decreases gradually because of ballistic deficit.

Such a large difference between the responses at positive and negative polarities is not a common trait. It is only observed in the particular channel at the particular amplitude.

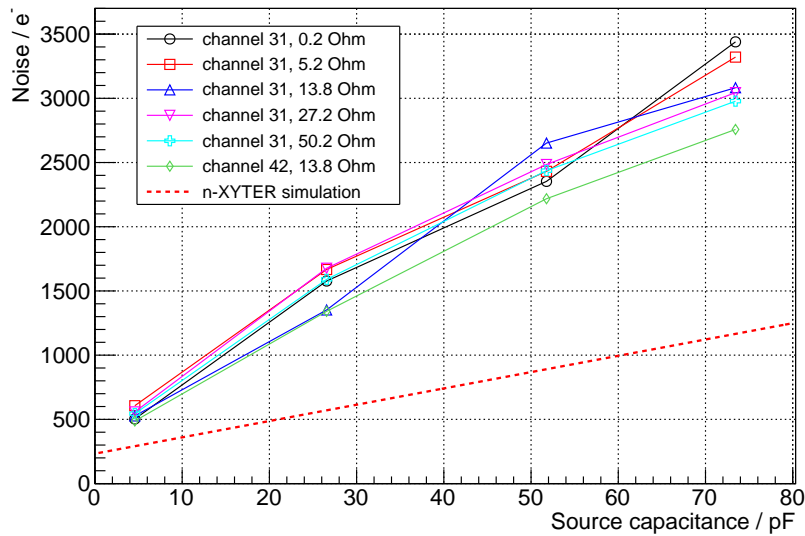


Figure 5.6: The noise in the slow shaper of n-XYTER as a function of the capacitance at the input, measured with various resistances in series.

5.6 Gain calibration

5.6.1 Generation of the reference charge pulses

Reference charge pulses were generated by applying voltage steps over a capacitor (Fig. 5.9). The amount of charge in a pulse in this case is: $Q = C \cdot \Delta V$, and the pulse duration corresponds to the transition time of the voltage step.

To generate charge pulses as low as 1 fC, a very small coupling capacitance as well as small voltage steps are required. Practical values are 1 pF capacitance and voltage steps of the order of 1 mV. Assembling such system requires special care. The circuit has to be properly shielded because any pick-up, even on a sub-millivolt level, can cause a large noise. Moreover, the coupling capacitance needs to be precisely known and stay constant during the operation. Also stray capacitances can reach fractions of a picofarad or more and can change through a slight change of setup’s geometry. The coupling capacitor was therefore mounted between two Lemo straight adapters (RMA.00 type), and the adapters were soldered to each other. Besides fixing the geometry, it made the capacitor detachable from the system and simplified the measurement of the actual coupling capacitance value (described below).

The voltage steps were generated using a “Philips PM 5786” laboratory pulse generator with a further attenuation by a factor of 100–1000 (in voltage) with passive attenuators. 2 to 3 attenuators (“Huber+Suchner”, type 6820.01.A) rated to 20 dB were used in series. Since the manufacturer specifies the attenuation

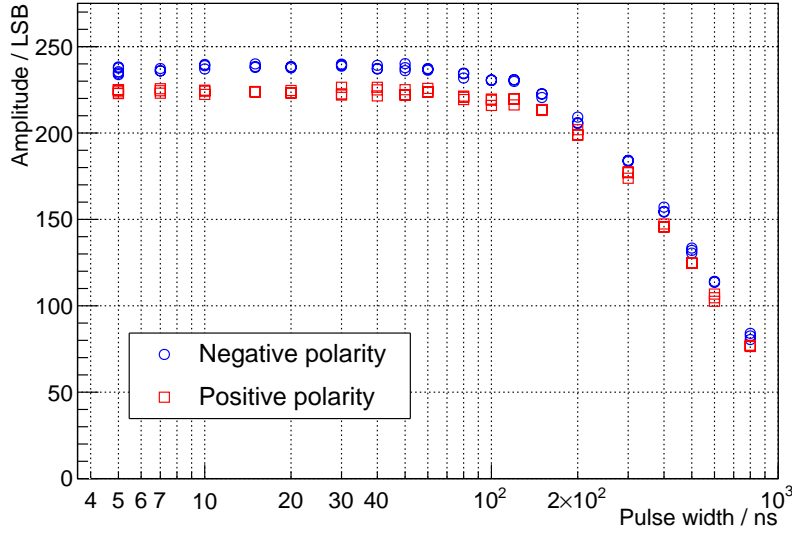


Figure 5.7: n-XYTER amplitude dependence on the input pulse width.

factor with 0.5 dB accuracy [69] (in the range from 0 to 2 GHz) the actual attenuation factor of each device was measured with better precision (described below).

The total output capacitance of the charge injector to the ground was found to be around 5 pF.

Coupling capacitance measurement. The actual coupling capacitance was measured with a “Quadtech 7600 Precision LCR Meter” with the maximal possible test signal frequency of 2 MHz and accuracy declared to be as good as 0.05 % [48]. After zeroing the meter its open circuit capacitance was below 500 aF. The coupling capacitance was found to be 1051 ± 1 fF (0.1 % accuracy). The measured value doesn’t depend neither on the test signal frequency (200 kHz to 2 MHz) nor on its amplitude (0.3 to 1 V).

Effect of capacitor type. For calibration an ordinary ceramic 1 pF SMD capacitor was used (“Multicomp”, part no. MCCA000939 [70]). Later, calibration of a single channel (FEB D53, channel 93, at negative polarity) was repeated with a special RF/Microwave capacitor (“AVX”, part no. 04023J0R8ABSTcR [71], rated as 0.8 ± 0.05 pF, measured value 0.832 ± 0.001 pF). The results are shown in Fig. 5.10. Very good agreement was observed.

Measurement of the attenuation factor. The attenuation factors were measured with a “Rohde & Schwarz” Vector Network Analyzer. The contribution of

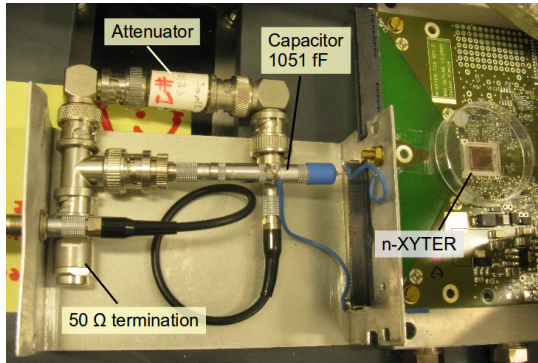


Figure 5.8: Calibration setup: the n-XYTER-based front-end board. Voltage steps were applied over the coaxial connector on the left.

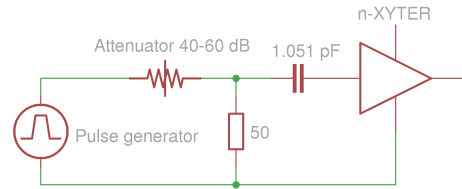


Figure 5.9: Charge pulse injection circuit connected to the cutit.

the leads was measured separately and subtracted. The dependence of the attenuation factor on the frequency was checked in the range from 10 to 500 MHz and found to be below 0.2 %. The obtained attenuation factors for the three attenuators were: 20.27, 20.30 and 20.31 dB.

5.6.2 Calibration results

n-XYTER calibration was performed in a range of input charges from around 0.5 to 25 fC. Below 0.5 fC a significant fraction of the pulses remained undetected because of the threshold, while the latter could not be decreased because of the baseline noise.

In order to check gain uniformity, the measurements were done with 3 n-XYTER chips, on several channels of every chip (in total 42 channels for negative polarity and 10 for positive). Results are shown in Figs 5.11 and 5.12. One can see that within the linear range (around 0–14 fC), most of the channels show rather homogeneous gain. Presumably other chips (within the current production batch) behave in the same way, so that a single calibration curve for all chips and channels appears to be practical. The gain variation, that is especially pronounced above 15 fC, can be then considered as a stochastic uncertainty of the calibration.

Positive and negative polarity data were fitted separately because of the small, but discernible difference in the gain at low input charges (0–5 fC). One can notice a small kink in the gains at around 17 fC. To adequately describe it, a 4th order polynomial was chosen for the fitting. All data points were taken with the same weight. The resulting calibration curves are shown in Figs. 5.11 and 5.12, and the parametrizations for the negative and positive polarity are as follows:

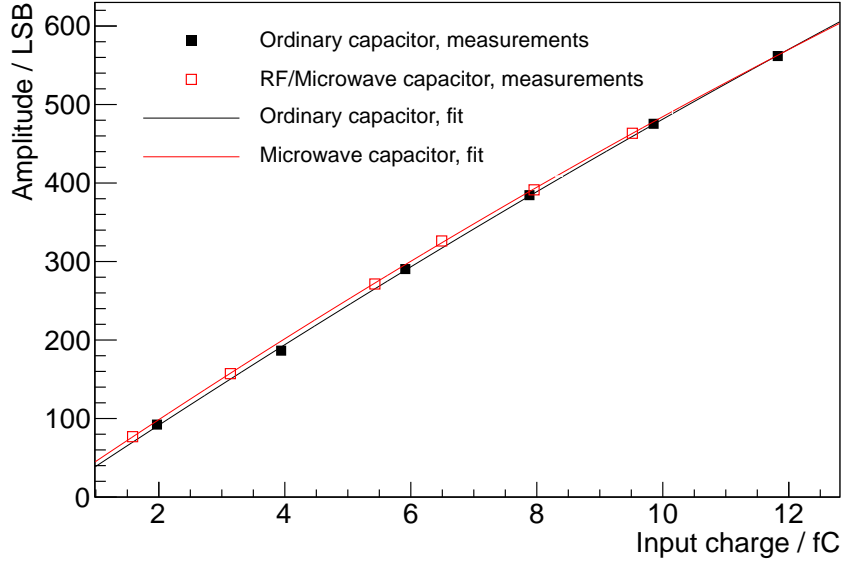


Figure 5.10: Calibration of a single n-XYTER channel using two capacitors of different types.

$$Q_- = 0.2025 + 20.53 \cdot 10^{-3} \cdot A - 6.733 \cdot 10^{-6} \cdot A^2 + 13.24 \cdot 10^{-9} \cdot A^3 - 3.566 \cdot 10^{-12} \cdot A^4$$

$$Q_+ = 0.3966 + 19.21 \cdot 10^{-3} \cdot A + 2.603 \cdot 10^{-6} \cdot A^2 - 10.62 \cdot 10^{-9} \cdot A^3 + 12.27 \cdot 10^{-12} \cdot A^4$$

where Q in fC and A in ADC LSBs.

Simple formulae were obtained for the linear range (0–700 LSB) by fitting within it with straight lines:

$$Q_- = 0.07757 + 0.02051 \cdot A$$

$$Q_+ = 0.3718 + 0.01960 \cdot A$$

or expressing through the amplitude in mV (U):

$$Q_- = 0.0776 + 10.01 \cdot 10^{-3} \cdot U$$

$$Q_+ = 0.3718 + 9.573 \cdot 10^{-3} \cdot U$$

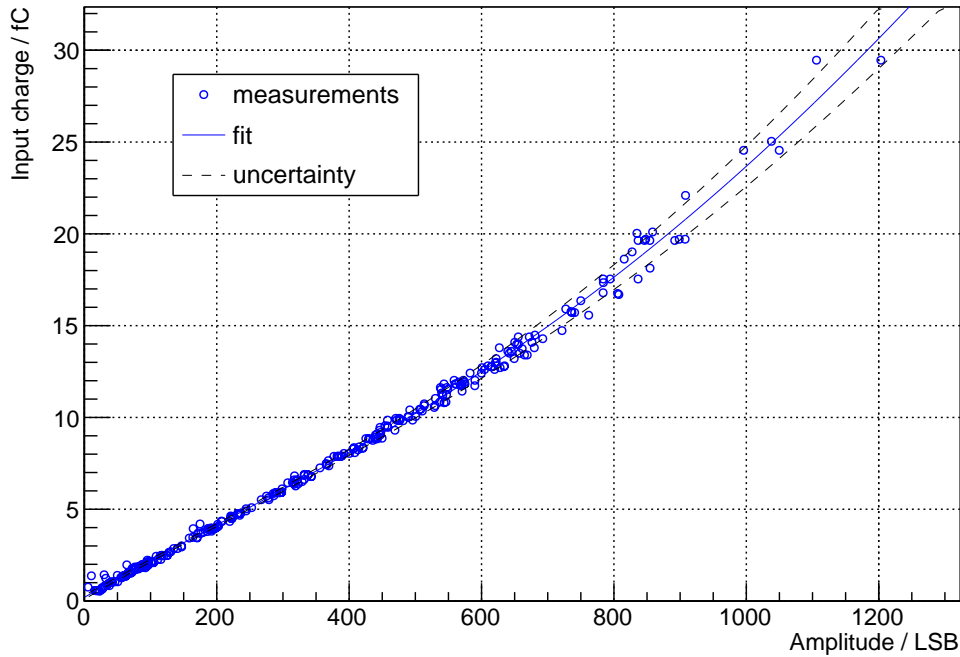


Figure 5.11: n-XYTER calibration at negative polarity.

5.6.3 Uncertainty estimate

There are three contributions to the calibration uncertainty. The dominant one comes from the approximation that a single calibration curve can be applied to all channels, while in fact the channels have slightly different gains. The uncertainty, caused by this approximation, can be considered as stochastic.

Another source of stochastic uncertainty is the uncertainty of each individual data point. It includes the effect of electronic noise and possibly other effects.

The total stochastic uncertainty has been estimated based on the following property: when a stochastic uncertainty is estimated correctly, the pull distribution (for a correct model, assuming Gaussian errors) has to have width of 1. Since the number of data points at the positive polarity is too small to build 3 pull distributions (see below, why 3), the uncertainty was assumed to be the same for both polarities, and their pull distributions were combined.

The uncertainty was parametrized with a 2nd order polynomial w.r.t. the amplitude (2nd — is the minimal order that allows to describe the minimum of the uncertainty at around 300 LSB). To determine the three coefficients of the polynomial the data was split into 3 subranges with equal number of points (0–195, 195–487 and 487–2000 LSB for the negative polarity and 0–58, 58–335 and 335–2000 for the positive), and the subranges from different polarities were combined:

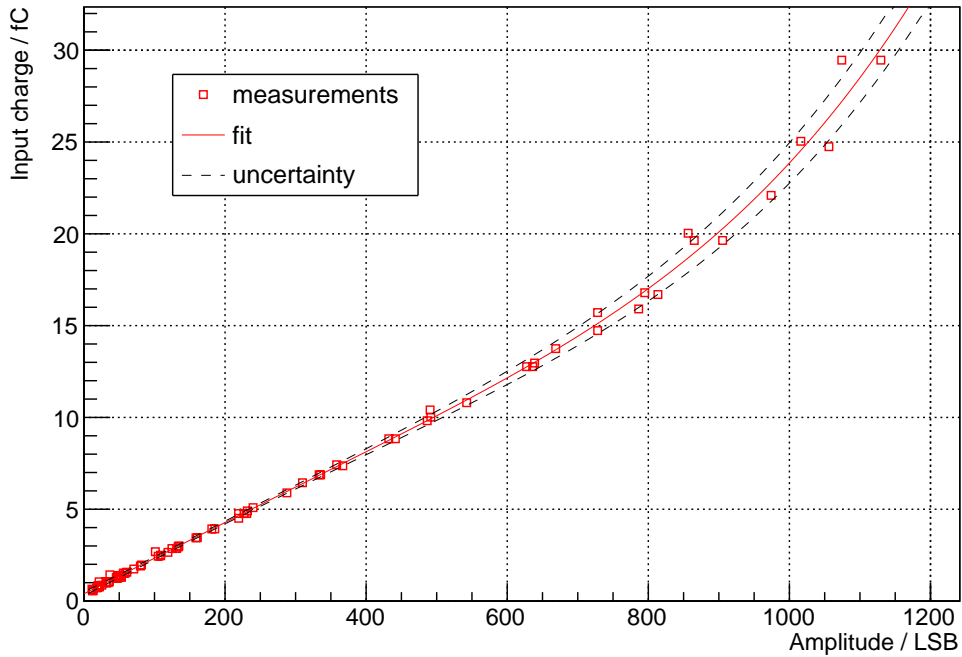


Figure 5.12: n-XYTER calibration at positive polarity.

lowes with lowest, and so on. Then the coefficients of the polynomial were picked (manually) such that the pull distributions evaluated from each subrange has width of 1. The resulting parametrization for the uncertainty is:

$$\Delta Q = 0.1 - 0.4 \cdot 10^{-3} \cdot A + 1.4 \cdot 10^{-6} \cdot A^2$$

where A is in ADC LSB, and Q is in fC.

The third contribution to the uncertainty is the systematic uncertainty on the injected charge. It originates from the uncertainty on the attenuation factor as well as on the capacitance. However, these two contributions are negligible compared to the stochastic uncertainty.

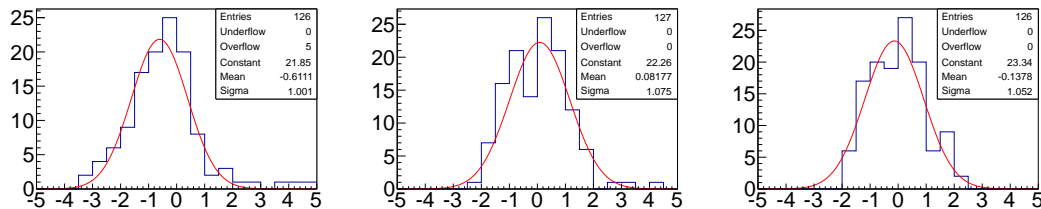


Figure 5.13: Pull distributions for the estimate of the stochastic error. From left to right: low, middle and high amplitude range.

5.6.4 Cross-check with a silicon detector

As a cross-check of the calibration, measurements with an alternative signal source — a single-pad planar silicon detector (Fig. 5.15) — has been performed. The detector was connected to one n-XYTER channel and the results were compared with calibration curves. The signal in the detector was induced by the gamma radiation of ^{241}Am as well as beta radiation of ^{90}Sr .

The detector had active area of $3 \times 3 \text{ mm}^2$ and thickness of $285 \mu\text{m}$. The signal was taken from the p-side. n-XYTER threshold was set such, that the noise rate was negligible compared to the signal rate. The detector was operated at a bias voltage of 140 V, while the full depletion voltage is expected to be at around 90 V (known from other detectors from the same batch). A test measurement was also performed at 110 V, and the same signal amplitudes as at 140 V were observed, which confirms that full depletion was achieved. The total output capacitance of the detector at the operation voltage was around 5 pF.

The resulting spectra are shown in Fig. 5.14. The most intense gamma lines of ^{241}Am are: 13.9 keV (37 %), 26.3 keV (2.3 %), and 59.5 keV (35.9 %) [72]. The peak at around 115 ADC LSB corresponds to the 59.5 keV line, and the large peak at low amplitudes — to the 13.9 keV line. Despite the lines have almost the same intensity, the 13.9 keV peak is much larger due to about factor 100 larger photoelectric absorption cross section in silicon at this energy. The 26.3 keV is not seen because of too low intensity and low energy resolution.

The exact position of the 59.5 keV peak was determined with a gaussian fit and yielded 114 ADC LSB. According to the calibration it corresponds to $2.61 \pm 0.07 \text{ fC}$ which is in agreement with the expected value of 2.64 fC.

The ^{90}Sr spectrum was fitted with a sum of a 2nd order polynomial and a convolution of a Landau distribution with a Gaussian. The resulting most probable amplitude is 167 LSB, which corresponds to the charge of $3.65 \pm 0.07 \text{ fC}$. Again a good agreement with the expected value (3.65 fC) is observed.

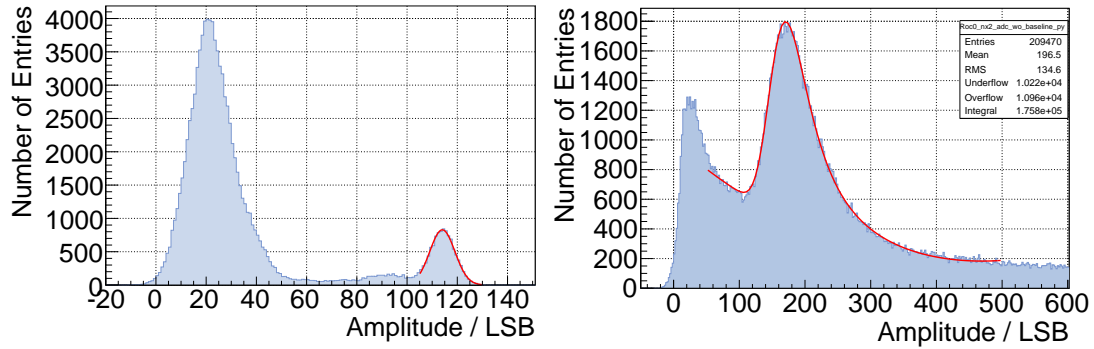


Figure 5.14: γ -spectrum of ^{241}Am measured with the single-pad planar silicon detector and n-XYTER readout. The red line is the gaussian fit of the 59.5 keV line. Right: Landau peak of electrons from the ^{90}Sr source, measured with the 285 μm thick, single-pad planar silicon detector and n-XYTER readout

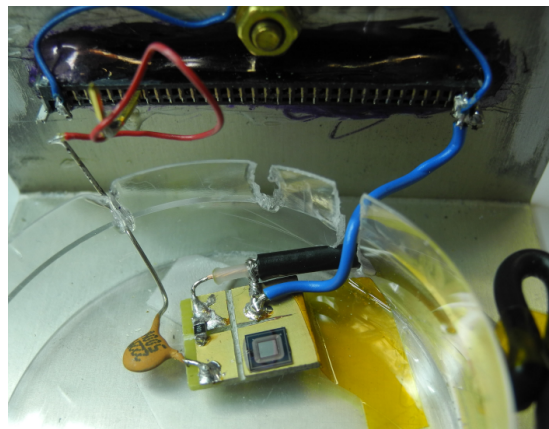


Figure 5.15: The planar single-pad silicon detector.

Chapter 6

Electronic noise reduction

Noise is an important characteristic of a detector system because it can limit the performance characteristics, such as efficiency and resolution. In a well designed system the dominant contribution to the total noise comes from the first amplification stage, so that all the other contribution can be neglected. To achieve this a certain effort is required. Detector signals can be distorted by electromagnetic pick-up, or by conductive coupling of noise. These effects should be minimized by, first of all, a well worked-out design of the system, but also by other measures like shielding, filtering and grounding. In this chapter various sources of noise, that were found in the prototype detector station systems, are described. For most of them ways to reduce the noise to a negligible level were found. Finally the noise level of around $700 e^-$ was achieved, with channel-to-channel variation about $50 e^-$. The noise was the same for all good-working CBM02, CBM03, and CBM04 sensors.

6.1 Noise of the bias voltage power supply

High-voltage power supplies often have a significant output voltage ripple¹. In particular, in the high voltage modules CAEN A1533 (operated in a CAEN SY2527 high-voltage mainframe), which were used in this work for biasing the sensors, the ripple can reach as high as 100 mV peak-to-peak.

For many applications such ripple can be neglected, but not for the front-end electronics of silicon detectors. As it can be seen in Figure 6.1, the bias voltage noise couples directly to the FEE. The effect of this noise can be easily estimated. Consider a short noise voltage pulse V_n , such that it lies within the bandwidth of the shaper. It will cause a noise charge pulse $Q_n = V_n / (2/C_{CSA} + 2/C_{coupling} + 1/C_{Sensor})$. Here C_{CSA} — is the input capac-

¹This is often because high-frequency switched analog circuitry is used in the device. Such circuitry can be used, for example, for internal powering of the device, or in the high voltage generator itself.

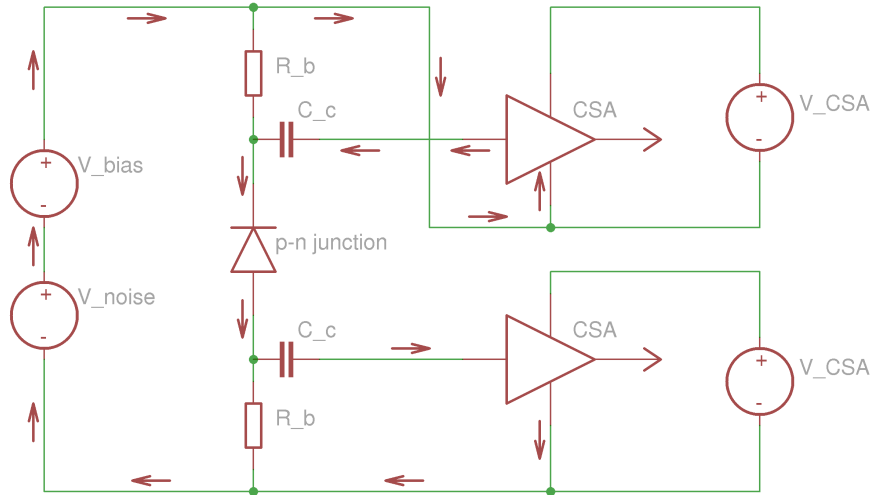


Figure 6.1: Coupling of the noise from the bias voltage power supply to the readout electronics. The noise originates in the bias voltage power supply. In the circuit diagram it is represented as a separate voltage source. The noise lies in the high-frequency region, so the CSAs, the coupling capacitances (C_c), and the p-n junction appear to the noise as low impedances. The bias resistors (R_b) have comparatively high impedance.

itance of the charge sensitive amplifier. The relevant capacitance of the sensor is the total bulk capacitance divided by number of the strips (because the noise current flows through the whole sensor bulk, and we are interested in the current through one strip). Normally, it is on the order of 0.1 pF per centimeter of the strip length. This it is much smaller than $C_{coupling}$ and C_{CSA} , so the latter two can be neglected, and $Q_n = V_n \times C_{Sensor}$. If one requires, for example, $Q_n < 0.01$ fC (62 e^-), then $V_n = Q_n / C_{Sensor}$ should be less than 0.01 fC / 0.1 pF = 10 mV.

The ripple can be suppressed by filtering. Initially, simple 1-stage RC filters were used in the CBM-STs group ($R = 0.1\text{--}1$ M Ω , $C = 1$ μ F). Such filters worked well for non-irradiated detectors, when the leakage current was small (order of 1 μ A), and the voltage drop on the filter was small (order of 0.1 V or 1 V). But for irradiated detectors the leakage current can reach milliamperes, and the voltage drop on the filter becomes significant (or even dominant). Therefore, the RC filters were been replaced with two-stage LC filters (first stage: $L = 22$ mH, $C = (2.2$ μ F + 10 nF); second stage: $L = 22$ mH, $C=2.2$ μ F).

In Fig. 6.2 the noise waveform, as well as the noise frequency spectra, are shown for the cases without and with different filters. A clear improvement is observed. The remaining, after the filtering, noise is the intrinsic noise of the oscilloscope.

In addition to the single-ended component of the bias voltage noise, a common

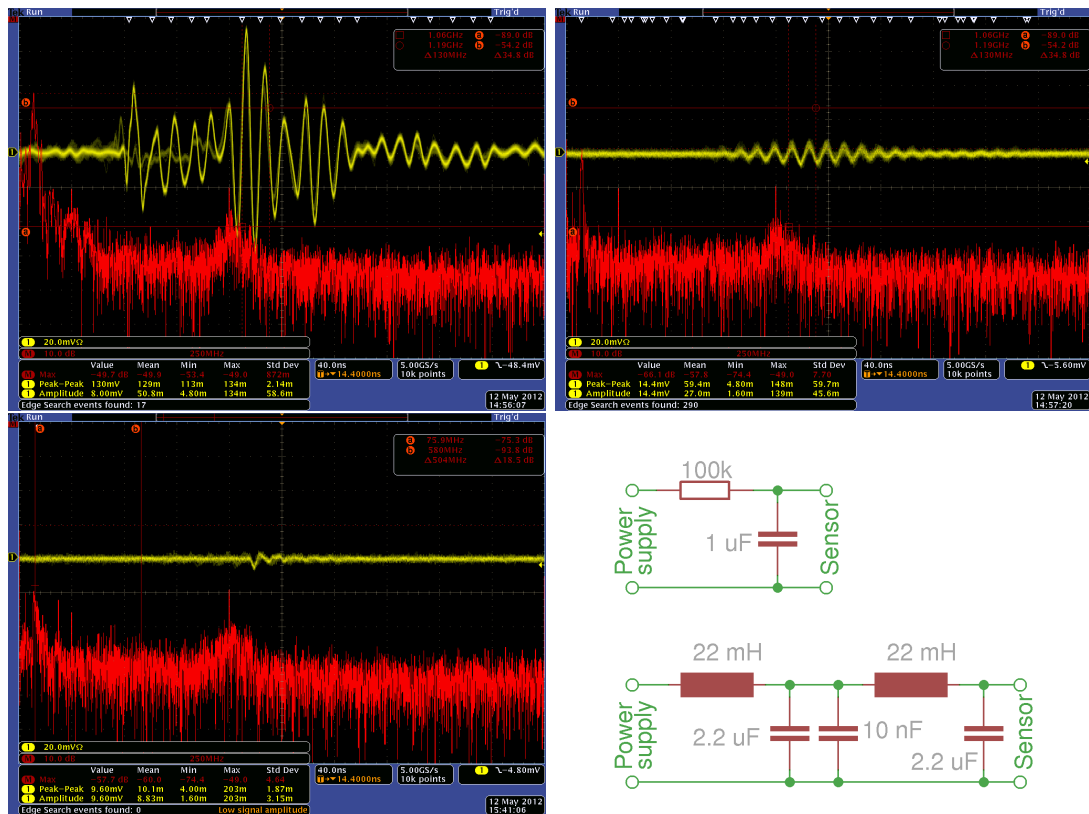


Figure 6.2: Noise waveform (yellow) and noise frequency spectrum (red) of the bias voltage, as provided by the CAEN A1533 high voltage power supply module. Top left: without filtering; top right: after the RC filter; bottom left: after the two-stage LC filter. Measurements were done with a 50Ω oscilloscope probe. Bottom right: the RC and the two-stage LC filter. The 10 nF capacitor is added to shunt high frequencies, because it has relatively small parasitic series inductance, as compared to the $2.2\text{ }\mu\text{F}$ capacitor.

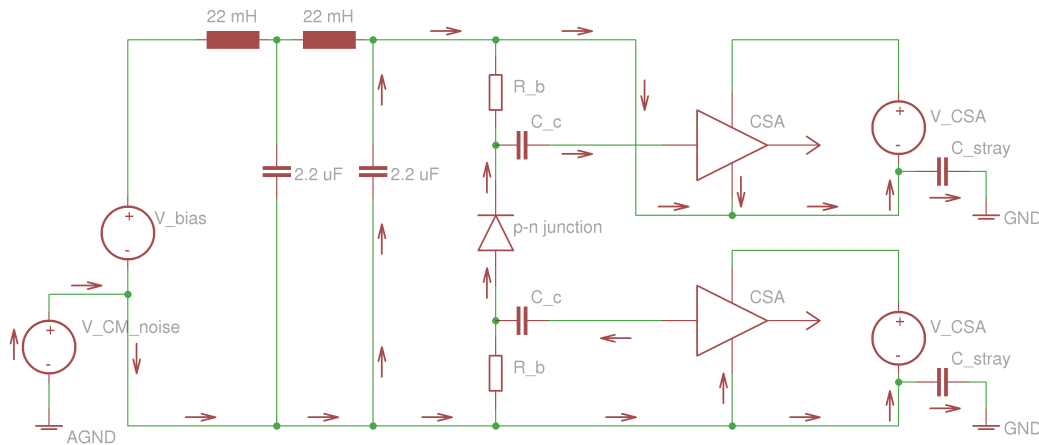


Figure 6.3: Coupling of the common-mode noise from the bias voltage power supply to the readout electronics.

mode component was found. It turned out that it also contributes to the total noise in the system. The exact mechanism of the coupling of the common-mode noise to the FEE is not studied in details, but it is conjectured to be the following (illustrated in Fig. 6.3). The common mode noise current flows through the grounds of the FEE to the ground terminals of the power supplies, and from there to the ground (the FEE power supplies are DC isolated from the ground, but they have a large stray capacitance to the ground, on the order of 1 nF). In the high voltage line this path has a larger impedance than in the current return line, because in the high voltage line there are inductances in the filter, while in the current return line they are absent. Due to the difference in the impedances, a fraction of the current flows through the sensor and the FEE inputs, which causes the observed noise.

The effect of a common-mode noise was suppressed by balancing the circuit — adding the same impedance in the current-return line in the filter, as shown in Fig. 6.4.

6.2 Common-mode noise of the FEE power supplies

Attention also has to be paid to the noise of the FEE power supplies. Especially malign is the effect of the common-mode component of the noise. As it is shown in Fig. 6.4, it couples directly to the FEE inputs, in a way, similar to the noise of the bias voltage supply.

The noise level of a power supply is determined by its operation principle and implementation. Especially large common mode noise can usually be found on power supplies, based on switched-mode DC-DC converters. Experience of

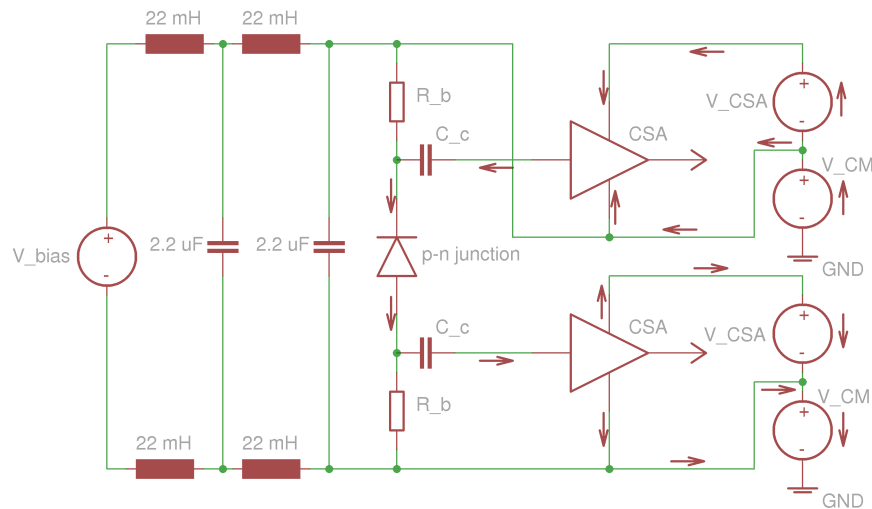


Figure 6.4: Common-mode noise coupling to the FEE. The common mode noise is shown as V_{CM} voltage source. The noise current path is shown with the arrows.

CBM-STs group shows that, if no special measures are taken, such supplies are not suitable for powering the FEE, because of the too large noise. Power supplies, based on linear DC-DC converters have, usually, much lower common mode noise, and since long time only this type of power supplies have been used for FEE powering in CBM-STs.

This common-mode noise can be filtered out with low pass filters. Ordinary LC filters would not work in this case, because during power-up of the FEE the supplied current need to change very rapidly from zero to the operation value, but such rapid changes would be blocked by the inductance in the LC filter. The problem can be overcome by using common-mode chokes, as shown in the Figure 6.5.

A common-mode choke is basically two identical inductors on a common yoke. The current is supplied to the FEE through one inductor, and returns through the other, so the currents in the inductors are equal and run in the opposite directions. Therefore, the magnetic fields induced by these currents in the yoke compensate each other. If suddenly the power consumption of the FEE changes, the changes of the magnetic field in the inductors again compensate each other, so no self-induction occurs, and the common-mode choke appears as a small (ideally, zero) inductance. The common-mode noise current, on the other hand, runs through the both inductors in the same direction, so the induced magnetic fields in the inductors don not compensate each other, but rather add up. Consequently, for common-mode currents a common-mode choke appears as a large inductance. In Figure 6.5 the common mode chokes are the inductors $L1$. To enhance the filtering, additional small inductors $L2$ were be added.

An LCL filter, as described above was assembled to prove the method

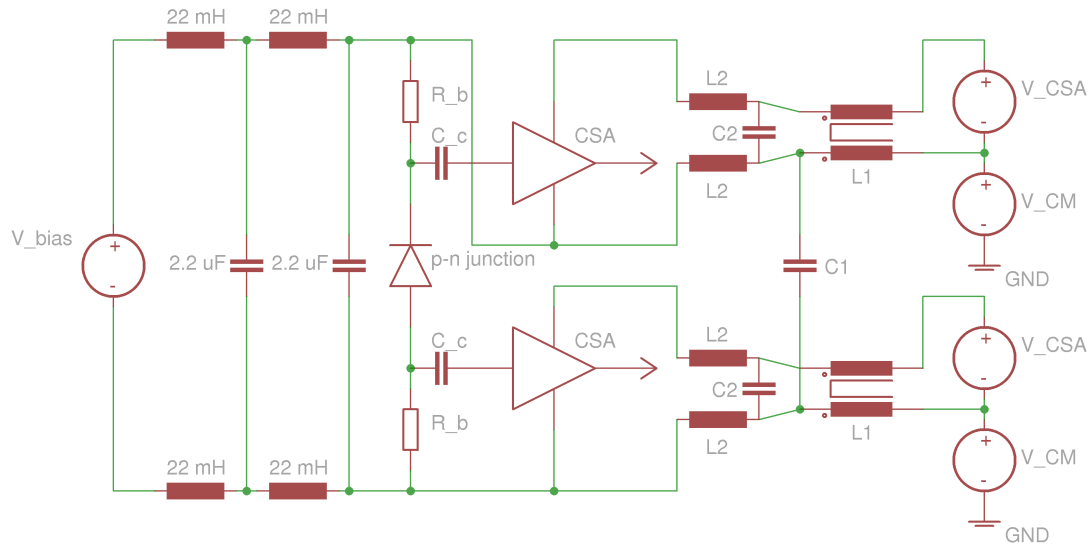


Figure 6.5: Suppression of the common-mode noise using LC filters with common-mode chokes

(Fig. 6.6). The selected component values were: $L_1=42 \mu\text{H}$, $L_2=1 \mu\text{H}$, $C_1=1 \text{ nF}$, $C_2=10 \text{ nF}$. The noise level in a prototype tracking station was measured in three different configurations (Fig. 6.7). First, the station was powered from power supplies, based on linear DC-DC converters, Elektro-Automatik PS 2316-050 [73]. These power supplies proved to work well in many previous measurements, and were used as a reference. Then, the station was powered from a power supply with switched-mode DC-DC converters, Hameg HMP 4040 [74]. Clearly, a much larger noise was observed. Finally, the station was powered from the same power supply with switched-mode DC-DC converters, but through through the LCL filter. It can be seen that applying the filter reduced the noise almost to the level of the reference power supplies.

6.3 Noise coupling through the 230 V power line

Common-mode noise can also couple to the power supplies from the 230 V power line. The noise can be produced by a broad range of hardware operated nearby: brushed DC motors, vacuum cleaners, forevacuum pumps, refrigerator starters, laser printers, etc. Whether the device is noisy depends more on the device implementation, rather than on the kind of the device, and it is difficult to guess it. For example, during performing this work, the major source of the common-mode noise on the power line was the high voltage mainframe CAEN SY2527, used for sensor biasing.

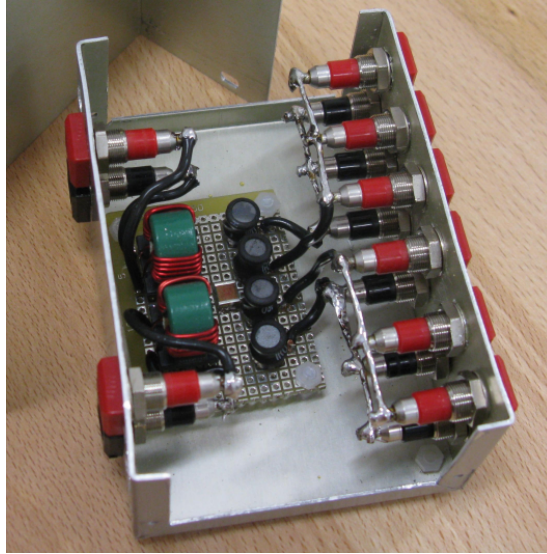


Figure 6.6: LCL filter for suppression of common-mode from the FEE power supplies.

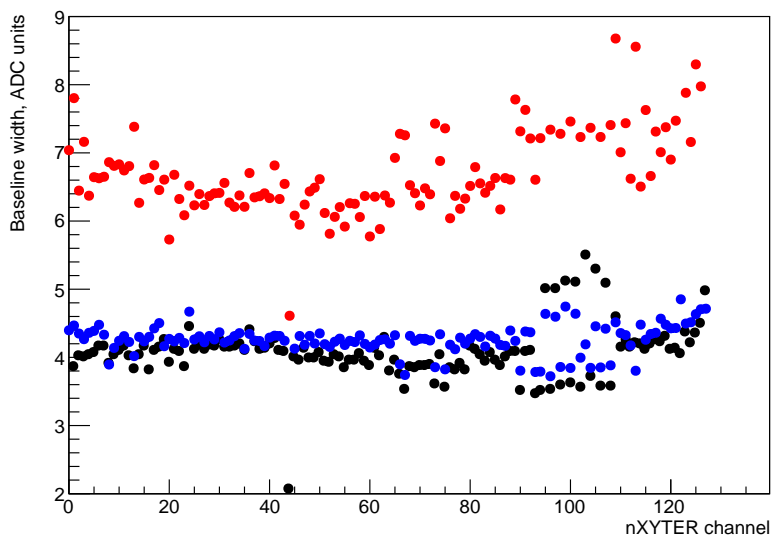


Figure 6.7: Comparison of the noise levels in a prototype tracking station, when the station is powered in three different ways: black markers — from power supplies with linear voltage regulators; red markers — from power supplies with switched-mode voltage converters; blue markers — from power supplies with switched-mode voltage converters through the LCL filter, as described in the text.

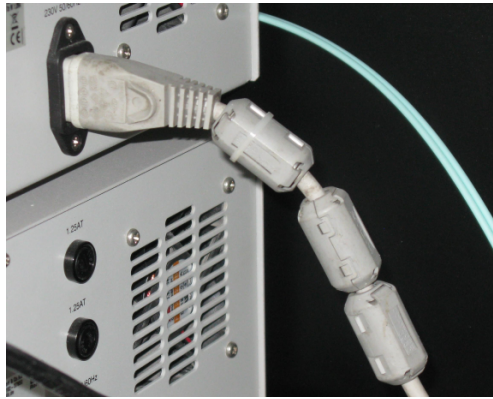


Figure 6.8: Ferrite beads on the power cord of one of the low voltage power supplies.

Coupling of the common-mode noise from the power line can also be suppressed with common-mode chokes. In this case it is easier to insert them in the power connection of the device to the power line. The simplest is just to clamp a few ferrite beads on the power cord (Fig. 6.8). This will increase the inductance of the cable for the common-mode component, but for the single-ended component the inductance will not change. This turned out to be sufficient in the present work. In harsh environments dedicated industrial LC network filters can be used (for example [75]).

If a noisy device is identified, it is better to prevent its noise from coupling to the network (again with the ferrite beads), rather than (or in addition to) blocking the common-mode noise on the power connection of each of the sensitive devices individually. It was also done for the noisy CAEN high voltage mainframe.

6.4 Noise radiation from the n-XYTER digital back end

Another source of noise in the system are the cables, over which the data is transmitted from the FEBs to the ROCs. They carry digital signals at clock frequencies up to 256 MHz, and some of the signals are transmitted over single-ended lines. This leads to a harsh electromagnetic radiation in a broad frequency range, including the bandwidth of the FEE. The radio waves reflect from the metal walls of the station and are picked up on the long traces of the sensor fan-out PCB. Detailed studies of this effect are presented in [76].

Unfortunately, this effect was not taken into account when the stations were designed. An obvious solution would have been to put the cables, as well as digital part of the FEB, outside of the metal box. Instead the back end cables, as well as the FEBs were enclosed in additional shielding (Fig. 6.9). Further



Figure 6.9: n-XYTER based front-end board, a shield for it, and a shielded back-end cable.

improvement was achieved by shielding the sensor fan-out PCB. This means that significant radiation remained even after the shielding. Surprisingly, it was found that the noise level does not depend on whether the shield of the back end cable is grounded or left floating ([77, pp. 105] recommends to ground the shield on one side). It was expected to observe minimum remaining radiation (minimum noise) when the shield is grounded.

The sensor shield had to be connected to the FEB ground. Indeed, the electromagnetic waves, that come from the FEB-ROC cable, induce noise on the shield, and it can capacitively couple to the long traces on the sensor fan-out PCB. This effect is suppressed, if the shield is kept at the same potential as the FEBs and hence n-XYTER inputs, or at a constant voltage with respect to them.

It was also found that the noise level depends on the length of the conductor, connecting the shield of the fan-out PCB and the FEBs. Even with 10 cm long connection the noise level is significantly higher, than with the minimal possible 3 cm connection. This should be taken into account during assembly of similar systems in future.

6.5 Noise shunting

As it was discussed in the previous section, even after shielding the FEB-ROC cables, significant amount of electromagnetic radiation still remains inside the box. This radiation induces a common-mode noise on the FEBs, which in the way, as described in 6.2, couples to the FEE inputs.

This noise can also be suppressed. If the voltage between the FEBs is kept

constant, then no noise current will flow through the sensor. The FEB grounds, of course, can not be just directly connected with each other, because they are at different potentials. But the noise can be shunted with a large capacitor. The large capacitor will appear as a small impedance, as compared to the impedance of the detector, and the noise current will flow predominantly through it. The shunting capacitor has to be physically close to the FEBs (another capacitor, connecting the FEB grounds, is in the bias voltage filter, but it is connected to the FEBs over a long cable with a significant inductance and significant propagation delay).

Mechanically, it is implemented in the following way: the FEBs, that are at high potential, were connected to the shield of sensor over large capacitors ($1\ \mu\text{F}$ and $10\ \text{pF}$ in parallel at the two nearest corners of the sensor shield). The capacitors can be seen in Fig. 2.13 (red and blue). The FEBs, that are at the ground potential, were connected to the shield of the sensor directly. Finally, this connection serves for: a) shunting of the common mode noise on the FEBs; b) keeping a constant voltage between the PCB shield and the FEBs; and c) closing the signal path over a low impedance.

6.6 Noise from the switched-mode DC-DC converters on the ROC

Yet another source of noise in the system are the switched-mode DC-DC voltage converters on the ROC. The noise level in the system was compared in two configurations: when ROCs with switched-mode and with linear DC-DC converters were used. During the comparison only the ROC was replaced and no other changes to the system was done. The results are shown in Fig. 6.10. The effect has not been investigated in details, but most probably the switched-mode DC-DC converters generate common-mode noise, and it couples to the FEE exactly as it is shown in Fig. 6.4. Unfortunately, this noise can be filtered out only on the ROC board (for example with a common-mode choke, as in 6.2). Inserting such a filter between the ROC and the FEB would impede the digital signal transfer, while inserting it between the FEB and the sensor would attenuate the signal. Still, the noise can be partially suppressed by shunting.

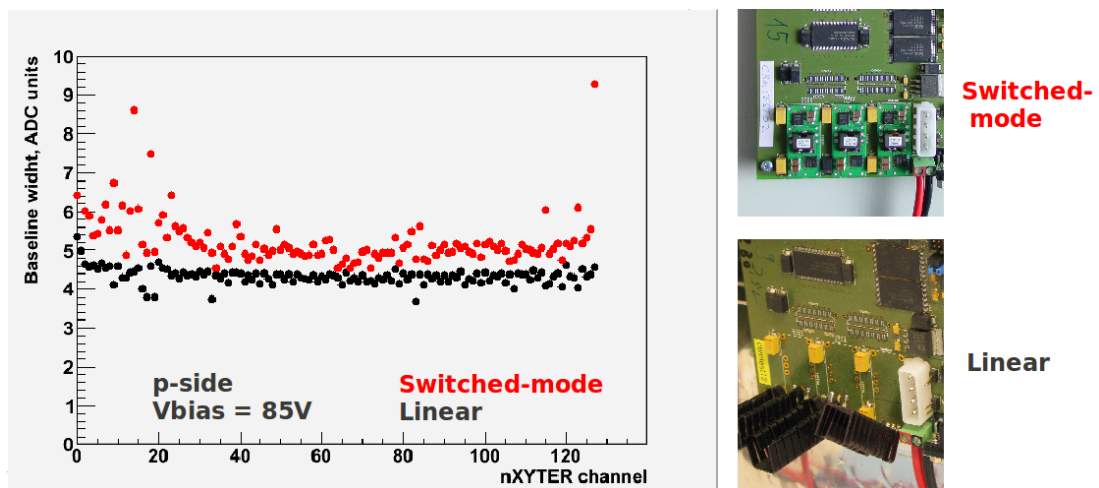


Figure 6.10: Noise level in the system shown on Fig. , on the p-side with linear and switched-mode voltage regulators (left). The noise is defined as dispersion of the baseline. On the right side the voltage regulators are shown.

Chapter 7

Operation of prototype detector systems

In the previous chapters the prototype tracking detectors (Section 2.3.2) with the n-XYTER-based front-end boards (Section 2.2) were described. After the digitization of the signal on the front-end board (FEB), the information has to be transferred to the PC and processed. In addition the n-XYTERs need to be configured before the measurements. The latter three operations are described in this chapter.

The interface between a PC and the FEBs is provided by the Universal Read-Out Controller (Section 7.1). The data acquisition software, running on the PC side is DABC (Section 7.2). DABC can store the data on a hard drive as well as broadcast it to client programs for on-line analysis (or any other purpose). In this work the analysis of the data was done partially with specially developed C++ programs, that used the `roclib` interface libraries for unpacking the data and ROOT [78] libraries for analysis, and partially with the specially developed analysis classes for the GO4 framework [79]. For on-line analysis only GO4 was used (Section 7.4).

For configuration of the ROCs and the FEBs (the n-XYTER and the ADC) a special console program, `rocutil`, is used (Section 7.3).

Operation of a system, comprising a few detectors during the in-beam tests makes it desirable to have a slow control system — a tool for remote control and monitoring of auxiliary electronics, such as power supplies, cooling, step engines for detector positioning, etc. For this the EPICS [80] was used (Section 7.5).

7.1 Universal Read-Out Controller (ROC)

The purpose of the Universal Read-Out Controller [81] (also called SysCore) is to provide an interface between the FEBs and the PC. Several versions of ROC exist. In this work only the version 2 was used, and in the text this version is

always meant implicitly. ROC was developed for laboratory tests of the prototype detector systems with front-end electronics, based on n-XYTER or GET4 [82] chips. The communication between ROC and PC is possible both through Ethernet and through an optical link over the CBM-net protocol (a dedicated high-throughput protocol for transporting data in the CBM experiment [83]). ROC version 2 is also an iteration in development of the future ROC version 3 (or SysCore v3) board [84], that is going to be used in the final CBM setup.

ROC is based on a FPGA (Virtex 4), which allows a graduate development and frequent updates of its functionality. The FPGA firmware is logically split into two modules: the front-end module, responsible for communication with the front-end boards, and the transport module, responsible for communication with the PC (or any other client). Such modular structure allows to combine any front-end part with any back-end interface.

In the n-XYTER front-end module the ROC firmware implements the necessary interfaces for configuring and receiving data from the n-XYTER and the ADC (i²c, SPI, and two other, special interfaces). It also provides the necessary clocks to the n-XYTER and the ADC. ROC can support up to 4 n-XYTER chips.

The data is transported from ROC to the client as a continuous stream of messages. There are 6 types of messages: NOP, EPOCH, HIT, SYNC, AUX, and SYS. The size of each message is 48 bit. NOP messages are empty, and might be useful only occasionally for some debug and development purposes. HIT messages contain the information about the hits, registered by the n-XYTERs. They carry the ID of the ROC, ID of the n-XYTER, and the n-XYTER channel, as well as the the amplitude, and the time information. The purpose of the other messages will be described later.

ROC assigns a *timestamp* to messages of types HIT, SYNC, and AUX. This is the time of, respectively, detecting the hit, or receiving the signal on the SYNC port, or on the AUX port (described below). The resolution (i.e. the least significant bit) of the timestamp is 1 ns, and the size is 46 bit (corresponds to 2^{46} ns \approx 8.14 hours).

In order to reduce the amount of transferred data, each HIT, SYNC, or AUX message carries only the lower 14 bit of the timestamp — a *reduced timestamp*. The higher 32 bits are transferred in the EPOCH messages. The epoch, that corresponds to an HIT, SYNC, or AUX message, is the one that that was transferred in the last EPOCH message. The HIT, SYNC, and AUX messages also have the last epoch flag — if it is set, the corresponding epoch is the one before the last.

The ROC has also four AUX ports and two SYNC ports (AUX0–AUX3, SYNC0, and SYNC1). The AUX ports are capable of receiving arbitrary digital signals in the LVDS standard. ROC measures the time of the level transitions and the kind of the level transition (rising edge or falling edge). The information about each transition is sent in an individual AUX message.

Two of the AUX ports have extra functions, that can be optionally enabled. The AUX2 port can be used as an input for an external trigger signal for the

n-XYTER chips. The port AUX3 can be used for receiving the throttling requests.

In the present work the AUX ports were mostly used for receiving signals from reference timing (scintillator) detectors — either for triggering the n-XYTERs or for further coincidence analysis on the offline level.

The SYNC ports are used for synchronization of several ROCs, working in the same system. Synchronization with the SYNC messages is only necessary when the ROC are operated over Ethernet, and each ROC runs on its own clock. In case ROCs are operated over optical links, then they all (within one system) run on the same clock, recovered from the optical link. Still, generation of SYNC messages has to be enabled on the ROCs because it is required by the data acquisition system.

The synchronization mechanism in case of operation over Ethernet is the following. One ROC, defined as the master, sends periodically SYNC signals to all ROCs, including itself. It is ensured, by equalizing the cable lengths, that the signals arrive to all ROCs at physically the same moment of time. By receiving the signal each ROC generates a SYNC message, and assign to it a timestamp according to the local time counter. Later, on the analysis level the timestamps are corrected such that the timestamps of the SYNC messages are the same on all ROCs. Each of the SYNC signals contains a unique number — the number of the epoch when it was sent by the master ROC. Therefore the correspondence between the SYNC messages from different ROCs can be established.

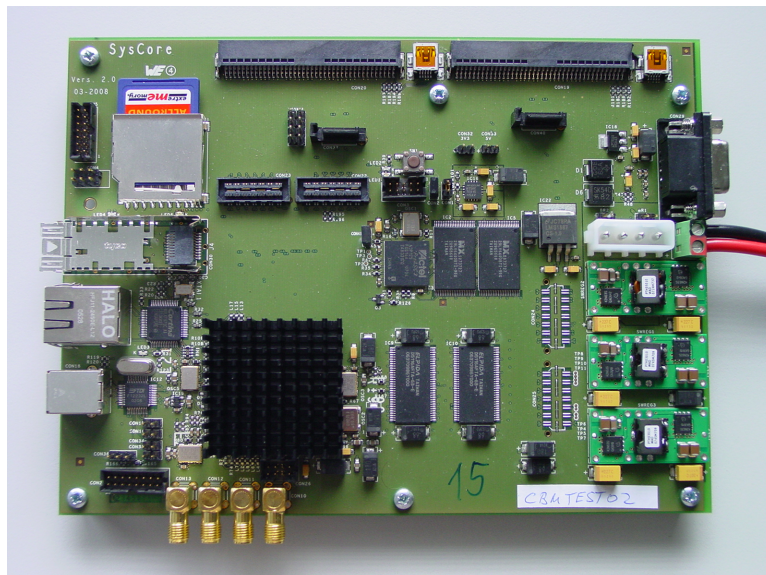


Figure 7.1: The Universal Read-Out Controller (ROC) version 2.

7.2 Data acquisition system

To receive the data from the ROC boards on the PC side, DABC is used. DABC (Data Acquisition Backbone Core) — is a software package for data acquisition and event building, designed especially for trigger-less systems with large number of data sources and high data rates. It was developed with an intention to make it the standard data acquisition system for the experiments at FAIR. The architecture and implementation of DABC are described in details in [68].

DABC is designed to work with arbitrary sources of free-streaming data (front-ends). A dedicated plug-in for DABC was used in order to receive the data from ROCs. A version of DABC, together with this plug-in is provided within the `roclib` package.

7.3 ROC and FEB configuration

Configuration of the ROC board, as well as the n-XYTER and ADC, located on the front-end boards, is performed with `rocutil`. `rocutil` — is a console application (included in the `roclib` package) that allows to establish a connection with the ROC (and through the ROC with the n-XYTER and the ADC) over the Ethernet or the optical link, to configure the register settings, to acquire data from the ROC, and to perform simple analyses.

The basic configuration procedures are done with the following sets of commands:

Initialization of ROC:

<code>board=<address></code>	Connect to the ROC; <code><address></code> — is the IP address or the IP name or the CBM-net name of the ROC.
<code>setrocdef</code>	Set the ROC registers to the default values.
<code>setsyncm=<N></code>	Activate the SYNC transmitter. SYNC signals will be sent every $2^{\langle N \rangle}$ epochs. Recommended $4 < \langle N \rangle < 8$ (smaller value for higher data rates)
<code>setsyncs=0,1,loop=1</code>	Activate SYNC receiver port 0 on the same ROC. Internally connect the receiver to the transmitter on the same ROC.
<code>putroc=ROC_ROCID,<ID></code>	Set ID of the ROC to <code><ID></code> .

Initialization of n-XYTER (after the ROC is initialized):

<code>feb <port></code>	Connect to the FEB. <code><port></code> = 0, if the FEB is connected to CON19, and 1, if to CON20
-------------------------------	---

<code>setfebdef pos0=<pol></code>	Set the n-XYTER and the ADC registers to the default values. <code><pol></code> = 0 for negative polarity, and 1 for positive.
<code>setnx=0,18,<thr></code>	Set the n-XYTER threshold to <code><thr></code> . Adjusted depending on the setup.
<code>setnx=0,19,50</code>	Set the n-XYTER <code>Vbfb</code> register to 50 (recommended).
<code>setnx=0,20,<val></code>	Set the n-XYTER <code>VbiasF</code> register to <code><val></code> . Recommended settings: 90 for positive polarity, or 120 for negative.
<code>autovbiass=0</code>	Find and set the optimal setting for the <code>VBiasS</code> register.

Configure the system for baselines measurement (after the previous steps):

<code>feb <port></code>	Connect to the FEB. <code><port></code> = 0, if the FEB is connected to CON19, and 1, if to CON20
<code>setnxmode=0,ttri=1</code>	Set the n-XYTER to the Test Trigger Mode.
<code>firepulser -a</code>	Enable the pulse generator on the ROC to trigger the n-XYTER periodically.

... and back to the self-triggered mode:

<code>setnxmode=0,ttri=0</code>	Set the n-XYTER back to the self-triggered mode.
<code>firepulser -s</code>	Disable the pulse generator on the ROC.

Apply test pulses from the n-XYTER internal generator:

<code>feb <port></code>	Connect to the FEB. <code><port></code> = 0, if the FEB is connected to CON19, and 1, if to CON20
<code>setnxmode=0,tpul=1</code>	Enable the n-XYTER test pulse generator.
<code>firepulser -a</code>	Enable the trigger pulse generator on the ROC.

If two FEBs are connected to the same ROCs, the following command has to be performed after the FEBs configuration:

<code>putroc=ROC_NX_NXACTIVE,5</code>	Acquire the data from the both n-XYTERs on the both FEBs.
---------------------------------------	---

7.4 GO4-based analysis

The on-line analysis, and partially the off-line analysis was performed within the GO4 framework [79]. GO4 — is a General purpose On-line and Off-line Object-Oriented analysis framework. It is developed at GSI, and based on the ROOT [78] and Qt [85] libraries.

The idea of using GO4 is the following. The user provides the analysis code in C++ classes, with interfaces, defined by GO4. GO4 executes the code, and takes care of the data input and output, including displaying of the results in the GUI. During execution of the analysis the user is able to pause and resume it, as well as to see and store the intermediate results. The possibility of viewing the intermediate results enables to use GO4 for on-line analysis, when a continuous stream of data is coming, and one needs to see the constantly updating up to the minute result. The execution of the analysis and displaying the GUI are performed by GO4 in different threads, which ensures that the GUI won't be blocked.

GO4 is an event-based system. It requires the data to be intrinsically divided on logically complete pieces — events. During the in-beam measurements, events were defined as time intervals around the time of arrival of the beam particle. In laboratory measurements with radioactive sources, events were defined just as arbitrarily chosen time intervals, going uninterruptedly one after another.

GO4 provides a possibility to perform the analysis in steps. An analysis step can be enabled or disabled, or substituted with a different implementation of the same step. This advantage was taken when the analysis for the in-beam in 2012 was developed: the analysis for STS and the GEM detectors shared the first step, where the data was unpacked and per-chip distributions were created, whereas the detector-specific analysis step was different for the STS and the GEM detectors.

Within the GO4 framework an analysis for the data from the STS prototype detectors was developed (Fig. 7.2). The main features of the analysis included (but not limited to):

- automatic determination of whether the acquired data is the measurement of the baseline or the real data (by the calibration markers in the data stream)
- automatic determination of the baseline position, and subtraction of it from the real data hits (individually for each readout channel)
- per-readout-channel distributions of the hit amplitude and the number of hits
- time correlation of the hits with the signals on the AUX ports (usually, time signals from reference detectors, such as scintillators)

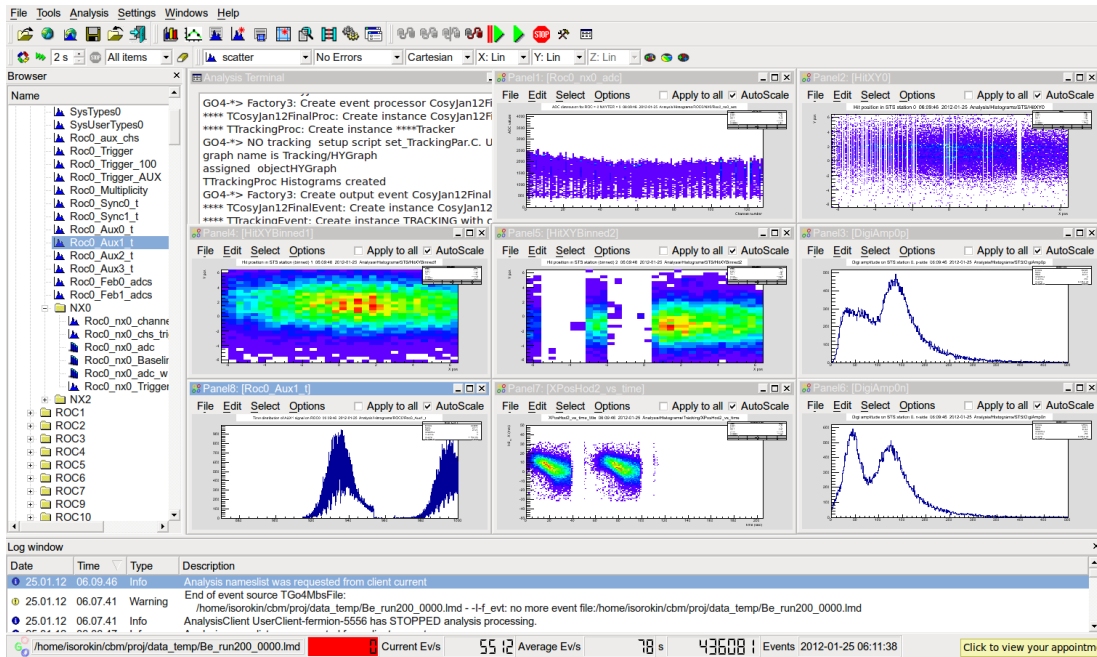


Figure 7.2: Screenshot of the GO4-based analysis, running on-line during the in-beam test of prototype STS detectors in 2012. Histograms of the hit amplitude (2nd and 3rd row, right), hit position (2nd row, left and middle), beam intensity (3rd row, left), beam position vs. time (3rd row, middle), and other are displayed.

- mapping of the ROC, n-XYTER, and channel number to the ID and side of the sensor, and the strip number
- reconstruction of hit clusters, based on the correlation of hits in time and space
- determination of the total cluster amplitude and the center of gravity
- reconstruction of 2-dimensional hit position by correlating in time the clusters on the opposite sides of one sensor

For the analysis of the in-beam test data, additional features were implemented:

- reconstruction of the 2-dimensional hit position in the reference scintillating-fiber hodoscopes
- reconstruction of the particle track using the hits in all available detectors: the STS and GEM stations, as well as in the fiber hodoscopes

In each case many other features were implemented for debug purpose. The STS detector-specific part of the analysis, as well as the part, related to the baseline measurement, is the author's contribution.

7.5 EPICS for slow control

To control and monitor the auxiliary electronics remotely during the in-beam test a slow control system, based on EPICS [80] was developed. The hardware pieces to be controlled included:

- high voltage power supply for sensor biasing
- low voltage power supplies for the readout electronics
- cooling system
- temperature monitoring sensors
- stepping motors for positioning of the sensors in the beam

The slow control system of the 2012' in-beam test included also management of the data acquisition (Fig. 7.3).

To provide an access to the monitored values on the analysis level, the momentary state of all monitored variables is periodically inserted in the data stream. The connection between the EPICS application and the DABC is realized through the DIM interface. The GUI is based on the Control System Studio [86].

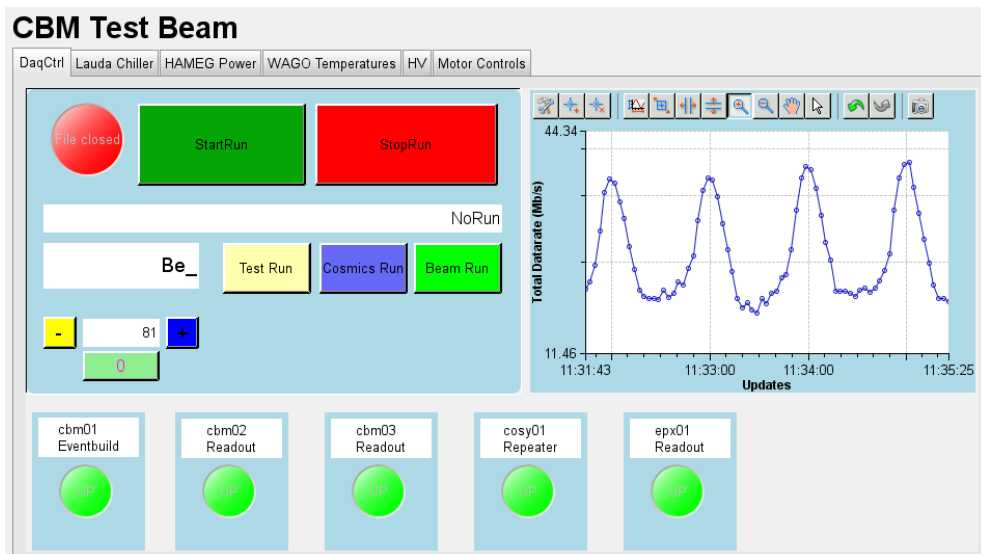


Figure 7.3: Screenshot of the EPICS-based program for slow control, used during the in-beam test in 2010. Data acquisition control tab is selected.

Chapter 8

Measurements of noise and amplitude response to β^- and γ radiation

8.1 Measurement of the noise and the baselines

The first measurement, that is usually to be done with any detector system is the measurement of the noise amplitude spectrum and the noise rate. The noise amplitude spectrum might be needed to interpret the amplitude spectra of the signal overlapping with the noise. The RMS value of the noise amplitude is the quantitative measure of the noise, used to evaluate the signal-to-noise ratio. In addition, measuring the amplitude spectrum of the noise is also a good test of the normal functioning of the system. The noise rate should be checked in order to make sure that the expected signal will not be overwhelmed by the noise counts, and that the data acquisition system will not be overloaded.

The measurement of the noise rate is straightforward: the system is simply run in the same configuration, as to be used in the further measurements with the ionizing radiation. In same measurement the amplitude spectrum of the noise. This is the spectrum of the noise, that is expected to be observed in the measurements with ionizing radiation. In self-triggering systems this spectrum is necessarily truncated by the threshold. To evaluate the RMS value of the noise, the unbiased (not truncated by the threshold) amplitude spectrum of the noise is required.

Fortunately, the present detector prototypes are based on the n-XYTER chip, which can be switched to the externally-triggered mode (also called Test Trigger Mode). If at the absence of the signal n-XYTER is triggered at arbitrary moments of time, non-correlated with the noise, then the obtained amplitude spectrum can be considered as an unbiased sample of the noise amplitude spectrum.

In fact, the obtained spectrum is not fully unbiased. This is because each

n-XYTER readout channel is equipped with the peak detection and hold circuit, which detects the highest (or lowest, depending on the set polarity) signal value within a period of around 200 ns after the trigger arrival. But taking into account the fact that this time is comparable to the rise time of the n-XYTER slow shaper, it is assumed that the spectrum, obtained in the above described, is a good approximation of the unbiased noise amplitude spectrum.

Measurement of amplitude with n-XYTER requires to know the baseline — the output amplitude, in the absence of the input signal. The baseline need to be subtracted from each measurement of the signal amplitude.

The baseline is measured in the same way, as the full amplitude spectrum of the noise, together with the measurement of the noise: n-XYTER is switched to the externally-triggered mode, and triggered from the SysCore. The obtained amplitude distribution is centered at the baseline position, and the smearing is caused by the noise. The baseline position is then determined either with a Gaussian fit of the spectrum, or as the median value (when fast calculations are required).

Baselines can be measured even when a signal source is connected to the n-XYTER. Indeed, the measurement of the baseline will be distorted only if the probability of a coincidence of the trigger and the signal is large, but normally it is not the case. The coincidence time window is approximately equal to the width of the signal pulse in the slow shaper, which is on the order of $\tau = 100$ ns. Even if the per-channel signal rate is as high as $f = 160$ kHz (the maximum n-XYTER per-channel rate capability), the probability of a coincidence of a trigger with an input signal is $f \cdot \tau = 1.6\%$. Then 98.4% of the counts will remain undistorted, and a Gaussian fit will allow to determined the baselines correctly.

8.2 Cluster and spacepoint reconstruction

Precise reconstruction of the coordinate of a particle traversing the detector requires reconstruction of the clusters and the spacepoints. *Cluster* is defined as a group of hits on one side of one sensor, caused by the same particle (or the same laser pulse). *Spacepoint* is the position of a particle in the sensor plane, obtained by combining two clusters, related to the same particle, on the opposite sides of the sensor. A cluster and spacepoint reconstruction algorithm was developed, and it is described below in details.

To reconstruct clusters one has to find hits on neighboring strip that coincide in time. Depending on the situation the reconstruction algorithm should allow or not gaps of one or more strips in the middle of a cluster.

The registration time of the hits within a cluster should not be expected to be identical — the readout electronics has a finite time resolution, and also the charge collection takes certain time. Therefore a proper time coincidence window has to be chosen.

If a detector is operated at high occupancy the clusters caused by two or more particles can overlap. The cluster reconstruction algorithm should correctly treat such situations. This is supposed to be done in the following way. On the first step groups of hits on the neighboring strips and coinciding in time are combined together without any attempt to identify and separate overlapping clusters. On the second step the combined groups are analyzed for overlapping clusters, and split. In the developed cluster reconstruction algorithm the second step was not implemented because it requires a detailed knowledge about the detector response (which was not available). Further in this work the effect of cluster overlaps is neglected, which is a good approximation because all the measurements were performed at low rates. Yet, a possibility to implement the cluster splitting was foreseen.

The time coincidence window was determined based on the data from the in-beam test of 2009 [87, 88]. All hits on one side of one sensor were sorted in time, and the time difference between every consecutive pair of hits was calculated (Fig. 8.2). One can see a large excess of the number of hit pairs at 0–40 ns. These counts are related to the pairs of hits, caused by the same particle. The rest of the counts is the combinatorial background (pairs of hits, caused by different particles, or noise). Based on this data, and including additional 10 ns as safety, the time window for cluster reconstruction was defined as 50 ns.

Additional experiment was carried out to check, if this time coincidence window is proper. In this case the signal in the sensor was induced by the β^- radiation from a ^{90}Sr source. Clusters were reconstructed using the coincidence time window of 100 ns, which is deliberately larger than the proper one. The time difference between the first (in time) and the last hits of each cluster was calculated and plotted (Fig. 8.1). One can see that the distributions for clusters of all sizes stretch up to 45-50 ns. This proves that the larger time window is not necessary. A smaller time window would lead to misreconstruction of a fraction of the clusters.

The spacepoints are reconstructed by correlating the clusters on the opposite sides of the sensor. All possible combinations of clusters within a predefined time window are considered. The proper time window was defined in the same way as for the cluster reconstruction, and is also 50 ns.

8.3 Measurement of the amplitude response to β^- and γ radiation

Amplitude response is one of the most important detector characteristics for STS because it, together with the threshold and the noise, determines the detection efficiency. Various failures in the sensor or other parts of the detector system may lead to degradation of the signal amplitude. To detect the presence of

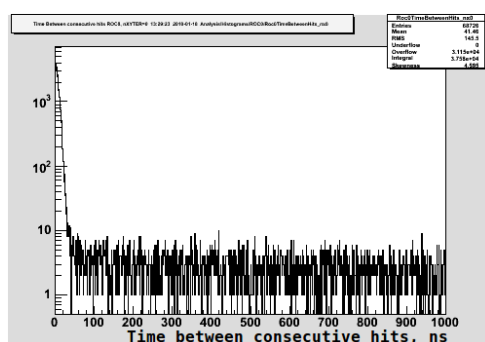
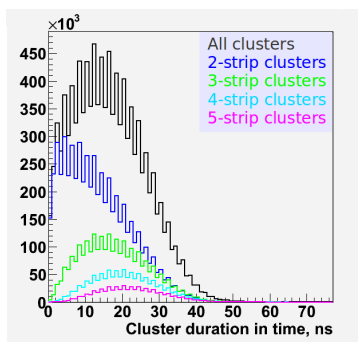


Figure 8.1: Cluster length in time distributions. Clusters were reconstructed allowing 100 ns time difference between adjacent fired strips.

Figure 8.2: Time difference between consecutive hits, extracted from the Aug 2009 in-beam test data. The hits were not required to be adjacent. The strong excess around 0 ns is considered to be due to hits which belong to the same clusters. The excess stretches up to about 40 ns.

such failures, or to ensure the expected detector performance, the total signal amplitude can be measured and compared with the expected value.

The amplitude response depends on both the detector properties, and on the kind of ionizing radiation. The effect of the detector properties, namely the ratio of the integrated charge to the total charge, created in the sensor, is evaluated in Section 3.1. In Section 5.6 the gain calibration of the front-end electronics is described, which allows to convert the integrated charge to the output amplitude or vice versa.

The Silicon Tracking System is designed to detect minimum ionizing particles (MIPs), so ideally, the amplitude response exactly to MIPs should be measured. To mimic MIPs in a laboratory without an accelerator, β^- radiation can be used. In the present work a ^{90}Sr source was used, which has the maximum energy of the β^- electrons of 2.28 MeV (coming from the daughter product ^{90}Zr) [89]. A better alternative would be to use ^{106}Ru , which is a β^- emitter with maximum electron energy 3.5 MeV [90] (electrons come from the daughter product ^{106}Pd). A disadvantage of the ^{106}Ru source is the comparatively short half-life (about one year). Unfortunately, no ^{106}Ru source was available during performing this work.

Alternatively, or in addition to β^- radiation, γ radiation can be used. Assuming that the signal amplitude is proportional to the ionization created by the particle the most probable amplitude for MIPs can be obtained by scaling the amplitude from γ quants. A practical radioactive source is ^{241}Am because it has the 59.5 keV line (Table 8.1), which is close to the most probable energy loss of a MIP in 285 μm Si (82 keV).

Energy, keV	Intensity, %
13.9	37
26.3	2.3
33.2	0.13
59.5	36

Table 8.1: ^{241}Am most intensive γ -lines.

Sensor name	Structured sides	Strips per side	Biasing technique	n-side isolation
CBM02 twpsp w.23	p, n	256	poly-Si and punch-through	p-stop
CBM03' am4ta w.10?	p	192	poly-Si resistors	—
CBM04 bo5tb w.	p, n	256	punch-trough	Schottky contact
CBM04 bo4nx w.	p, n	256	poly-Si and punch-trough	p-spray

Table 8.2: Distinct characteristics of the tested sensors

In this section, selected results of testing 4 different non-irradiated prototype sensors from 3 production batches will be presented.

All the tested sensors were produced on n-type silicon, had strip pitch of $50\ \mu\text{m}$, and the stereo angle between the strips on the opposite sides 90° (if both sides were structured). The distinct characteristics of the sensors are summarized in Table 8.2.

All 4 sensors were tested with the β^- radiation from a ^{90}Sr source. In addition, results of testing 2 sensors with the γ radiation from an ^{241}Am source will be presented.

The sensors were operated in a tracking station, as described in Section 2.3.2, and the radioactive sources were placed in front of the sensor. In each case the sensor was operated beyond the full depletion voltage.

In the test of the CBM04 sensors with the β^- radiation a reference scintillator was placed behind the sensor, and a coincidence between the hits in the sensor and signals from the scintillator was required on the analysis level. This way only hits from the β^- electrons with a certain minimal energy were selected, because they better reproduce signals of MIPs.

Clusters of hits were reconstructed, and the distribution of the total cluster amplitude is shown in Figs. 8.3–8.11.

In all amplitude spectra, acquired with the β^- radiation the Landau peak can be clearly seen. In the spectra from the both sides of the CBM02 sensor (Figs. 8.3, and 8.4) a number of low amplitude counts is present (approximately 0–70 ADC units). At the moment of performing the experiment the origin of these counts was not known. Later studies, presented in Section 9.6.1, have shown that these counts are caused by the dead strips on the sensor. Similar low amplitude counts, but more in number, are present in the spectra from the p-sides of the CBM03' and CBM04-b05tb sensors (Figs. 8.6, and 8.8 respectively). These counts remain unexplained.

In the spectra from the CBM04-bo4nx sensor, the fraction of 3-strip and larger clusters is much smaller than in the spectra from CBM02 and CBM03' sensors. This is because in the tests of the CBM04 sensors, hits from only the high energy β^- electrons were selected by requiring the coincidence with the scintillator. Low energy electrons undergo strong multiple scattering, and can traverse sideways, perpendicularly to the strip direction, and hence create a large cluster.

In the tests with the γ radiation from the ^{241}Am source, 2 peaks are clearly seen: from the 13.9 keV and the 59.5 keV lines. Despite of approximately the same intensities of the lines, the peak from the 13.9 keV line is much higher, because at this energy the photoelectric absorption cross-section is much higher (about factor 100) than at 59.5 keV.

The 2-strip cluster peak from the 59.5 keV line has lower amplitude, than the 1-strip cluster peak. This is attributed to inefficient charge collection from the interstrip gap. Indeed, the secondary electrons, originated from the photoelectric absorption of the γ quanta have range around $15\ \mu\text{m}$, so the charge deposition is very localized. A 2-strip cluster is detected only when the interaction happened close to the center of the interstrip gap, where the electrical field lines bifurcate, and where the longitudinal (lying in the sensor plane and perpendicular to the strip direction) component of the electrical field is small, even in the vicinity of the detector surface.

The left shoulder of the 1-strip cluster peak is attributed to the interstrip events, when the hit on one of the nearest strips was not detected.

The most probable total cluster amplitude for each cluster size was determined. For this the spectra, obtained with the β^- sources were fitted with a convolution of a Landau and a Gaussian, and the γ spectra — with the a Gaussian. The uncertainty on the measured amplitude was estimates as a sum in quadrature of the n-XYTER calibration uncertainty (Section 5.6.3), and the uncertainty of the amplitude measurement, as estimated in Section 8.5. The results are summarized in Table 8.3.

In general, in all the measurements the observed most probable signal amplitude is smaller than the expected from the model (3.1) by around 20 %. This effect could not be explained and to be investigated further.

For CBM04 sensors the observed signal amplitude is approximately the same as for the the CBM02, and CBM03'. The expected from the model (3.1) signal

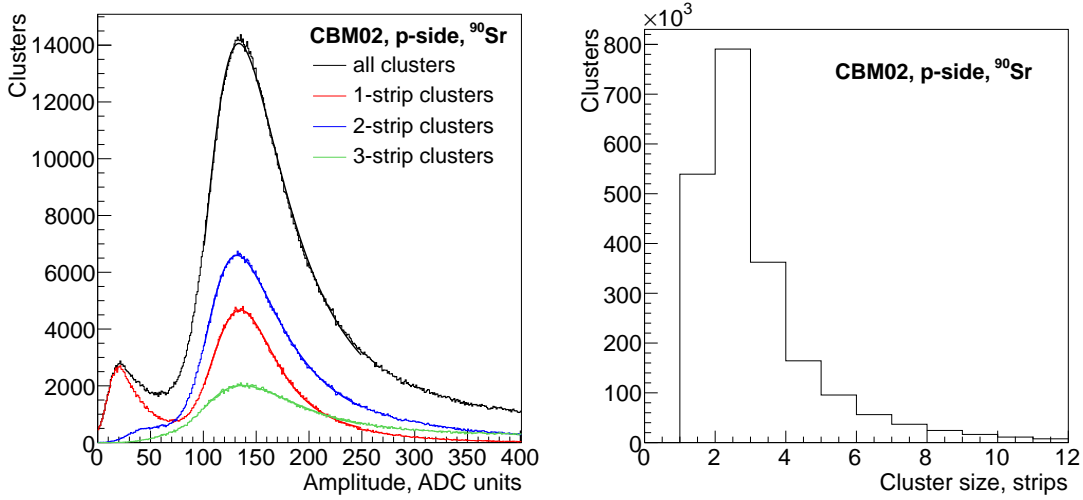


Figure 8.3: Total cluster amplitude distribution (left) and distribution of the cluster size (right) from the p-side of the CBM02-twpsp (wafer 23) sensor, operated at 95 V, and exposed to the ^{90}Sr source.

amplitude for CBM04 was not calculated because the model parameters are missing. However, the parameters are not expected to be very much different from these of CBM02 and CBM03' sensors because the relevant fabrication technologies were the same. One can therefore make a preliminary conclusion, that for the CBM04 sensors the amplitude deficit takes place as well.

8.4 Amplitude vs. bias voltage in a CBM02 sensor

Signal amplitude in the CBM02-twpsp (wafer 23) sensor (the same sensor as in the previous section) was measured as a function of the bias voltage (Fig. 8.12). The same setup, as used for the previous measurements (described in 2.3.2) was used, and the same analysis procedures were applied.

As expected, on the p-side the signal amplitude increases linearly up to the full depletion voltage (70 V). On the n-side the measurement is done starting from 80 V, because at lower voltages the isolation of the strips is not achieved, and the noise is too large. Further increase of the voltage on both sides leads to slight increase of the amplitude. The exact reason for this effect is not known, but it can be assumed that it is caused by the gradual improvement of the charge collection efficiency in interstrip gap because of the increase of the electrical field.

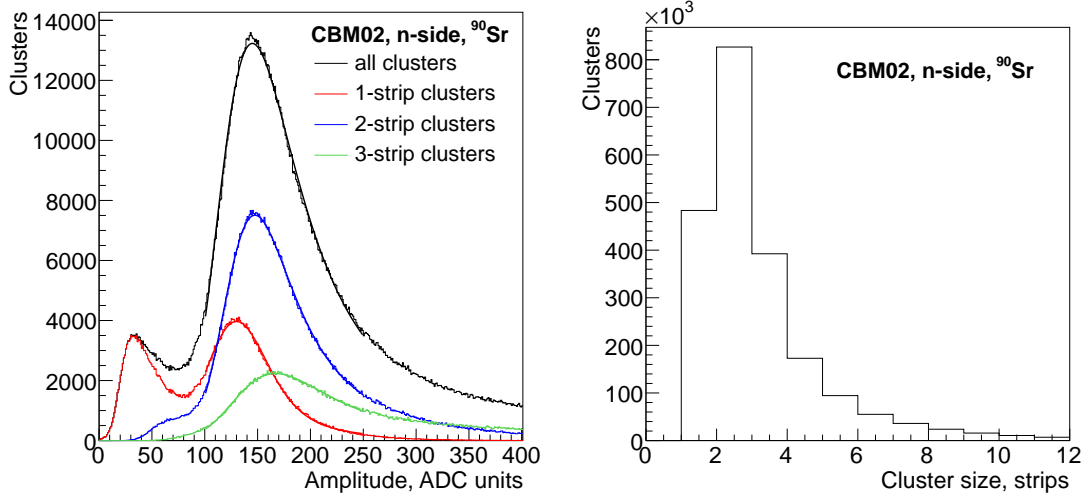


Figure 8.4: Total cluster amplitude distribution (left) and distribution of the cluster size (right) from the n-side of the CBM02-twpsp (wafer 23, demonstrator N003) sensor, operated at 95 V, and exposed to the ^{90}Sr source.

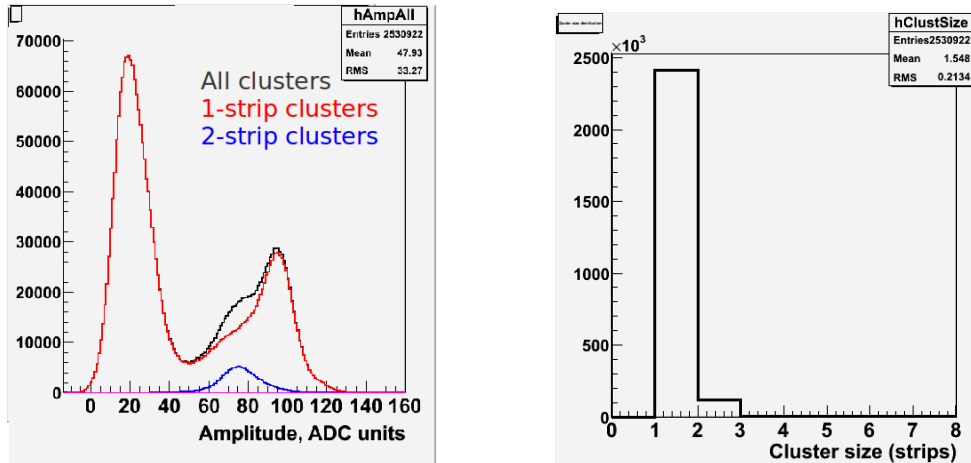


Figure 8.5: Total cluster amplitude distribution (left) and distribution of the cluster size (right) from the p-side of CBM02-twpsp (wafer 23) sensor, operated at 85 V, and exposed to the ^{241}Am source.

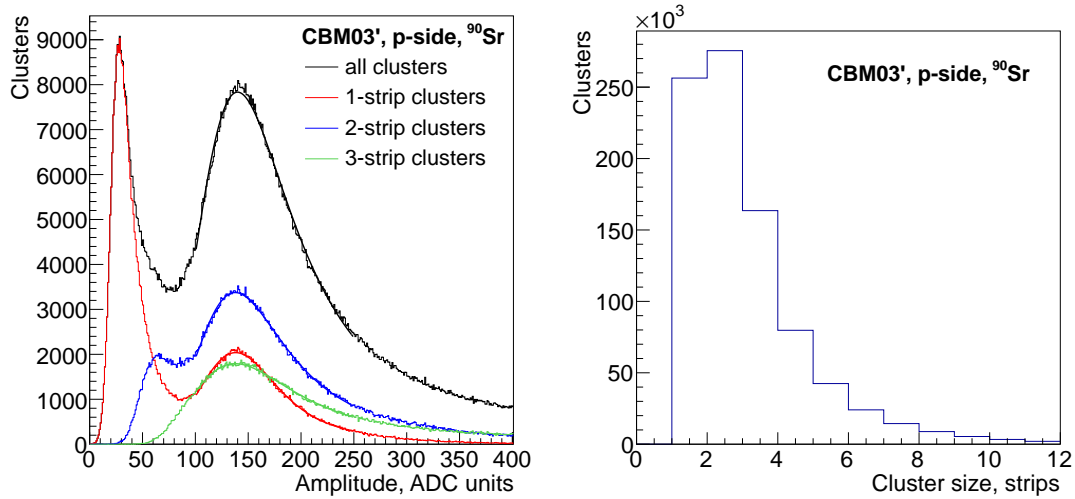


Figure 8.6: Total cluster amplitude distribution (left) and distribution of the cluster size (right) from the p-side of the CBM03'-am4ta-f3 (wafer 10) sensor, operated at 150 V, and exposed to the ^{90}Sr source.

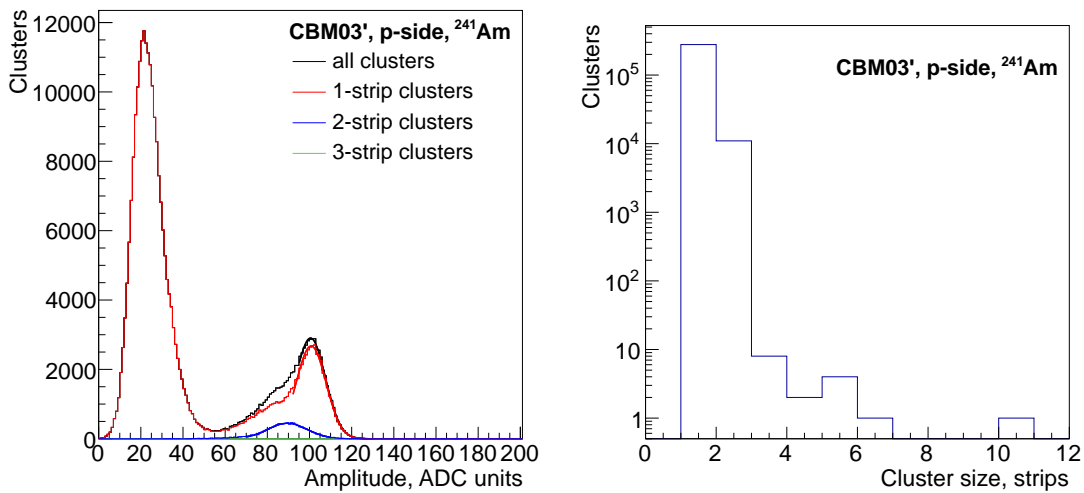


Figure 8.7: Total cluster amplitude distribution (left) and distribution of the cluster size (right) from the p-side of the CBM03'-am4ta-f3 (wafer 10) sensor, operated at 150 V, and exposed to the ^{241}Am source.

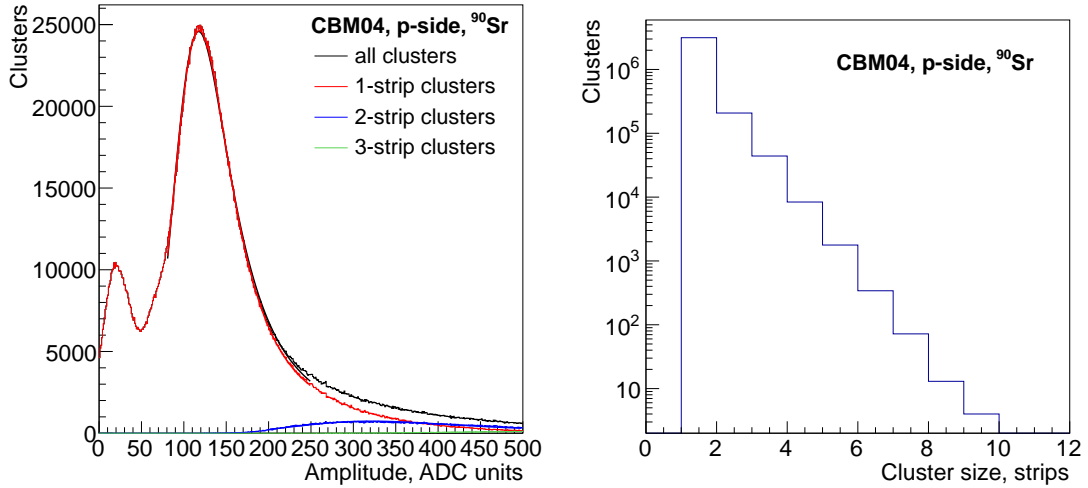


Figure 8.8: Total cluster amplitude distribution (left) and distribution of the cluster size (right) from the p-side of the CBM04-bo5tb sensor, operated at 45 V, and exposed to the ^{90}Sr source.

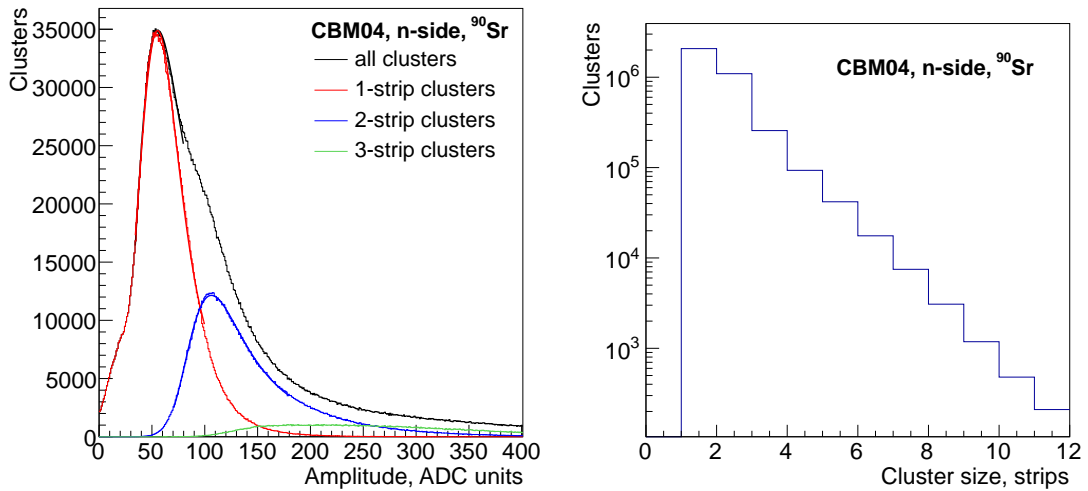


Figure 8.9: Total cluster amplitude distribution (left) and distribution of the cluster size (right) from the n-side of the CBM04-bo5tb sensor, operated at 45 V, and exposed to the ^{90}Sr source.

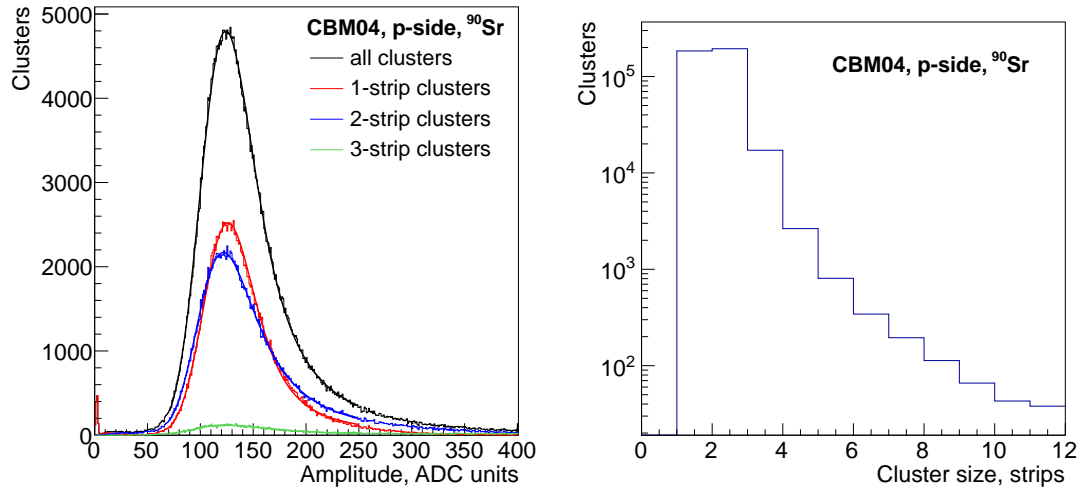


Figure 8.10: Total cluster amplitude distribution (left) and distribution of the cluster size (right) from the p-side of the CBM04-bo4nx sensor, operated at 42 V, and exposed to the ^{90}Sr source.

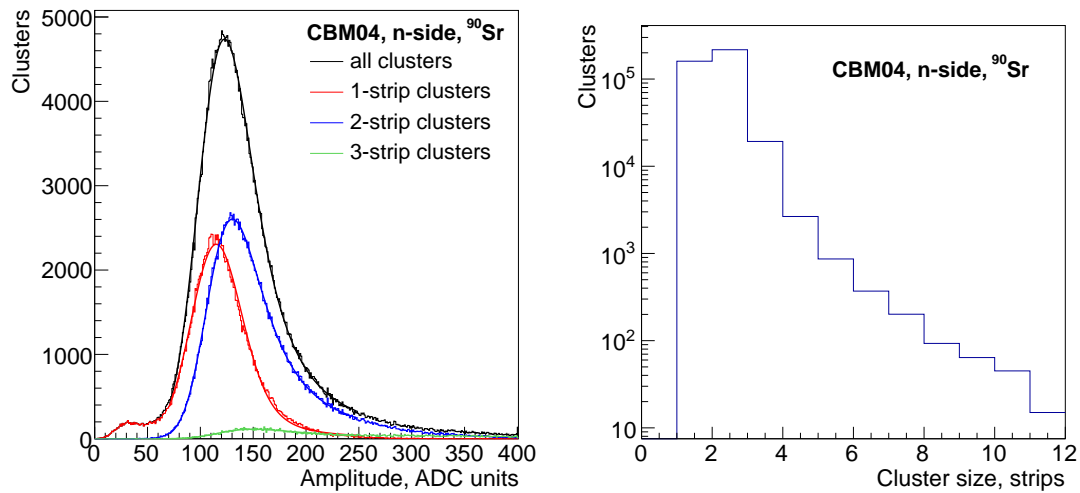


Figure 8.11: Total cluster amplitude distribution (left) and distribution of the cluster size (right) from the n-side of the CBM04-bo4nx sensor, operated at 42 V, and exposed to the ^{90}Sr source.

Sensor	Side	Source	Cluster size	Most probable amplitude				
				Measured, ADC units	Measured, ke ⁻	Expected, ke ⁻	(Exp.–Meas.) / Exp.	
CBM02	p	⁹⁰ Sr	all	132	17.4±0.6	—	—	
			1	127	16.7±0.6	21.73 ± 0.27	0.23 ± 0.03	
			2	129	17.0±0.6	22.04 ± 0.13	0.23 ± 0.03	
			3	135	17.8±0.6	22.18 ± 0.09	0.20 ± 0.03	
	n	⁹⁰ Sr	all	141	19.6±0.6	—	—	
			1	121	17.1±0.6	21.39 ± 0.29	0.20 ± 0.03	
			2	142	19.7±0.6	21.89 ± 0.16	0.10 ± 0.03	
			3	161	22.0±0.6	22.05 ± 0.11	0.00 ± 0.03	
	p	²⁴¹ Am	all	94	12.5±0.6	—	—	
			1	95	12.6±0.6	15.77 ± 0.20	0.20 ± 0.04	
			2	75	10.1±0.6	16.00 ± 0.10	0.37 ± 0.04	
			3	—	—	16.10 ± 0.08	—	
CBM03'	p	⁹⁰ Sr	all	135	17.8±0.6	—	—	
			1	128	16.9±0.6	21.1 ± 0.6	0.20 ± 0.04	
			2	131	17.3±0.6	21.73 ± 0.29	0.20 ± 0.03	
			3	132	17.4±0.6	21.93 ± 0.21	0.20 ± 0.03	
CBM03'	p	²⁴¹ Am	all	100	13.3±0.6	—	—	
			1	101	13.4±0.6	15.3 ± 0.4	0.12 ± 0.05	
			2	90	12.0±0.6	15.77 ± 0.22	0.24 ± 0.04	
			3	—	—	15.92 ± 0.15	—	
CBM04 bo5tb	p	⁹⁰ Sr	all	111	14.7±0.6	—	—	
			1	110	14.6±0.6	—	—	
			2	—	—	—	—	
			3	—	—	—	—	
	n	⁹⁰ Sr	all	55	9.0±0.6	—	—	
			1	50	8.4±0.6	—	—	
			2	104	15.0±0.6	—	—	
			3	—	—	—	—	
	CBM04 bo4nx	p	⁹⁰ Sr	all	117	15.5±0.6	—	—
				1	119	15.7±0.6	—	—
				2	116	15.3±0.6	—	—
				3	147	19.3±0.6	—	—
n		⁹⁰ Sr	all	115	16.4±0.6	—	—	
			1	109	15.7±0.6	—	—	
			2	124	17.5±0.6	—	—	
			3	147	20.3±0.6	—	—	

Table 8.3: Comparison of the measured and the expected signal amplitudes in the prototype CBM sensors.

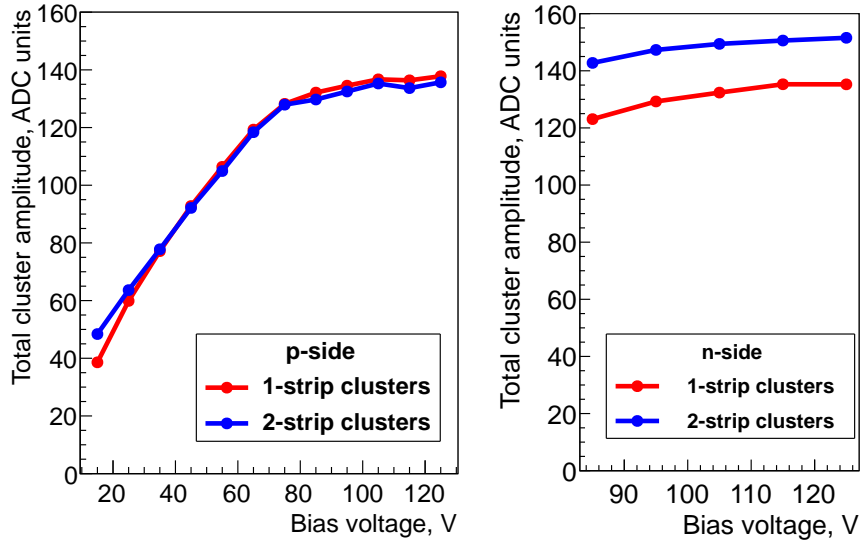


Figure 8.12: Most probable total cluster amplitude in the CBM02-twpsp sensor, exposed to the ^{90}Sr source, as a function of the bias voltage.

8.5 Reproducibility of the amplitude measurement

In order to estimate the stochastic error of the amplitude measurement, one measurement was repeated 6 times, and the variation of the measured signal amplitude was studied. The test was done on the same CBM02-twpsp (wafer 23) sensor, operated at 95 V, in the same experimental setup, as in the previous section (described in 2.3.2).

In each of the 6 measurements the amplitude of 1-, 2-, and 3-strip clusters was determined, and the corrected sample standard deviation¹ was calculated (Table 8.4). It is not known, what causes this variation. Possible sources of the variation are: instability of the response of n-XYTER with time, instability in determining the baselines, and instability of the sensor response.

Since the source of the instability is not known, it is not possible to judge, whether the variation of the signal amplitude should be specific to the sensor, or to the cluster size, or to the sensor side (and front-end polarity), or to the mean amplitude. Because the data sample is small, and a certain statistical uncertainty on the calculated standard deviation is expected anyways, for the

¹Corrected sample standard deviation of a set x_1, x_2, \dots, x_N , with mean \bar{x} , is defined as:

$$\sigma = \sqrt{\frac{1}{N-1} \sum_{i=1}^N (x_i - \bar{x})^2}$$

Side	Cluster size	Std.dev., ADC units
p	1	1.34
	2	3.22
	3	3.51
n	1	1.83
	2	3.22
	3	4.89
average		3.00

Table 8.4: Mean and corrected sample standard deviation of the signal amplitude on the p- and the n-side of CBM02-twpsp (wafer 23) sensor, determined for various cluster sizes.

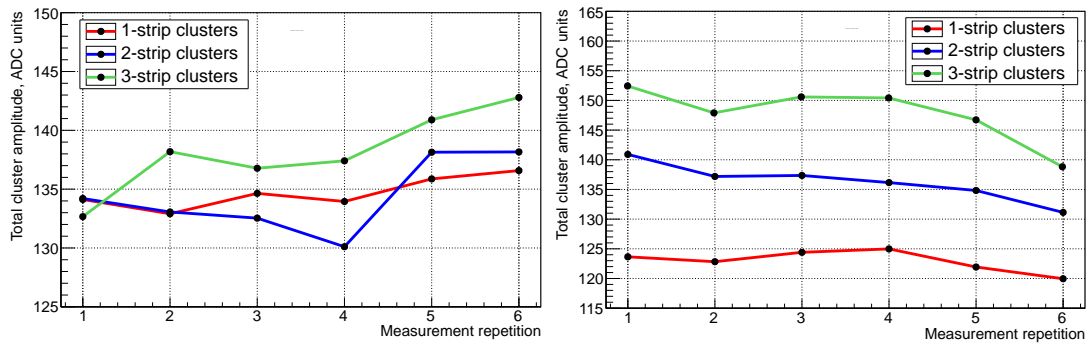


Figure 8.13: Most probable total cluster amplitude in the CBM02-twpsp sensor, exposed to the ^{90}Sr source, in six consequent measurements (horizontal axis). The sensor was operated at 95 V.

sake of simplicity the average standard deviation over both sides and all cluster sizes is calculated and equals to 3.0 ADC units. This value is taken as the stochastic uncertainty for all amplitude measurements.

Chapter 9

Study of the amplitude response of the CBM02 sensors on a proton beam

In December 2010, within a joint initiative of several experimental groups, a test of prototype CBM detectors and readout electronics on a proton beam was carried out. The experiment was done at the COSY synchrotron in the Research Center Jülich (Germany) [91]. Together with the group of the Silicon Tracking System, the group of Muon Detector from VECC (Kolkata), as well as the experimental electronics group from Heidelberg participated in the experiment. For the latter two groups, the goals were, respectively: to measure the detection efficiency and the resolution of the GEM detector, and to measure radiation tolerance of an FPGA to the high energy hadron beam.

The goals for the Silicon Tracking System were:

- to perform a general test of the full system
- to measure the amplitude response of the prototype detectors, including the dependence on the bias voltage
- to study the correlation of the signal amplitude on the p- and n-sides
- to test the system with front-end electronics, operated in the floating mode

Since only two tracking stations were available up to the moment of the beam test, it was not possible to study the spatial resolution of the detectors.

9.1 Experimental setup

The whole experimental setup comprised two STS tracking stations, a GEM detector station, a setup for FPGA tests, and reference scintillators. The layout of the setup is sketched in Fig. 9.1.

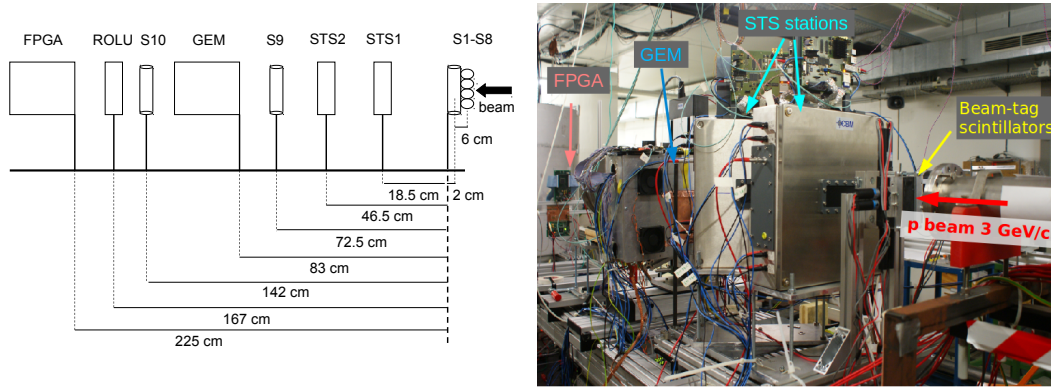


Figure 9.1: A sketch and a photograph of the in-beam test setup. See the text for details.

The STS stations are described in details in Section 2.3.2. They hosted CBM02 sensors of the same type. In front of the STS stations a beam positioning and tagging detector, based on four horizontal and four vertical plastic scintillator bars was located (S1–S4 and S5–S8). Behind — the GEM detector, surrounded with two scintillators S9 and S10. The scintillators S9 and S10 were planned to be used as reference detectors for GEM detection efficiency studies. ROLU, placed after the GEM setup, was yet another scintillator detector, aimed on the beam position monitoring and optional vetoing of the halo particles. The FPGA single event upset test setup was put to the very end of the beam line, because it was least sensitive to beam focusing and energy. All detectors were permanently present on the beam line.

Due to certain problems with the scintillators S1–S4, only scintillators S5–S8 (second plane) were finally used. Signals from S5–S8 were logically OR-ed and (optionally) used on the off-line level to reject the background by requiring a time coincidence.

The baselines were measured during the 10 s pause between the beam spills. The signal, indicating the beginning and the end of the spills was taken from the accelerator and send to an AUX port of one of the ROCs. The data acquisition system, the DABC, watched for the AUX message and reconfigured the n-XYTERs accordingly: at the beginning of each spill they were set into the self-triggering mode, and at the end — into the externally triggered mode, for baseline measurement.

This idea, however, didn't work well, because sometimes the data acquisition system missed the AUX messages, because of too large data flow.

The COSY accelerator (COoling SYnchrotron) [92] could provide a well focused 3 GeV/c proton beam, with intensities from few times 10^3 protons/s up to very high intensities, much beyond the detection capabilities of the STS detectors. COSY is well suited for testing of CBM-STS detector prototypes.

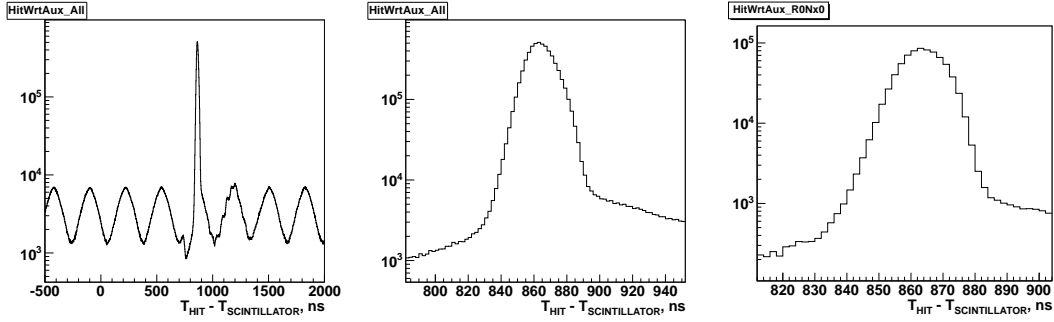


Figure 9.2: Time of hit w.r.t. the scintillator signal; *left*: all hits from both station together; *center*: the same as left, but now zoomed to the peak; *right*: hits from only one n-XYTER (station 0, p-side, n-XYTER 0; run 174, VBias=70 V).

9.2 Time correlation with the reference scintillator signal

One of the first things that was checked in the beam test setup was the time correlation between the hits in the STS detector stations and signals from the reference scintillators. If a lack of correlation would have been found, it would indicate a problem of time measurement or time synchronization. In addition, by requiring a time coincidence of hits in the STS stations with the scintillator signal one can reject a significant fraction of the noise hits at the off-line level.

To study the correlation, the time difference between STS hits and scintillator signals was calculated, and its distribution is shown in Fig. 9.2. All possible combinations of STS hits and scintillator signals, that are separated in time by a value, smaller than the range of the plot, were considered.

The correlation peak is clearly seen at around 860 ns. The time difference comes mainly from a constant shift between the timestamp counters of ROC and n-XYTER.

In addition to the main peak, a series of minor peaks can be seen. These peaks are combinatorial background, modulated by the time structure of the beam. As it will be shown in the next section, the probability density to get a beam particle at a certain moment of time was not uniform, but had a shape, similar to these minor peaks. Plotting a time difference between a single scintillator signal and all possible beam particles will result in a structure, similar to the probability density function of the beam. Since the scintillator signals are correlated with beam particles, the contributions to the time difference plot from many scintillator signals add up coherently and result in a series of the satellite peaks.

Another source of background on this plot was the noise hits in the STS station. Since they are not correlated with the scintillator signal, their contribution to the plot is uniform.

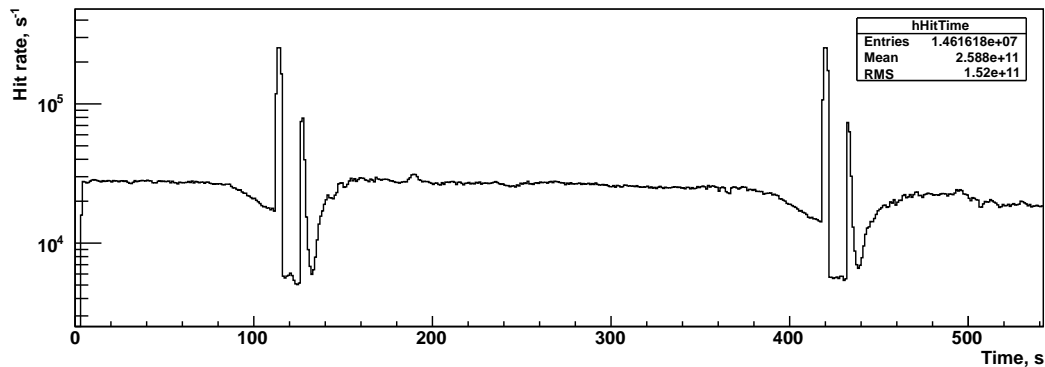


Figure 9.3: Hit rate versus time on the p-side of station 0 (Run 174).

9.3 Beam intensity and temporal structure

After the time correlation, the beam intensity was checked. The hit rate on one side of one of the stations versus time is shown in Fig. 9.3. One can clearly see the structure of the beam spills. In average, during the spill, the beam intensity was around $2 \cdot 10^4 \text{ s}^{-1}$. However, at the beginning and at the end of each spill a splash of intensity up to $7 \cdot 10^4 \text{ s}^{-1}$ and $2.5 \cdot 10^5 \text{ s}^{-1}$ respectively was observed. The data, corresponding to the splashes, was rejected at the off-line level. The length of the spills was about 295 seconds, and the pause between the spills — about 10 seconds. The hits between the beam spills were caused by the electronic noise.

The observed minor peaks in the time correlation plot (Fig. 9.2) motivated to study the microstructure of the beam. Plotting the beam rate versus time with small time bins would not help in this case, because the number of particles per time bin would be very small (with 10^4 s^{-1} intensity and 100 ns time bins, the average number of particles per time bin is 10^{-5}). Therefore, the time difference between all possible pairs of the beam particles was plotted (Fig. 9.4). The sharp peak at 0 ns correspond to groups of hits, caused by the same particle (hit clusters). The other peaks appear because of the beam microstructure. In case of a uniform beam one would expect only the sharp peak at 0 ns and a uniform distribution in the rest of the range.

9.4 Beam profile

In Figure 9.5, one-dimensional profile of the beam is shown. In general, a Gaussian shape is seen, as expected. However, some of the channels, appear irresponsive, while the others exhibit double, or even triple number of counts, as compared to the neighbors. This can be explained in the following way. There were two kinds of irresponsive channels in the system: certain channels were masked because of excessive noise, and in some of the channels the strip was not connected

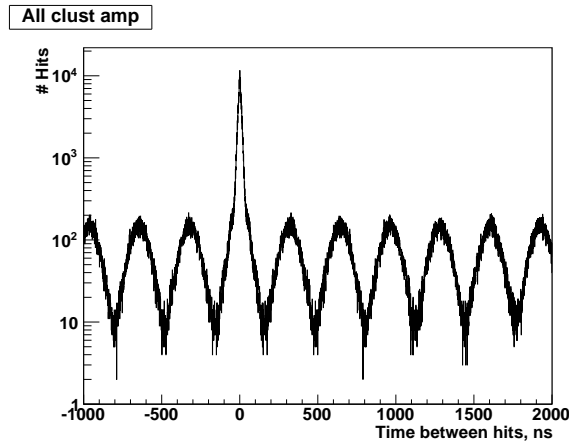


Figure 9.4: Time between hits on station 1, n-side. All possible hit pairs, separated in time less than the histogram range, were considered. (Run 174)

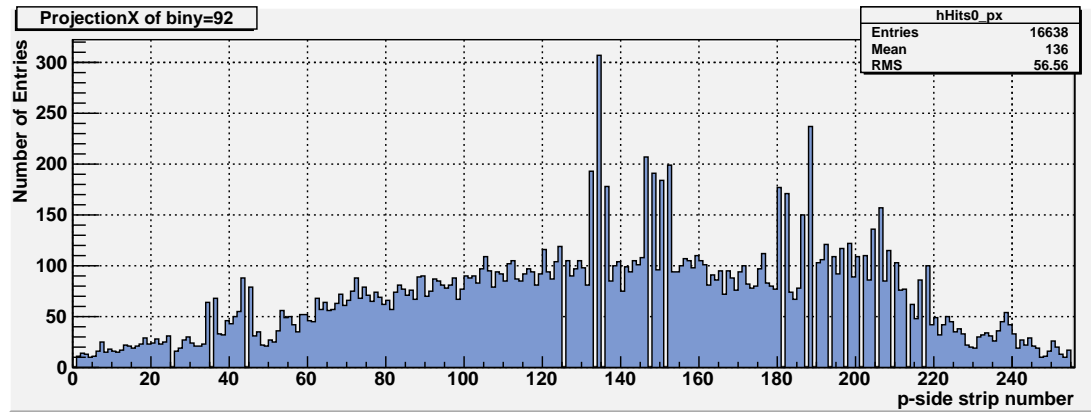


Figure 9.5: Profile of the histogram on Fig. 9.6, left, along strip 92 of the n-side. (i.e. hit distribution on the p-side along strip 92 of the n-side.)

to the preamplifier input. If a masked channel is hit by a particle, the collected charge flows into the preamplifier, but no hit is produced. If an unconnected strip is hit, the collected charge couples to the nearest neighboring strips, and creates hits on them.

In Figure 9.5, the unconnected channels are 35, 44, 133, 135, 147, 151, etc. Their neighbors have got a double number of hits. The channels 134 and 188 have got triple number of counts, because they have two unconnected neighbors. The channels 0, 25, 45, 125, 193, 197, etc. were masked. The slight excess of the hit number in the region 190–212 was caused by the noise.

Two-dimensional beam profiles were also plotted (Fig. 9.6). Elliptical shape of the beam is clearly seen in both stations. The size of the beam is: $\sigma_x=3.0$ mm, $\sigma_y=2.7$ mm. The stations appear slightly misaligned vertically, by 3 mm, and by

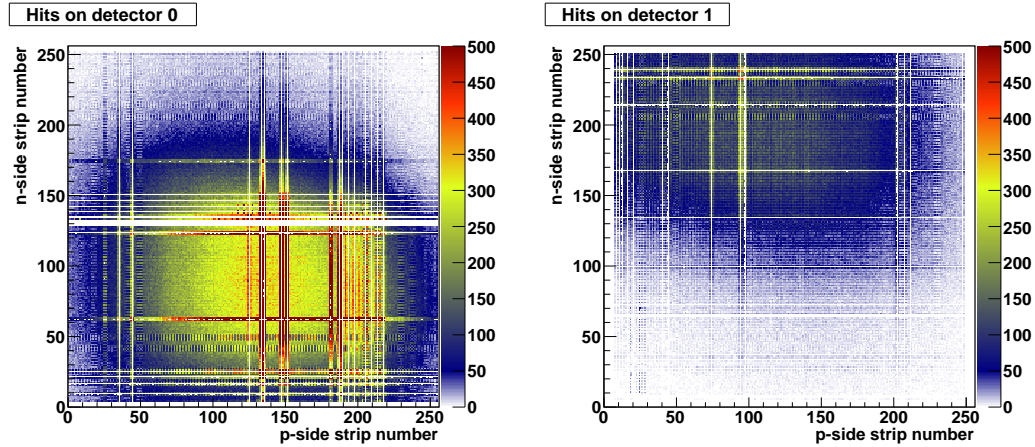


Figure 9.6: Hit position distributions on station 0 (left) and station 1 (right). Vertical axis on the picture correspond to physically vertical direction (top and bottom might be confused). (run 174, $V_{bias}=70$ V).

5 mm respectively. This misalignment is tolerable.

9.5 Baseline measurement and stability

Before coming to the signal amplitude analysis, stability of the baseline positions was checked. As it explained in 9.1, the baselines were measured between the beam spills, approximately every 5 minutes. The baseline positions were plotted versus time for each individual n-XYTER channel (Fig. 9.7).

In most of the channels the baseline position does not change by more than 6 ADC units between the measurements. This is about $6/130 = 4.5\%$ of the MIP most probable amplitude. Such instability is tolerable. Worthy of note is the fact that the baselines of most of the channels change in a correlated way.

A fraction of the channels, however, exhibited a much larger baseline drift, up to 40 ADC units, which is about 30% of the MIP most probable amplitude. Such baseline drift significantly distorts the amplitude information. The cause of so large baseline drift is not known.

The Figure 9.7 shows the baseline in only one n-XYTER chip. The other chips exhibit approximately the same behavior. The number of channels, that exhibit such a large baseline drift is different in every chip. In occasional chips no channels exhibit the large baseline drift.

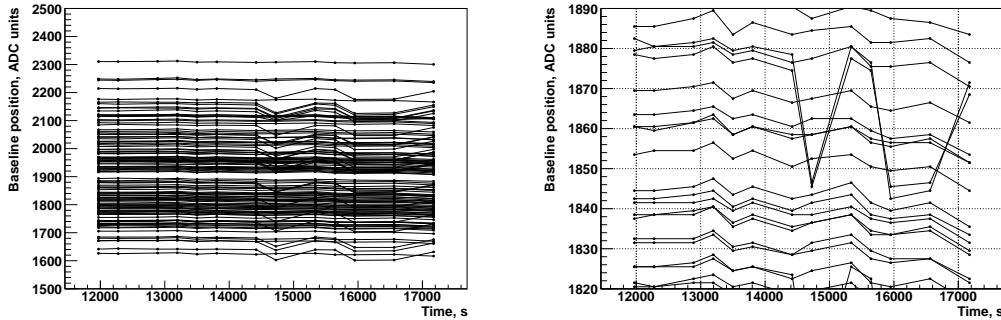


Figure 9.7: Baseline positions of each individual channels of one n-XYTER versus time. All non-masked channels are shown. The right plot is a zoomed view of the left one. (Station 1, p-side, n-XYTER 1, runs 104–112, $V_{bias}=90$ V.)

9.6 Total cluster amplitude

After the all previous cross-checks, one can proceed to the amplitude analysis. Total signal amplitude is one of the most important characteristics of a detector. To determine it, the hits, produced by the same particle, were combined into clusters, and the amplitude within each cluster was summed up. The cluster reconstruction procedure is described in details in 8.2.

Measuring the total signal amplitude in a self-triggered system is biased. A fraction of the collected charge always couples to the neighboring strips, and if it appears to be below the threshold, it remains undetected. However, if the threshold is sufficiently low, this effect can be neglected.

First, the amplitude spectra will be studied only qualitatively. The effect of the selection criteria on the shape will be discussed. Then, when the features on the spectrum are understood, a systematic quantitative analysis of the most probable total signal amplitude will be done.

In all plots the signal amplitude will be expressed in ADC units, and converted to electrons only in the text. The reason for this is that the data analysis was done, and the plots were prepared before the n-XYTER calibration was performed, and never redone later. The conversion from the ADC units to electrons will always be done with the n-XYTER calibration, described in 5.6.

9.6.1 Qualitative analysis of the spectra

In Figure 9.8, the cluster amplitude spectrum from the p-side of station 0 is shown. The only selection criterion, applied here, was that the data was taken from the beam spill, excluding the high-intensity edges (Section 9.3).

The reconstruction yields mostly 1- and 2-strip clusters (for definition of 1- and 2-strip clusters see Section 8.2). The number of 3-strip and larger clusters is

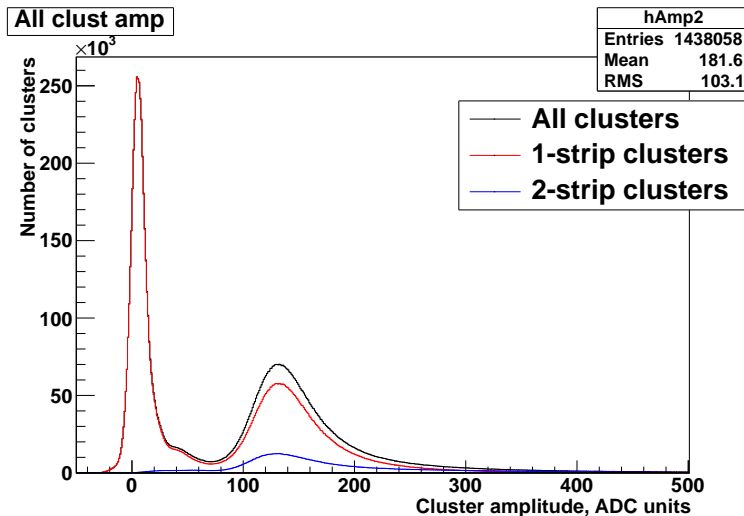


Figure 9.8: Spectra of the total cluster amplitude, taken from the p-side of station 0, at $V_{bias}=80$ V (Run 173). No selection criteria was applied, except selection of the data from the beam spill, without the high-intensity edges.

about two orders of magnitude smaller. For 1- and 2-strip clusters Landau peak are clearly seen (approximately, in the range between 80 and 300 ADC units).

In the left part of the plot a large number of low amplitude counts is present. The fact that there are mostly 1-strip clusters (no time and space correlated hits) suggests that these are fake hits, caused by the electronic noise. To reject them a coincidence with the scintillator signal was required, and the result is shown in Fig. 9.9.

The remaining counts in the low-amplitude region can not be explained with the fake hits from the electronic noise, that are present in the selected time window. Indeed, the fraction of the background in Fig. 9.2 is below 1%, while the fraction of low amplitude counts in Fig. 9.2 is 13% (determined as the fraction of counts left to the the bottom of the valley).

The low amplitude counts can be explained with the presence of the channels with unconnected strips, as well as with the masked channels. If a particle hits an unconnected strip, the charge is coupled to the neighboring strips, and a hit is produced on each of the neighbors (providing the threshold is not too large). These hits are not combined in a single cluster, and two low-amplitude 1-strip clusters are reconstructed.

Similar happens when a particle hits the interstrip gap between a working and a masked channel. In this case the charge, collected on the masked channel, is lost, and instead of a 2-strip cluster with the full amplitude, a 1-strip cluster with a low amplitude is reconstructed.

The observed fraction of the low-amplitude counts (13%) agrees very well with the fraction of faulty channels. There are 14 channels with non-connected strips

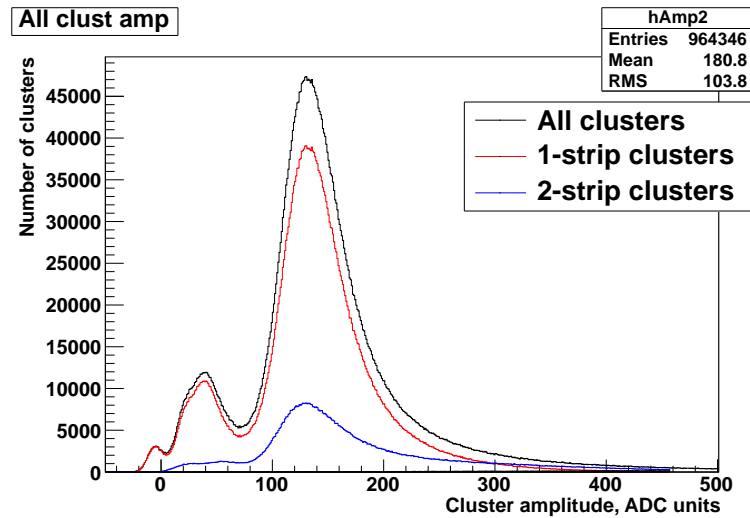


Figure 9.9: Spectra of the total cluster amplitude, taken from the p-side of station 0, at $V_{bias}=80$ V (Run 173). Coincidence with the scintillator signal was required.

and 5 masked channels. The channels with unconnected strips are expected to result in $14 / 256 \times 2 = 11\%$ of low-amplitude counts, and the masked channels — in $5 / 256 = 2\%$, which in total sums up into 13%.

To prove that exactly the faulty channels cause the low-amplitude counts, clusters from only the fully-working regions of the detectors were selected (Fig. 9.10). The region of interest was chosen to be 2 strips away from the nearest faulty channel. In order to avoid the problem of clusters, that lie on the boundary of the selected region, first the cluster reconstruction was performed in the whole detector, and then the selection was done. The resulting amplitude distribution is shown in Fig. 9.11.

The spectra from the n-side of station 0 (Fig. 9.12) look very similar: the peak positions and shapes are roughly the same, as expected.

Now the spectra from the station 1 will be discussed. The spectra from the n-side (obtained with various selection criteria) are shown in Fig. 9.13. The top left plot shows the amplitude distribution with only one selection criterion applied: data from the beam spill only was selected. Besides of the clear Landau peak, one can see two other peaks in the region of low amplitudes.

To investigate the cause of these peaks, the effect of applying two selection criteria was examined. Requiring a coincidence with the scintillator does not change the relative height of these peaks (w.r.t. the Landau peak). This indicates that these peaks are not caused by the uncorrelated (preamplifier) electronic noise. Another indication for this will be deduced in Section 9.6.3, from the amplitude correlation plots (Fig. 9.17, 9.18), where the time coincidence between the signal on the n- and p-side was required. There the low amplitude counts on the n-side are correlated with high amplitude (hence, caused by the beam

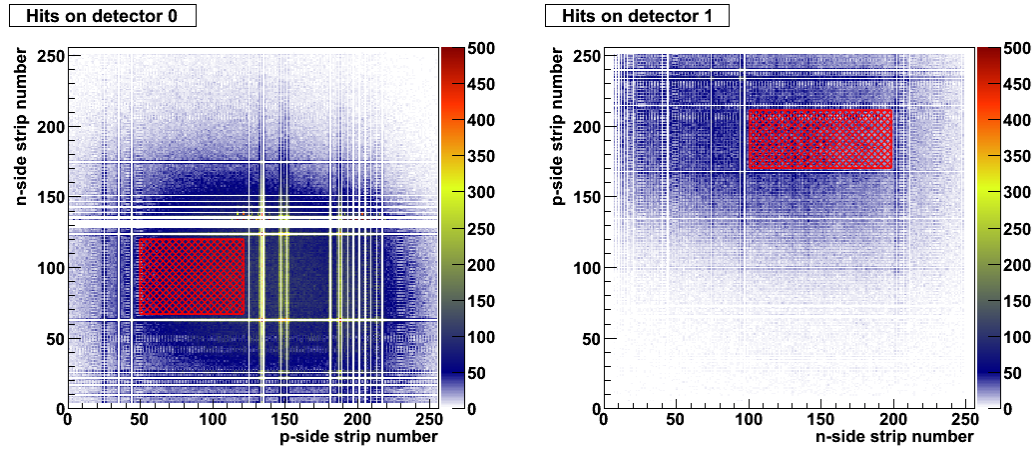


Figure 9.10: Hit position distributions (same as in Fig. 9.6), with the selected fully-working regions marked.

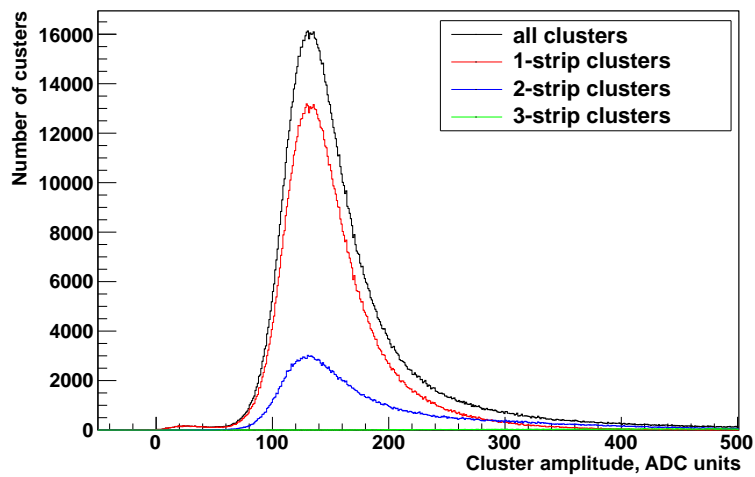


Figure 9.11: Total cluster amplitude spectra from the p-side of station 0, operated at $V_{bias}=80$ V (Run 173). Coincidence with the scintillator signal was required. Clusters from only the good regions (Fig. 9.10) were selected.

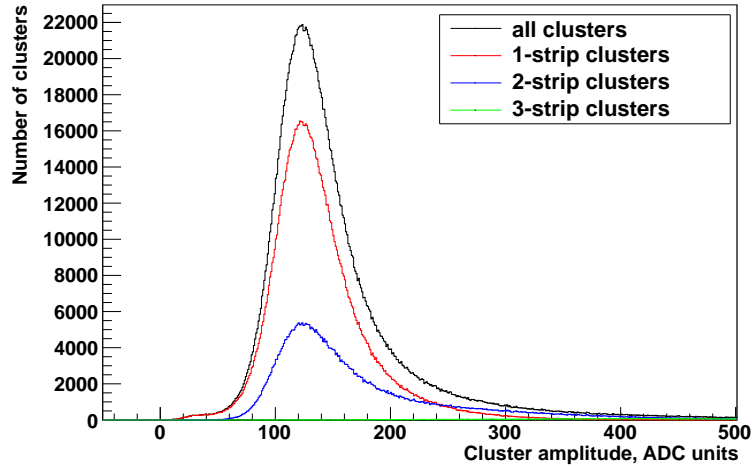


Figure 9.12: Total cluster amplitude spectra from the n-side of station 0, operated at $V_{bias}=80$ V (Run 173). Coincidence with the scintillator signal was required. Clusters from only the good regions (Fig. 9.10) were selected.

particles) counts on the p-side.

Selection of the clusters from a region of the sensor without dead strips reduces the relative (w.r.t. the Landau peak) height of the larger of the low amplitude peaks, but increases the the relative height of the smaller one. Still, the both peaks remain pronounced. Hence, unlike to the low-amplitude peaks in Fig. 9.9, these peaks are not caused by the faulty strips.

The peaks can not be explained by the large n-XYTER baseline jumps (Section 9.5) because a similar pattern would have been expected to be present in the 2-strip cluster spectrum as well.

Another potential explanation of the peaks, that will be rejected now, is that under certain conditions a fraction of charge is lost in the sensor, and this causes the low amplitude counts. Such an effect would lead to a spectrum, where the right edges of the two peaks coincide. Indeed, in a given amplitude bin one would expect to have the same number of counts from the both readout chips (because each of the chips reads out every other strip of the sensor).

A possible explanation, that has not been excluded yet, is that the peaks are caused by a noise, correlated with the beam. As potential sources of such noise the other detectors on the beamline can be suspected. The spectrum can then be explained as follows. Each of the peaks is the counts comes from the correlated noise counts on one n-XYTER. The left edge of the peak is the threshold cut. Because the uncorrelated noise was very different in the two n-XYTERs, the threshold were set to very different levels, which makes the two peaks appear separately, and not coincide. The threshold cuts are not sharp, but rather Gaussian-smeared, because in n-XYTER the threshold is applied in the fast chan-

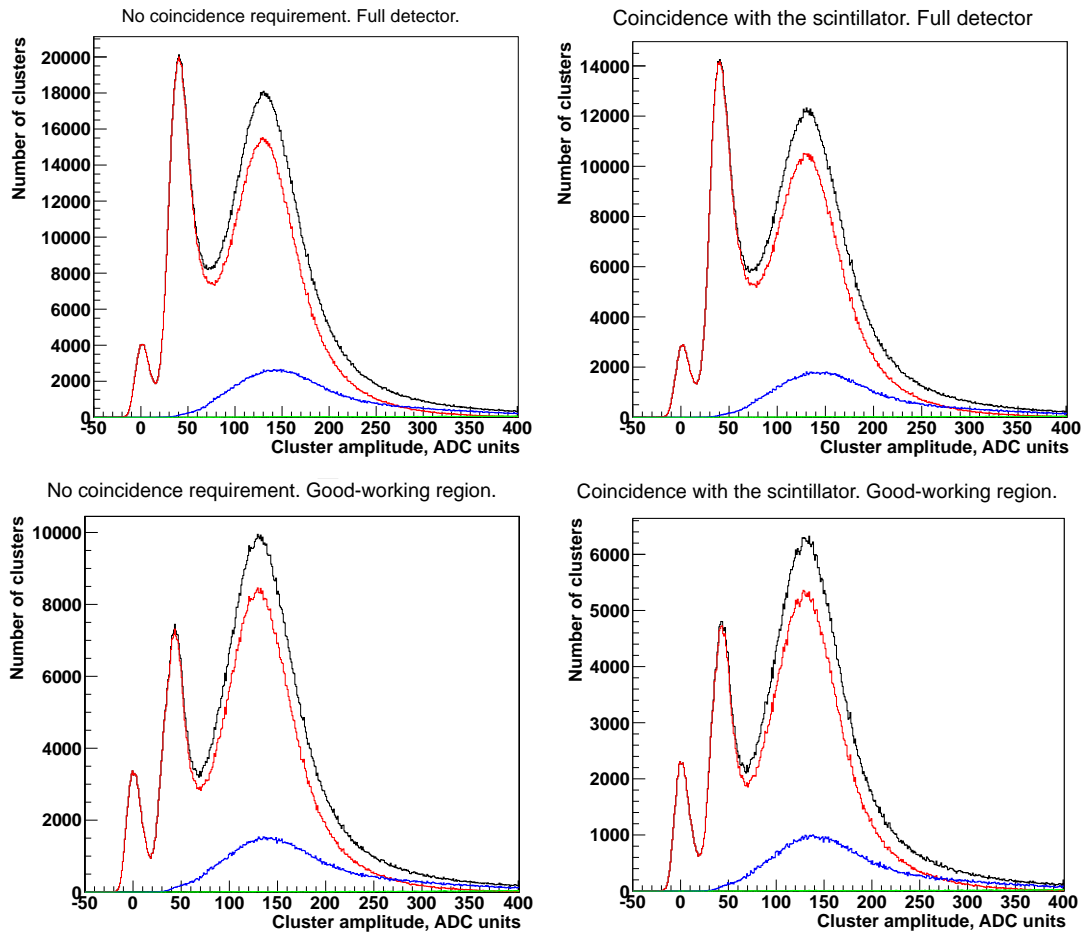


Figure 9.13: Total cluster amplitude spectra from the n-side of station 1, with various selection criteria: with/without the requirement of the correlation with the scintillator signal and with/without selection of clusters from the good-working region of the detector (Fig. 9.10). The detector was operated at $V_{bias}=80$ V (Run 173).

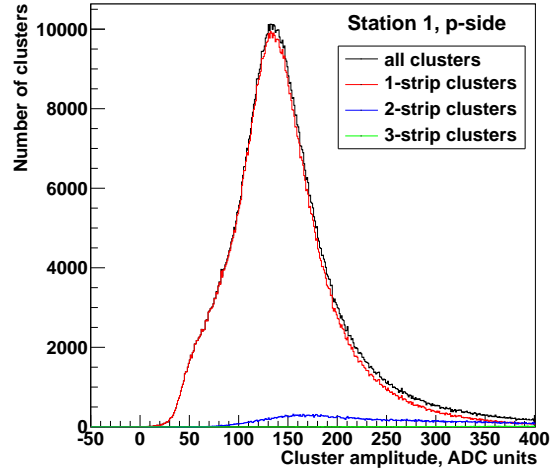


Figure 9.14: Total cluster amplitude spectra from the p-side of station 1. Coincidence with the scintillator signal was required. Clusters from only the good regions (Fig. 9.10) were selected.

nel, and the amplitude is measured in the slow channel, and the amplitudes in the fast and the slow channels are not fully correlated (Section 5.1). Such explanation requires also an assumption that the correlated noise couples much stronger to one n-XYTER, than to another. Still, a definite conclusion about the origin of the low amplitude peaks would require additional studies, but they were not done because of limitation in experimental time on the beamline. No such low amplitude peaks were observed with this detector station in further experiments in the laboratory.

At the p-side of station 1 the noise was also large, and the thresholds were set high. This results in a suppression of the 2-strip clusters, because the signal on the minor of the strips, from the 2-strip cluster, appears more often below the threshold. The left edge of the 1-strip clusters peak looks also to be cut by the threshold. In this case it is not clear, whether the maximum on the spectrum is the maximum of the Landau peak. It might be just the tail of the Landau distribution, cut on the left side by the threshold. Therefore, the most probable amplitude can not be determined.

After the qualitative analysis of the spectra, the exact Landau peak positions can be extracted. Instead of discussing the values, that can be obtained from only the spectra, that were presented in this section, we will go directly to a the dependence of most probable amplitude on the bias voltage.

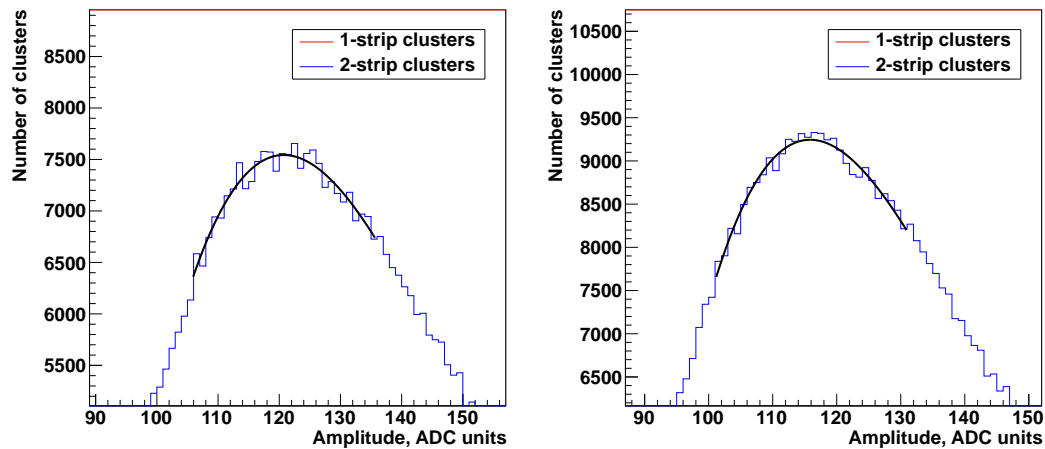


Figure 9.15: Examples of the fits of the total cluster amplitude spectra. Both plots are 2-strip clusters spectra from the n-side of station 0, 70 V bias voltage.

9.6.2 Total cluster amplitude and its dependence on the bias voltage

Most probable signal amplitude was determined from the data of many runs, with the sensors operated at various bias voltages. The amplitude spectra, were produced with the requirement of coincidence with the scintillator, but without the selection of clusters from the good-working region of the detectors. It was done so, because this analysis had been finished before the effect of the dead strips was understood. The analysis was not redone, because it was considered that rejection of the low amplitude counts will not change the result in any significant way. It will be seen below, that the results are anyways poor reproducible, which introduces a large uncertainty in the determined signal amplitude. Some examples of the spectra, obtained at various bias voltages are shown in Fig. 9.22 and 9.23.

To determine the position of the Landau peak on each of the spectrum, the top of each peak was fitted with a third order polynomial, and the maximum was extracted. In all cases the fitting curve described well the shape of the distribution. Examples of the obtained fits are shown in Figure 9.15. The obtained results were combined in two plots, and are shown in Fig. 9.16.

Up to three runs with the same bias voltage were performed and analyzed in order to check whether the results are reproducible. All this data was taken within about 5 hours, without making any other modifications to the setup. From the Figure 9.16 one can see that the reproducibility is poor. In the extreme case, for the 2-strip clusters on the n-side at 90V, the discrepancy between the measurement reaches 13 ADC units (10% of the absolute value). The cause of the poor reproducibility could not be identified. Most probably, it is the change

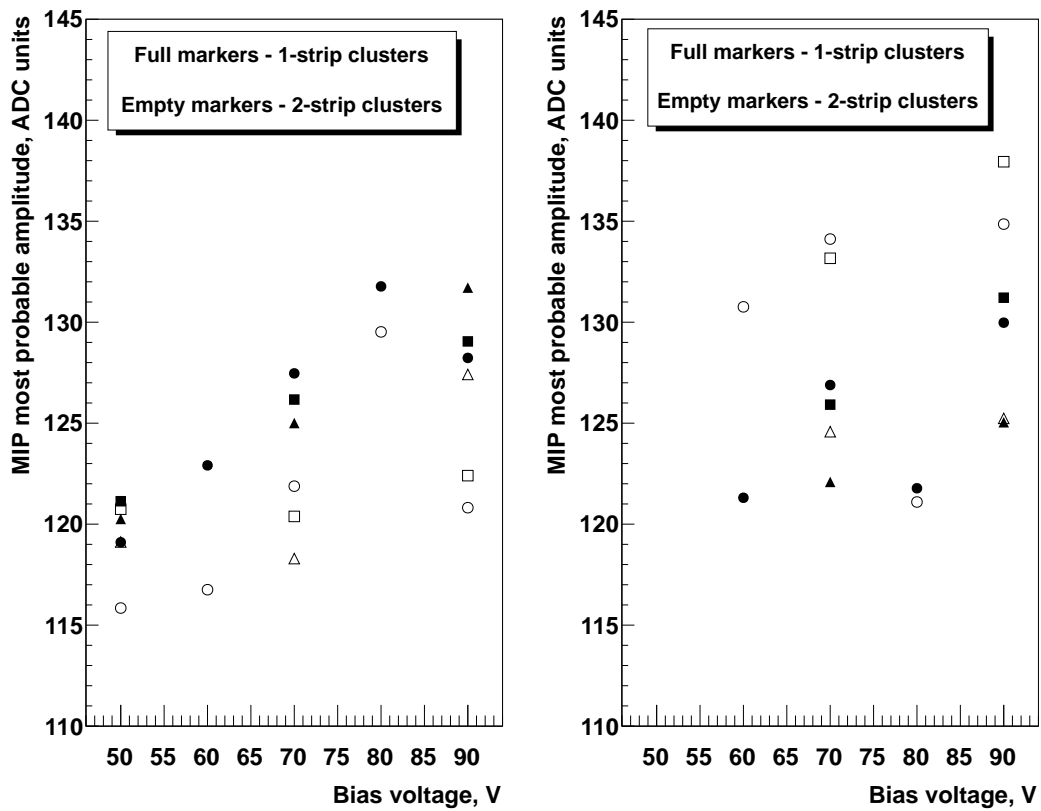


Figure 9.16: Most probable MIP amplitudes on the p- (left) and the n-side (right) of the station 0 at various bias voltages. Full markers correspond to the 1-strip clusters, empty — to the 2-strip clusters. The markers of the same shape correspond to the same, uninterrupted, series of runs. Note the offsets in the vertical scales.

Sensor side	Cluster size	Most probable total cluster amplitude		
		measured, ke ⁻	expected ke ⁻	(exp. - meas.) / exp.
p	1-strip	17.0 ± 0.5	21.73 ± 0.27	0.22 ± 0.03
	2-strip	16.3 ± 0.6	22.04 ± 0.13	0.26 ± 0.03
n	1-strip	18.0 ± 0.6	21.39 ± 0.29	0.16 ± 0.03
	2-strip	18.6 ± 0.9	21.89 ± 0.16	0.15 ± 0.04

Table 9.1: Most probable total cluster amplitude in the CBM02 sensors, operated at 90 V, and exposed to the proton beam.

of the detector response, and not a change of the response of the n-XYTER. It is considered so, because during the n-XYTER calibration (5.6) a very good reproducibility and uniformity over chips was observed. It is also known that the cause is neither the statistical error, nor the error of the fit. The plots in Figure 9.15 correspond to the maximum and the minimum points of the 2-strip cluster amplitude at the n-side, at 70 V (10 ADC units difference), and they show low statistical fluctuations and good quality fits.

It can be seen, that in average the signal amplitude increases with the bias voltage within the scanned range. At 90 V it reaches the following values:

Here both the uncertainty of the calibration and the uncertainty of the measurement was taken into account (uncertainties were added up in quadrature). The measurement uncertainty was estimated as the sample standard deviation.

The observed signal amplitude is systematically lower than the expected from the simple model, described in chapter 3. The reason for this could not be identified.

Another observation, that can be made from Figure 9.16, is that on the n-side the amplitudes of the 2-strip clusters are systematically higher than of the 1-strip clusters, while on the p-side it is vice versa. Generally, it is expected that 2-strip clusters have in average larger amplitude than the 1-strip ones. The reason for this is the following. If a particle hits an interstrip gap, a 2-strip cluster is reconstructed when the amplitude on the both nearest strips exceeds the threshold. Given a constant position of the particle in the interstrip gap, and a constant ratio of the charge sharing between the strip, the particles that deposit more energy in the sensor are more likely to create 2-strip clusters. On the p-side the opposite is observed. This can be caused, for example, by a charge loss in the interstrip gap. More detailed investigations have to be done in future.

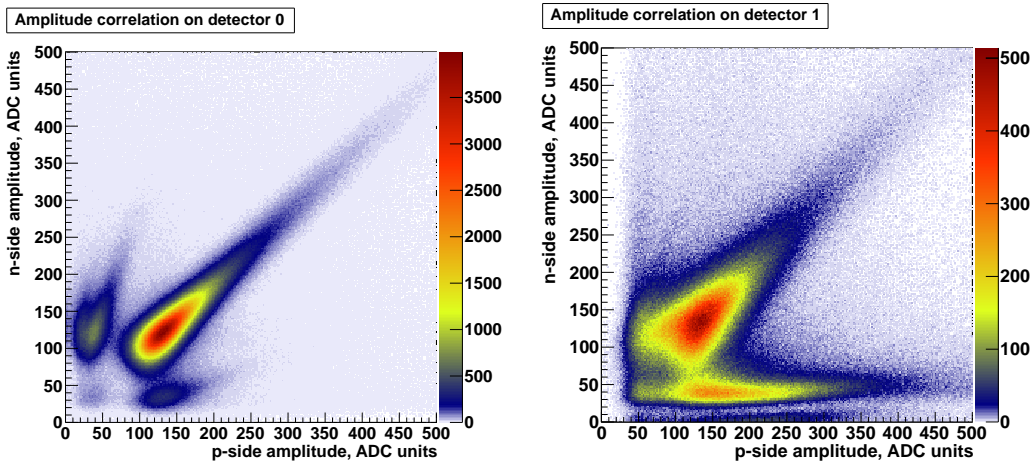


Figure 9.17: Correlation of the total cluster amplitude on the p- and the n-sides in stations 0 (left) and 1 (right). Correlation with the reference scintillator was required. Both detectors were operated at 80 V bias voltage (run 173).

9.6.3 Correlation of the total cluster amplitude on the p- and the n-sides

Ideally, one would expect to observe the same signal amplitude on the p- and n-side of the detector. This is because the free electrons and holes are produced in pairs. In a practical device the actual collected charge on the p- and the n-side may differ from each other because of possible charge collection inefficiencies. Studying of the correlation of the signal amplitude on the opposite sides is a powerful tool to investigate the charge collection.

Amplitude correlations plots have been produced based on the beam test data for both stations (Fig. 9.17). The only hit selection criterion, applied in this case, was the requirement of a coincidence with the scintillator. This requirement, however, does not have a significant impact on the result, because a similar selection is applied implicitly. Indeed, to plot the amplitude correlation, clusters on the opposite sides of the sensor, that coincide in time, are selected. If the noise hit rate is moderate, the probability of a random coincidence of a real hit with a noise hit on the opposite side is very small, so the noise is suppressed.

In the plots from the both stations, in addition to the main locus that is stretched along the diagonal, minor loci are observed. Detailed investigation showed that in the station 0 the minor loci appear because of incomplete cluster reconstruction in the cases when a fraction of the charge is collected on a dead strip. To confirm this, the correlation plots were produced using only the hits from the good-working region of the detector, and the results are shown in Figure 9.18. The side loci in the plot from station 0 disappeared. In the plot from the station 1 the minor locus is suppressed, but doesn't disappear. This effect was discussed

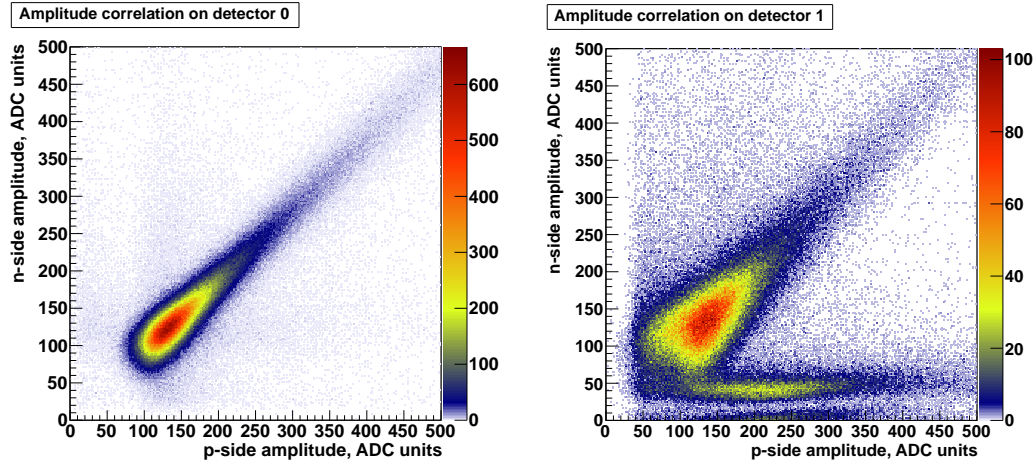


Figure 9.18: Correlation of the total cluster amplitude on the p- and the n-sides in stations 0 (left) and 1 (right). Correlation of the hits with the reference scintillator was required. Clusters from only the good regions of the detectors were selected. Both detectors were operated at 80 V bias voltage (run 173).

in the previous section.

On station 0 a clear amplitude correlation can be seen, as expected. A rough estimate of the ratio of the amplitudes, taking into account the difference of calibration coefficients for positive and negative signals (5.6), gives $A_{n-side}/A_{p-side} \approx 0.99$. The fact that there is no difference in the charge collection efficiencies is an indication for a good performance of the sensor.

In station 1 the ratio of the amplitudes is $A_{n-side}/A_{p-side} \approx 1.09$. This indicates a charge collection inefficiency on the p-side of at least 8% (assuming full charge collection on the n-side). The reason for this charge collection inefficiency is not known.

9.7 Major strip amplitude

In the previous sections the total cluster amplitude was examined in order to study the charge collection efficiency. Now the impact of the signal amplitude on the detection efficiency will be studied.

A particle is detected when the amplitude on at least one of the strips exceeds the threshold. The detection efficiency is therefore determined by the relation between the threshold and the amplitude on the major strip, i.e. the strip with the highest amplitude within the cluster.

The distributions of the major strip amplitude are shown in figs. 9.19 and 9.20. The hits from only the good regions of the detectors were selected, in order to avoid the misreconstruction of the clusters. No coincidence with the scintillator was required in order to see the noise.

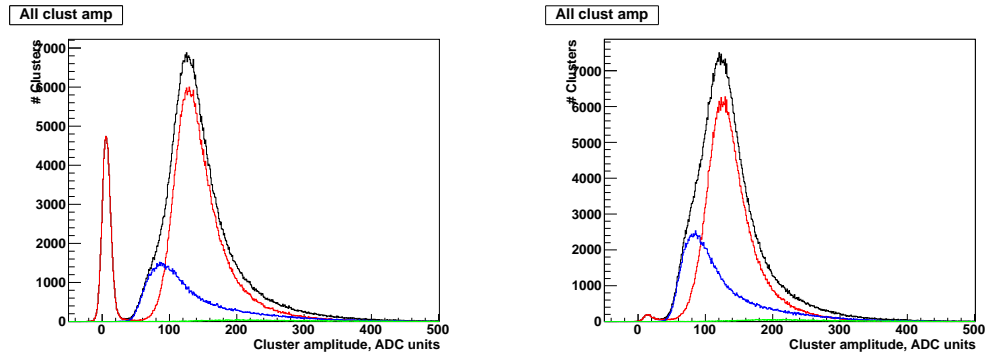


Figure 9.19: Distribution of the amplitude on the major strip within the clusters on the p-side (left), and the n-side (right) of the sensor in Station 0 (run 174, 70 V)

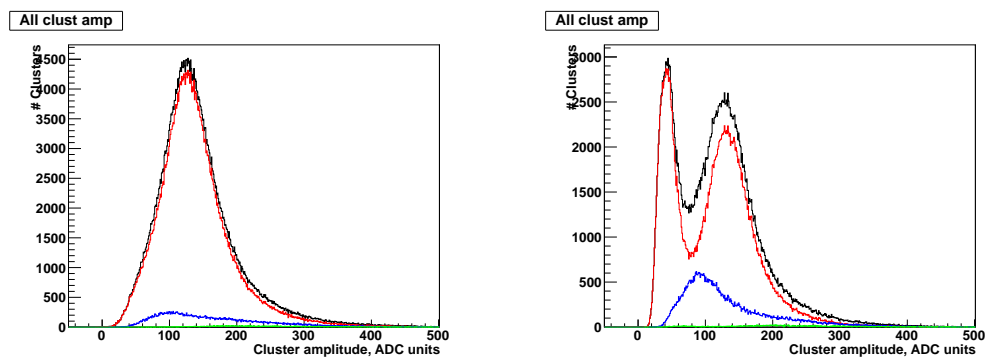


Figure 9.20: Distribution of the amplitude on the major strip within the clusters on the p-side (left), and the n-side (right) of the sensor in Station 1 (run 174, 70 V).

Station	Positive polarity			Negative polarity		
	ROC	n-XYTER	resolution	ROC	n-XYTER	resolution
0	0	0	7.0 ns	1	0	6.2 ns
0	0	2	6.5 ns	1	2	5.8 ns
1	3	0	8.7 ns	2	0	7.8 ns
1	3	2	7.0 ns	2	2	7.8 ns

Table 9.2: Time resolution of the prototype tracking detectors.

On the p-side of detector 0 the noise is clearly seen and well separated from the signal peaks. It is therefore possible to fully reject it either on the software or on the hardware level. On the n-side of the detector 0 only a tiny noise bump is seen. The noise is suppressed by the hardware threshold.

For both p- and n-side of detector 0, it is possible to increase the threshold up to 40 ADC units without any significant loss of the efficiency. This corresponds to $7.2 \pm 0.5 \text{ ke}^-$ for the p-side and $5.3 \pm 0.5 \text{ ke}^-$ for the n-side, according to the n-XYTER calibration (Section 5.6).

On the both sides of detector 1 the threshold cuts in the signal.

9.8 Time resolution

Taking the advantage of the beam test, the time resolution of the complete prototype detector system was measured.

Two ways of determining the time resolutions were considered. First, is to use the scintillator as the reference detector. In general, this requires to know the inherent time resolution of the scintillator, but, as it will be shown below, in the particular case the time measurement error of the scintillator can be neglected. The second way is to measure the time difference between hits in two silicon detectors, or in two n-XYTERs reading the same silicon detector. Assuming that the time resolution of the two readout chips together with the respective detectors are the same, the time resolution of each of them will be the $1/\sqrt{2}$ of the standard deviation of the time difference. The second method was rejected, because it was intended to compare the time resolutions of the chips and detectors with each other, rather than to assume them to be the same.

Selecting the first method, the time difference between hits in each of the n-XYTER chips and the scintillator was calculated. All possible combinations of the hits in the silicon detectors and the scintillator were considered. Examples of the obtained distributions are shown in Fig. 9.21. The distributions, related to other n-XYTER chips look similar. The distributions were fitted with Gaussians and the width was extracted and considered as the time resolution (see Table 9.2).

The time resolution of the scintillator was assumed to be better than 1 ns.

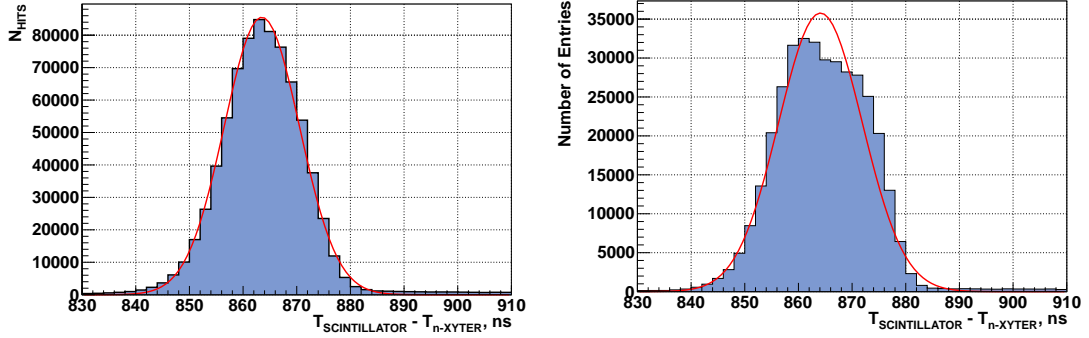


Figure 9.21: Amplitude on the main strip, left: p-side, right: n-side. (run 174, 70V, station 1).

It is because the scintillating material was a plastic, and the photomultiplier signal was read out with time walk compensated discriminator. The time of the scintillator signal was measured with one of the ROCs. If the above assumption is correct, the neglect of the scintillator time resolution introduces a systematic error, less than $5.8 - \sqrt{5.8^2 - 1^2} \approx 0.09$ ns (the extreme case of n-XYTER 2 on ROC 1 was considered).

The observed time resolution is considered as satisfactory.

9.9 Experience with the floating FEE

It was the first beam test of CBM-STS prototype detectors, when the readout electronics was operated in the floating mode. One problem, connected with this operation mode, was encountered: after a long operation time an increase of the consumption of the biasing current was observed. Later on it was found that this was caused by a current leakage in the FEE power supplies: the output terminals of the FEE power supplies, that are stated to be floating, were in fact, by design, connected to the ground over Zenner diodes for overvoltage protection. After a long operation time a leakage current ranging up to $15 \mu\text{A}$ developed in these Zenner diodes. This problem was solved for the future beam tests by replacing the Zenner diodes with spark gaps in all the FEE power supplies.

No other problems, connected with the floating FEE operation has been encountered.

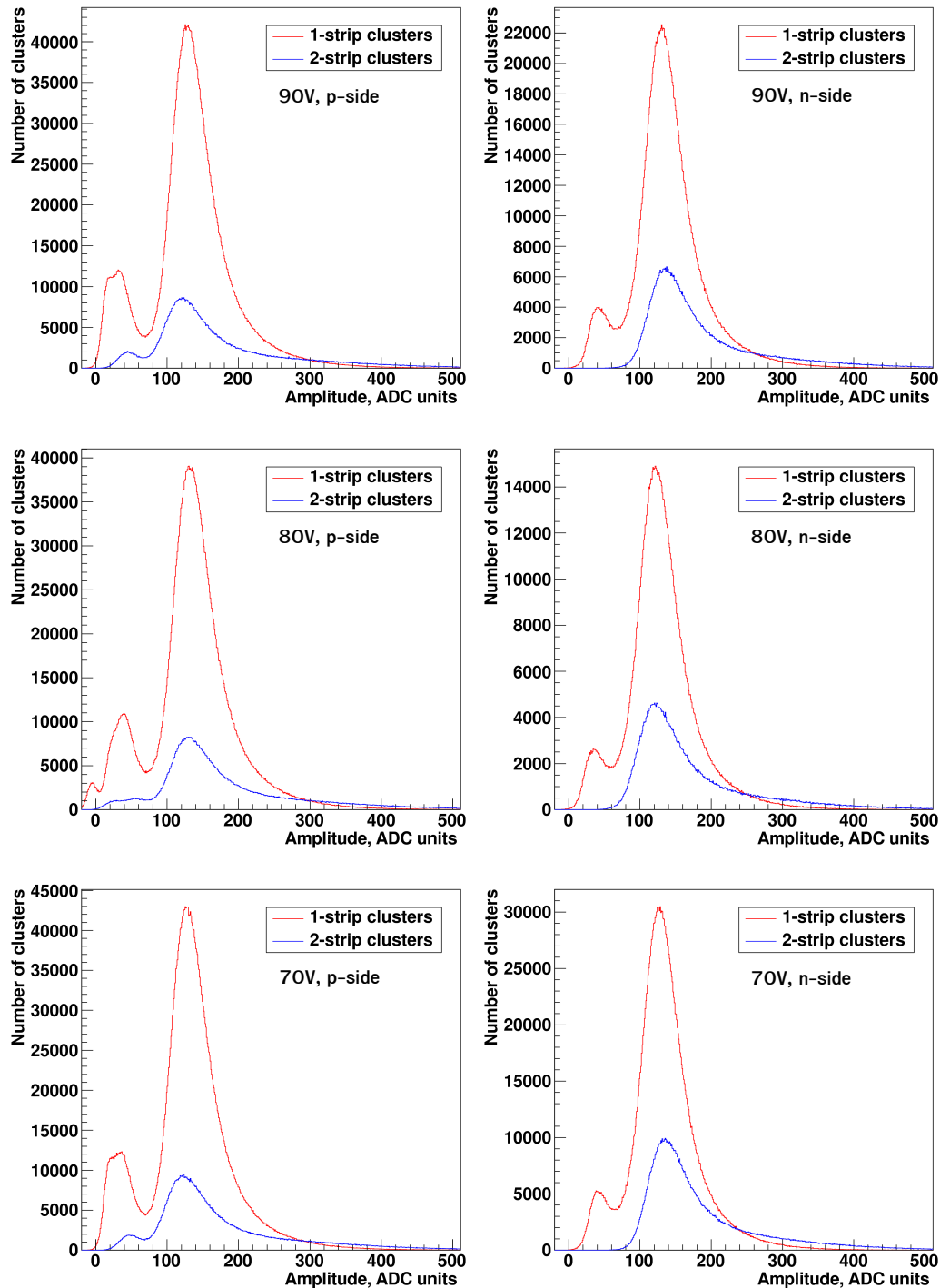


Figure 9.22: Distributions of the total cluster amplitude, from the p- and the n-side of station 0, obtained at various bias voltages. Coincidence with the scintillator signal was required. Clusters from the whole sensor area were considered.

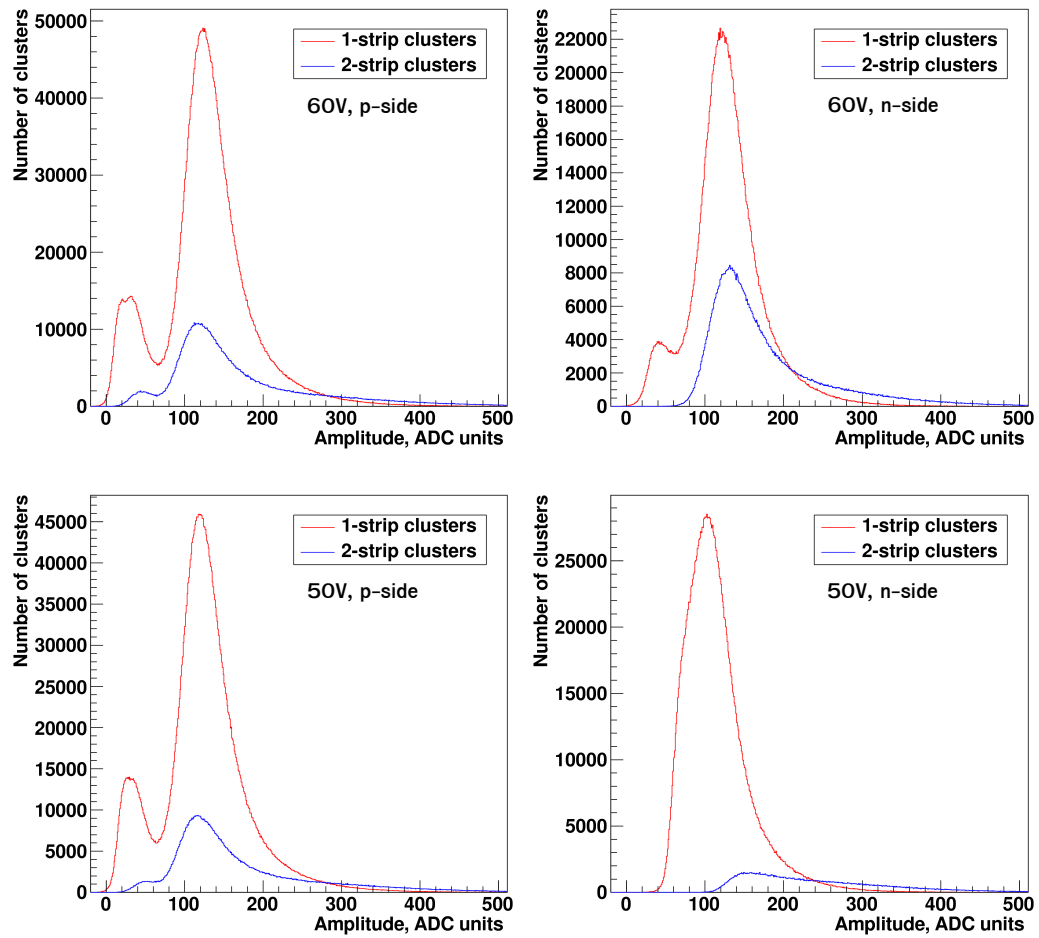


Figure 9.23: Distributions of the total cluster amplitude, from the p- and the n-side of station 0, obtained at various bias voltages. Coincidence with the scintillator signal was required. Clusters from the whole sensor area were considered.

Chapter 10

Test of the radiation hardness of CBM04 sensors on a proton beam

Radiation hardness is one of the main requirements to the STS sensors. Radiation load of up to 10^{13} n_{eq}/cm² is expected on the innermost sensors of the first stations during the operation at SIS-100, and up to 10^{14} n_{eq}/cm² at SIS-300.

Radiation hardness of the CBM04 sensors was tested in a proton beam at the Cooling Synchrotron (COSY) at Research Center Jülich (Germany). The sensors were irradiated beforehand with neutrons to fluences 10^{12} , 10^{13} , $3 \cdot 10^{13}$, and 10^{14} n_{eq}/cm². One sensor was left not irradiated. The intention was to test five sensors of bo4nx type, which proved to work well in the tests with a β^- source (Section 8.3). Unfortunately, because of mishandling, for the irradiation to $3 \cdot 10^{13}$, and 10^{14} n_{eq}/cm² sensors of bo5tb type were taken. After the irradiation the sensors were installed on fan-out boards as shown in Fig. 10.1 in order to connect them to the front-end electronics.

10.1 Experimental setup

The experimental setup included three STS tracking stations (Figure. 10.2). The sensors under test (CBM04) were by turns installed in the middle station. The outer two stations served as reference tracking detectors, and were based on the CBM02 sensors. On the same beamline a test of prototype GEM (Gas Electron Multiplier) detectors for the CBM Muon Detector was carried out. The GEM detector was installed behind the STS stations. In front and behind the setup two scintillating fiber hodoscopes were located. They were used as another reference tracking detectors with larger acceptance, but lower resolution, as compared to the STS reference stations. The forward hodoscope was used for triggering the n-XYTERs in the middle STS station.

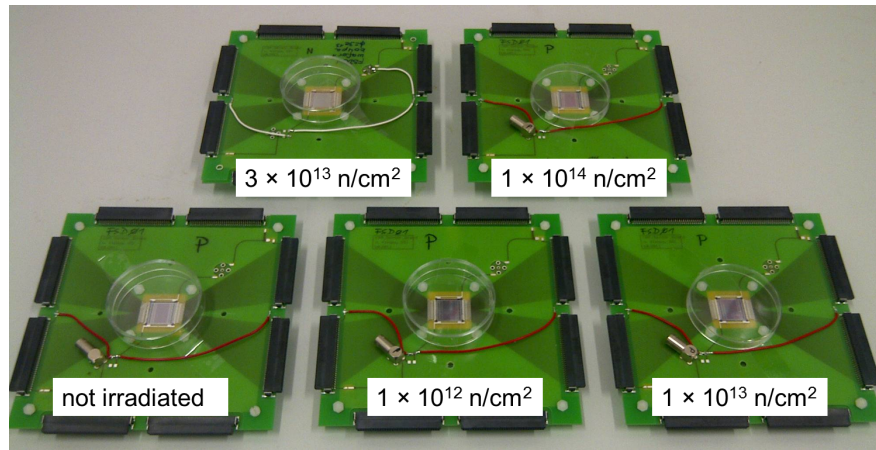


Figure 10.1: Sensors of the CBM04 type in the fan-out boards, prepared for the in-beam test.

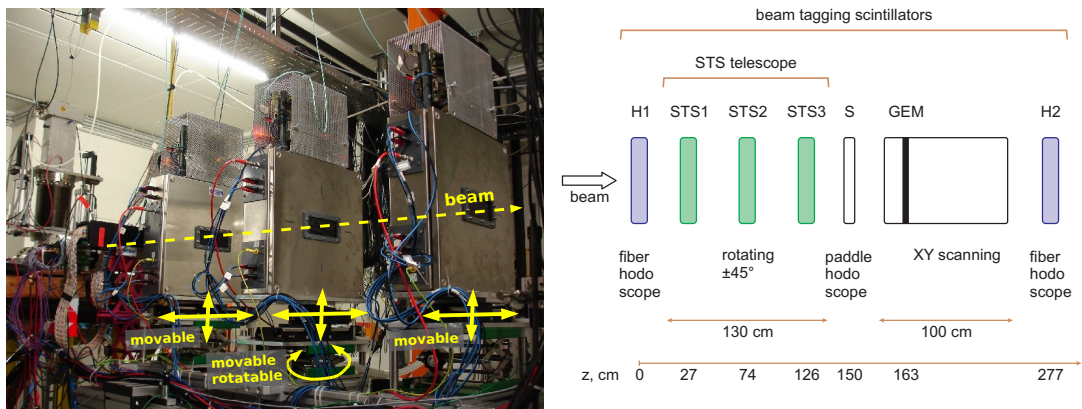


Figure 10.2: A sketch and a photograph of the in-beam test setup. See the text for details.

Because of a large electronic noise the middle STS station was operated in a triggered mode. In all other detectors (the reference STS stations, hodoscopes, GEM) the n-XYTERs were operated in the self-triggered mode.

The STS stations, as well as the hodoscopes were installed on remotely controlled moving tables. This helped in fine alignment of the detectors on the beam. It was also possible to rotate the middle station along the vertical axis (also remotely), in order to study how the detector response depends on the incidence angle of the particles.

10.2 Individual events and cluster reconstruction

In order to determine the total signal amplitude, clusters were reconstructed. In 8.2 the procedure of the cluster reconstruction for the case, when the front-end electronics is running in the self-triggered mode, is described. In that case the cluster is defined as an uninterrupted sequence of strips, on which hits were simultaneously registered. In contrast, when the front-end electronics is running in the triggered mode, a hit in each readout channel is generated in every event (Fig. 10.3). Therefore, to reconstruct clusters, a selection of hits, based on the amplitude has to be applied (zero suppression).

To reconstruct the clusters, the following procedure was applied: hits with amplitude higher than 40 ADC units (after the baseline subtraction) were selected, and considered as cluster seeds. If neighboring (in space and time) hits with amplitude more than 10 ADC units were found, they were attached to the seeds. Examples of events with 1- and 2-strip clusters are shown in Fig. 10.3.

10.3 1-strip cluster amplitude in irradiated sensors

Signal amplitude in 1-strip clusters was determined in each of the sensors. The obtained amplitude distributions are shown in Figs. 10.4, 10.5. In the spectra from the sensors of bo4nx type (0, 10^{12} and 10^{13} n_{eq}/cm^2 fluence) the Landau peaks can be clearly seen. Slight decrease of the amplitude, as well as slight broadening of the peak is observed in the sensor, irradiated to 10^{13} n_{eq}/cm^2 .

The amplitude distributions were fitted with a convolution of a Landau distribution and a Gaussian, and the most probable amplitude was extracted (Table 10.1). No degradation of the signal amplitude in the sensor, irradiated to 10^{12} n_{eq}/cm^2 , was observed as compared to the non-irradiated sensor. In the sensor, irradiated to 10^{13} n_{eq}/cm^2 , the relative degradation of the amplitude was 8 % and 18 % on the n- and the p-side respectively, which is considered as acceptable.

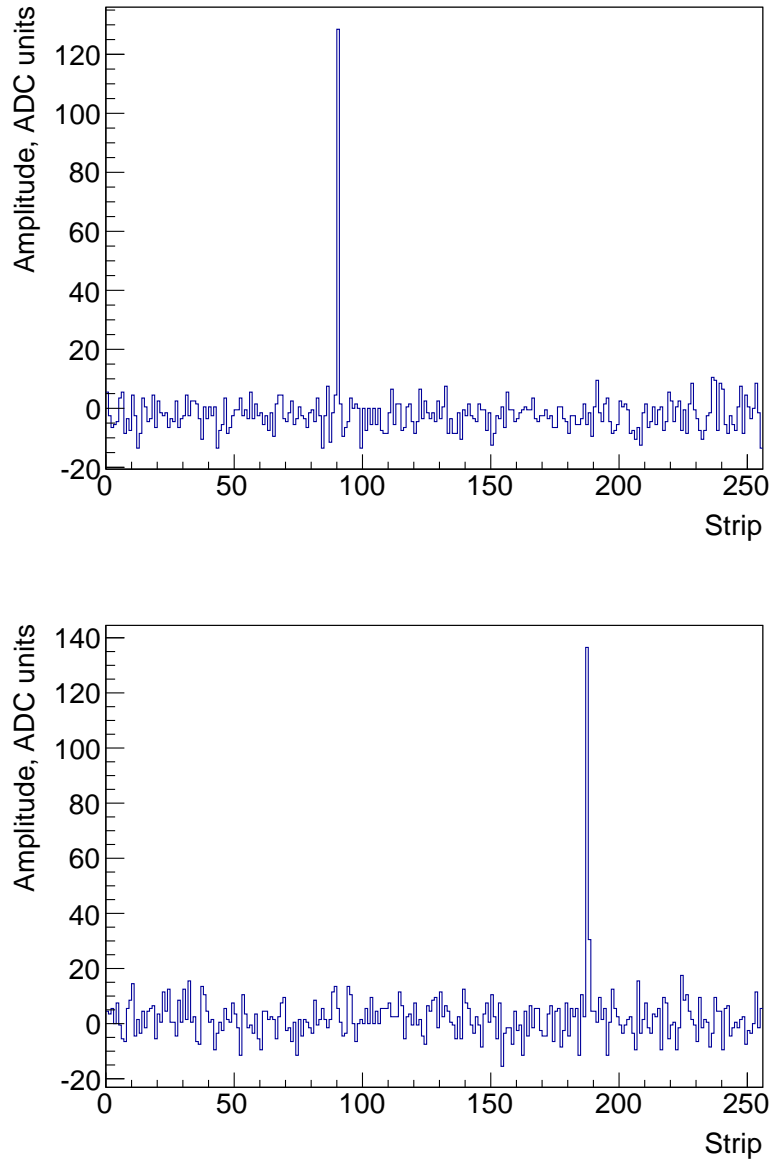


Figure 10.3: Examples of individual events in the CBM04 sensor, irradiated to 10^{12} $n_{\text{eq}}/\text{cm}^2$, operated at 60 V (middle STS station). Top: 1-strip cluster, bottom: 2-strip cluster.

Type	Fluence, $n_{\text{eq}}/\text{cm}^2$	Side	Amplitude, ADC units	Amplitude, ke^-	Amplitude, relative to non-irradiated
bo4nx	0	p	137 ± 3	18.0 ± 0.6	—
		n	131 ± 3	18.3 ± 0.6	—
bo4nx	10^{12}	p	135 ± 3	17.8 ± 0.6	0.99 ± 0.05
		n	129 ± 3	18.1 ± 0.6	0.99 ± 0.05
bo4nx	10^{13}	p	112 ± 3	14.8 ± 0.6	0.82 ± 0.04
		n	120 ± 3	17.0 ± 0.6	0.92 ± 0.04
bo5tb	$3 \cdot 10^{13}$	p	—	—	—
		n	—	—	—
bo5tb	10^{14}	p	—	—	—
		n	—	—	—

Table 10.1: Signal amplitude and charge collection efficiency (CCE) in irradiated CBM04 sensors.

The sensors, irradiated to the higher fluences ($3 \cdot 10^{13}$ and 10^{14} $n_{\text{eq}}/\text{cm}^2$) appeared inoperative. However, this is not necessarily because of the irradiation. Later studies have shown low signal amplitude in sensors of bo5tb type even without irradiation (8.3). As mentioned above, the bo5tb sensors were taken for irradiation by mistake. The intention was to test all sensors of bo4nx type.

10.4 Track fitting and residual distributions

To demonstrate the capability of track reconstruction, straight lines were fitted to the hits in all the detectors on the beam line. For this events with exactly one reconstructed spacepoint in each detector were selected.

Distributions of the residuals (difference between the reconstructed particle position and the position of the fitted line in the detector) were evaluated (Fig. 10.7). The X and Y position of the detectors in the global coordinate system was not known precisely enough, and was picked such that the pull distributions are centered at 0. The Z positions of all detectors were measured.

An example of event with a straight track fitted to the spacepoints in the detectors is shown in Fig. 10.6

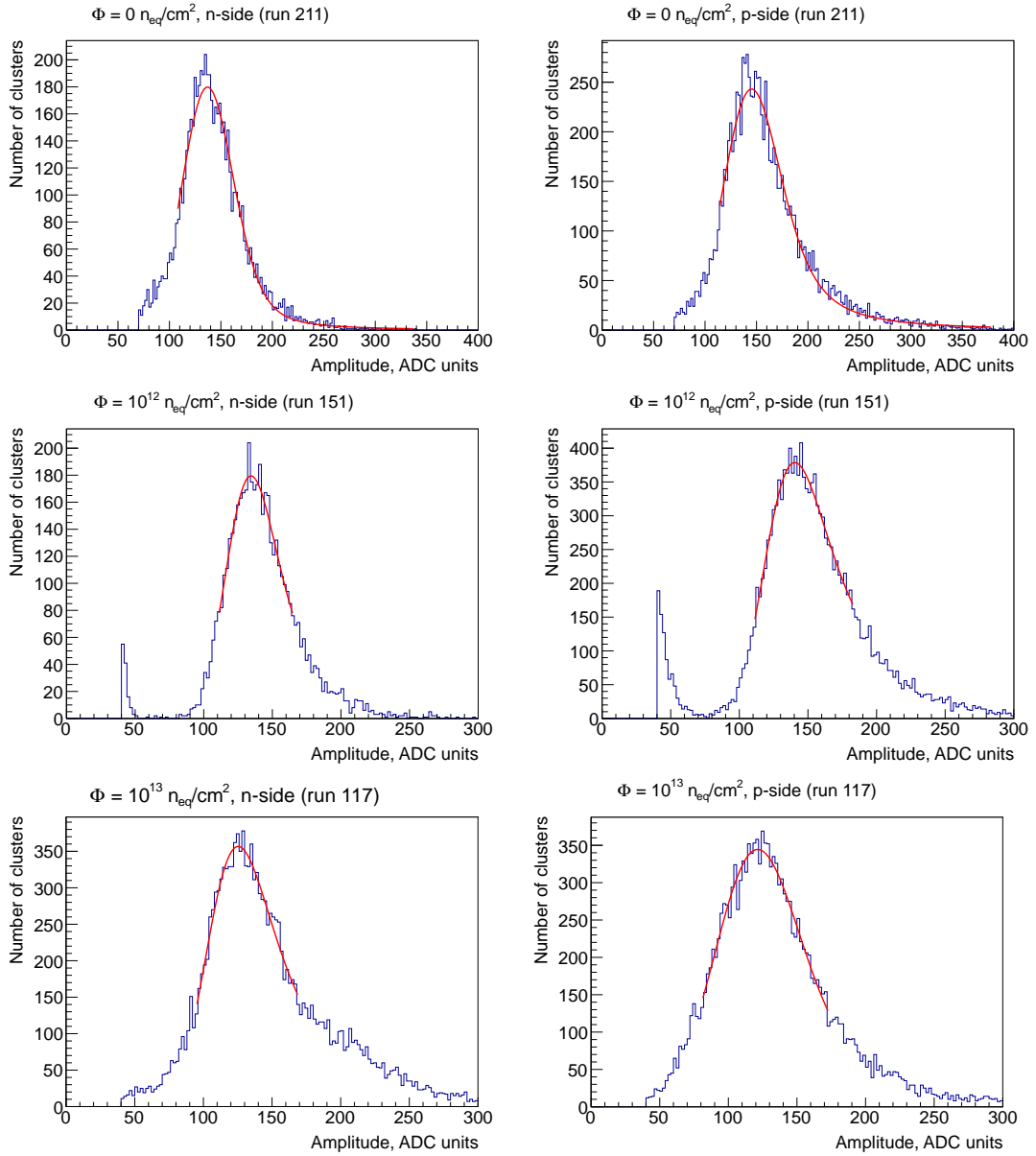


Figure 10.4: Amplitude distribution of 1-strip clusters on the n- (left) and p-side (right) of CBM04 sensors, irradiated to various fluences.

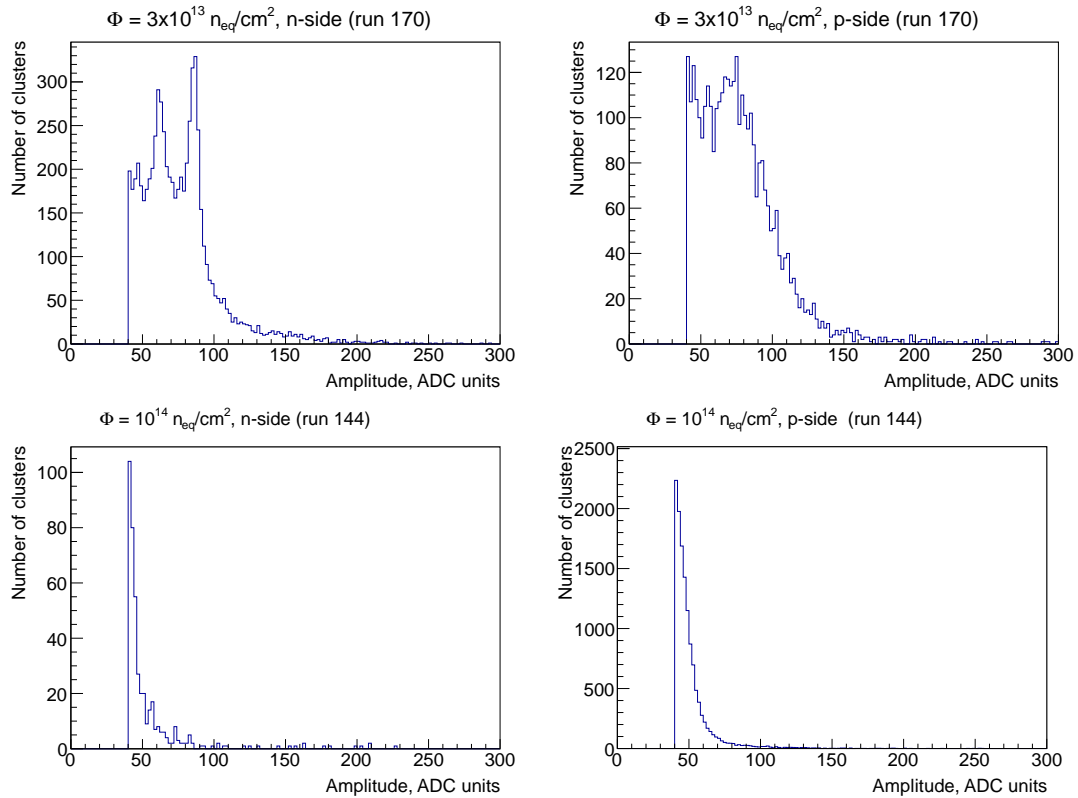


Figure 10.5: Amplitude distribution of 1-strip clusters on the n- (left) and p-side (right) of CBM04 sensors, irradiated to various fluences.

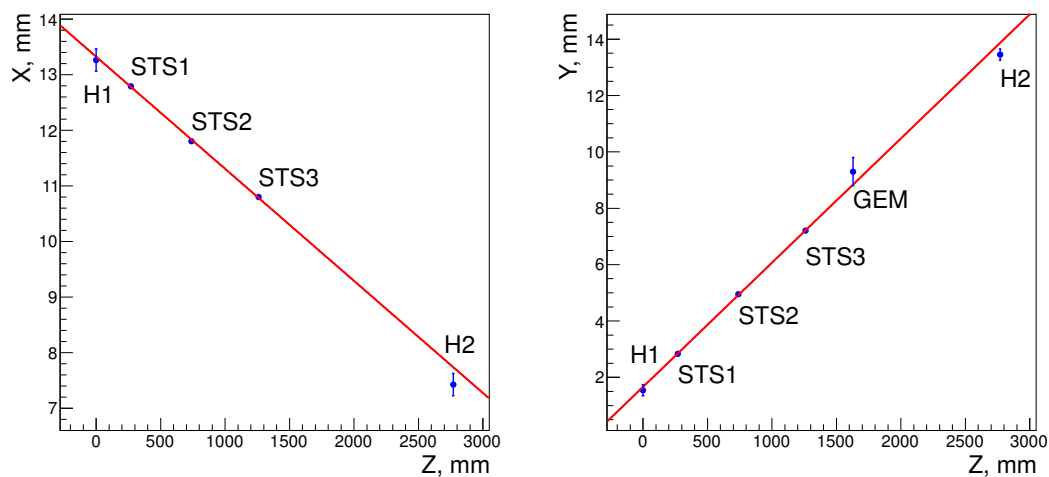


Figure 10.6: Track fit through all the detectors on the beamline.

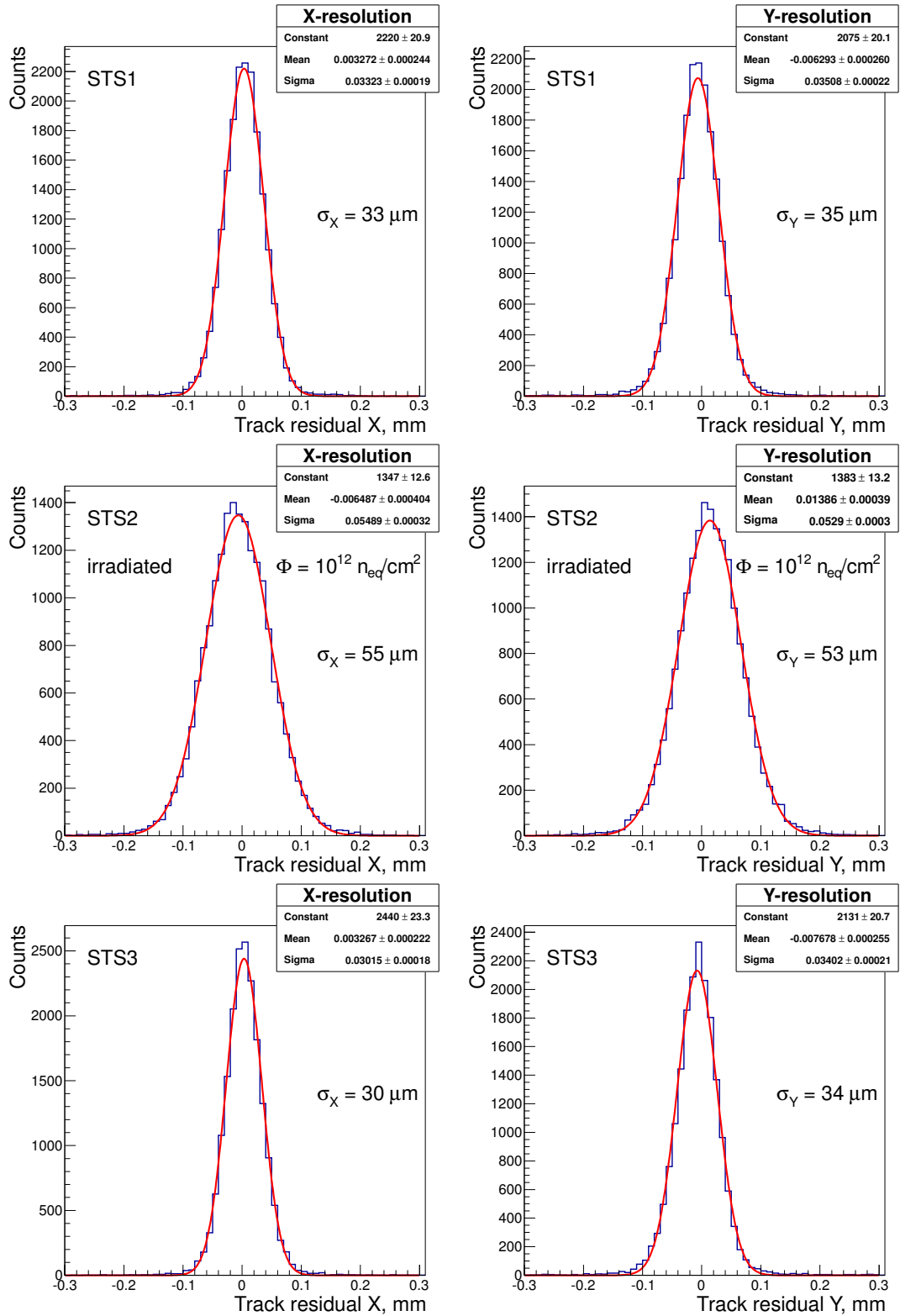


Figure 10.7: Residual distributions of the track fit.

Summary

The Compressed Baryonic Matter (CBM) experiment. The CBM experiment at FAIR will explore the phase diagram of strongly interacting matter in the region of high net baryonic densities. The interest to this region of the phase diagram is driven by the predictions of the deconfinement phase transition and restoration of the chiral symmetry at high net baryonic densities or temperatures. Investigation of these phenomena may help to understand fundamental properties of QCD — the confinement and the generation of mass.

Matter at extreme conditions will be studied in nuclear collisions. The rich physics program of CBM advances high demands to the detector system. In order to achieve unprecedented¹ statistics of probes, CBM has to operate on a fixed target at very high interaction rates, up to $10^6/s$ – $10^7/s$. The detector system has to enable efficient reconstruction of up to 1000 charged reaction products, measurement of momentum with the resolution close to 1 %, identification of the secondary vertices, reconstruction of the reaction plane, and excellent particle identification.

The Silicon Tracking System (STS). STS is the key component of the CBM. Its task is to reconstruct the charged reaction products and to measure their momenta. STS will be based on double-sided silicon strip sensors. The sensors will be arranged in eight planes (stations) in the aperture of the dipole magnet. The front-end electronics will be placed on the periphery, outside of the detector acceptance and connected to the sensors with low-mass microcables.

The main challenges in constructing the STS are: to cope with the large hit densities and rates, to keep the material budget down to $0.01 X_0$, to sustain the radiation load of up to $10^{13} n_{eq}/cm^2$ ($10^{14} n_{eq}/cm^2$ at SIS-300), to achieve a good time resolution and yet, keep the noise rate on the tolerable level, to integrate the readout electronics in a very constrained volume, remaining in the aperture of the superconducting magnet, and to evacuate 40 kW of power out of it.

Motivation and scope of this work. Important milestones in development of the STS is construction of prototype detectors and evaluation of their performance. In addition, on the way towards the pre-series and series production

¹in heavy ion collisions at these energies

of the components techniques and tools for their characterization and quality assurance need to be developed.

Within this work three similar prototype tracking detectors were built (2.3.2). Significant attention is paid to minimization of the electronic noise (Chapter 6). The choice of the of the grounding scheme is discussed (Section 2.3.1). Performance of the detectors is evaluated in measurements with radioactive sources, as well as on a proton beam. The major attention paid to the signal amplitude, as it is one of the most important detector characteristics, and because since long time a discrepancy between the expected and observed signal amplitude in the prototype CBM detectors was observed (e.g. [93]).

To calculate the expected signal amplitude an analytical model of the detector is developed (Section 3.1). The model parameters, related to the sensor, are measured in Chapter 4, and related to the front-end electronics — in Chapter 5. The described characterization techniques will also be used for quality assurance of the components during the pre-series and series production.

The value of work is both in the obtained results, and in the gained experience in constructing the detectors, and the developed characterization techniques.

Evaluation of the signal amplitude. First, an analytical model for accurate calculation of the expected signal amplitude was developed (3.1). The model takes into account the processes of charge sharing between the strips as well as the finiteness of the input capacitance of the front-end electronics. Similar models already existed earlier [42]. The distinctive feature of the developed model is that it correctly takes into account the fact that the charge is collected on the implant and not on the metal strip. As a result it is shown that the capacitance of an implant to the neighboring strips, and not the capacitance of a strip to the neighboring strips, is relevant for the process of the charge sharing between the strips. The measurements in the Sections 4.9, and 4.10 show a difference by factor of 1.5–2 between the latter two quantities.

The developed model is later used to calculate the expected signal amplitude in the prototype sensors. The model requires the following parameters: the coupling and the interstrip capacitances of the sensors, the capacitance of the analog cable (or the fan-out PCB), and the input capacitance of the front-end electronics.

Measurement of the passive electrical characteristics of the sensors. There are several reasons to measure the passive electrical characteristics of the sensors:

- they enter as parameters in models for the signal and the noise evaluation
- deviations of certain characteristics from their nominal values can indicate a defect in the sensor; therefore to measure the passive electrical characteristics is a good approach for the sensor quality assurance

- passive electrical characteristics are the macroscopic observables, which can be put in relation with the microscopic properties of the sensors, and can help to study the latter

Techniques for measuring the coupling capacitance, the capacitance of a strip to neighbors, and the capacitance of an implant to neighbors have been developed and described in details. Measurements on several prototype sensors have been performed. Most of the observed features on the C-f plots could be explained.

Techniques for measuring the interstrip resistance (4.5), the bias resistance (4.6), and the strip leakage current have been adopted from [56]. A contribution is made to the development of techniques for measuring the bulk I-V and C-V characteristics. In particular the appropriate values for the decoupling capacitors and resistors have been proposed and substantiated analytically. Detailed recommendations on using the LCR meter are also given (4.2).

The established methods for measuring the passive electrical characteristics will be used for the quality assurance of the sensors during the mass production. The bulk C-V and I-V characteristics, as well as the coupling capacitance of all strips will be checked for each sensor. The other characteristics will be checked only on the selected sensor samples, because of the complexity of the measurements.

Definition of the front-end electronics connection scheme for the prototype tracking detectors and the STS. Before assembling the prototype tracking detectors, the connection of the front-end electronics (FEE) to the sensor had to be defined (2.3.1). It turned out that there is more than one connection scheme possible (Figs. 2.10, 2.11, 2.12). The difference is in the connection of the ground of the front-end electronics to the sensor. The latter determines the potential of the front-end electronics with respect to the side of the sensor, that is read out. If the front-end electronics on the both sensor sides is at the same potential (Fig. 2.10 or 2.11), then a large voltage drop on the coupling capacitances of the sensor is set in. A breakdown of a single capacitor will make it impossible to bias the sensor and the whole detector (or detector module) becomes inoperative. It was therefore decided to use the floating connection scheme (Fig. 2.12), which does not suffer from such shortcoming. A breakdown, or other defect, of a coupling capacitor will lead in this case to malfunction of only the corresponding readout channel, while the rest of the detector can be operated normally.

It is decided to use the floating front-end electronics connection scheme in the STS.

Construction of the detector prototypes. After the front-end electronics connection scheme was defined, three prototype tracking detector stations were assembled (2.3.2, Fig. 2.13). The stations hosted various (CBM02, CBM03', and CBM04) prototype baby sensors, which were often exchanged. The sensors had

256 (CBM02, CBM04) or 192 (CBM03') strips per side at 90° stereoangle, and $50\ \mu\text{m}$ pitch (2.1).

Four n-XYTER chips (two per side) were used for the sensor readout. The temperature of the n-XYTERs was stabilized with water cooling, in order to minimize the baseline drift (5.1, 9.5).

The stations were assembled in metal boxes, which provided a mechanical protection of the fragile components as well as shielded the sensitive front-end electronics from external electromagnetic interference. It also protected the sensor from the ambient light.

The assembled tracking stations provided a basis for characterization of the prototype sensors with radioactive sources (Chapter 8), with an infrared laser [94, 95], and on the proton beam (Chapters 9, 10).

Reduction of the electronic noise in the detector prototypes. The major challenge in refining the above mentioned tracking stations was to identify and to suppress the sources of electronic noise. A particular difficulty was that even a millivolt level noise, that can not be detected with a normal oscilloscope, is tangible for the high gain front-end electronics.

It was found that the major source of noise is the digital back-end cables of the Front-End Boards (6.4). To suppress it the cables as well as the sensor were properly shielded. In addition, to shunt off the remaining pick-up, the FEBs were interconnected with each other and the sensor shield with large capacitors. To avoid the same problem in further prototypes, the front-end electronics is placed outside of the sensor shielding enclosure.

The noise of the power supply for biasing the sensor (6.1), as well as for powering the front-end electronics (6.2), was suppressed by the special LC-filters (Figs. 6.4, 6.5). In order to minimize the effect of the common mode noise of the FEE power supplies, the STS powering scheme is going to be designed symmetrically for the p- and the n-sides.

It was also found that the system is not protected against coupling of the noise through the 230 V power line. This can be easily improved by clamping the ferrite beads on the power cords, or by using the dedicated industrial network filters (for example [75]).

The last is the noise of the switched-mode DC-DC converters on the Read Out Controller board. To break its coupling the design of the board has to be changed.

Finally the noise level of around $700\ e^-$ was achieved, with channel-to-channel variation about $50\ e^-$. The noise was the same for all good-working CBM02, CBM03, and CBM04 sensors.

Characterization of the n-XYTER readout ASIC. The next step in preparation of the tracking stations to operation was the configuration and char-

acterization of the front-end electronics. Thus, the settings for n-XYTER registers `Vbfb` and `VbiasF` were optimized (5.3). The dependence of the n-XYTER response on the pulse duration (5.5) and on the series resistance (5.4) was measured to ensure that the latter two parameters do not affect the signal amplitude in the assembled prototype detectors. From the measured dependence of the n-XYTER response on the parallel capacitance the input capacitance of n-XYTER was extracted (5.4). The latter value is necessary for the amplitude calculation. The observed dependence of the noise on the input load was (5.4) does not agree with the n-XYTER simulations [36], and this discrepancy could not be explained.

In order to compare the measured signal amplitude to the expected from the model value, gain calibration of the n-XYTER chip was performed (5.6). A particular difficulty of this work was to measure the differentiating capacitor precisely (5.6.1). Finally, accuracy on the level of a few fF was achieved (0.1 %). The overall accuracy of the calibration was limited by the channel-to-channel gain variation (5.6.3). Finally, the obtained results were confirmed by the measurements with a silicon pad sensor (5.6.4). The n-XYTER calibration has been published in [96].

Test of the Rice formula for estimation of the noise rate. The work on n-XYTER characterization was extended with a study, related to the estimation of the noise rate in self-triggering systems. Self-triggering systems are intrinsically more vulnerable to the noise, than triggered ones. Indeed, in a triggered system a noise hit is produced only if: a) the noise exhibits a fluctuation, that exceeds the zero-suppression threshold, and b) this noise fluctuation coincides in time with the trigger signal. In contrast to that, in a self-triggering system a noise hit is produced already as soon as the noise fluctuation exceeds the threshold (no coincidence with any other signal is needed). An excessive noise rate can overwhelm the DAQ, and cause inadmissible losses of the physical data.

The noise rate can be estimated with the Rice formula [44, 45]. It is derived with the assumptions that the noise on the discriminator is Gaussian, and that the system has no dead time. These assumptions are not necessarily valid for real systems. The Rice formula was therefore tested on the n-XYTER chip (3.3.2). A reasonable agreement along more than six orders of magnitude ($1-10^6$ Hz per channel) was observed (Fig. 3.9). Since the front-end of the STS-XYTER (the dedicated STS readout chip), is similar to the front-end of n-XYTER, the Rice formula is considered to be applicable to STS-XYTER as well. It was already used to choose the rise times of the STS-XYTER shapers.

Detector operation and development of the basic data analysis procedures. In Chapter 7 the data acquisition and the data analysis software is described. Instructions on configuration of the electronics for various operation modes are given in Section 7.3. The contribution of the author is the detector-

specific analysis code (7.4) as well as the algorithm for the baseline subtraction for the n-XYTER. The algorithms for the cluster and spacepoint reconstruction are described in details in Section 8.2.

Results of measurements of the amplitude response with the radioactive sources and on the proton beam. The amplitude response of the various prototype CBM sensors was measured both with radioactive sources (^{90}Sr , ^{241}Am) and with a proton beam. Total signal amplitude within the reconstructed hit clusters was determined in each case (8.3, 9.6.2, 10.3). For most of the sensors, in the measurements with the β^- source as well as in the beam a clear Landau distribution can be seen and the signal is well separated from the noise. However, for all sensors the observed signal amplitude is systematically lower by 15–25% than the expected from the model. The reason for that is not identified. Most probably, it is connected with the design of the sensors, and not with the front-end electronics. Indeed, the dependence of the n-XYTER response on various conditions was studied in details, and the significant effects, such as the effect of charge division between the sensor and the n-XYTER due to the finite input capacitance of the latter, were taken into account.

The n-XYTER calibration is also considered to be correct, because it was confirmed by measurements with an independent signal source, a silicon pad diode. Moreover, this planar diode was fabricated on one of the CBM02 wafers.

One of the possible reasons, that could lead to observed amplitude deficit is an incomplete charge collection inside the sensors. The analytical model of the sensor, developed in 3.1, assumes that the charge is collected fully. The charge collection depends strongly on the configuration of the electrical field in the sensor, and that is considerably different in the silicon pad diode, and the strip sensors. The investigation of the charge collection processes in the sensors goes far beyond the scope of this thesis.

If a similar amplitude deficit will be observed for the CBM05 sensors, the investigation of this problem has to become one of the priority tasks for the STS group.

Test of radiation hardness of CBM04 sensors on the proton beam.

Radiation hardness of the CBM04 sensors was studied. No degradation of the signal amplitude after neutron irradiation to 10^{12} n_{eq}/cm² is observed. After irradiation to 10^{13} n_{eq}/cm², the signal amplitude drops down by 8 % and 18 % on the n- and the p-side respectively, which is considered as acceptable. Further studies with irradiation up to 10^{14} n_{eq}/cm² are still to be performed.

System tests in the experiments in the beam. In the experiments on the beam (Chapters 9, and 10), in addition to the evaluation of the performance of the detectors, a general test of the the complete system was done. This includes

the test of the data acquisition system, the online analysis software, and the slow control system, and the auxiliary infrastructure.

Various solutions, such as for example the readout with the floating electronics (9.9), the time synchronization with the deterministic latency messages [81], the remote operation of the auxiliary hardware with the EPICS control system [93], the stabilization of the n-XYTER baseline with the water cooling (9.5), and other, have proven their success. Techniques for detector operation and data analysis were worked out. Among the most representative results is the successful reconstruction of the tracks in the three prototype tracking stations, the two reference hodoscopes, and the GEM detector (10.4). In general, a reliable operation of all systems on a long-term scale was demonstrated.

Conclusions and outlook

Significant progress in development of the STS detector module is achieved. Prototype tracking detectors were constructed and refined in respect of the electronic noise. The gained experience in construction of the detectors will be applied in designing the STS detector module

Successful operation of the detector prototypes in the experiments in the proton beam was demonstrated. The CBM04 sensors are proven to withstand the radiation load of 10^{13} n_{eq}/cm². Further studies with irradiation up to 10^{14} n_{eq}/cm² are still to be performed.

Amplitude response of the assembled prototype detectors to β^- and γ radiation, as well as to 3 GeV/c protons was measured. With the sensor prototypes CBM02, CBM03', and CBM04 (assuming the same interstrip and coupling capacitance as in CBM02) the observed most probable signal amplitude is systematically lower by around 20 % than the expected. Presumably, it is connected with the design of the sensors. If a similar amplitude deficit will be observed with the newest CBM05 sensors, a detailed investigation of the effect has to be carried out.

Techniques for characterization of the sensors, the front-end electronics, and the complete detector systems were developed and worked out. They will be applied for quality assurance of the components during the pre-series and the series production, as well as for further studies of the detector properties for their realistic simulations.

Zusammenfassung

Das Compressed Baryonic Matter (CBM) Experiment. Das CBM-Experiment am Beschleunigerzentrum FAIR wird mit dem Ziel errichtet, das Phasendiagramm stark wechselwirkender Materie bei höchsten baryonischen Dichten zu untersuchen. Das Interesse an den Eigenschaften von Kernmaterie unter diesen Bedingungen ist motiviert durch Vorhersagen aus der Theorie zur Natur des Phasenübergangs von in Nukleonen eingeschlossenen zu freien Partonen, sowie zur Wiederherstellung der chiralen Symmetrie bei hohen baryonischen Dichten oder Temperaturen. Es wird allgemein erwartet, dass detaillierte Untersuchungen dieser Phänomene zum Verständnis fundamentaler Eigenschaften der Theorie der starken Wechselwirkung (Quanten Chromo Dynamik) beitragen können, insbesondere dem erwähnten “confinement” von Partonen sowie dem Zustandekommen der Nukleonmassen.

Materie unter extremen Bedingungen kann in Kollisionen von Kernen untersucht werden. Das reiche wissenschaftliche Programm des CBM-Experiments verlangt dazu hohe Anforderungen an das Detektorsystem. Um die von der CBM-Physik geforderten Meßstatistiken erzielen zu können, wird das Experiment die Strahlwechselwirkung mit einem stationären Target bei hohen Kollisionsraten bis zu $10^6/s$ – $10^7/s$ vermessen. Dabei müssen pro Kollision bis zu 1000 geladene Reaktionsprodukte mit hoher Effizienz vermessen und ihre Impulse mit einer Auflösung von etwa 1% bestimmt werden. Aus den Spurtopologien selbst müssen Zerfälle instabiler Teilchen erkennbar werden. Weitere wichtige Fähigkeiten umfassen exzellente Teilchenidentifikation und die Bestimmung von Eigenschaften gesamter Kollisionen, wie der Reaktionsebene.

Das Silicon Tracking System (STS). Das STS-Detektorsystem ist die zentrale Komponente des Experiments. Seine Aufgabe ist die Rekonstruktion der Bahnen der geladenen Reaktionsprodukte und die Bestimmung ihrer Impulse. Das Detektorsystem wird aus doppelseitigen Silizium-Mikrostreifensensoren aufgebaut, die in acht sogenannte Stationen integriert in die Öffnung eines supraleitenden Dipolmagneten eingebaut werden. Die Ausleseelektronik wird am Rande der Stationen angelegt, außerhalb der physikalischen Apertur, und mit den Sensoren über massearme Mikrokabel verbunden.

Die technischen Herausforderungen bei der Entwicklung und Konstruktion des

STS sind: Kompatibilität mit hohen Spurdichten und grosse Datenraten, geringes Materialbudget von etwa $0.01 X_0$ pro Station, Strahlenhärte der Sensoren bis zu $10^{14} \text{ n}_{\text{eq}}/\text{cm}^2$, Elektronik mit hoher Zeitauflösung und geringem Rauschen, Integration der Elektronik im verbleibenden Raum zwischen Sensoren und Magnet verbunden mit der Abführung von ihr produzierten Verlustleistung von bis zu 40 kW.

Motivation und Ziele dieser Arbeit. Wichtige Meilensteine bei der Entwicklung des STS-Detektorsystems sind die Konstruktion von Prototypen und die Auswertung ihrer Leistungseigenschaften. Des weiteren müssen Techniken und Werkzeuge zur Charakterisierung und Qualitätssicherung von Komponenten für die Serienproduktion entwickelt werden.

Im Rahmen dieser Arbeit wurden drei STS-Prototypen gebaut und evaluiert (siehe Kapitel 2.3.2). Besondere Aufmerksamkeit wurde auf die Minimierung des elektronischen Rauschens gelegt (siehe Kapitel 6). Die Wahl des Erdungsschemas wird in Kapitel 2.3.1 diskutiert. Die Leistungsdaten der Prototypen wurden im Laborbetrieb mit radioaktiven Quellen als auch im Test an einem Protonenstrahl bestimmt.

Zu den verschiedenen detaillierte Messungen zählten insbesondere Studien zu den Signalamplituden der verschiedenen Prototypensensoren. Um die zu erwartenden Signalhöhen bestimmen zu können, wurde ein analytisches Modell des Detektors entworfen (siehe Kapitel 3.1). Die Modellparameter wurden in Messungen bestimmt und sind für die Sensoren in Kapitel 4 und die Ausleseelektronik in Kapitel 5 dargelegt. Die dort entwickelten Techniken werden später zur Qualitätssicherung der Komponenten einsetzbar sein.

Die erzielten Ergebnisse, sowohl zu den Leistungseigenschaften der Prototypen als auch zur Vorgehensweise bei der Konstruktion der Detektoren und ihrer Auswertung, sind wichtige Zwischenschritte auf dem Weg zur Entwicklung des gesamten STS-Detektorsystems.

Auswertung der Signalhöhen. Als Referenz zu den Messungen wurde zunächst ein genaues Modell zur Berechnung der zu erwartenden Signalhöhen in den Mikrostreifensensoren entwickelt (siehe Kapitel 3.1). Das Modell berücksichtigt sowohl den Prozess der Ladungsverteilung auf benachbarte Streifen als auch die endliche Eingangskapazität der Ausleseelektronik. Während ähnliche Modelle schon früher eingesetzt wurden [42], besteht die Besonderheit dieses Modells darin, daß es korrekt die Ladungssammlung auf dem implantierten Streifen und nicht dem metallenen Auslestreifen wiedergibt. Als Ergebnis wird gezeigt, daß die Kapazität des Implantats zu den Nachbarstreifen und nicht die Kapazität des Auslestreifens zu seinen Nachbarn relevant für den Prozess der Ladungsteilung von benachbarten Detektorkanälen ist. Die Messungen, welche in den Kapiteln 4.9 und 4.10 diskutiert werden, zeigen Differenzen um einen Faktor

1.5–2 zwischen diesen beiden Größen.

Das Modell wird später zur Berechnung der erwarteten Signalgrößen in den Prototypensensoren angewandt. Es benötigt die folgenden experimentell zu bestimmenden Parameter: Die Kopplungs- und Zwischenstreifenkapazitäten der Sensoren, die Kapazität der Auslekabel oder des verwendeten Leiterbahnstruktur, und die Eingangskapazität der Ausleseelektronik.

Messung der passiven elektrischen Sensorparameter. Die Messungen der passiven Parameter der Sensoren hat folgende Motivation:

- sie gehen, wie oben dargelegt, in die Simulation von Signal und Rauschen ein;
- Abweichungen von ihren Nominalwerten kann Defekte in den Sensoren anzeigen. Die Messung der passiven elektrischen Parameter kann also zur Qualitätssicherung beitragen;
- Passive elektrische Parameter sind makroskopische Observablen, die zum Verständnis der mikroskopischen Parameter in Bezug gesetzt werden und somit zu ihrem Verständnis beitragen können.

Die Techniken zur Messung der Kopplungskapazitäten, der Kapazitäten zwischen Nachbarstreifen und zwischen Implant und seinen Nachbarn werden ausführlich beschrieben und anhand von Messungen an mehreren Prototypensensoren dargelegt. Die meisten der beobachteten Strukturen, etwa in Kapazitäts-Frequenz-Graphen, konnten so erklärt werden. Die Techniken zur Messung der Zwischenstreifenkapazität (siehe Kapitel 4.5), des Widerstandes zur Spannungsversorgung der Streifen (siehe Kapitel 4.6) und des Leckstroms einzelner Streifen wurden auf der Basis von Referenz [56] durchgeführt. Eine Weiterentwicklung wurde insbesondere zur Bestimmung der I-V und C-V Kennlinien gemacht und mit der Auswahl geeigneter Entkopplungskondensatoren und Widerständen und ihrer analytisch-rechnerischen Begründung motiviert. Auch detaillierte Empfehlungen zur Anwendung von LCR-Messinstrumenten wurden gemacht (siehe Kapitel 4.2).

Die so etablierten Methoden zur Messung der passiven elektrischen Charakteristiken werden zur Qualitätssicherung der Sensoren in der Serienfertigung Anwendung finden. Die globalen C-V und I-V-Charakteristiken als auch die Kopplungskapazitäten der einzelnen Streifen, können für jeden Sensor bestimmt werden. Andere Parameter werden nur an ausgewählten Objekten, d.h. stichprobenartig, bestimmt, begründet durch die Komplexität der Messungen.

Definition des Anschlußschemas der Ausleseelektronik. Im Vorfeld der Konstruktion der STS-Prototypdetektoren wurde das Anschlußschema der Ausleseelektronik an den Sensor definiert. Es stellte sich heraus, daß mehrere

Möglichkeiten existierten (siehe Abb. 2.10, 2.11, 2.12). Sie unterscheiden sich im Erdungsschema der Elektronik zum Sensor. Der Sensor bestimmt das elektrische Potential der Elektronik, je nachdem, auf welcher Sensorseite sie angeschlossen ist. Wären beide Elektroniken in Bezug auf das selbe Potential, dann läge eine große Spannungsdifferenz über den integrierten Kopplungskapazitäten einer Sensorseite (siehe Abb. 2.10 or 2.11). Schon der Durchbruch eines einzigen Kondensators würde den Betrieb des ganzen Detektors verhindern. Daher wurde die Ausleseelektronik so angeschlossen, dass die Potentialdifferenz nicht an dieser Stelle auftritt (siehe Abb. 2.12). Ein Durchbruch oder anderer Defekt eines Streifenkondensators führt somit nur zum Ausfall des betroffenen Kanals, während der Rest des Detektors funktionsfähig bleibt. Diese Anschlußschema wurde als Konstruktionsgrundlage für den gesamten STS-Detektor bestimmt.

Konstruktion der Prototypdetektoren. Unter Anwendung des obigen Elektronikaschlussschemas wurden drei Prototypen der STS-Detektorstationen gebaut, welche in Kapitel 2.3.2 und Abb. 2.13 beschrieben werden. In den Stationen kamen verschiedene Prototypen der CBM-Sensorentwicklung zur Anwendung (CBM02, CBM03', and CBM04), die auch für unterschiedliche Messungen ausgetauscht werden konnten. Die Sensoren waren kleine Testversionen der Vollgrößen-Prototypen und besaßen 256 (CBM02, CBM04) or 192 (CBM03') Streifen pro Seite unter 90° Stereowinkel und 50 μm Streifenabstand (siehe Kapitel 2.1).

Vier n-XYTER Chips (zwei pro Seite) wurden zur Auslese der Sensoren verwendet. Die Betriebstemperatur der Chips wurde durch eine Wasserkühlung stabilisiert, um die Drift der Nulllinie der Kanäle zu minimieren (siehe Kapitel 5.1, 9.5).

Die Stationen wurden in je einer Metallbox aufgebaut, welche sowohl mechanischen Schutz der fragilen Komponenten als auch Abschirmung der empfindlichen Ausleseelektronik von elektromagnetischen Interferenzen gewährleisteten. Auch dienten sie zum Schutz vor Umgebungslicht.

Die Detektorstationen boten eine Basis zur Bestimmung der Leistungsparameter bei der Erkennung von Signalen induziert mit radioaktiven Quellen (siehe Kapitel 8), mit einem fein fokussierten Infrarotlaser (siehe Kapitel [94, 95], und beim Betrieb in einem hochenergetischen Protonenstrahl (siehe Kapitel 9, 10).

Minimierung des elektronischen Rauschens in den Prototypdetektoren. Eine zentrale Herausforderung bei der Entwicklung und Inbetriebnahme der Prototypdetektoren war die Identifikation und Unterdrückung der Quellen elektronischen Rauschens. Eine besondere Schwierigkeit bestand darin, dass bei der äußerst empfindlichen Ausleseelektronik sogar Rauschen im Bereich von Millivolt, das mit normalen Oszilloskopen nicht detektiert werden kann, quasi zum Betriebsausfall führt. Es stellte sich heraus, daß die Hauptquelle des Rauschens das digitale Auslesekabel des Front-End Boards war (siehe Kapitel 6.4). Die Kabel

als auch die Sensoren wurden geeignet abgeschirmt. Weitere Verbesserung wurde durch Verbindung der einzelnen Ausleseboards durch große Kondensatoren erzielt. Dieses Problem wird bei weiteren Prototypdetektoren von vorneherein dadurch vermieden, dass sich die Elektronik außerhalb der Abschirmung befindet.

Der Beitrag der Hochspannungsversorgung des Sensors zum Rauschen (siehe Kapitel 6.1) als auch der Niederspannungsversorgung der Elektronik (siehe Kapitel 6.2) wurde durch speziell gefertigte LC-Filter unterdrückt (siehe Abb. 6.4 und Kapitel 6.5). Um den Effekt des Common-Mode-Rauschen weiter zu minimieren, wird das Spannungsversorgungsschema des STS symmetrisch bezüglich der p- und n-Seiten der Sensoren ausgelegt werden.

Es stellte sich heraus, daß das Prototypsystem nicht gegen Einkopplung von Rauschen über die 230 V Anschlußleitung geschützt war. Dies wurde einfach Anbringung von Ferriten am Versorgungskabel oder durch geeignete industrielle Filter (etwa wie in Referenz [75]) gelöst.

Als letzte Rauschquelle wurden die getakteten DC-DC Konverter auf den Read Out Controller Boards identifiziert. Nur ein geändertes Design der Boards kann weitere Abhilfe schaffen.

Characterisierung der n-XYTER Ausleseelektronik. Die weiteren Schritte zur Vorbereitung der Prototypdetektoren betrafen die Konfiguration und Charakterisierung der Ausleseelektronik. Dazu wurden die Einstellungen der n-XYTER Register `Vbfb` und `VbiasF` optimiert (siehe Kapitel 5.3). Die Abhängigkeit der n-XYTER Messung von der Pulslänge 5.5 und des Serienwiderstandes am Eingang (siehe Kapitel 5.4) wurde bestimmt, um eine Auswirkung auf die detektierte Signalhöhe ausschließen zu können. Aus der Abhängigkeit der Signalmessung auf die parallele Eingangskapazität wurde die Eingangskapazität pro Kanal des n-XYTER Chips bestimmt (siehe Kapitel 5.4). Die beobachtete Abhängigkeit des Rauschens von der Eingangslast (siehe Kapitel 5.4) stimmte nicht mit der Simulationserwartung (Referenz [36]) überein und konnte nicht erklärt werden.

Zum Vergleich der gemessenen Signalamplituden mit den aus dem Modell erwarteten wurde eine Kalibrierung des Verstärkungsfaktors im n-XYTER Chip durchgeführt. Eine Schwierigkeit dabei betraf die präzise Bestimmung des Differentialkondensators (siehe Kapitel 5.6.1). Schließlich wurde eine Genauigkeit im Bereich weniger fF erreicht, entsprechend etwa 0.1 %. Die letztlich erreichbare Genauigkeit bei der Kalibrierung wurde durch die Kanal-zu-Kanal-Variationen gegeben (siehe Kapitel 5.6.3). Die Ergebnisse wurden bestätigt durch Messungen von Quellen-induzierten Signalen in einem Silizium-Pad-Detektor. Die n-XYTER Kalibrierung wurde in Referenz [96] publiziert.

Test der Rice-Formel zur Bestimmung von Systemrauschen. Die Arbeiten zur Charakterisierung des n-XYTER Chips wurden mit einer Studie zur Be-

stimmung des Rauschens in einem selbst-triggernden Detektorsystem erweitert. Solche Systeme sind konstruktionsbedingt besonders anfällig auf Rauschen, was bei von außen getriggerten Anwendungen weit weniger der Fall ist. Denn in getriggerten Systemen wird ein Datensatz nur produziert, wenn a) das Rauschen eine gewisse Fluktuation jenseits der Schwelle der Nullunterdrückung überschreitet, und b) diese Fluktuation zeitlich mit dem Triggersignal zusammenfällt. In einem selbst-triggernden System wird dagegen ein durch Rauschen hervorgerufener Datensatz bereits erzeugt, wenn die Fluktuation größer als die gesetzte Schwelle ist; es wird keine weitere Koinzidenz mit einem anderen Signal benötigt. Massives Rauschen kann also das Datenaufnahmesystem überlasten und so unwiederbringlich Datenverlust verursachen.

Die zu erwartende Datenrate durch Rauschen kann mit der Rice-Formel (Referenz [44, 45]) abgeschätzt werden. Sie wird hergeleitet mit unter den Annahmen, dass das Rauschen des Diskriminators gaußisch ist und das System keine Totzeit hat. Diese Annahmen sind bei einem realen System nicht notwendigerweise gegeben. Daher wurde die Formel am n-XYTER chip getestet (siehe Kapitel 3.3.2). Eine bemerkenswerte Übereinstimmung über mehr als sechs Größenordnungen (1– 10^6 Hz pro Kanal) wurde festgestellt (siehe Abb. 3.9). Dies erlaubt einen Ausblick auf den dedizierten STS-Auslesechip STS-XYTER, der eine in den Grundzügen dem n-XYTER chip ähnliche Architektur besitzt. Schon während seiner Designarbeiten wurde die Anstiegsflanke seiner Shapers auf diesen Ergebnissen beruhend gewählt.

Betrieb der Prototypdetektoren und Entwicklung der Prozeduren zur Datenanalyse. Das Datenaufnahmesystem und die Analysesoftware werden in Kapitel 7 beschrieben. Eine Übersicht und Anleitung zur Konfiguration der Elektronik für verschiedene Betriebsmodi werden in Kapitel 7.3 behandelt. Der besondere Beitrag des Autors sind der detektorspezifische Analysecode (siehe Kapitel 7.4) als auch der Algorithmus zur Baseline-Kompensation in den Daten des n-XYTER Chips. Die Algorithmen zur Konstruktion von Ladungsclustern und der Rekonstruktion der Raumpunkte der Teilchenspuren im Detektor werden detailliert im Kapitel 8.2 behandelt.

Ergebnisse der Messung von Signalamplituden mit radioaktiven Quellen und im Protonenstrahl. Die Signalamplituden der verschiedenen CBM Prototypensensoren wurde sowohl mit radioaktiven Quellen (^{90}Sr , ^{241}Am) als auch in einem hochenergetischen Protonenstrahl gemessen. Dabei wurden die Signale, die zeitgleich auf benachbarten Sensorkanälen auftraten, zu einer Clusterladung zusammengefasst (siehe Kapitel 8.3, 9.6.2, 10.3). Bei den meisten Sensoren kann sowohl in den Messungen mit der β^- -Quelle als auch in Signalen vom Protonenstrahl die Landau-Signalverteilung klar erkannt werden. Das Signal ist klar vom Rauschen getrennt. Jedoch fällt auf dass bei allen Amplituden der gemessene

Wert systematisch 15–25% kleiner als vom Modell erwartet ausfällt. Der Grund für diese Abweichung konnte nicht gefunden werden. Jedoch wird vermutet, daß er im Sensordesign zu suchen und nicht ein Effekt der Ausleseelektronik ist. Es wurden ja detaillierte Studien der Signalmessung mit der n-XYTER Elektronik in Abhängigkeit verschiedener Faktoren durchgeführt, so wie der Effekt der Ladungsteilung zwischen Sensor und Auslesechip durch die endliche Eingangskapazität der Elektronik. Deren Kalibrierung wird auch als korrekt angesehen, denn sie wurde durch Messung mit Quellen und einer unabhängigen Signalquelle, einer Pad-Diode, bestimmt. Diese stammte sogar von einem der gleichen Wafer wie die untersuchten segmentierten Sensoren (CBM02).

Ein möglicher Grund, der zum beobachteten Amplitudendefizit führen kann, wäre eine unvollständige Ladungssammlung im Sensor. Das analytische Modell des Sensors, in Kapitel 3.1 entwickelt, nimmt eine vollständige Ladungssammlung an. Die Ladungssammlung hängt stark von der elektrischen Feldkonfiguration im Sensor ab und ist beim segmentierten Sensor deutlich anders als in der Pad-Diode. Die detaillierte Studie des Ladungssammelungsprozesses jedoch geht weit über die Zielsetzung dieser Arbeit hinaus.

Wenn ein ähnlicher Signalverlust bei den jüngsten Prototypsensoren CBM05 auftreten sollte, muss dieses mit Priorität untersucht werden.

Untersuchung der Strahlenhärte von CBM04 Sensoren im Protonenstrahl. Die Strahlenhärte des CBM04-Sensors wurde untersucht. Es wurde keine Abschwächung der Signalamplitude nach Neutronenbeschuss mit von 10^{12} $n_{\text{eq}}/\text{cm}^2$ festgestellt. Nach Neutronenbeschuss von 10^{13} $n_{\text{eq}}/\text{cm}^2$ fällt die die Signalamplitude um 8 % auf der n-Seite und um 18 % auf der p-Seite, was als akzeptabel angesehen wird. Weitere Studien mit Bestrahlung von bis zu 10^{14} $n_{\text{eq}}/\text{cm}^2$ stehen aus.

Systemtests unter Strahlbedingungen. Ein genereller Test des entwickelten Detektorsystems wurde unter Strahlbedingungen durchgeführt und wird in den Kapiteln 9 und 10 behandelt. Dabei wurden das Datenaufnahmesystem, die Online-Analysesoftware, und das Detektorkontrollsystem betrieben und bewertet.

Verschiedene konzeptionelle Ansätze und technische Lösungen, wie beispielsweise die Auslese der Sensoren mit “floating Elektronik (siehe Kapitel 9.9), die Zeitsynchronisation mit deterministischen “latency messages” (Referenz [81]), der ferngesteuerte Zugriff und Kontrolle von Betriebshardware mit dem EPICS Kontrollsystem (Referenz [93]), die Stabilisierung der Wasserkühlung (Referenz 9.5), sowie andere, haben ihre Tauglichkeit bewiesen. Geeignete Prozeduren zum Betrieb des Detektorsystems wurden ausgearbeitet. Unter den aussagekräftigsten Ergebnissen der Systemleistung muss die erfolgreiche Rekonstruktion von Protonenspuren mit den drei STS-Prototypstationen, den zwei Referenzodoskopen,

und einem GEM-Detektor genannt werden (siehe Kapitel 10.4). Es wurde ein verlässlicher Betrieb des gesamten Systems über einen langen Zeitraum demonstriert.

Schlussfolgerung und Ausblick. Die Arbeit detailliert wesentlichen Fortschritt bei der Entwicklung des STS-Detektormoduls. Verschiedene Prototypen wurden gebaut und insbesondere auf geringes elektronisches Rauschen hin optimiert. Die gewonnene Erfahrung beim Bau des Detektors wird in das Design und die Herstellung der finalen STS-Modulprototypen einfließen.

Die Funktionsfähigkeit der Detektoren konnte durch erfolgreichen Betrieb in einem Aufbau an einer Protonen-Strahllinie demonstriert werden. Anhand von CBM04 Prototypensensoren wurde eine Strahlungshärte von 10^{13} n_{eq} gezeigt. Weitere Studien mit Bestrahlung von bis zu 10^{14} n_{eq}/cm² stehen aus.

Die Amplitudenausbeute der zusammengebauten Prototyp-Detektoren bei Beschuss mit β^- - und γ -Strahlung sowie 3 GeV/c Protonen wurde vermessen. Die Sensor-Prototypen CBM02, CBM03', und CBM04 (unter der Annahme der zu CBM02 identischen Zwischenstreifen- und Kopplungskapazität) zeigen eine gegenüber dem analytischen Modell um etwa 20% reduzierte, wahrscheinlichste Amplitude. Vermutlich ist dies mit dem Sensordesign in Verbindung zu bringen. Wird ein vergleichbarer Amplitudenverlust ebenfalls bei der neuesten Sensorgeneration CBM05 beobachtet, muss eine detaillierte Untersuchung des Effekts erfolgen.

Zur Charakterisierung der Mikrostreifensensoren, der Ausleseelektronik und des gesamten Prototyp-Detektorsystems wurden Techniken und Prozeduren entwickelt und zur Anwendungsreife ausgearbeitet. Sie werden später in der Phase der Serienfertigung zur Qualitätssicherung der gefertigten Komponenten einsetzbar sein, sowie für weiterführende Studien zum detaillierten Verständnis des Detektorsystems.

References

- [1] N. Cabibbo and G. Parisi, Phys. Lett. B59, 67 (1975).
- [2] J. C. Collins and M. J. Perry, Phys. Rev. Lett. 34, 1353 (1975).
- [3] B. Friman et al., The CBM Physics Book Compressed Baryonic Matter in Laboratory Experiments, Springer (2011)
- [4] F. Karsch, E. Laermann and A. Peikert, Nucl. Phys. B605, 579 (2001).
- [5] Y. Aoki, G. Endrodi, Z. Fodor, S. D. Katz and K. K. Szabo, Nature 443, 675 (2006).
- [6] M. D'Elia, A. Di Giacomo, C. Pica, Phys. Rev. D72, 114510 (2005)
- [7] P. de Forcrand, O. Philipsen, JHEP 01, 077 (2007)
- [8] Z. Fodor, S. D. Katz, JHEP 0404 (2004) 050. Preprint: arXiv: hep-lat/0402006
- [9] S. Weinberg, The quantum theory of fields. Vol. 2: Modern applications, Cambridge University Press (1996)
- [10] B. C. Barrois, Nucl. Phys. B129, 390 (1977).
- [11] D. Bailin and A. Love, Phys. Rept. 107, 325 (1984).
- [12] R.D. Pisarski, Phys. Lett. B110, 155 (1982)
- [13] <http://www.fair-center.eu/>
- [14] W. Cassing, E.L. Bratkovskaya, and A. Sibirtsev, Nucl. Phys. A691 753 (2001)
- [15] A. Andronic, P. Braun-Munzinger, J. Stachel, Nucl. Phys. A772 167 (2006)
- [16] P. Koch, B. Müller, J. Rafelski Phys. Rep. 142, 167 (1986)
- [17] F. Antinori, et al. [NA57 Collaboration], J. Phys. G 32, 427 (2006) 723
- [18] S.V. Afanasiev, et al., Phys. Lett. B538, 275 (2002) 723

-
- [19] S.V. Afanasiev, et al., Phys. Rev. C66, 054902
- [20] C. Adler, et al., Phys. Rev. Lett. 90, 082302 (2003) 754
- [21] R. Rapp, J. Wambach and H. van Hees, in Relativistic Heavy-Ion Physics, edited by R. Stock and Landolt Brnstein (Springer), New Series I/23A (2010), arXiv:0901.3289 hep-ph
- [22] T. Matsui and H. Satz, Phys. Lett. 178B (1986) 416
- [23] R. Arnaldi, Nucl.Phys.A830 (2009) 345c
- [24] F. Karsch and E. Laermann, Quark-Gluon Plasma 3, Hwa and Wang (ed.) (2003).
- [25] M. Stephanov, K. Rajagopal, and E. Shuryak, Phys. Rev. Lett. 81, 4816–4819 (1998). arXiv:hep-ph/9806219v2
- [26] M.Stephanov, Phys. Rev. Lett. 102, 032301 (2009)
- [27] C. Drietsa, Design of the Micro Vertex Detector of the CBM experiment: Development of a detector response model and feasibility studies of open charm measurement, dissertation thesis, Frankfurt a.M., 2012.
- [28] M. Devaux. Development of fast and radiation hard Monolithic Active Pixel Sensors (MAPS) optimized for open charm meson detection with the CBM-vertex detector, dissertation thesis, Frankfurt a.M./Strasbourg, 2007.
- [29] J.Baudot, First Test Results of MIMOSA-26, a Fast CMOS Sensor With Integrated Zero Suppression and Digitized Output, IEEE Nuclear Science Symposium, Orlando (25-31 October 2009).
- [30] D. Kresan and C. Höhne, Event-by-Event Fluctuations of the K/p Yield Ratio in the CBM Experiment, CBM Progress Report 2008, p. 63 (2009)
- [31] Technical Design Report for the CBM Silicon Tracking System (STS), GSI, Darmstadt (2013)
- [32] <http://www.cismst.org/>
- [33] A. Kotynia, J. M. Heuser, CBM Progress Report 2011 (2012) 14
- [34] A. Webber et al., Impact of Radiation on VELO Sensors, VERTEX 2012
- [35] A. Affolder et al., Radiation damage in the LHCb Vertex Locator, arXiv 1302.5259 and J. Instr. 8 (2013) P08002
- [36] A.S. Brogna et al., n-XYTER reference manual, unpublished, <http://hipex.phys.pusan.ac.kr/drupal/sites/default/files/nXYTER.pdf>

-
- [37] A.S. Brogna et al., Nuclear Instruments and Methods in Physics Research Section A 568 (2006) 301–308
- [38] S.A. Bass et al, Prog. Part. Nucl. Phys. 41 (1998) 225
- [39] <http://wwwasd.web.cern.ch/wwwasd/geant>
- [40] I. Kisel, Event reconstruction in the CBM experiment, Nucl. Instr. Meth. Phys. Res. A566 (2006) 85
- [41] ALICE Inner Tracking System (ITS): Technical Design Report, Geneva 1999
- [42] C. Bozzi, Signal-to-Noise Evaluations for the CMS Silicon Microstrip Detectors, CMS Note 1997/026, 1997
- [43] H. Spieler, Semiconductor Detector Systems, Oxford University Press 2005.
- [44] Dabrowski et.al., “Notes on requirements on noise level and threshold matching for the DETNI ASIC and on design validation”.
- [45] S.O. Rice, “Mathematical analysis of random noise”, Bell System Techn. J. 23 (1944), 282.
- [46] Capacitance Measurements of HPK Full-sized Prototype Detector
http://hep.phys.s.u-tokyo.ac.jp/SVD/SVD0/Capacitance_HPK.html
- [47] Capacitance measurements of SII full-size prototype detector
http://hep.phys.s.u-tokyo.ac.jp/SVD/SVD0/Capacitance_SII.html
- [48] 7600 Precision LCR Meter Model B Instruction Manual, QuadTech Inc., 1997. http://www.testequipmentdepot.com/quadtech/pdf/7600_man.pdf
- [49] LCR Measurement Primer, 3rd Edition, Quadtech, July 2003.
www.oz6frs.dk/oz6frsold/2004/DATAblade/LCR-primer.pdf
- [50] Belden, 8216 Coax - RG-174/U Type, detailed Specifications & Technical Data, metric measurement version.
www.belden.com/techdatas/metric/8216.pdf
- [51] RD50 Technical Note 2003/03 Version 5/15.10.04
http://rd50.web.cern.ch/rd50/doc/Internal/rd50_2003_003_version_15-10-2004.doc
- [52] <http://rd50.web.cern.ch/>
- [53] Petra Riedler, Radiation Damage Effects and Performance of Silicon Strip Detectors using LHC Readout Electronics, Dissertation, 1998, Wien.

- [54] D. Bortoletto, Development of thin silicon sensors for tracking,
http://www.hep.uiuc.edu/LCRD/LCRD_UCLC_proposal_FY05/5_17_bortoletto_silicon.pdf
- [55] Yoshinobu Unno, private communication
- [56] A.Chilingarov, Interstrip resistance measurement, RD50 Technical Note, 2010. <http://cds.cern.ch/record/1405706/files/PH-EP-Tech-Note-2011-001.pdf?version=1>
- [57] P. Dolejschi et al., Interstrip Parameters on Silicon Sensors for the Belle II Vertex Detector, submitted to Elsevier.
http://www.hephy.at/fileadmin/user_upload/Publikationen/Interstrip_Parameters_on_Silicon_Sensors_for_the_Belle_II_Vertex_Detector.pdf
- [58] S. Lindgren et al. "Interstrip characteristics of n-on-p FZ silicon detectors," Nuclear Science Symposium Conference Record (NSS/MIC), 2009 IEEE , vol., no., pp.157,162, Oct. 24 2009-Nov. 1 2009 doi:10.1109/NSSMIC.2009.5401828
- [59] M.M Angarano, et al. Nuclear Instruments and Methods in Physics Research Section A, 477 (2002) 308-312 doi:10.1016/S0168-9002(01)01841-1
- [60] P. Dolejschi, Characterisation of interstrip parameters on silicon sensors for the Belle II vertex detector, Diploma thesis, TU Wien, 2012.
http://www.hephy.at/fileadmin/user_upload/Publikationen/Diplomarbeit%20Paul.pdf
- [61] K. Hara et al., Beam splash effects on ATLAS silicon microstrip detectors evaluated using 1-w Nd : YAG laser, Nucl. Instr. Meth. A 541 (2005) pp. 15–20. DOI:10.1016/j.nima.2005.01.033
- [62] K. Hara et al., Design of Punch-Through Protection of Silicon Microstrip Detector against Accelerator Beam Splash, Physics Procedia 37 (2012) pp. 838–843 (Proceedings of TIPP 2011) DOI:10.1016/j.phpro.2012.02.427
- [63] E. Barberis, Measurement of Interstrip and Coupling Capacitances of Silicon Microstrip Detectors, Conference Record of the 1992 IEEE
DOI:10.1109/NSSMIC.1992.301193
- [64] E. Barberis, Nucl. Instr. Meth. A342 90-95 (1994)
- [65] M. A. Frautschi, Capacitance Measurements of Double-Sided Silicon Microstrip Detectors (1995), CDF Note CDF/DOC/SEC VTX/CDFR/2546
http://www-cdf.fnal.gov/physics/preprints/cdf2546_svxii_capacitance.ps

-
- [66] A. Chilingarov, D. Campbell, G. Hughes, Interstrip capacitance stabilization at low humidity, Nucl. Inst. Meth. A 560 (2006) 118–121
<http://dx.doi.org/10.1016/j.nima.2005.11.198>
- [67] N. Abel et al., CBM Progress Report 2007 (2008) 53
- [68] J. Adamczewski-Musch, H.G.Essel, S. Linev, IEEE TNS Vol.58, No.4, August 2011, pp. 1728-1732
- [69] Huber+Suchner data sheet RF attenuator: Type 6820.01.A
<http://www.hubersuhner.com.sg>
- [70] AECQ MLCC Automotive Capacitors Qualified to AEC-Q200
<http://www.farnell.com/datasheets/1010757.pdf>
- [71] Thin Film Technology. Accu-F / Accu-P. Thin Film RF/Microwave Capacitors
<http://www.farnell.com/datasheets/88813.pdf>
- [72] M. S. Basunia, Nuclear Data Sheets 107, 3323 (2006)
<http://www.nndc.bnl.gov/chart/decaysearchdirect.jsp?nuc=241AM&unc=nds>
- [73] Double-laboratory power supplies serie EA-PS 2000
<http://www.farnell.com/datasheets/27742.pdf>
- [74] Programmable 3[4] Channel High-Performance Power Supply HMP4030 [HMP4040], Datasheet
[http://www.hameg.com/datasheets.0.html?&no_cache=1&tx_hmdownloads_pi1\[mode\]=download&tx_hmdownloads_pi1\[uid\]=3554](http://www.hameg.com/datasheets.0.html?&no_cache=1&tx_hmdownloads_pi1[mode]=download&tx_hmdownloads_pi1[uid]=3554)
- [75] Epcos general-purpose filters with normal insertion loss, Type: B84111A, Data sheet. http://www.epcos.com/inf/30/db/emc_fi_06/b84111a.pdf
- [76] I. Sorokin, *RF pickup on nXYTER from ... nXYTER!*, talk on CBM-STG Group Meeting, August 25, 2010.
http://cbm-wiki.gsi.de/pub/STS/25Aug2010/nX_pickup.pdf
- [77] H. Ott Noise reduction techniques in electronic systems, 2nd ed., Wiley, 1988
- [78] <http://root.cern.ch>
- [79] <http://go4.gsi.de>
- [80] <http://www.aps.anl.gov/epics/>
- [81] N. Abel, S. Manz, U. Keschull, GSI Scientific Report 2009 323 (2010)

-
- [82] H. Flemming, H. Deppe CBM Progress Report 2012 70 (2013)
- [83] F. Lemke, S. Schenk and U. Bruening, The Hierarchical CBM Network Structure and the CBMnet V2.0 Protocol, DPG Spring Meeting, March 19-23, 2012, Mainz, Germany
- [84] J. Gebelein et al., CBM Progress Report 2012 87 (2013)
- [85] <http://qt.digia.com/>
- [86] <http://css.desy.de/>
- [87] J.M. Heuser et al., CBM Progress Report 2009 8 (2010)
- [88] V. Friese et al., CBM Progress Report 2009 9 (2010)
- [89] Nuclear Data Sheets 82, 379 (1997)
<http://www.nndc.bnl.gov/chart/decaysearchdirect.jsp?nuc=90SR&unc=nds>
<http://www.nndc.bnl.gov/chart/decaysearchdirect.jsp?nuc=90Y&unc=nds>
- [90] Nuclear Data Sheets 109, 943 (2008)
<http://www.nndc.bnl.gov/chart/decaysearchdirect.jsp?nuc=106RU&unc=nds>
<http://www.nndc.bnl.gov/chart/decaysearchdirect.jsp?nuc=106RH&unc=nds>
- [91] <http://www.fz-juelich.de/>
- [92] <http://www.fz-juelich.de/ikp/cosy/en/>
- [93] J. M. Heuser et al., CBM Progress Report 2010 19 (2011)
- [94] P. Ghosh, J. Eschke, CBM Progress Report 2012 12 (2013)
- [95] P. Ghosh, Quality Assurances for double-sided silicon microstrip sensors in the Silicon Tracking System of the CBM Experiment at FAIR, PoS (Bormio 2013) 018
http://pos.sissa.it/archive/conferences/184/018/Bormio%202013_018.pdf
- [96] I. Sorokin et al., Nucl. Instr. Meth. A 714 136-140 (2013).
DOI:10.1016/j.nima.2013.02.013

Acknowledgements

Carrying out of this work would not be possible without the promotion of Peter Senger, Valeriy Pugatch, Johann Heuser, and the Helmholtz Graduate School for Heavy Ion Research (HGS-HIRe). To them I express my deep gratitude for this excellent opportunity.

Working on a Ph.D. has been an exciting and unforgettable experience. To a considerable degree this is owing to the friendliness and openness of the whole CBM team, which I appreciate sincerely. Special thanks to Johann Heuser for his inexhaustible patience and invariably positive attitude. Thanks to Volker Kleipa, Christian Schmidt, Carmen Simons, and Sergey Linev for the provided technical support. A particular pleasure was to work with Walter Müller, and to learn from him a great variety of interesting, and sometimes amusing facts about electronics and technology. I am grateful to Christian Sturm, Peter Senger, and Piotr Koczon for reviewing the text, as well as to Anton Andronic for his help as the external supervisor.

I also want to thank to the Helmholtz Research School for Quark Matter Studies (H-QM) for the numerous lecture weeks and other educational events they organized.

I am deeply indebted to my friends, Vitalii Ozvenchuk, and Valentina Akishina, whose company was so important for me at tough times, and with whom I spend the best and unforgettable moments of these four years.

Here I want to recollect my school teacher of physics and informatics, Yuri Yakovlevich Pasichov, and make a special mention of his devotion to his job which laid the foundation for my career as a physicist.

Finally, I want to thank to my Family for all they have been doing for me.

Iurii Sorokin

GSI Helmholtzzentrum für Schwerionenforschung GmbH
Planckstr. 1, 64291 Darmstadt ◦ Room: KBW.2.003
Phone: +49-6159-71-1612
E-mail: i.sorokin@gsi.de

Born: 14.12.1987, Vinnitsa, Ukraine.



Education:

- 04.2010 – 02.2014 Ph.D. in Physics, GSI Helmholtzzentrum für Schwerionenforschung GmbH, Darmstadt (enrolled to Goethe University Frankfurt).
Dissertation title: “*Characterization of silicon microstrip sensors, front-end electronics, and prototype tracking detectors for the CBM experiment at FAIR*”.
Supervisor: Prof. Dr. Peter Senger.
- 09.2008 – 06.2009 M.S. in Nuclear and Elementary Particle Physics, Taras Shevchenko National University of Kyiv. Thesis title: “*Development of prototype silicon strip detector module for the CBM experiment*”.
Supervisor: Prof. Dr. Valeriy Pugatch.
- 09.2004 – 06.2008 B.S. in Physics (honors diploma), Taras Shevchenko National University of Kyiv. Thesis title: “*Matching of muon track segments in the ZEUS detector*”. Supervisor: Dr. Vladimir Aushev.

Employment history:

- 12.2008 – 04.2010 Kyiv Institute for Nuclear Research, Engineer
- 01.2008 – 11.2008 Deutsches Elektronen-Synchrotron DESY, Hamburg, Guest scientist
- 01.2006 – 03.2006 National Taras Shevchenko University of Kyiv, Physics department, Engineer

Awards:

Prize-winner in the scholar competitions in physics, informatics, mathematics and chemistry of up to all-Ukraine level